Soils and Rocks

Volume 43, N. 1

2020

ISSN 1980-9743

Soils and Rocks

Soils and Rocks

An International Journal of Geotechnical and Geoenvironmental Engineering

Volume 43, N. 1
January-March 2020

SOILS and ROCKS

An International Journal of Geotechnical and Geoenvironmental Engineering

Editor Renato Pinto da Cunha - University of Brasília, Brazil

Co-editor José Couto Marques - University of Porto, Portugal

Soils and Rocks publishes papers in English in the broad fields of Geotechnical Engineering, Engineering Geology and Geoenvironmental Engineering. The Journal is published in March, June, September and December. Subscription price is US$ 90.00 per year. The journal, with the name "Solos e Rochas", was first published in 1978 by the Graduate School of Engineering, Federal University of Rio de Janeiro (COPPE-UFRJ). In 1980 it became the official magazine of the Brazilian Association for Soil Mechanics and Geotechnical Engineering (ABMS), acquiring the national character that had been the intention of its founders. In 1986 it also became the official Journal of the Brazilian Association for Engineering Geology and the Environment (ABGE) and in 1999 became the Latin American Geotechnical Journal, following the support of Latin-American representatives gathered for the Pan-American Conference of Guadalajara (1996). In 2007 the journal acquired the status of an international journal under the name of Soils and Rocks, published by the Brazilian Association for Soil Mechanics and Geotechnical Engineering (ABMS), Brazilian Association for Engineering Geology and the Environment (ABGE) and Portuguese Geotechnical Society (SPG). In 2010, ABGE decided to publish its own journal and left the partnership.

Soils and Rocks

1978,	1 (1, 2)
1979,	1 (3), 2 (1,2)
1980-1983,	3-6 (1, 2, 3)
1984,	7 (single number)
1985-1987,	8-10 (1, 2, 3)
1988-1990,	11-13 (single number)
1991-1992,	14-15 (1, 2)
1993,	16 (1, 2, 3, 4)
1994-2010,	17-33 (1, 2, 3)
2011,	34 (1, 2, 3, 4)
2012-2019,	35-42 (1, 2, 3)
2020,	**43 (1,**

ISSN 1980-9743 CDU 624.131.1

ISSN 1980-9743

SOILS and ROCKS

An International Journal of Geotechnical and Geoenvironmental Engineering

Publication of

ABMS - Brazilian Association for Soil Mechanics and Geotechnical Engineering

SPG - Portuguese Geotechnical Society

Volume 43, N. 1, January-March 2020

Table of Contents

Articles

Orientational Analysis of the Vesic's Bearing Capacity of Shallow Foundations

L. F. dos Santos, A.C.de Freitas

Abstract. The determination of the bearing capacity of shallow foundations can be considered as a complex elasto-plastic deformation problem, which is often studied phenomenologically. The phenomenological equations are naturally constructed based on the typical dimensions of the variables involved (unit weight, foundation size, etc.) – all physical laws must guarantee the principle of dimensional balance. Nevertheless, there is another requirement physical laws must obey that is less often explored: all equations must be orientationally balanced. While this requirement is obvious for vectorial equations, the laws of continuum mechanics often mix tensors, vectors and scalar quantities. Moreover, not all scalar quantities are considered orientationless (for instance, areas and angles define an orientation determined by the unit vector normal to the plane). Here, the main equations found in the literature for the bearing capacity of soils will be analyzed, testing the orientational balance of the phenomenological equations. It will be shown that not all equations are well balanced – in particular the critical rigidity index for the generalized failure of soils determined by Vesic (1973) is not balanced. Perhaps not surprisingly, the equations that are well balanced lead to a good agreement with experimental data from the literature, while the critical rigidity index fails systematically when compared to tests in model foundations on sand.

Keywords: bearing capacity, critical rigidity index, orientational balance, shallow foundations.

1. Introduction

Analyzing the variables that govern a physical phenomenon, one may extract (at least partially) the mathematical relations between these variables. This is the principle behind the dimensional analysis, which provides the means to determine physical laws even before any analytical or phenomenological derivation is attempted. A complementary approach is provided by the orientational analysis.

This method is based upon assigning orientational symbols to physical quantities such as force, velocity and position, which are spatially oriented. While the orientational symbols are evident for these vector quantities, they may become rather intricate for tensorial quantities or even for some scalars, which may identify an orientation. These symbols sustain a multiplication rule that forms a noncyclic Abelian group with four members, and they can be used to derive additional information that resolves problems incompletely solved by conventional dimensional analysis.

The goal of this work is to provide the orientational analysis of the equations for the bearing capacity (Vesic, 1975), as well as the orientational analysis of the rigidity index I_r and the critical rigidity index $I_{r\,crit}$ which are proposed by Vesic for determining if a soil-foundation system will fail in a generalized or non-generalized mode.

The limit stress to generate soil rupture is called Terzaghi's equation (1943) for foundation shapes with $L >> B$ (Vesic (1973), as shown in Fig. 1, has already proposed a shape correction factor for different foundation forms of $L >> B$), given by:

$$q_{rup} = c \cdot N_c + q \cdot N_q + \frac{1}{2} \gamma \cdot B \cdot N_\gamma \tag{1}$$

where c is the soil cohesion intercept, q is the uniformly distributed load due to the overburden, γ is the soil unit weight, B is the smallest size of the foundation base and the N_c, N_q and N_γ are dimensionless bearing capacity factors, defined by:

$$N_c = (N_q - 1)\cot\phi \tag{2}$$

$$N_q = e^{(\pi \tan\phi)}\left(\tan\left(\frac{\pi}{4} + \frac{\phi}{2}\right)\right)^2 \tag{3}$$

$$N_\gamma = 2(N_q + 1)\tan\phi \tag{4}$$

These equations are stated for lower compressibility soils, *i.e.*, idealized soil-foundation systems that fail as a rigid-plastic medium, instead of elasto-plastic. This idealization is considered by Vesic (1975) to be adequate as long as the rigidity index (Eq. 5) is larger than a critical rigidity index (Eq. 6).

Luiza Fernandes dos Santos, M.Sc. Researcher, Programa de Projeto de Estruturas, Escola Politécnica, Universidade Federal do Rio de Janeiro, Av. Athos da Silveira Ramos 149, Ilha do Fundão, Centro de Tecnologia - Bloco A, 2° andar, Cidade Universitária, Rio de Janeiro, RJ, Brazil. e-mail: luizadosfs@gmail.com.
Alessandra Conde de Freitas, D.Sc., Associate Professor, Programa de Projeto de Estruturas, Escola Politécnica, Universidade Federal do Rio de Janeiro, Av. Athos da Silveira Ramos 149, Ilha do Fundão, Centro de Tecnologia - Bloco A, 2° andar, Cidade Universitária, Rio de Janeiro, RJ, Brazil. e-mail: alessandracfreitas@poli.ufrj.br.
Submitted on October 1, 2017; Final Acceptance on February 13, 2020; Discussion open until August 31, 2020.
DOI: 10.28927/SR.431003

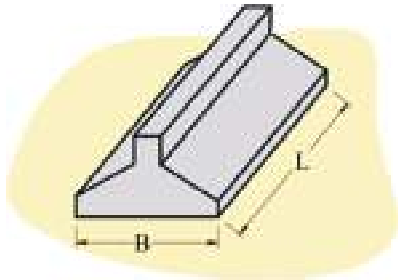

Figure 1 - Shallow foundation supported on a soil without overburden.

$$I_r = \frac{G}{c + \sigma_{med} \tan\phi} \tag{5}$$

$$I_{r\,critical} = \frac{1}{2} e^{\left(3.30 - 0.45\frac{B}{L}\right)\cot\left(\frac{\pi}{4} - \frac{\phi}{2}\right)} \tag{6}$$

where G is the shear modulus, ϕ is soil friction angle and σ_{med} is a characteristic stress scale, estimated as the mean stress at a depth $B/2$ below the base of the footing. The shear modulus and mean stress can be defined respectively as:

$$G = \frac{E}{2(1+\nu)} \tag{7}$$

$$\sigma_{med} = \frac{\sigma'_v + 2\sigma'_h}{3} \tag{8}$$

where E is Youngs modulus, ν is the Poisson ratio and σ_v and σ_h are the effective vertical and horizontal stresses at a depth $B/2$ below the base of the footing, respectively. The expressions for σ_v and σ_h are respectively:

$$\sigma'_v = \frac{1}{2} B \cdot \gamma \tag{9}$$

$$\sigma'_h = \sigma'_v \cdot k_0 \tag{10}$$

where k_0 is the at-rest earth pressure coefficient and it is defined as

$$k_0 = 1 - \sin\phi \tag{11}$$

The Eq. 11 applies only for sands.

2. Material and Methods

2.1. Orientational analysis in general

The symbol $\doteq$ will denote a orientational equality (Siano, 1985a), *i.e.*, two quantities that carry the same orientational symbol will be related by the symbol $\doteq$. The symbols for orientations in the Cartesian directions x, y and z are respectively l_x, l_y and l_z. Equivalent symbols and their multiplication table may be found for other coordinate systems (Siano, 1985b), but will not be necessary for our purpose here. Quantities without an orientation [some scalars (mass, time, ...) and tensor elements (normal stress, normal strain, ...)] will be denoted by the symbol l_0 (identity). To understand why quantities such as normal strain are deemed orientationless, the multiplication table for these symbols will be shown now.

The product between two quantities with different orientations will also have an orientation, following the respective multiplication table, which is analogous to the vector product rule, but commutative (without taking the signal into account), *i.e.*,

$$l_y \cdot l_z \doteq \boldsymbol{l_x} \doteq l_z \cdot l_y \tag{12}$$

$$l_x \cdot l_z \doteq \boldsymbol{l_y} \doteq l_z \cdot l_x \tag{13}$$

$$l_x \cdot l_y \doteq \boldsymbol{l_z} \doteq l_y \cdot l_x \tag{14}$$

There is also a rule of multiplication between two oriented quantities with same orientation, which always generates a quantity without orientation (l_0):

$$l_x \cdot l_x \doteq l_0 \tag{15}$$

$$l_y \cdot l_y \doteq l_0 \tag{16}$$

$$l_z \cdot l_z \doteq l_0 \tag{17}$$

$$l_0 \cdot l_0 \doteq l_0 \tag{18}$$

The identity of this multiplication operation is l_0, such that multiplying it by any orientational symbol generates the same orientation:

$$l_x \cdot l_0 \doteq \boldsymbol{l_x} \doteq l_0 \cdot l_x \tag{19}$$

$$l_y \cdot l_0 \doteq \boldsymbol{l_y} \doteq l_0 \cdot l_y \tag{20}$$

$$l_z \cdot l_0 \doteq \boldsymbol{l_z} \doteq l_0 \cdot l_z \tag{21}$$

And finally, every symbol of orientation is the inverse of itself, that is,

$$l_0^{-1} \doteq l_0 \tag{22}$$

$$l_x^{-1} \doteq l_x \tag{23}$$

$$l_y^{-1} \doteq l_y \tag{24}$$

$$l_z^{-1} \doteq l_z \tag{25}$$

It is possible to summarize all this in a single matrix (Fig. 2).

Therefore, these symbols and this multiplication operation form an Abelian group.

There is no definition of fractional powers of orientational symbols, so one may not have rational exponents in the original equation (physical law) when applying orientational analysis. In order to analyze the directionality of an equation which contains some root (fractional exponent), it is necessary to eliminate it by exponentiation.

For example, the orientational symbol of the area of the square A is l_z, since

$$A = L^2 \doteq l_x \cdot l_y \doteq l_z \doteq A \tag{26}$$

	l_0	l_x	l_y	l_z
l_0	l_0	l_x	l_y	l_z
l_x	l_x	l_0	l_z	l_y
l_y	l_y	l_z	l_0	l_x
l_z	l_z	l_y	l_x	l_0

Figure 2 - General orientational matrix.

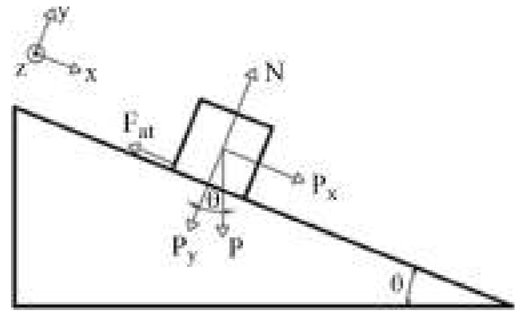

Figure 3 - Schematic of an inclined plane block.

This also illustrates how a scalar quantity may bear an orientation symbol. In this example, the symbol is carried by the area of a square, which is a natural notion when dealing with the calculus of multivariate fields (for instance, the calculation of a flux in Gauss' theorem is dependent on the orientation of the area of the Gaussian surface of choice).

The fractional power would also be eliminated if the equation of the area represented as fractional power ($L = \sqrt{A}$) were raised to the fourth power:

$$(L)^4 = (\sqrt{A})^4 \tag{27}$$

$$L^4 = A^2 \tag{28}$$

But this choice of exponent makes the orientational analysis less effective. Eqs. 15-18 show that even powers of any quantity will lead to the trivial conclusion $l_0 \doteq l_0$. The form of Eq. 26 is referenced as the normal form, highlighting its usefulness for orientation analyses.

It can be concluded that the orientation of unknown quantities can be identified by balancing the orientational symbols derived from the physical law that defines this quantity.

2.2. Orientational analysis of angles

Angles are dimensionless, but they do carry an orientational symbol, so that equations associating vectors in different directions become directionally homogeneous, which is an important characteristic of orientational analysis.

An example of orientational angle analysis is found in the simple problem of the dynamics of a body in a tilted plane (Fig. 3).

Balancing the forces on the *x* and *y* axes leads to the conclusion that the friction coefficient is given by $\mu = \tan\theta$. The orientational analysis of the Amontons first law gives

$$F_{at} = \mu \cdot N \tag{29}$$

$$l_x \doteq l_\mu \cdot l_y \tag{30}$$

Therefore, by homogeneity,

$$l_\mu \doteq l_x \cdot l_y^{-1} \doteq l_z \tag{31}$$

with this, it can be concluded that $\tan\theta$ has direction l_z.

3. Results

3.1. Orientational analysis of bearing capacity factors for the Terzaghi's equation

When analyzing Eq. 1, it can be verified that N_c, N_q and N_γ are adimensional:

$$\begin{gathered} [q_{rup}] = [c]\cdot[N_c] + [q]\cdot[N_q] + \frac{1}{2}[\gamma]\cdot[B]\cdot[N_\gamma] \\ \left[\frac{M}{LT^2}\right] = \left[\frac{M}{LT^2}\right]\cdot[N_c] + \left[\frac{M}{LT^2}\right]\cdot[N_q] + \left[\frac{M}{LT^2}\right]\cdot[N_\gamma] \end{gathered} \tag{32}$$

Now, the orientational balance of the equations discussed in Siano (1985a) for N_c, N_q and N_γ (Eq. 2-4) will be analyzed. Since all three equations contain tan (ϕ), and N_γ contains $(\tan(\frac{\pi}{4} + \frac{\phi}{2}))^2$, what will be discussed is how to obtain the orientational analysis of these functions. While the tangent function was already discussed, it is useful for other purposes to obtain its orientational symbol by analyzing its Taylor's series expansion. For both expressions, it can be written as:

$$\tan\phi = \phi + \frac{\phi^3}{3} + \frac{2\phi^5}{15} + \ldots \tag{33}$$

$$\left(\tan\left(\frac{\pi}{4} + \frac{\phi}{2}\right)\right)^2 = 1 + 2\phi + 2\phi^2 + \frac{5\phi^3}{3} + \frac{4\phi^4}{3} + \frac{61\phi^5}{60} + \ldots \tag{34}$$

If angles had a dimension ascribed to them, this expression would make no sense, since it would add distinct powers (for example, $\phi^3 + \phi^5$). However, they can bear an orientational symbol. Indeed, since all powers in the Taylor expansion are odd, the orientation of the tangent function is the same as that of the friction angle ϕ. Notice that Eq. 34 involves the square of a tangent function, which is orientationless. Indeed, its Taylor series expansion contains even and odd powers of ϕ, and it cannot be balanced unless each term is orientationless (notice that the series terms containing odd powers of ϕ may still be orientationless, as long as the series coefficient has orientation).

Functions with no definite parity (which are neither even nor odd) need to have both dimensionless and directionless arguments. For example, e^x

$$e^x = 1 + x + \frac{x^2}{2} + \frac{x^3}{6} + \frac{x^4}{24} + \ldots \quad (35)$$

If $x \doteq l_z$, it can be concluded that the orientational balance of Eq. 35 is:

$$l_{e^x} \doteq l_0 + l_z + \frac{l_z^2}{2} + \frac{l_z^3}{6} + \ldots \quad (36)$$

$$l_{e^x} \doteq l_0 + l_z + l_0 + l_z + \ldots \quad (37)$$

which is not directionally balanced. Therefore,

$$e^x \doteq l_0, \text{ for } x \doteq l_0 \quad (38)$$

Frequently, an apparently orientational exponent is rendered orientationless by a pre-factor with a directionality that must be taken into account. This prefactor often contains π (3.1415 ...), which is observed in the expression for N_q, since $e^{(\pi.\tan\phi)}$ would violate the orientational balance, if π had no direction. Because $\tan\phi \doteq l_z$, its can be concluded that $\pi \doteq l_z$:

$$\pi \tan\phi \doteq l_z \cdot l_z \doteq l_0 \quad (39)$$

and therefore

$$e^{(\pi \tan\phi)} \doteq l_0 \quad (40)$$

The whole expression for N_q is therefore balanced as

$$N_q = e^{(\pi \tan\phi)} \left(\tan\left(\frac{\pi}{4} + \frac{\phi}{2} \right) \right)^2 \quad (41)$$

The balance of N_γ is also obtained as

$$\begin{aligned} N_\gamma &= 2(N_q + 1)\tan(\phi) \\ N_\gamma &\doteq l_0 \cdot (l_0 + l_0) \cdot l_z \doteq l_z \end{aligned} \quad (42)$$

And finally, orientational analysis of N_c gives

$$\begin{aligned} N_c &= (N_q - 1)\cot(\phi) \\ N_c &\doteq (l_0 - l_0) \cdot l_z^{-1} \doteq l_0 \cdot l_z \doteq l_z \end{aligned} \quad (43)$$

The orientational balance of Eq. 1 will be checked by determining the orientational symbol for q_{rup}, q, c, γ and B. The coordinate system in Fig. 4 will be adopted, with the load applied vertically along the y axis.

Some symbols are readily recognized as:

$$\sigma = \frac{P}{A} \doteq \frac{l_y}{l_x \cdot l_z} \doteq \frac{l_y}{l_y} \doteq l_0 \quad (44)$$

$$q_{rup} = \frac{weight\ of\ structure}{Area} \doteq \frac{l_y}{l_x \cdot l_z} \doteq \frac{l_y}{l_y} \doteq l_0 \quad (45)$$

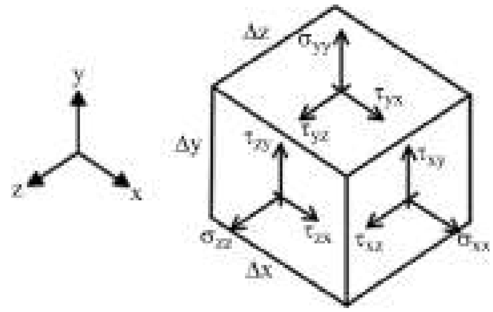

Figure 4 - Stress components in the Cartesian coordinate system.

$$q = \frac{weight\ of\ overburden}{Area} \doteq \frac{l_y}{l_x \cdot l_z} \doteq \frac{l_y}{l_y} \doteq l_0 \quad (46)$$

$$\gamma = \frac{weight\ of\ sand\ mas}{Volume} \doteq \frac{l_y}{l_x \cdot l_y \cdot l_z} \doteq \frac{l_y}{l_0} \doteq l_y \quad (47)$$

$$\begin{aligned} &B \doteq l_y \\ &\sigma = \frac{P}{A} \doteq \frac{l_y}{l_x \cdot l_z} \doteq \frac{l_y}{l_y} \doteq l_0 \end{aligned} \quad (48)$$

To determine the orientational symbol of c, its definition will be used in terms of the shear failure envelope curve, given by $\tau = c + \sigma.\tan\phi$. This gives:

$$\tau = c + \sigma \tan\phi \doteq c + l_0 \cdot l_z \doteq c + l_z \quad (49)$$

which is balanced only if c has orientation l_z. Then, it is obtained by dimensional analysis of Eq. 1:

$$\begin{aligned} q_{rup} &= c \cdot N_c + q \cdot N_q + \frac{1}{2}\gamma \cdot B \cdot N_\gamma \\ l_0 &\doteq l_z \cdot N_c + l_0 \cdot N_q + l_0 \cdot l_y \cdot l_x \cdot N_\gamma \\ l_0 &\doteq l_z \cdot N_c + l_0 \cdot N_q + l_z \cdot N_\gamma \end{aligned} \quad (50)$$

with this, it is concluded that the orientational symbol of N_q, N_γ and N_c should be respectively l_0, l_z and l_z, in agreement with the results in Eqs. 41, 42 and 43. So Eq. 1 is directionally balanced.

3.2. Orientational analysis of the Vesic equation for determination of generalized and non-generalized rupture

As already shown in Eq. 5, the rigidity index, proposed by Vesic (1973), is given by:

$$I_r = \frac{G}{c + \sigma_{med} \tan\phi}$$

First, a orientational analysis of the Elasticity Theory equations must be performed, especially the relationship between stresses and strains. At first, normal strain does not carry a directionality

$$\varepsilon_x = \frac{\Delta L_x}{L_x} \doteq \frac{l_x}{l_x} \doteq l_0 \tag{51}$$

But ε_{ij} is a tensor. In fact, for tensors, the diagonal elements have no direction, so that $\varepsilon_{xx} \doteq l_0$ is to be expected.

This helps to understand the direction of the elastic modules. Hooke's law can be expressed in three dimensions, where each normal strain is related to the three components of normal stress by the material properties, E and ν:

$$\varepsilon_x = \frac{1}{E}[\sigma_x - \nu(\sigma_y + \sigma_z)] \tag{52}$$

$$\varepsilon_y = \frac{1}{E}[\sigma_y - \nu(\sigma_x + \sigma_z)] \tag{53}$$

$$\varepsilon_z = \frac{1}{E}[\sigma_z - \nu(\sigma_x + \sigma_y)] \tag{54}$$

Since the orientational symbols of σ_x, σ_y, σ_z, ε_x, ε_y and ε_z, are l_0, as shown in Fig. 5 and Eq. 51 ,then by balancing it can be seen that E and ν are also l_0. With this, it can be concluded that G, shear modulus, also has direction l_0, since:

$$\begin{gathered} G = \frac{E}{2(1+\nu)} \\ G \doteq \frac{l_0}{2(1+l_0)} \doteq l_0 \end{gathered} \tag{55}$$

Thus, the rigidity index (Eq. 5) has direction l_z, since:

$$\begin{gathered} I_r = \frac{G}{c + \sigma_{med} \cdot \tan\phi} \\ I_r \doteq \frac{l_0}{l_z + l_0 \cdot l_z} \doteq \frac{l_0}{l_z + l_z} \doteq \frac{l_0}{l_z} \doteq l_0 \cdot l_z^{-1} \doteq l_z \end{gathered} \tag{56}$$

In order to be comparable to I_r, the critical rigidity index of soil $I_{r\,crit}$ should be orientationally consistent, *i.e.*, it should carry an orientational symbol l_z. However, when analyzing the orientational balance of this equation, a orientational inconsistency is found. According to Eq. 6, the critical rigidity index, for the cases of drained sand analysis, is given by:

$$I_{r\,critical} = \frac{1}{2} e^{(3.30 - 0.45\frac{B}{L})\cot\left(\frac{\pi}{4} - \frac{\phi}{2}\right)}$$

$$\begin{pmatrix} \sigma_x & \tau_{xy} & \tau_{xz} \\ \tau_{yx} & \sigma_y & \tau_{yz} \\ \tau_{zx} & \tau_{zy} & \sigma_z \end{pmatrix} \doteq \begin{pmatrix} l_0 & l_z & l_y \\ l_z & l_0 & l_x \\ l_y & l_x & l_0 \end{pmatrix}$$

Figure 5 - Strain matrix and orientational deformation matrix.

Keeping the axes as in Fig. 4, the directions of the length and width of the foundation base are respectively $l_B \doteq l_x$ and $l_L \doteq l_z$.

As demonstrated previously in Eq. 38, $e^x \doteq l_0$, for $x \doteq l_0$, and the exponent cannot be directionally non-trivial. Therefore $(3.30 - 0.45\frac{B}{L})\cot(\frac{\pi}{4} - \frac{\phi}{2})$ should be l_0. But what happens is:

$$\begin{gathered} \left(3.30 - 0.45\frac{B}{L}\right)\cot\left(\frac{\pi}{4} - \frac{\phi}{2}\right) \doteq \left(l_0 - l_0 \cdot \frac{l_x}{l_z}\right) \cdot l_{\cot\left(\frac{\pi}{4} - \frac{\phi}{2}\right)} \\ \left(3.30 - 0.45\frac{B}{L}\right)\cot\left(\frac{\pi}{4} - \frac{\phi}{2}\right) \doteq (l_0 - l_0 \cdot l_y) \cdot l_{\cot\left(\frac{\pi}{4} - \frac{\phi}{2}\right)} \\ \left(3.30 - 0.45\frac{B}{L}\right)\cot\left(\frac{\pi}{4} - \frac{\phi}{2}\right) \doteq (l_0 - l_y) \cdot l_{\cot\left(\frac{\pi}{4} - \frac{\phi}{2}\right)} \end{gathered} \tag{57}$$

The operation $\left(3.30 - 0.45\frac{B}{L}\right)$coton the right-hand side of Eq. 57 is inconsistent with orientational balancing, and therefore there must be something unphysical about this empirical critical rigidity index.

4. Conclusions

One may conclude that bearing capacity factors are directionally consistent. Often, a new proposal for a more accurate estimation of the bearing capacity factors N_c, N_q and N_γ is presented in the literature (Michalowski, 1997). The analysis presented here may provide a fast consistency check for these expressions. For instance, N_c and N_γ must be odd functions of the friction angle ϕ, while N_q must be even.

Although a orientational balance does not guarantee the accuracy of the equation, something may be stated about an unbalanced equation. For instance, the rigidity index equation for determining the limit between a generalized and a non-generalized rupture is not balanced. Vesic, in his article entitled "Bearing Capacity of Deep Foundations in Sand" (Vesic, 1963), shows experimental results in tests with circular and rectangular plates on the surface of the sandy soil. In each test, the rupture is classified as generalized, local or punching.

In Table 1, the experimental results are compared with the predictions from the analytical equation of critical rigidity index. The results shown in bold do not match those obtained experimentally. With this, it can be concluded that the criterion of Vesic is inaccurate in this regime. Furthermore, the injudicious use of this criterion jeopardizes the safety of the foundations, since a prediction of generalized failure when the soil is actually well-compressible may result in an overestimated ultimate load capacity (disregarding the necessary correction factor). The inadequacy of this equation could be anticipated by the orientational analysis of the proposed equation, which clearly raises doubts about this expression.

Table 1 - Experimental results (Vesic, 1963) and the analytical result (Vesic, 1975).

Test #	Experimental results [Vesic (1963)]				Rigidity Index criterion [Vesic (1975)]			
	B (m)	γ_d (kN/m^3)	ϕ (°)	Failure	E (kN/m^2)	$(I_r)_{crit}$	I_r	Failure
34	0.05	15.37	43.15	General	1,821.75	359.58	3,463.46	General
21		14.90	41.09	Local	1,820.36	263.39	3,681.14	**General**
22		14.38	38.85	Local	1,820.43	192.85	3,934.37	**General**
23		13.23	34.10	Punching	1,811.57	107.58	4,581.91	**General**
44	0.10	15.50	43.72	General	2,476.09	393.74	2,506.39	General
41		15.02	41.61	Local	2,476.26	284.25	2,665.09	**General**
42		14.58	39.70	Local	2,479.70	216.41	2,815.84	**General**
43		13.34	34.54	Punching	2,464.05	113.11	3,317.25	**General**
61	0.15	15.41	43.33	General	3,057.14	369.95	2,053.11	General
62		14.89	41.04	Local	3,059.30	261.49	2,193.6	**General**
63		14.69	40.18	Local	3,059.14	231.33	2,250.15	**General**
64		15.22	42.49	Punching	3,058.21	324.55	2,103.16	**General**
84	0.20	15.41	43.33	General	3,530.08	369.95	1,778.05	General
81		15.25	42.62	General	3,531.21	331.10	1,814.55	General
82		15.25	42.62	General	3,531.21	331.10	1,814.55	General
83		14.09	37.63	Local	3,528.89	164.46	2,105.97	**General**
16	rectangular 0.051 x 0.30	15.44	43.46	General	1,764.97	903.27	3,542.85	General
1		14.99	41.48	Local	1,766.13	640.82	3,750.94	**General**
2		14.72	40.31	Local	1,766.21	529.55	3,882.37	**General**
3		13.45	34.98	**Punching**	1,759.65	244.54	4,586.13	**General**

In Civil Engineering problems, the power of orientational analysis, unlike dimensional analysis, is not yet well explored and can lead to important advances. The mathematical structure of the laws of elasticity and plasticity allows their broad application and can guide efforts in determining appropriate empirical equations for quantities of interest.

The elastic modulus E was not provided in Vesic (1963), but an expression is reported in Vesic (1973) associating this modulus to the mean normal stress $E = E_1 \sqrt{\sigma_m / \sigma_1}$, with E_1 = 39,180.65 kN/m^2 (364 ton/ft^2) being the modulus at mean normal stress of σ_1 = 104.64 kN/m^2 (1 ton/ft^2).

References

Michalowski, R.L. (1997). An estimate of the influence of soil weight on bearing capacity using limit analysis. Soils and Foundations, 37(4):57-64.

Siano, D.B. (1985a). Orientational Analysis - A Supplement to Dimensional Analysis – I. Journal of the Franklin Institute, 320(6):267-283.

Siano, D.B. (1985b). Orientational Analysis, Tensor Analysis and the Group Properties of the SI Supplementary Units – II. Journal of the Franklin Institute, 320(6):285-302.

Terzaghi, K. (1943). Theoretical Soil Mechanics. John Willey & Sons, New York.

Vesic, A.B. (1963). Bearing capacity of deep foundations in sand. Highway Research Record, 39:112-153.

Vesic, A.B. (1973). Analysis of ultimate loads of shallow foundations. J. Soil Mech. Found. Div., 99(1):45-73.

Vesic, A.B. (1975). Bearing Capacity of Shallow Foundations. Foundation Engineering Handbook, McGraw-Hill, New York, pp. 121-147.

List of Symbols

B - smaller length of shallow foundations
c - soil cohesion intercept
E - Young's modulus
G - shear modulus
I_r - rigidity index
$I_{r\ critical}$ - critical rigidity index
k_0 - coefficient of earth pressure at rest
L - longer length of shallow foundations
N_c, N_q, N_γ - bearing capacity factors
q - uniformly distributed load
q_{rup} - rupture stress/ ultimate pressure
ε - normal strain

ϕ - friction angle

γ - unit weight

γ_d - unit weight of the dry soil

ν - Poisson ratio

σ_h - horizontal stress

σ_{med} - mean stress at a depth $B/2$ below the base of the footing

σ_v - vertical stress

Experimental Study of the Group Effect on the Bearing Capacity of Bored Piles in Sandy Soil

J. Melchior Filho, V.H.F. Bonan, A.S. Moura

Abstract. A foundation design must meet at least the following basic requirements: a) acceptable deformations under the working conditions; b) adequate safety against soil failure; and c) adequate safety against failure of structural elements. For the pile design, depending upon the spacing adopted among them, a pile may affect the other's behavior. This occurs both in terms of bearing capacity and settlement. Researches on the group effect of bored piles in typical soils of Fortaleza (Northeast Brazil) is scarce, which justifies and motivates studies on the subject. The aim of the research reported here was to evaluate the group effect of bored piles in sandy soil, typical condition of the city of Fortaleza. An experimental campaign with 26 piles was performed on a site inside the campus of the Federal University of Ceará (Experimental Field of Geotechnics and Foundations of the Federal University of Ceará). The results of tests on single piles and groups were compared with estimations based on methods presented in the literature. The tested piles were observed to behave only by side friction, and group effect was noticed for all spacings investigated.

Keywords: bearing capacity, bored pile, group effect, pile group.

1. Introduction

The execution process of bored piles can cause changes in geostatic stresses due to decompression of ground during excavation. In cohesive soils and above the water table, decompression is expected since no casing is used. On the other hand, in non-cohesive soils, metallic casing is placed with the advance of excavation, which may reduce soil expansion and, consequently, stress relief. Between these two extremes, there is the possibility of execution with the use of stabilizing fluid.

During the execution of bored piles, a portion of loose soil remains at the pile toe, which cannot be removed by the drilling tool (piling auger). This effect will cause a reduction in the pile bearing capacity (Scallet, 2011). Pérez (2014) studied the behavior of these piles via slow-type static load tests. Three diameters of instrumented bored piles were evaluated. The author shows that the load transfer occurred to a large extent by side resistance, and a larger displacement would be necessary to mobilize the base resistance because of the loose soil at the pile toe.

The load-displacement response of piles is different if executed alone or in groups. When executed in groups, interactions occur among several piles during the load transfer to the soil mass. This interaction creates a stress superposition, which affects the load-displacement response of the pile group. In order to quantify this group effect, several authors use mainly the spacing among piles of the same group or neighboring caps and the soil characteristics (Vesic 1969).

The geotechnical literature provides several methods for the estimation of bearing capacity and displacement of single piles. However, pile groups are often adopted in foundation design. When piles are executed close to each other, the load-displacement response of the group can change according to the spacing between piles, when compared to a single pile.

According to NBR 6122 (ABNT, 2010) the group effect on piles is the interaction of various elements that constitute a foundation when transferring loads to the ground. This interaction involves a superposition of stresses, usually causing different displacement of isolated elements, which changes the individual behavior of each pile of the group. The Canadian Foundation Engineering Manual, CGE (1992), recommends that the group effect can be disregarded if the space between two piles is larger than 8 diameters (D).

The soil-structure analysis of a pile group represents a complex problem because the group effect can be influenced by: the pile installation method; the type of load transfer (floating pile or end bearing pile); the nature of the foundation soil mass; the three-dimensional geometry of the group; the presence of the pile cap; the pile cap relative stiffness. (Chan, 2006).

According to Poulos (1993), there are several uncertainties in the applicability of the different methods for pre-

José Melchior Filho, M.Sc., Geotechnical Master's Degree Student, Departamento de Engenharia Hidráulica e Ambiental, Universidade Federal do Ceará, Fortaleza, CE, Brazil. e-mail: melchior_filho@hotmail.com.
Victor Hugo Fernandes Bonan, M.Sc., Departamento de Engenharia Hidráulica e Ambiental, Universidade Federal do Ceará, Fortaleza, CE, Brazil. e-mail: victorhfbonan@gmail.com.
Alfran Sampaio Moura, D.Sc., Associate Professor, Departamento de Engenharia Hidráulica e Ambiental, Universidade Federal do Ceará, Fortaleza, CE, Brazil. e-mail: alfransampaio@ufc.br.
Submitted on November 29, 2017; Final Acceptance on October 1, 2019; Discussion open until August 31, 2020.
DOI: 10.28927/SR.431011

dicting the behavior of pile groups, regarding bearing capacity and displacement, mainly due to the scarcity of documented cases, particularly for bored piles.

The efficiency of a pile group can usually vary with the influence of soil excavation, the type of soil and its compactness, and the spacing between the piles. Silva & Cintra (1996) performed 6 static load tests, two of them on single piles with cap, and the others on pile groups with cap. The pile groups were: one 2-pile group (1 x 2); two 3-pile groups, one in line pile group (1 x 3) and the other in triangular shape pile group (3Δ); and one 4-pile group arranged in square shape (2 x 2). The authors also analyzed the influence of the cap on the bearing capacity of the pile groups. The efficiencies found with and without contribution of the cap, respectively, are: 1.15 and 0.90 (1 x 2); 1.17 and 0.92 (1 x 3); 1.20 and 1.09 (3Δ); 1.07 and 0.97 (2 x 2). All the piles were manually drilled type piles with 0.25 m diameter (D), 6 m length, and 3D pile spacing.

Sales (2000) found efficiency of 100 % for piled footings with 4 bored piles with 0.15 m diameter, 5 m in length and 5D pile spacing (s). On the other hand, Garcia (2015) found efficiencies of 79.1 % (2 piles), 69 % (3 piles) and 76.1 % (4 piles). Garcia (2015) carried out static load tests on piled rafts composed of mechanically excavated piles of 0.25 m in diameter and 5 m in length. The piled rafts comprised two, three and four piles, spaced 5D.

For piles embedded in loose sandy soils, the literature reports that the efficiency would be maximum for a spacing of 2D due to the effect of compaction caused by the vibration of the process (Kézdi, 1957; Stuart *et al.*, 1960). The efficiency returns to about 100 % for a pile spacing of 6D. Meyerhof (1976) suggests adopting efficiency of 2/3 for a pile spacing (s) from 2 to 4D for groups of bored piles in sand.

Vesic (1969) conducted a study in which a series of experiments in a reduced scale model was performed in the field with groups of 4 and 9 instrumented piles in sand. The author compared the bearing capacity of pile groups with the bearing capacity of single piles. The piles had 10 cm in diameter and 150 cm in length, and were driven into the ground using a pile driver, with spacing between axes from 2 to 6 diameters. The groups were tested in two scenarios: in medium dense homogeneous deposit (Dr = 65 %); the second one is composed of two layers, a top layer of loose sand (Dr = 20 %) and a bottom layer of dense sand (Dr = 80 %)

Few studies are observed in the literature related to the group effect of bored piles in sandy soils, and still less in tropical soils typical of those that occur in Fortaleza. Within this context, this work aims to contribute to better understanding of the group effect on bored piles in sandy soils. The objective of this research is to evaluate, experimentally, through static load tests performed on groups of excavated piles, the group effect on sandy soil profiles in terms of the bearing capacity of the piles.

2. Materials and Methods

2.1. Experimental site

The present study was carried out in the Experimental Field of Geotechnics and Foundations of the Federal University of Ceará (-3.752297 S, -38.572821 W), located according to Fig. 1.

2.2. Characterization tests

The sieve analysis was performed on soil samples obtained at depths of 1.0 to 2.0 m, because it is the length of the piles. The particle-size distribution of the soil samples obtained are shown in Fig 2.

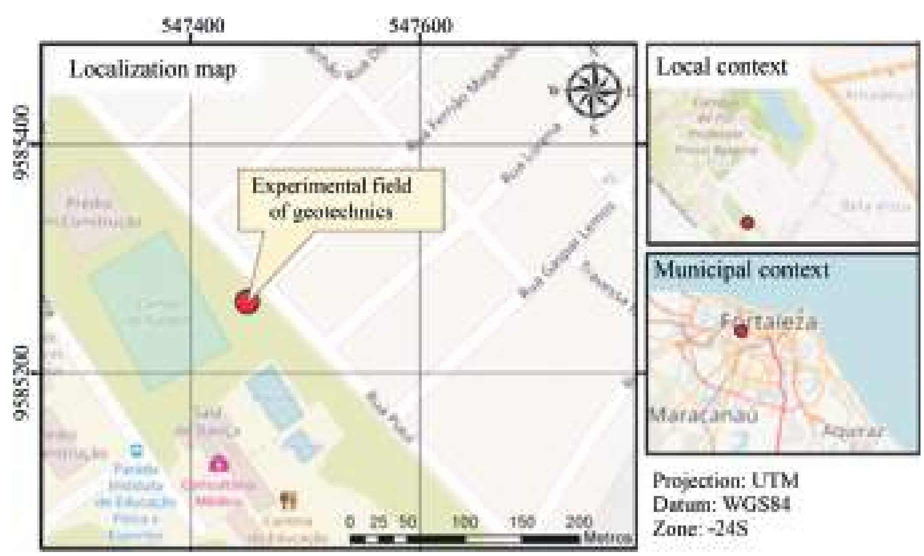

Figure 1 - Location of the experimental site.

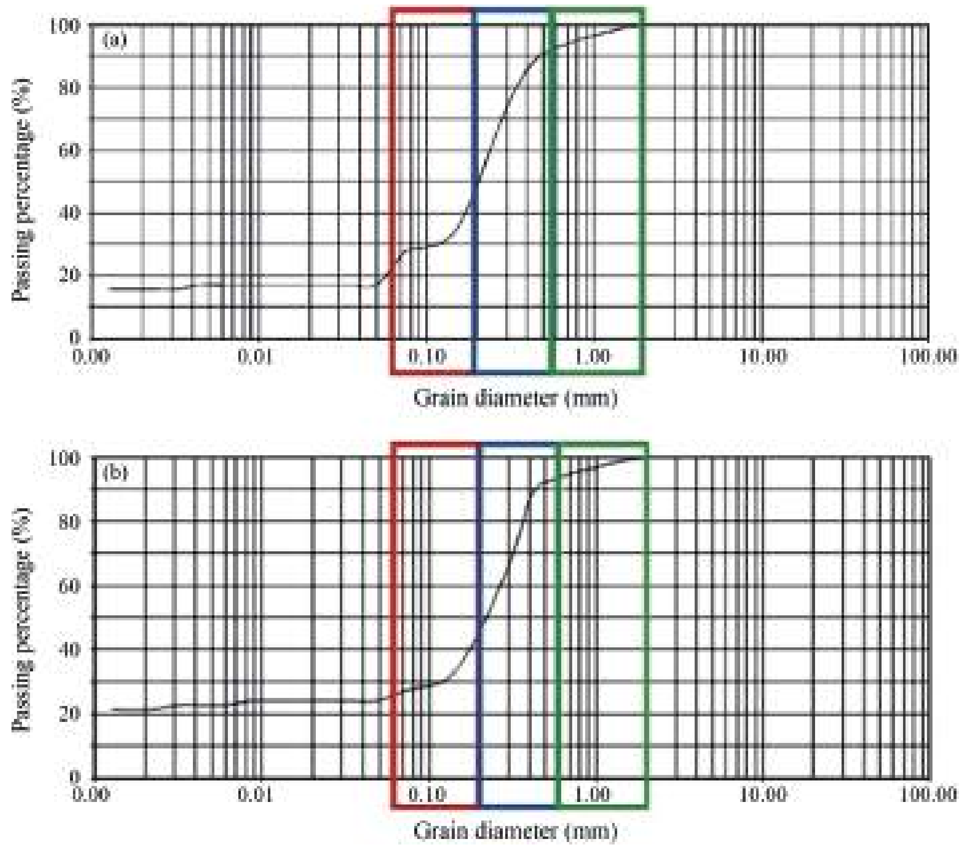

Figure 2 - Granulometric curve of the soil layer in depths of (a) 1.0 m and (b) 1.5 m.

According to the particle-size distribution, the soil is predominantly sandy, and its composition is approximately 78 % sand in the most superficial portion and 73 % sand in the soil present between the depths of 1.5 to 2.0 m, which was classified according to NBR 6502 (ABNT, 1995). In the curves, the portions of fine sand, medium sand and coarse sand are highlighted, respectively, by red, blue and green lines. The values of specific gravity of grains in depths of 1.0 and 2.0 m varied between 2.62 and 2.64, respectively.

2.3. Standard penetration test

The soil sampling carried out together with the Standard Penetration Test indicated a predominantly sandy-silt soil profile up to 7.45 m depth. The water level was found at the depth of 7.36 m. The N_{SPT} values varied from 12 to 18 blows/30 cm at 4.45 m depth and, from there, decreased to 4 blows/30 cm at 7 m depth.

Using the method proposed by Odebrecht (2003), the efficiency of percussion drilling was estimated at 72 %. The value of 72 % is nearly coincident with the standard adopted in Brazil. To evaluate whether the semi-empirical methods used in this research, which do not specify reference efficiency could lead to more consistent Q_{ult} predictions, the N_{SPT} values used in this research were also corrected to the reference efficiency of 60 % (Table 1), which is the standard adopted in the United States (Odebrecht, 2003; Skempton, 1986).

2.4. Execution of isolated and group piles

The pile work load was defined according to the Brazilian Standard for Design and Construction of Foundations NBR 6122 (ABNT, 2010). Groups of 2 and 4 piles were constructed varying the spacing between the piles, in addition to two other isolated piles. Table 2 presents some geometric information of the pile groups.

Table 1 - Corrected values of N_{SPT} for 60 % efficiency.

Depth (m)	N_{SPT}	Corrected values of N_{SPT}		
		Odebrecht (1st case)	Odebrecht (2nd case)	Average values
0.4	15	20	18	19
1.0	12	16	14	15
2.0	15	20	18	19
3.0	18	24	22	23
4.0	18	24	22	23
5.0	6	8	7	8
6.0	3	4	4	4
7.0	4	5	5	5

The construction of the piles happened within two consecutive days, being constructed 13 piles per day. The groups of 4 piles had two piles constructed per day, in diagonal arrangement and the groups of 2 piles had one pile constructed per day. The excavation was performed with a shell-type driller. At the beginning of the procedure, a certain amount of water was added to the hole to facilitate the excavation. The following procedure was used for pile grouting: placement of the steel cage; concrete mixing into a 400 L concrete mixer, then measuring the slump of the mixture through the Slump test and releasing for launch. The concrete was poured with buckets of 18 L in order to estimate the volume released. Finally, the concrete was densified manually using a metal rod. The slump adopted was between 22 and 24 cm, and the characteristic compressive strength (f_{ck}) was 20 MPa.

The piles caps were executed later with no contact with the ground and, therefore, there was no contribution of the caps for group capacity. For caps with 2 and 4 piles, the spacing between piles was adopted as 2D, 2.5D, 3D and 4D, in which D is the pile diameter. In addition, two caps for single piles were executed, which gives 26 piles distributed in 10 caps. To avoid the group effect between nearby caps, a minimum distance of 8D between caps was adopted, as suggested by the literature (CGE, 1992). In order to evaluate the load distribution on the pile, two separate piles were executed, one of them with Styrofoam at the toe, thus the toe bearing capacity is assumed to be null.

Regarding the application of the methods for designing larger piles than those in this study, Nasr (2014) stated that the factors that must be considered in the usage of small-scale models are the soil particle size, construction techniques and boundary conditions. According to Franke & Muth (1985), scale error is not relevant for a ratio of the pile diameter to the mean grain size (D_{50}) greater than 30. Since in this study the pile diameter is 10 cm, and D_{50} is approximately 0.3 mm, such condition is fulfilled. Regarding the remaining factors, the tests presented in this research are supposed to represent the behavior of full-scale bored piles installed in a similar type of soil as the models. Therefore, the small-scale tests performed are considered as representative of full-scale foundations.

As previously reported, a similar study was performed by Vesic (1969) in which a series of experiments in a reduced scale model was performed in field with groups of 4 and 9 instrumented piles. The piles had 10 cm in diameter and 150 cm in length but were driven into the ground using a pile driver, with spacing between axes from 2 to 6 diameters. The groups were installed in sand profiles of different relative density.

2.5. Static load tests

The Static Load Tests (SLT) were performed with the load applied in quick stages based on the recommendations of the Brazilian Standard NBR 12131 (ABNT, 2006). Ho-

Table 2 - Summary of geometric information of piles and caps.

Group	Number of piles	s/D	Pile caps			Piles					
			Length (cm)	Width (cm)	Height (cm)	Total length (cm)	Reductions			Pile length (cm)	Pile diameter (cm)
							Cap height (cm)	Lean conc. (cm)	Excavation (cm)		
1	1	-	30	30	20	180	20	5	5	150	10
2	1	-	30	30	20	180	20	5	5	150	10
3	2	2	50	30	20	180	20	5	5	150	10
4	2	2.5	55	30	25	185	25	5	5	150	10
5	2	3	60	30	30	190	30	5	5	150	10
6	2	4	70	30	35	195	35	5	5	150	10
7	4	2	60	60	30	190	30	5	5	150	10
8	4	2.5	65	65	35	195	35	5	5	150	10
9	4	3	70	70	40	200	40	5	5	150	10
10	4	4	80	80	50	210	50	5	5	150	10

wever, during the tests, 7 to 9 loading stages and 3 unloading stages were performed. The number of load stages was defined aiming to adjust the duration of the tests to the time available for the research. For this reason, only 3 stages were adopted for the unloading stages. In addition, situations occurred in which, before reaching the maximum expected load stage, failure happened, which led to the end of the loading stage.

The displacements were monitored with 4 dial gages, in 0, 1, 2, 5 and 10 min. The arrangement of the dial gages in diametrically opposite positions allows for the evaluation whether, throughout the tests, the applied load remains centered over the cap. In cases where displacement stabilization was observed before 10 min, the next stage was performed. The limiting factor for the execution of these tests was the reaction system.

The reaction system was composed of a loaded truck and a metallic I-beam, whose axis was positioned over the pile cap (transversely). The load tests assembly is shown in Fig. 3.

Initially, slow load tests (SLT) were performed on 2 isolated piles. The first test was performed by subjecting the pile to the predicted compressive capacity taking into account both shaft and toe bearing capacities. The second load test was performed on an identical pile to the previous one, including, however, a Styrofoam disc at the pile toe in order to eliminate the toe bearing contribution to the pile bearing capacity.

Subsequently the load tests were performed in groups of 2 and 4 piles varying the spacing between piles (2D, 2.5D, 3D and 4D).

2.6. Bearing capacity predictions

The semi-empirical methods of Aoki & Velloso (1975), Décourt & Quaresma (1978) with contributions by Décourt (1996), and Teixeira (1996) were used to estimate the bearing capacity of the isolated piles.

In order to predict the bearing capacity of the groups of piles, methods commonly found in the literature were used to estimate the efficiency (Feld’s Rule (Feld, 1943) and a rule of uncertain origin - both found in Poulos & Davis (1980), Converse-Labarre (Bolin, 1941), Los Angeles Group Action equation - in Das (1998), and Sayed & Bakeer, 1992).

3. Analysis and Discussion of Results

3.1. Results and analysis of load tests

Figure 4 shows the results of the slow load tests performed on the isolated pile, with and without the toe bearing capacity. Both tests were performed with the application of 8 loading stages and 3 unloading stages. Figure 4 shows practically coincident curves, which implies that in the piles’ bearing capacity there is no contribution from the toe.

It is worth mentioning that the maximum displacement of the pile without Styrofoam at its toe was 7.12 mm and its residual displacement was 6.83 mm. And for the pile with Styrofoam at its toe the maximum displacement was 9.59 mm and the residual displacement was also 9.59 mm.

Figure 5 shows the load-displacement responses obtained from the tests performed on the groups with 2 piles and Fig. 6 shows the results of the tests performed on the groups of 4 piles.

The pile group with 4D spacing exhibited failure at the 4th loading stage, corresponding to 68.7 kN. Subsequently, an integrity problem in one of the piles of the group was confirmed by means of excavation around the pile, which prevented the test to be continued.

3.2. Bearing capacity predictions

Table 3 shows the estimated bearing capacity, Q_{ult}, of the isolated piles, as well as the portion due to the shaft friction, Q_1, and to the toe resistance, Q_p, respectively, considering the two groups of N_{SPT} values considered.

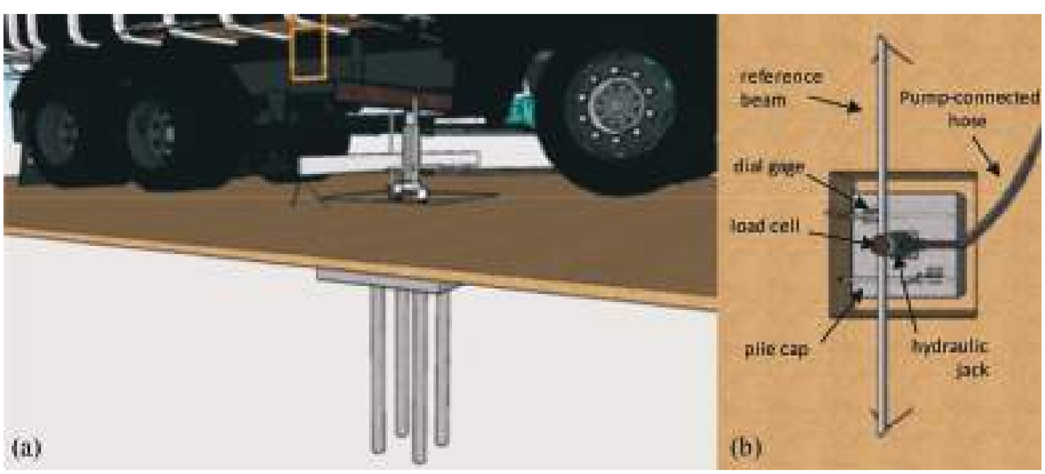

Figure 3 - Illustration of SLT performed: (a) perspective; (b) top view.

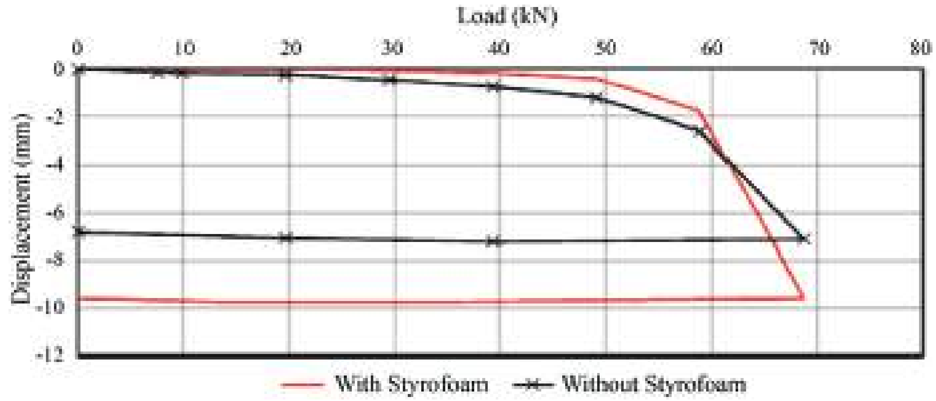

Figure 4 - Load-displacement curves of the isolated piles with and without toe bearing contribution.

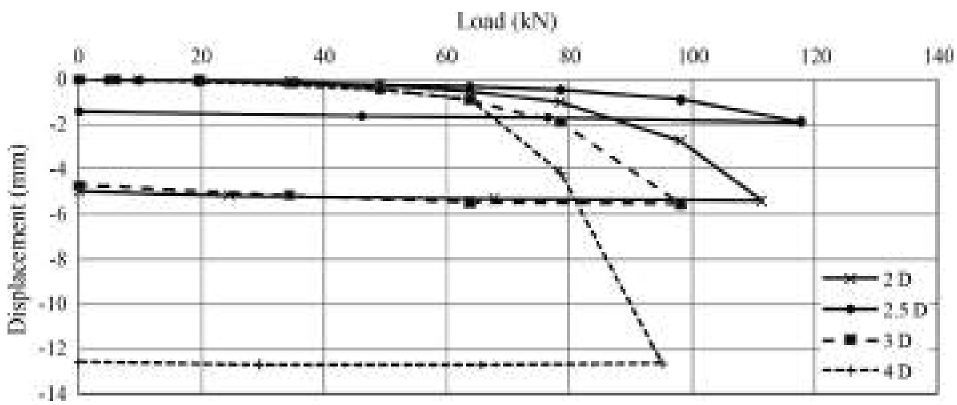

Figure 5 - Load-displacement curves of the groups with 2 piles.

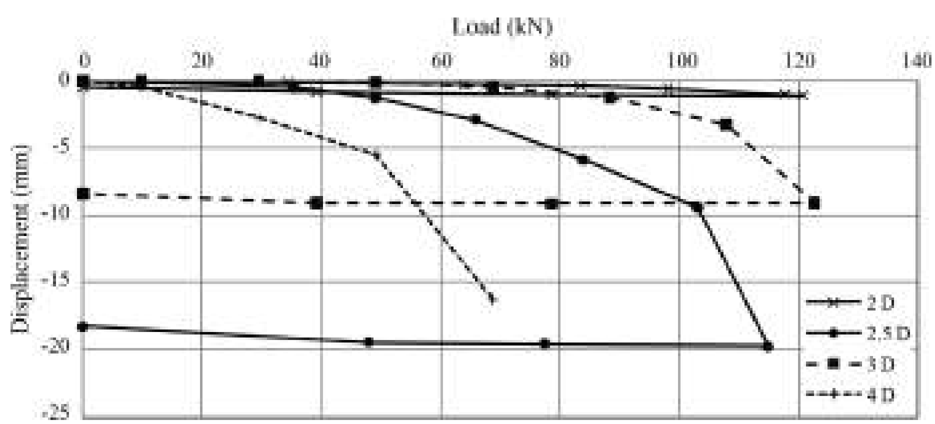

Figure 6 - Load-displacement curves of the groups with 4 piles.

The method of Teixeira (1996) presents the highest estimated values of Q_{ult}, followed by Aoki & Velloso (1975) and Décourt & Quaresma (1996) methods. By comparing the estimates made from corrected and uncorrected values of N_{SPT}, the correction of the efficiency to 60 % increased, in all methods used, the Q_{ult} estimates by about 25 % above those made using N_{SPT} values without efficiency correction.

Table 4 shows a comparison of the estimated Q_{ult} of the isolated pile, obtained from corrected and uncorrected N_{SPT} values as a function of the efficiency, with the reference value, 68.6 kN, which was obtained through the results of the SLT. The mentioned table presents the values of Factor of Safety (FS) obtained for each method when the values presented in Figure 7 are divided by 2 and taken as the pile work load. The Q_{ult} predictions using semi-empirical methods are lower than the reference value, with values up to 4.4 times lower, even when the corrected N_{SPT} values are used. The closest estimate was obtained with the

Table 3 - Summary of Q_{ult}, Q_l, and Q_p estimated of isolated piles.

Method	N_{SPT}	Q_{ult} (kN)	Q_l (kN)	Q_p (kN)
Aoki & Velloso (1975)	Field	37.3	15.7	21.6
	Corrected e = 60 %	47.1	19.8	27.4
Décourt & Quaresma (1996)	Field	33.1	17.2	15.9
	Corrected e = 60 %	40.9	20.8	20.0
Teixeira (1996)	Field	50.5	26.0	24.5
	Corrected e = 60 %	63.6	32.8	30.8

Table 4 - Comparison of the estimated Q_{ult} of the isolated pile, obtained from corrected and uncorrected N_{SPT} values and values of Factor of Safety (FS) obtained for each method.

Method	N_{SPT}	Q_{ult}	FS
Aoki & Velloso (1975)	Field	37.3	3.7
	Corrected e = 60 %	47.1	2.9
Décourt & Quaresma (1996)	Field	33.1	4.1
	Corrected e = 60 %	40.9	3.4
Teixeira (1996)	Field	50.5	2.7
	Corrected e = 60 %	63.6	2.2
Slow load test		68.6	-

method of Teixeira (1996) and using the corrected N_{SPT} values. However, even in this case, the estimated value was 2.6 times lower than the reference value.

Tables 5 presents estimated values of efficiency for groups of 2 and 4 piles, respectively. And Table 6 presents the predicted bearing capacity for the groups of piles as a function of spacing (s/D), which were determined by multiplying the number of piles in the group by the estimated efficiency and by the ultimate capacity of a single pile (68.6 kN), obtained via load test on the isolated pile.

For almost all methods, except for the Feld's Rule that provides a constant value, the efficiency of the group increased with the pile spacing increase. The highest values were obtained for the rule of uncertain origin (Poulos & Davis, 1980). The values of efficiency below unit obtained in the current study are in agreement with the indications for bored piles in sand by Meyerhof (1976), it suggests that an efficiency of 2/3 for pile spacing from 2 to 4 diameters.

3.3. Bearing capacity determination

The bearing capacity of the isolated piles and the groups of piles were determined from the results of each slow load tests.

Figures 7 and 8 show the graphs for the determination of the ultimate load (Q_{ult}) using the Van der Veen (1953) method and the Décourt (1996) method, which is based on the stiffness of the foundation.

The load value corresponding to the failure obtained visually in the load-displacement curve for the single pile, was compared with values obtained by Van der Veen (1953) and Décourt (1996). Figures 7 and 8 present similar values obtained by Van der Veen (1953) and Décourt (1996). Van der Veen (1953) estimated the ultimate load at 68.6 kN and by Décourt (1996) the estimated value was slightly higher, 74.2 kN. So the value adopted for the ultimate load (Q_{ult}) from the SLT's is 68.6 kN. The adoption of this value is due to the fact that Van der Veen's (1953) method provides the physical ultimate load, in the same way as the semi-empirical methods used in the present research, and the results are compared below.

Table 7 shows the Q_{ult} values obtained by the Van der Veen (1953) method for single pile and pile groups. The efficiency (η) of the pile groups is also shown in Table 7, obtained by dividing Q_{ult} of the group by the number of piles in the group, times Q_{ult} of the single pile (68.6 kN). According to these results, the group efficiency was lower than one. For groups with larger spacing, the efficiency reduced or remained almost constant. Finally, groups with s/D greater than or equal to 3 showed that the efficiency remained lower than one, and it indicates that there was group effect at all spacings investigated.

Table 5 - Efficiencies of the groups with 2 and 4 piles.

Methods			Efficiencies				
			Feld's Rule	Rule of uncertain origin	Converse-Labarre	Los Angeles	Sayed & Bakeer (1992)
Groups with 2 piles	s/D	2	0.94	0.94	0.84	0.92	0.76
		2.5	0.94	0.95	0.87	0.94	0.79
		3	0.94	0.96	0.89	0.95	0.80
		4	0.94	0.97	0.92	0.96	0.83
Groups with 4 piles	s/D	2	0.81	0.83	0.68	0.78	0.61
		2.5	0.81	0.86	0.75	0.83	0.67
		3	0.81	0.89	0.79	0.86	0.71
		4	0.81	0.92	0.84	0.89	0.76

Table 6 - Estimates of capacity for the groups with 2 and 4 piles corrected with efficiency.

Methods			Bearing capacity (kN)				
			Feld's Rule	Rule of uncertain origin	Converse-Labarre	Los Angeles	Sayed & Bakeer (1992)
Groups with 2 piles	s/D	2	128.6	128.6	115.4	126.3	103.8
		2.5	128.6	130.3	119.7	128.5	107.8
		3	128.6	131.5	122.6	129.9	110.4
		4	128.6	132.9	126.3	131.7	113.7
Groups with 4 piles	s/D	2	223.0	228.0	187.0	215.3	168.3
		2.5	223.0	237.3	204.5	227.1	184.1
		3	223.0	243.4	216.2	235.0	194.5
		4	223.0	251.2	230.7	244.8	207.7

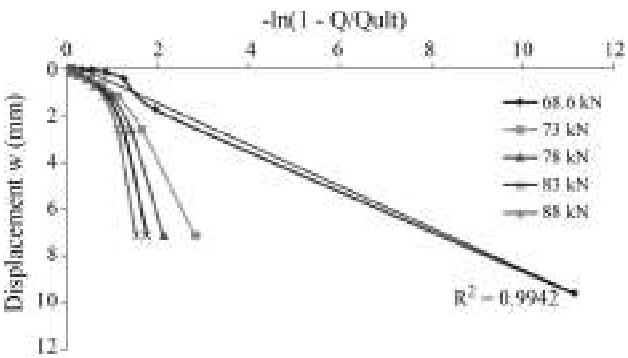

Figure 7 - Determination of Q_{ult} for the isolated pile using the Van der Veen (1953) method.

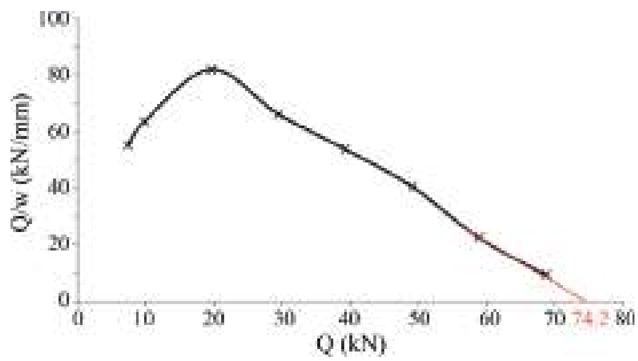

Figure 8 - Determination of Q_{ult} for the single pile using the Décourt (1996) method.

Afterwards, a comparison between the estimated ultimate load of the groups of 2 and 4 piles was carried out, for all the spacings investigated, and the respective reference values, obtained experimentally from the load tests.

For the 2-pile group and s/D = 2, the method that presented the closest estimate to the reference value was Converse-Labarre method, being 2.4 % higher. The other methods presented values ranging from 7.9 % lower to 21.8 % higher than the reference value. In the same way, for the 2-pile group and s/D = 2.5, it is noted that the closest estimate to the reference value was Converse-Labarre, being 0.5 % lower. The other values obtained presented variations from 10.4 % lower to 14.1 % higher in relation to the reference value.

Table 7 - Q_{ult} values estimated for the single pile and pile groups.

Number of Piles	s/D	Q_{ult} (kN)	η
Isolated	-	68.6	-
2	2	114.0	0.82
2	2.5	121.7	0.88
2	3	99.0	0.71
2	4	95.5	0.69

On the other hand, for the 2-pile group and s/D = 3, the method that provided the closest estimate to the reference value was Sayed & Bakeer (1992) method, however with a value higher than the one obtained in SLT. Again it is observed that, for the 2-pile group and s/D = 4, the prediction closest to the reference value was given by the Sayed & Bakeer (1992) method, however, with a value higher than the one obtained in SLT. And all the other estimates were higher than the reference value.

For the 4-pile group and s/D = 2 and 2.5, the predictions closest to the reference value were the ones proposed by the Sayed & Bakeer (1992) method, however, with a value higher than the reference value. The predictions made with the other methods were higher than the reference value, obtained through the SLT. Comparing the values of Q_{ult} with the reference value for the 4-pile group and s/D = 3, the estimates provided by all methods were higher than the reference value, with the Sayed & Bakeer (1992) method showing the most concordant result with the reference value.

Figures 9 and 10 compare the bearing capacity obtained by the SLTs for the groups with 2 and 4 piles. In these same figures are also indicated the Q_{ult} that the groups would have if there was no group effect (without GE), and

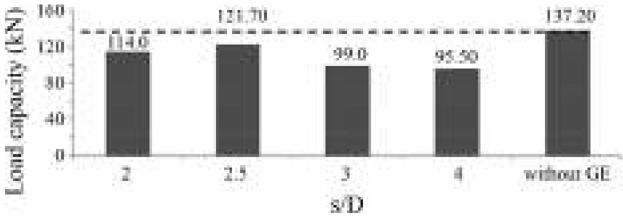

Figure 9 - Comparison of the Q_{ult} values obtained by SLT for the groups of 2 piles with s/D = 2, 2.5, 3 and 4.

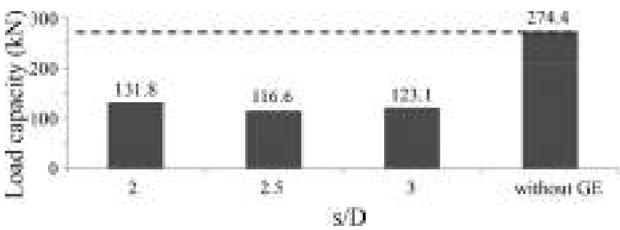

Figure 10 - Comparison of Q_{ult} values obtained via SLT for the 4-pile groups with s/D = 2, 2.5 and 3.

which were determined by the Q_{ult} product of the isolated pile obtained experimentally by the number of piles in each group.

According to Figs. 9 and 10, the group effect can be noticed in all the groups and all the spacings, because the bearing capacity of the groups was lower than the product of single pile Q_{ult} by the number of piles in the group. For the 4-pile group, this effect was more intense, reaching a value 2.4 times lower than when compared to the hypothesis of disregarding the group effect. It is worth mentioning that, if disregarding the group effect, the designer can lead the structure to failure, since the FS normally adopted is 2. Finally, a graph of the efficiency *vs.* the spacing is presented in Fig. 11.

Figure 11 shows that the group efficiency was, in all cases, less than 1.0. For the groups of 2 piles, an average value of η = 0.78 is observed and, for groups of 4 piles, the average efficiency was 0.44. Values of η lower than 1.0 are in agreement with the literature for bored piles in sand (Meyerhof, 1976 and O'Neil, 1983).

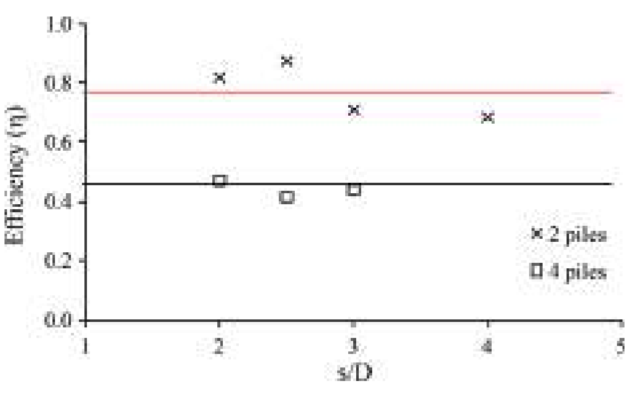

Figure 11 - Efficiency *vs.* spacing for groups with 2 and 4 piles.

For 2-pile groups, the larger the pile spacing the lower the group efficiency is. This trend was not observed in tests with pile spacing between 2D and 2.5D. Similarly, for 4-pile groups, no reduction of η is observed with the increase of pile spacing.

4. Conclusion

The accomplishment of this research allowed us to conclude that:

- Comparing the results of the SLTs performed in isolated piles, with and without Styrofoam disc at the toe, it was observed that the excavated piles bore all the applied load only by its lateral friction;
- The estimates of bearing capacity of isolated piles calculated by the semi-empirical methods proposed by Aoki & Velloso (1975), Décourt & Quaresma (1978) and Teixeira (1996) were in disagreement with the experimentally obtained values. Among the methods used, Teixeira's method (1996) provided the closest estimates to the values obtained from the load tests performed;
- For isolated piles, the use of N_{SPT} values corrected for 60 % efficiency led to closer Q_{ult} predictions than experimentally obtained values;
- Regarding the pile groups, the methods of Converse-Labarre and Sayed & Bakeer (1992) initially presented convergent estimates (2 piles and s/D equal to 2 and 2.5). On the other hand, for the other configurations, the estimated values were higher than those measured in the static load tests performed. The methods of Feld's rule, uncertain origin rule and Los Angeles equation presented estimates higher than the values obtained in the load tests performed in all situations;
- In all groups of piles (with 2 and 4 piles and s/D equal to 2, 2.5, 3 and 4) the group effect was verified;
- Lower efficiency values (η) were obtained in the 4-pile groups than in the 2-pile groups, indicating that for the investigated spacings, the group effect was more intense in the groups with the highest number of piles. This was due to the larger volume of soil contained between the piles of these groups. In this research, the group effect was even more intense because the piles worked exclusively by lateral friction.

References

ABNT (2010). Projeto e Execução de Fundações. NBR 6122, Rio de Janeiro, Brazil, 91 pp.

ABNT (1995): Rochas e Solos. NBR 6502, Rio de Janeiro, Brazil, 18 pp.

ABNT (2006). Estacas - Prova de Carga Estática - Método de Ensaio. NBR 12131, Rio de Janeiro, Brazil, 8 pp.

Aoki, N. & Velloso, D.A. (1975). An Aproximate Method to Estimate the Bearing Capacity of Piles. Proceedings of the 5th Pan American Conference on Soil Mechanics and Foundation Engineering, Bueno Aires, v. 1.

Bolin, H.W. (1941). The pile efficiency formula of the Uniform Building Code. Bldg. Standards Monthly, 10(1):4-5.

Chan. R.K.S. (2006). Foundation design and construction. The Government of the Hong Kong Special Administrative Region. Hong Kong. Geo Publication n. 1, 376 pp.

CGE. (1992). Canadian Foundation Engineering Manual. 3th ed. Canadian Geotechnical Society, Ottawa, 512 pp.

Das, B.M. (1998). Principles of Foundation Engineering. Brooks/Cole Publishing Company, Pacific Grove, California, 862 pp.

Décourt, L. & Quaresma, A.R. (1978) Capacidade de carga de estaca a partir de valores de SPT. Proc. 6° CBMSEF, Rio de Janeiro, v. 1, pp. 45-53.

Décourt, L. (1996). A ruptura de fundações avaliada com base no conceito de rigidez. 3° Seminário de Engenharia de Fundações Especiais e Geotecnia (SEFE III), São Paulo, pp. 215-224.

Feld, J. (1943). Discussion on friction pile foundations. Transactions of the American Society of Civil Engineers, 108:143-144.

Franke, E. & Muth, G. (1985). Scale effect in 1 g model tests on horizontally loaded piles. Proc. 11th International Conference of Soil Mechanics and Foundations, San Francisco. v. 2, pp. 1011-1014.

Garcia, J.R. (2015). Análise Experimental e Numérica de Radiers Estaqueados Executados em Solo da Região de Campinas/SP. Tese de Doutorado, Universidade Estadual de Campinas, Campinas, 359 pp.

Kézdi, A. (1957). Bearing capacity of piles and piles groups. Proc. 4th ICSMFE, London, v. 2, pp. 47-51.

Meyerhof, G.G. (1976). Bearing capacity and settlements of piled foundations. Journal of the Geotechnical Engineering Division, 102:197-228.

Nasr, A.M.A. (2014). Experimental and theoretical studies of laterally loaded finned piles in sand. Canadian Geotechinical Journal, 51(4):381-393.

Odebrecht, E. (2003) Medidas de Energia no Ensaio SPT. Tese de Doutorado, Universidade Federal do Rio Grande do Sul, Porto Alegre, 232 pp.

O'Neil, M.W. (1983). Group action in offshore piles. In: Proc. Conference on Geotechinical Practice in Offshore Engineering, Austin, pp. 25-64.

Pérez, N.B.M. (2014). Análise de Transferência de Carga em Estacas Escavadas em Solo da Região de Campinas/SP. Dissertação de Mestrado, Universidade Estadual de Campinas, Campinas, 171 pp.

Poulos, H.G & Davis, E.H. (1980). Pile Foundation Analysis and Design. Rainbow-Bridge Book Co, Sydney, 397 p.

Poulos, H.G. (1993). Settlement prediction for bored pile groups. Proc. 2nd. International Geotechnical Seminar on Deep Foundations on Bored an Auger Piles. Ghent, pp. 103-117.

Sales, M.M. (2000). Análise do Comportamento de Sapatas Estaqueadas. Tese de Doutorado, Universidade de Brasília, Brasília, 229 pp.

Sayed, S.M. & Bakeer, R.M. (1992). Efficiency formula for pile groups. Journal of Geotechnical Engineering, 118:278-299.

Scallet, M.M. (2011). Comportamento de Estacas Escavadas de Pequeno Diâmetro em Solo Laterítico e Colapsível da Região de Campinas/SP. Dissertação de Mestrado, Universidade Estadual de Campinas, Campinas, 166 pp.

Skempton, A.W. (1986). Standard penetration test procedures and the effects in sands of overburden pressure, relative density, particle size, ageing and over consolidation. Géotechnique, 36(3):425-447.

Silva, P.A.B.A & Cintra, J.C.A. (1996). Capacidade de carga de grupos de estacas escavadas de pequeno diâmetro. Proc. 3° Seminário de Engenharia de Fundações Especiais e Geotecnia (SEFE III), São Paulo, v. 1. pp. 247-256.

Stuart, J.G.; Hanna, T.H. & Naylor, A.H. (1960). Notes on the behavior of model pile groups in sand. Proc. Symposium on Pile Foundations, Stockholm, pp. 97-103.

Teixeira, A.H. (1996). Projeto e execução de fundações. Proc. 3° Seminário de Engenharia de Fundações Especiais e Geotecnia (SEFE III), São Paulo, v. 1. pp. 35-50.

Van der Veen, C. (1953). The bearing capacity of a pile. Proc. III International Conference on Soil Mechanics and Foundation Engineering, Zurich, v. 2, pp. 125-151.

Vesic, A.S. (1969). Experiments with instrumented pile groups in sand. Performance of Deep Foundations. ASTM Special Technical Publication, Philadelphia, n. 444, pp. 177-222.

Swelling Research of Expansive Soil Under Drying-Wetting Cycles: A NMR Method

G.F. Wei, J.G. Dong

Abstract. The main purpose of this study is to examine the influence of drying-wetting cycles on the swelling of disturbed expansive soil at the micro-scale. Swelling curve - the relationship between swelling displacement and water-absorbing time - is measured based on specimens that experienced 0-4 drying-wetting cycles. Assisted by Nuclear Magnetic Resonance (NMR), the stage characteristic and mechanism influencing swelling curve are analyzed from a pore-change perspective. Specimens that experienced 1-4 cycles show a higher swelling rate when compared with the specimens without drying-wetting cycles; the swelling rates of each swelling curve are found to decrease with an increasing water-absorbing time. These swelling curves are divided into rapid-swelling stage, slow-swelling stage, and slow-stable stage, where three straight lines are used to fit these stages to each curve. The swelling displacement of the specimen increases after the first cycle, whereas it decreases gradually during the following cycles. Changes of pore structure at each stage are considered to be the main factor affecting the swelling rate during the saturating process. Some fine particles and water-soluble cements are lost after multiple cycles, and some smaller pores are converted into larger pores, resulting in an increase in volume and a decrease of swelling displacement. Moreover, the increase of larger pores and the suction difference after various cycles are important factors leading to the difference of the swelling curve and the swelling displacement.

Keywords: drying-wetting cycles, expansive soil, NMR test, pore change, suction.

1. Introduction

Expansive soil, a special clay with high expansibility, fissures, and overconsolidation, is found in more than 40 countries such as China, the United States, and Canada (Laureano & John, 2017). Because of its constitutive hydrophilic minerals, for example, montmorillonite, illite, and kaolinite, expansive soil undergoes volumetric swelling or shrinkage with adsorption or desorption of water; moreover, these displacement changes based on water content have a certain repeatability (Osman, 2018). Swelling displacement is considered to be a main expansive soil disaster causing the most serious damage (Khazaei & Moayedi, 2019). The swelling ratio is approximately predicted by the initial water content, the plastic index, and the initial dry density, as these factors are considered to be important factors affecting the swelling characteristics in previous studies (Villar & Lloret, 2008; Signes *et al.*, 2016; Elbadry, 2017). Furthermore, factors such as mineral composition (Lin & Cerato, 2012), matric suction (Fredlund, 1983), and pH value have also been proved to have a good linear relationship with the swelling ratio; however, the displacement of expansive soil cannot be accurately calculated by the general unsaturated soil model due to its change of stress state and softening characteristics (Qi & Vanapalli, 2016). In addition, different stages of the swelling curve have their own particularity rather than a linear relationship between swelling displacement and water-absorbing time (Xiao *et al.*, 2005), whose mechanism is not clear yet.

On the other hand, expansive soil in shallow layers inevitably experiences drying-wetting cycles because of rainfall and evaporation. After repeated drying-wetting, the attenuation of modulus (Li *et al.*, 2013), penetration resistance (Wang *et al.*, 2016), and shear strength (Raja & Thyagaraj, 2019) are observed, which seriously threatens the buildings founded on it (Jablonowski *et al.*, 2012). Jablonowski *et al.* (2012) suggested that the drying-wetting cycle promotes the enrichment of inorganic materials in the soil, forming cementation with certain cohesion whose dilatancy is one of the factors affecting the expansive potential of soil (Mehta & Sachan, 2017). After the repeated action of “in and out” of rainwater, how the swelling characteristic of expansive soil changes is also a problem to be considered in preventing engineering disasters. Similar to the drying-wetting cycle, the change of pore structure is another important factor related to the difference of swelling characteristics (Tahasildar & Rao, 2016). Mercury intrusion porosimetry, a traditional method for pore structure testing, causes error when operated at a high pressure (Aldaood *et al.*, 2014). By being non-destructive, convenient, and keeping the pore intact, NMR is becoming more and

Guo-fang Wei, M.Sc., Assistant Professor, Sanmenxia Polytechnic, Sanmenxia City, China. e-mail: yang_jy2016@163.com.
Jun-gui Dong, Ph.D., Teaching Assistant, School of Civil Engineering and Transportation, South China University of Technology, Guangzhou City, China. e-mail: dhunter110@163.com.
Submitted on July 20, 2018; Final Acceptance on February 13, 2020; Discussion open until August 31, 2020.
DOI: 10.28927/SR.431021

more important in the study of geotechnical works (Kleinberg *et al.*, 2003).

This study focuses on exploring the intrinsic relationship between swelling displacement and changes of pore structure. Based on the previous researches, the swelling characteristics of disturbed expansive soil under various drying-wetting cycles are investigated in this study; NMR technology is then used to discuss the changes of pore structure of expansive soil with the variation of water content and the accumulating cycles. The swelling rate of each stage and the total swelling displacement are tested. Moreover, the soil-water characteristic curve (SWCC) after various drying-wetting cycles is also discussed because of its influence on the swelling characteristics.

2. Material and Methods

2.1. Basic properties of the soil used

Expansive soil used in this study is from depths between 2.0 m and 4.0 m under the subsurface of Nanning City, China. The soil was typical gray expansive soil with fissures, plasticity, strong stickiness, high water content, a small quantity of unweathered rock, and iron-manganese concretions. This soil, whose basic parameters and minerals are listed in Table 1, was classified as weak expansive soil according to relevant standards (GB 50112, 2013; ISO 17892-4, 2016; ISO 17892-12, 2018).

2.2. Specimen preparation

Compared with undisturbed soil, disturbed soil is without natural composition and cementation, which causes greater swelling displacement that threatens the buildings when meeting water (Frías-Guzmán & Hernández-Marín, 2019). Therefore, disturbed soil was used in this study. To achieve an equalized water content, wet soil with a water content of 12.0 % was firstly prepared and maintained in a sealed bag for more than 48 h before performing the tests. To eliminate the impact of iron on the magnetic field, a polytetrafluoroethylene-cutting sample ring (Φ 40 mm $\times$ 60 mm) was used instead of a conventional steel one. Subsequently, using the static pressure method, specimens with a diameter of 40.0 mm and a height of 40.0 mm were compacted at optimum moisture content (OMC), as the soil of subgrade and foundation engineering is usually compacted at OMC. Finally, three specimens with a density difference less than 0.02 g/cm^3 were divided into one group for the swelling test.

2.3. Swelling test

The swelling test was performed by a lever-consolidometer, where the swelling displacement was recorded by a dial indicator (range: 10.0 mm, accuracy: 0.01 mm). To avoid the specimen going beyond the top of the cutting sample ring during the swelling process, the selected specimen was removed into a cutting sample ring specially designed with a diameter of 40.0 mm and a height of 60.0 mm. The specimen together with the polytetrafluoroethylene cutting sample ring were placed into the consolidometer by using the testing method recommended by standards (JTG E40, 2007; ISO 17892-7, 2017), and the reading of the dial indicator was then recorded. Subsequently, distilled water was added to cover the bottom surface of the specimen to provide a free water-absorbing process. During the first 20 min, the reading of the dial indicator was recorded every 5 min while it was recorded every 10 min in the rest of the first 2 h, and then the recording time was changed according to the swelling rate of the specimen. When the value difference between the two readings in 2 h was less than 0.01 mm, the swelling displacement was considered to be stable. If the reading difference of them was less than 0.1 mm, the average value of three specimens was recorded as the vertical swelling displacement; otherwise, additional parallel tests were needed. Following the swelling process, the saturated specimen was dehydrated to a scheduled weight in a humidity-controlled chamber (range: from -20 to +120 °C, accuracy: ± 0.05 °C) at a temperature of 40 °C (here, the water content was approximately 5 %). At this point, a drying-wetting cycle was completed. The follow-up process of swelling and drying-wetting cycle is similar, where the repetition is unwanted.

2.4. NMR testing instrument and procedure

The testing instrument used in this work is a MiniMR-60 made in China. The magnetic field intensity of the instrument is 0.52 T, the temperature of the magnet is maintained at 32 ± 0.01 °C, and the effective testing area of the testing tube is Φ 60 mm $\times$ 60 mm. The testing procedure of this study is as follows: (1) Preparing soil specimens (Φ 40 mm $\times$ 40 mm); (2) Different drying-wetting cycles were completed in the polytetrafluoroethylene cutting sam-

Table 1 - Selected geotechnical properties of the soil obtained by testing.

w_L (%)	w_P (%)	I_P (%)	δ_{ef} (%)	G_s	P_e (kPa)	Mineral composition (%)			
						Gibbsite	Kaolinite	Illite	Quartz
45.30	22.10	23.20	57.00	2.72	169.00	6.44	23.1	25.46	45.00

Note: w_L is liquid limit; w_P is plastic limit; I_P is plastic index; δ_{ef} is free swelling ratio; G_s is specific gravity of soil particle; P_e is swelling force.

ple rings, except for the specimen of cycle 0; (3) All specimens were saturated with distilled water for 48 h; (4) Performing NMR relaxation measurement on saturated specimens experienced various cycles; (5) Collection and analysis of testing data.

3 Result Analysis and Discussion

3.1. Swelling curves under different cycles

To better discuss the influence of drying-wetting cycles on swelling characteristics, swelling curves of samples subjected to between 0 to 4 drying-wetting cycles are listed in Fig. 1, where the *X* axis is water absorbing time and the *Y* axis is vertical-swelling displacement. As the focus of this study is the swelling characteristic of soil affected by various drying-wetting cycles, the values observed within the N^{th} cycle disregarded the displacements of the previous cycle. Vertical displacements of the N^{th} cycle start from the same initial condition, since these displacemens are net displacements based on a dried specimen that experienced $(N - 1)^{th}$ cycles.

3.2. Trend analysis of swelling curves

Cumulative vertical displacement, in this study, is equal to the volume swelling of the specimen since the lateral swelling is restricted by the cutting sample ring. Having similar trend, swelling curves under various cycles rapidly grow with the increase of water-absorbing time, and then slow down and achieve a stable state (Fig. 1). Before cycling, a lowest swelling rate is observed, in which 230 min are consumed to finish ninety percent of the swelling displacement. From the 1st to the 4^{th} cycle, however, only 100 min are consumed to achieve the same quantity of swelling displacement, cutting off about 130 min. This phenomenon can be explained by the changes of pore structure. During the absorbing process of cycle 0, the specimen is compacted with a low water content, the diameter and distribution of pores are approximately uniform, where water is forced to rise evenly and slowly by capillarity. After the larger pores are filled with water and are swelled, water is allowed to enter smaller pores to complete the remaining 10 % of the swelling displacement. A dehydration process is experienced during the drying-wetting cycle, causing a smaller contact angle between water and particles than that caused in the wetting process (Kholodov *et al.*, 2015). These changes reduce the distance between particles and shrink the pores. Moreover, some fine particles are moved by the water to a smaller pore and stopped to form a pore throat. Therefore, when the specimen encounters water again, the water rises rapidly along the finer holes, completing more than 90 % of the expansion in two hours because of the larger suction caused by smaller capillart cross section.

As shown in Fig. 1, the relationship between the swelling displacement and water-absorbing time cannot be accurately fitted by one curve alone because of its differences between stages, where the hyperbola (Xiao *et al.*, 2005), a combination of curve, and straight line are used to fit these relationships. Considering the water absorbing characteristics of each swelling stage, the example data of cycle 3 are divided into 3 stages, namely, 0-30 min, 30-90 min, and beyond 90 min, and then three straight lines are used to approximate each stage. Figure 2 shows the fitting curve with a good conformance and high correlation coefficients (all above 0.9); the maximum error between observed displacement and the fitted displacement is about 0.1 mm; the swelling rate, the angular coefficient in the equation of the fitted lines, decreases in turn along the three stages.

3.3. Swelling rate analysis of each stage

Noticed from Fig. 2, a significant difference in the swelling rate is observed among the three stages, namely the rapid-swelling stage (0-30 min), slow-swelling stage (30-90 min), and slow-stable stage (beyond 90 min). For a clearer understanding of the influence of drying-wetting

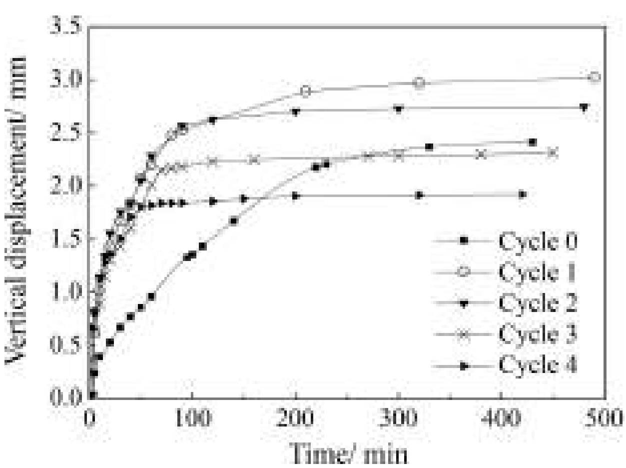

Figure 1 - Relationship between vertical displacement and time under different cycles.

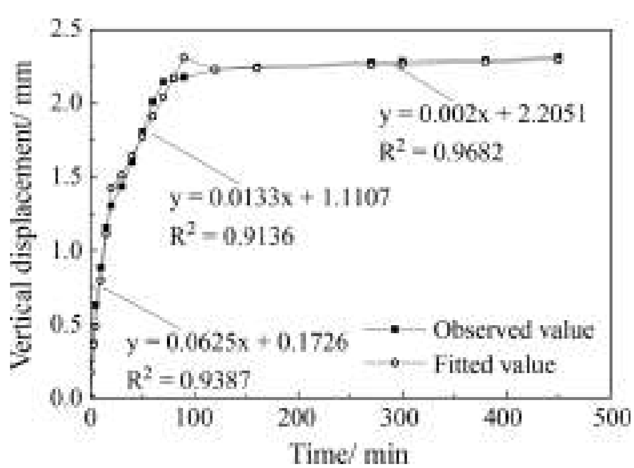

Figure 2 - Comparison between the fitted and observed data.

cycles on swelling rate, these swelling rates experienced in different cycles are listed in Fig. 3, where the X axis represents the swelling stage and the Y axis is the gradient of the fitting line (Fig. 2) at each swelling stage.

Figure 3 shows that the swelling rates of the second and the third stage are close to each other, while a large gap (about 300 %) among first stages is observed. For the specimens that experienced no drying-wetting cycles, the difference of swelling rate at each stage is not so eye-catching (about 60 %). For the specimens that experienced 1-4 cycles, a significant difference (about 290 %-370 %) of swelling rate at each stage is revealed, where the largest swelling rate at stage one is about 4 times that of stage two. The relationship between swelling rate and water absorbing stage under 1-4 cycles can be approximated by a logarithm curve (Eq. 1), where k is the swelling rate, x represents the water absorbing stage (value 1, 2, 3).

$$k = -0.05581 \ln(x) + 0.0584 \tag{1}$$

The authors believe that the water absorption and swelling is a process where pores are gradually filled with water, which is also a process of gradual transition from the unsaturated state to saturated state. Therefore, an unsaturated part always remains before the entire saturation is reached because of the gradual spreading of water from the bottom to the top of the specimen. Based on the difference of saturating process, the unsaturated soil is acceptably divided into three stages, *i.e.*, the water sealing stage, the both opening stage, and the gas sealing stage (Yu & Chen, 1965). In the first swelling stage with a low degree of saturation, the gas in pores is connected only, and the water is separated by gas and soil particles. At this point, a water film is formed due to the migration of capillary water, swelling rapidly the particles (Gonen *et al.*, 2015). The gas in pores is compressed and driven out of the specimen as the pore is contracted, so that water rapidly flows into the inner part of the specimen and the outside water quickly enters the pores. At this stage, the specimen has a higher swelling rate corresponding to the first stage of the swelling curve (Fig. 2). With the gradual increase of the saturation degree, the both opening stage it reached, in which both water and gas are connected and with their own channels to soil particles. Here, the swelling displacement of the soil particles contacting with water is basically completed, reducing the gas in pores, blocking some local pores, and causing a need of larger pressure to expel gas out. Accordingly, the reduced swelling rate at this stage shows a similar characteristic to the second stage in Fig. 2. After the swelling curve grows to the third stage, the gas sealing stage is reached via increasing the water in the specimen, gas in pores are surrounded and divided into bubbles. The water in the pores, in this case, is connected although few remaining bubbles are not, and the stability of swelling is coming.

3.4. Swelling under different drying-wetting cycles

After different cycles of drying and wetting, the total swelling displacement (vertical displacement) shown in Fig. 4 is obviously different. The swelling displacement of the specimen increases by about 20 % after the first cycle, and it then decreases with the accumulating of cycle number. The radial shrinkage of the specimen is found to be greater than the vertical shrinkage during the drying process due to the larger radial size of the specimen, which causes vertical compression of the soil particles. Therefore, after a drying process, the height of the specimen is greater than 20.0 mm (initial height), and the radial size of the specimen is less than 61.8 mm. Based on previous studies, the authors think that during the process of drying, pores are contracted after the water is discharged, and contraction stress on the pore is applied because of the surface tension of water, which intensifies the shrinkage of the pore (Dadashev & Dzhambulatov, 2015). Moreover, since some non-recoverable displacement is destined to occur in the drying process, the vertical swelling capacity of the specimen is greater than that of the radial after the first cycle

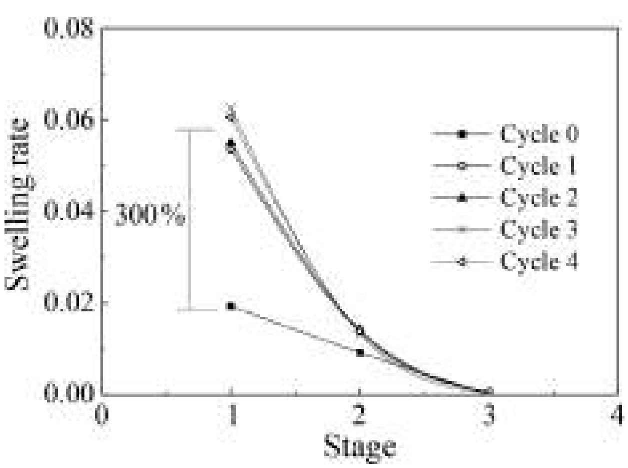

Figure 3 - Swelling rate at each stage under different cycles.

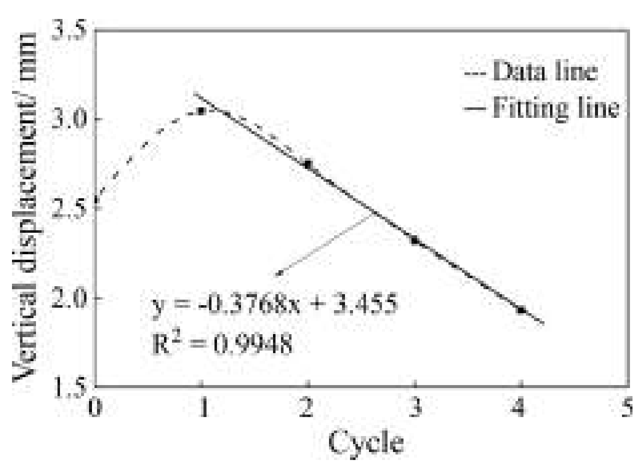

Figure 4 - Swelling displacement under various drying-wetting cycles.

(Komine & Ogata, 1994; Steiner, 1993). After the 2-4 cycles, however, the swelling displacement decreases with the accumulating of drying-wetting cycles, because the cycles all carried out on a same basis of dehydration and contraction, and because of the gradual accumulation of non-recoverable displacement.

The fissure in the specimen is believed to also be a reason for the differential swelling displacement. The SEM image of the specimen after one cycle is shown in Fig. 5a, while a similar image after four cycles is displayed in Fig. 5b. Soil particles after cycle 1 are closely contacted as the specimen is in a shrinking state (Fig. 5a). After the 4^{th} cycle, nevertheless, obvious fissures are observed, and most of them are developed along the vertical direction (Fig. 5b). The force hindering the lateral displacement is decreased because of the loss of strength between particles on the fissure surface. Consequently, the specimen is further broken with the increasing number of drying and wetting cycles, weakening the swelling ability gradually.

4. Nuclear Magnetic Resonance Test

The NMR refers to the resonant transition nucleus between energy levels under an external magnetic field. Under such a field, the number of protons and the duration (T_2) of the spin axis of protons restored to initial equilibrium after being deflected are obtained (Schaumann, 2011; Conte *et al.*, 2017). This quantity can be represented as an area distribution of the T_2 curve, from which the pore size and the ratios of different sizes in the soil can be calculated, allowing calculation of the water content. When a pore is spherical, the duration (T_2) is related to the pore radius by Eq. 2, where ρ_2 is the surface duration strength determined by the physical and chemical properties of the particle surface (Coates *et al.*, 1999), R represents the pore radius, and $(S/V)_{pore}$ is the ratio of the pore surface area to the volume of fluid inside. As a fast, nondestructive testing technique, the NMR technique is widely used in the fields of medicine, well water exploration, and oil exploration, for example (Malz & Jancke, 2005; Pauli *et al.*, 2012). In this study, the proton was used to explore the effect of the water content and drying-wetting cycles on the pores.

$$\frac{1}{T_2} = \rho^2 \left(\frac{S}{V}\right)_{pore} = \rho^2 \frac{3}{R} \tag{2}$$

4.1. Analysis of T_2 curves with different water content

Specimens (Φ 40 mm × 40 mm) in this section were free to swell vertically. After a quantity of distilled water was dropped into, the specimens were maintained in a sealed bag for more than 48 h to obtain a uniform water content. Experiments on 7 specimens with water contents of 10 %-28 % were completed using the method in section 2.4, and the T_2 curves were compared and analyzed, as shown in Fig. 6.

The NMR relaxation time related to the pore distribution is proportional to the pore radius of the specimens. Figure 6a shows that only one peak is observed in the T_2 curves with different water contents (from 10 % to 28 %), and these peaks are concentrated between 0.75 ms-2.3 ms. A uniform pore size was obtained by the static pressure method because the pore size of the specimen is mainly distributed between 0.10 ms-11.02 ms, and micropores (0.01 ms-0.1 ms) and macropores (≥ 11.02 ms) are seldom found. The movement of the T_2 peaks to the right proved that some smaller pores gradually transform into larger pores to increase the proportion of larger pores in the specimen.

The integral area of the T_2 curve represents the total quantity of pores in the specimen (Fig. 6a), and a non-negligible difference among these areas was observed for multiple water content values (Chukov *et al.*, 2015). When the water content increases from 19 % to 22 %, the volume of water in the pore increases greatly. However, only a small increase in the water volume is observed when the moisture content is within 10 %-19 % and within 22 %-28 %. This can be explained by the local expansion in the soil swelling process. After the entry of water, the crystal layer as well as the soil particle swells, the pores are

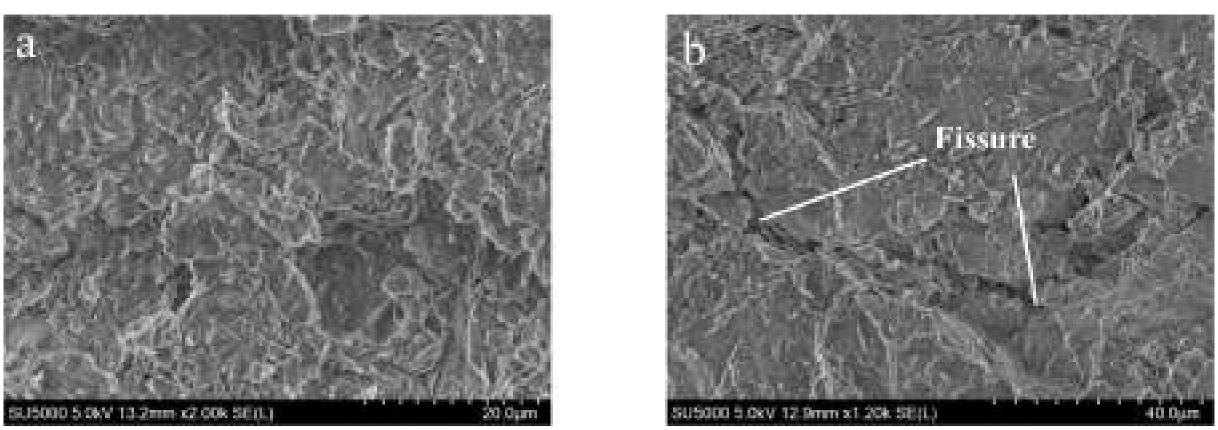

Figure 5 - SEM images after (a) cycle 1, (b) 4 cycles.

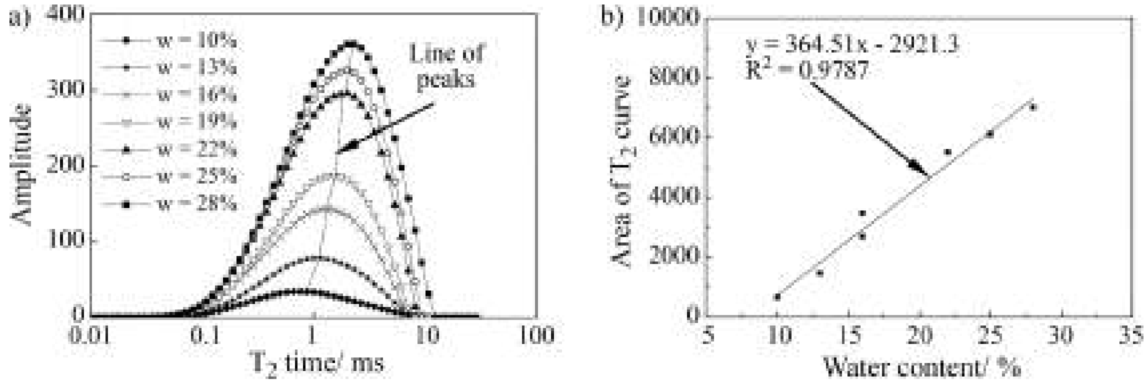

Figure 6 - T_2 curves affected by water content in saturating process: (a) T_2 curves with water content from 10 % to 28 %, (b) Areas of the T_2 curves under different water content.

squeezed, and larger suction and expansion rate are observed. For continuous water entry, the maximum water film on the particle surface is achieved, and the swelling of the soil tends to stability.

The integral area of the T_2 curve relative to the X axis is listed in Fig. 6b, which shows the variation in the integral area of the T_2 curve with varying water absorption. The integral area of the T_2 curve and the water content can be represented by a linear function ($y = 364.51x - 2921.3$), and the correlation coefficient is $R^2 = 0.9787$. The integral area of the T_2 curve is very sensitive to the change in the water content because it increases by approximately 11.6 times for a small change (18 %) in water content, and the water absorption is also directly related to the swelling characteristics of expansive soil. Therefore, the NMR can be used as an important method to study the displacement characteristics of expansive soil.

4.2. Analysis of T_2 curves under different cycles

The T_2 curves that experienced various cycles have two peaks (Fig. 7a). These former peaks are larger but indicate a shorter relaxation time, and the peak value of the latter peaks having a larger relaxation time is smaller. The relaxation time is proportional to the pore radius of the specimen, and the quantity of voids of a size less than this radius is represented by the size of the peak (Conte *et al.*, 2017). The integral area of the T_2 curve represents the total quantity of pores in the specimen. The smaller pores are represented by the integral area of the first peak, whereas the larger pores are characterized by the integral area of the second peak.

Figure 7a shows that the peaks of the T_2 curves do not change significantly with accumulating drying-wetting cycles, but the T_2 curves tend to increase as the cycle number increases, particularly the later peaks. In conclusion, the larger pores (5 ms-100 ms) are significantly affected by drying-wetting cycles, whereas smaller pores (0.01 ms-5 ms) are insensitive to the change in cycles. This may be due to the difference in pore structure caused by specimen particle composition, which results in the distinction of "*S/V*" inside the specimen, and ultimately leads to diverse relaxation time. The relaxation is weakened with larger aperture, and the amplitude of the T_2 curve is smaller (Jaeger *et al.*, 2006). On the contrary, the smaller aperture enhanced the relaxation, and a larger amplitude of the T_2 curve is observed. Each integral area is shown in Fig. 7b, where A

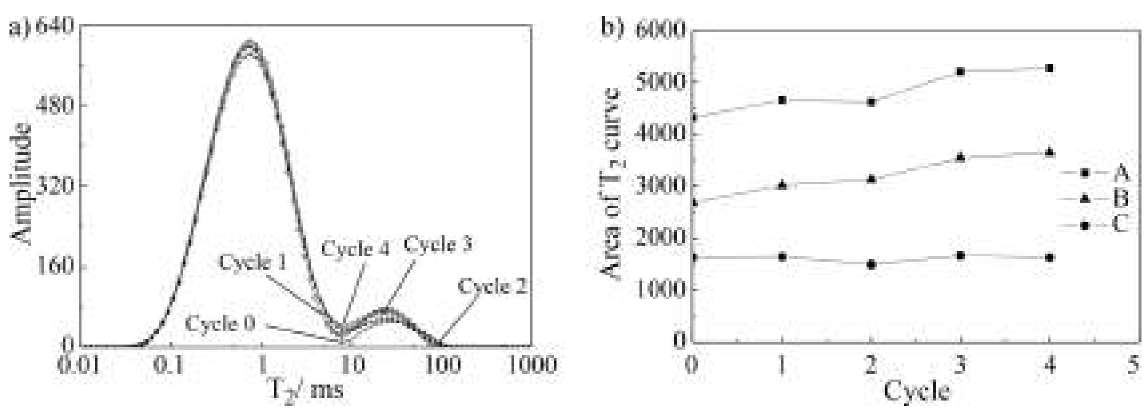

Figure 7 - T_2 curves under different number of drying-wetting cycle: (a) T_2 curves under 0-4 cycles, (b) Integral areas of T_2 curves, where A represents the total quantity of pores, B is the integral area of larger pores, and C is the integral area of smaller pores.

represents the total quantity of pores, B is the integral area of larger pores (the later peaks), and C is the integral area of smaller pores (the former peaks). Both the total integral area and the integral area of larger pores are found to increase with the accumulation of drying-wetting cycles. A slight fluctuation (about 5.3 %) of the integral area of smaller pores is discovered after the 4^{th} cycle; whereas, the integral area of the larger pores increased by about 35 %, which is close to the increase of the total integral area. In short, the total volume and the average radius of the pores are significantly increased with the growing of cycle numbers. These results can be explained by the structural effect caused by the drying-wetting cycles. Water quickly enters the specimens along the formed fissures, an expansive force is produced on the fissures. Therefore, some small pores swell into larger pores and new small pores are formed at the same time. As indicated by curve B in Fig. 7b, the increasing quantity of larger pores is associated with additional cycles. The change between the integral area of larger pores and the cycle number is expressed by Eq. 3, where S is the integral area of larger pores and N represents the number of cycles; the correlation coefficient is $R^2 = 0.9464$.

$$S = 245.41N + 2712.7 \quad (3)$$

Generally, there are two reasons for the change in pore structure of soil, one is the change of the position and the contact state between soil particles (Shein *et al.*, 2017), and the dissolving of the cementation formed by water-soluble salt is the other factor. During the drying-wetting cycles, the physical and chemical effects of the soil-water system accelerate the dissolving of cementation, smoothing or expanding the pores. Accordingly, the pore structure of the soil is changed. A specimen without drying-wetting cycles has smaller pore volume, and the proportion of smaller pores and larger pores is relatively close (Fig. 7b). At this point, the water holding capacity of unsaturated soil is limited with a uniform pore radius, and a relatively gentle swelling rate is observed (Fig. 1). After various cycles, however, the small pore that provides higher water holding capacity is almost unchanged while the larger pore increases, which increases the contact area between the specimen and water. Ther.efore, the swelling rate of the specimen obviously increases after experiencing drying-wetting cycles (Fig. 1). When it comes to the change law of swelling displacement, the authors think that a greater electrostatic force is found on the surface of the fractured soil divided by fissures in the cycling process, increasing the total swelling displacement of the specimen (Rojvoranun *et al.*, 2012). After some cementation and fine particles being taken away by the repeated streaming of water, the swelling capacity of the specimen is reduced.

4.3. Microstructure analysis in drying-wetting cycle

During the drying-wetting cycles, the pores of expansive soil can be divided into two types: the pores between agglomerates and the pores inside agglomerates (Pulat *et al.*, 2014). After the first cycle, smaller solid particles form a larger particle (agglomerate) because of flocculation. The pores between such agglomerates are larger than those inside the agglomerates, achieving a skeleton-gap structure as indicated in the right part of Fig. 8. Weaker polymers are observed between such agglomerates, where smaller particles are easier to be taken away by water. Figure 8 shows the process how water flows into and out during the drying-wetting cycle, gradually taking away smaller particles and water-soluble cementation in soil. Subsequently, pores between particles increase, the ratio of macropores increases, and the total swelling displacement decreases.

4.4. Suction effect on swelling

The matric suction, an important factor forcing the water migration, changes a lot after different drying-wetting cycles (Espitia *et al.*, 2019). To further explore the relationship between cycle number and the swelling characteristic, soil water characteristic curves (SWCC) under different cycles were tested via the saturated salt solution method where the specimens that experienced different cycles were dehydrated in a humidity-controlled chamber. These SWCCs at high pressure were then determined following the drying path. The saturated salt solution and the corresponding suction value used in this test are shown in Table 2. The water content of the specimen is changed because of the difference of pressure produced by various solutions. The Young-Laplace formula and Kelvin formula (Gane *et al.*, 2009) were used to deduce the measured data of water content *vs.* matric suction, as shown in Fig. 9.

The water content gradually decreases with an accumulating suction, and the influence of drying-wetting cycles on suction mainly occurs at the higher water content (above 3 %). A weak influence is observed when the water content is lower than 3 %; subsequently, the SWCCs tend to be stable and to be close to each other (Zhang *et al.*, 2014). A lower water content provides a larger suction causing a greater swelling rate of specimen. Then the suction attenuates with the increase of water content, and a lower swelling rate is observed (Fig. 2). In conclusion, as a result of the suction caused by the drying and wetting cy-

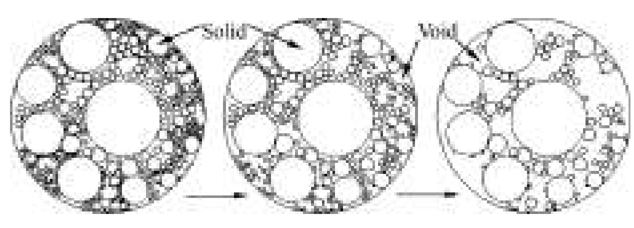

Figure 8 - Microstructure of expansive soil in drying-wetting cycle.

Table 2 - Saturated salt solution and corresponding suction (25 °C).

Saturated salt solution	HR (%)	Matric suction (MPa)
LiBr	6.37	371.79
$LiClH_2O$	11.30	294.40
CH_3COOK	22.51	201.35
$MgCL_26H_2O$	32.78	150.60
K_2CO_3	43.16	113.45
NaBr	57.57	74.55
KI	68.86	50.38
NaCL	75.29	38.32
KCL	84.34	22.99
K_2SO4	97.60	3.28

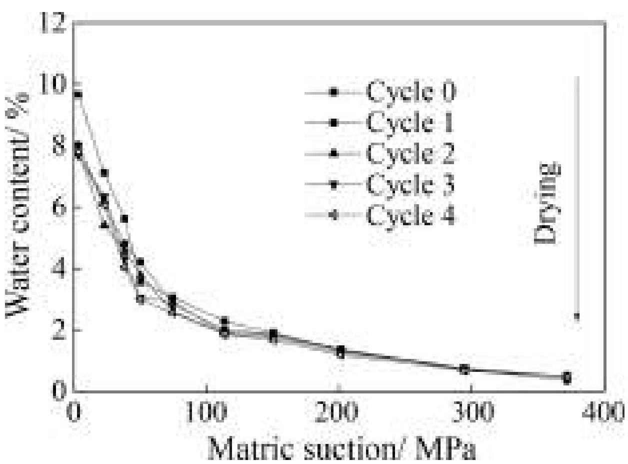

Figure 9 - Soil water characteristic curves by saturated salt solution method.

cles, especially at the higher water content, the divergence of swelling rate and the swelling displacement is smaller at the first swelling stage, while it is larger at the second and the third stages (Fig. 2).

5. Conclusion

This study characterized the influence of drying and wetting cycles on the swelling characteristics and the swelling displacement of expansive soil. Drawing support from the T_2 curves measured by the NMR technique, changes of pore structure under different water content and under various drying-wetting cycles were analyzed. Moreover, affecting the swelling characteristic, the SWCCs after different cycles were also discussed. The following conclusions can be drawn.

1) A similar trend of swelling characteristics and swelling displacement are found among specimens that experienced different cycles. The studied expansive soil, completing 90 % of the total swelling displacement in a short time, is sensitive to water, and the swelling rate (swelling speed) slows down with the increase of water-absorbing time.
2) The swelling rate of each stage is significantly different, which is roughly divided into the rapid-swelling stage, slow-swelling stage, and slow-stable stage. Fitted by three straight lines, the swelling curves under different cycles show a reasonable fitting error (less than 0.1 mm).
3) Based on NMR tests, a good linear relationship between pore volume and water content is observed. The change of pore structure during the drying-wetting process is believed to be the key inducer leading to the difference of the swelling rate. The drying-wetting cycle mainly increases the volume of larger pores, while showing a less influence on the smaller. Some smaller pores are converted into larger pores because of the loss of fine particles and water-soluble cement.
4) The three-stage difference of unsaturated soil, namely, the water sealing, both opening, and gas sealing is a key reason related to the difference of the swelling rate. In addition, fragmentation and the suction performance after experiencing multiple cycles are also associated with the swelling characteristic.

Acknowledgments

Financial support for this study was provided by the National Natural Science Foundation of China (Grant no. 51169005). The support is greatly appreciated. The authors also gratefully acknowledge the Guangxi Key Laboratory of Geomechanics and Geotechnical Engineering for the help on tests.

References

Aldaood, A.; Bouasker M. & Al-Mukhtar, M. (2014). Impact of freeze-thaw cycles on mechanical behavior of lime stabilized gypseous soils. Cold Regions Science and Technology, 99(1):38-45.

Chukov, S.N.; Abakumov, E.V. & Tomashunas, V.M. (2015). Characterization of humic acids from antarctic soils by nuclear magnetic resonance. Eurasian Soil Science, 48(11):1207-1211.

Coates, G.R.; Xiao, L.L. & Prammer, M.G. (1999). NMR Logging Principles and Application. Halliburton Energy Services Publication, Houston, 253 p.

Gonen, T.; Yazicioglu, S. & Demirel, B. (2015). The influence of freezing-thawing cycles on the capillary water absorption and porosity of concrete with mineral admixture. KSCE Journal of Civil Engineering, 19(3):667-671.

Conte, P.; Stefano, C.D.; Ferro, V.; Laudicina, V.A. & Palazzolo, E. (2017). Assessing hydrological connectivity inside a soil by fast-field-cycling nuclear magnetic resonance relaxometry and its link to sediment delivery processes. Environmental Earth Sciences, 76:526.

Dadashev, R.Kh. & Dzhambulatov, R.S. (2015). Features of the concentration dependences of the surface tension of water suspensions of bentonites. Russian Journal of Physical Chemistry A, 89(8):1504-1506.

Elbadry, H. (2017). Simplified reliable prediction method for determining the volume change of expansive soils based on simply physical tests. HBRC Journal, 13(3):353-360.

Espitia, J.M.; Caicedo, B. & Vallejo, L. (2019). Comparison of the uniaxial compressive strength of the belencito claystone under stress control and suction control paths. Rock Mechanics and Rock Engineering, 52(1):19-34.

Fredlund, D.G. (1983). Prediction of ground movements in swelling clays. Proc. 31st Annual Soil Mechanics and Foundation Engineering Conference, University of Minnesota, Minneapolis.

Frías-Guzmán, D.H. & Hernández-Marín, M. (2019). Experimental study on tensile strength of undisturbed and disturbed sandy soil samples from Aguascalientes Valley, Mexico. Geotechnical and Geological Engineering, 37(2):833-843.

Gane, P.A.C.; Salo, M.; Kettle, J.P. & Ridgway, C.J. (2009). Comparison of Young-Laplace pore size and microscopic void area distributions in topologically similar structures: A new method for characterising connectivity in pigmented coatings. Journal of Materials Science, 44(2):422-432.

GB 50112-2013. (2013). Technical Code for Building in Expansive Soil Region. China Architecture & Building Press, Beijing, China, 130 p.

ISO (2016). Geotechnical Investigation and Testing - Laboratory Testing of Soil - Part 4: Determination of Particle Size Distribution-17892-4. International Organization for Standardization, Switzerland, 31 p.

ISO (2017). Geotechnical Investigation and Testing - Laboratory Testing of Soil - Part 7: Unconfined Compression Test-17892-7. International Organization for Standardization, Switzerland, 20 p.

ISO (2018). Geotechnical Investigation and Testing - Laboratory Testing of Soil - Part 12: Determination of Liquid and Plastic Limits-17892-12. International Organization for Standardization, Switzerland, 36 p.

Jablonowski, N.D.; Linden, A.; Koeppchen, S.; Thiele, B. & Hofmann, D. (2012). Dry-wet cycles increase pesticide residue release from soil. Environmental Toxicology and Chemistry, 31(9):1941-1947.

Jaeger, F., Grohmann, E. & Schaumann, G.E. (2006). ^{1}H NMR relaxometry in natural humous soil samples: Insights in microbial effects on relaxation time distributions. Plant and Soil, 280(1-2):209-222.

JTG E40-2007. (2007). Test Methods of Soils for Highway Engineering. China Communications Press, Beijing, 423 p.

Khazaei, J. & Moayedi, H. (2019). Soft expansive soil improvement by eco-friendly waste and quick lime. Arabian Journal for Science and Engineering, 44(10):8337-8346.

Kholodov, V.A.; Yaroslavtseva, N.V.; Yashin, M.A.; Frid, A.S.; Lazarev, V.I.; Tyugai, Z.N. & Milanovskiy, E.Y. (2015). Contact angles of wetting and water stability of soil structure. Eurasian Soil Science, 48(6):600-607.

Kleinberg, R.L.; Flaum, C.; Straley, C.; Brewer, P.G. & Malby, G.E. (2003). Seafloor nuclear magnetic resonance assay of methane hydrate in sediment and rock. Journal of Geophysical Research Solid Earth, 108(B3):2137-2150.

Komine, H. & Ogata, N. (1994). Experimental study on swelling characteristics of compacted bentonite. Canadian Geotechnical Journal, 31(4):478-490.

Laureano, R.H. & John, M. (2017). Advances in characterization and analysis of expansive soils and rocks. Proc. 1st GeoMEast International Congress and Exhibition, Sustainable Civil Infrastructures, Sharm El Sheikh, v. 1, pp. 232-249.

Li, D.X.; Ling, J.M.; Qian, J.S. & Wang, H.L. (2013). Influence of moisture content change cyclicity on modulus evolution law of cohesive subgrade soil. Journal of Tongji University (Natural Science), 41(7):1051-1055.

Lin, B.T. & Cerato, A.B. (2012). Prediction of expansive soil swelling based on four micro-scale properties. Bulletin of Engineering Geology and the Environment, 71(1):71-78.

Malz, F. & Jancke, H. (2005). Validation of quantitative NMR. Journal of Pharmaceutical & Biomedical Analysis, 38(5):813-823.

Mehta, B. & Sachan, A. (2017). Effect of mineralogical properties of expansive soil on its mechanical behavior. Geotechnical Geological Engineering, 35(6):2923-2934.

Osman, K.T. (2018). Expansive soils. In: Management of Soil Problems. Springer, Cham, pp. 117-143.

Pauli, G.F.; Godecke, T. & Jaki, B.U. (2012). Quantitative 1H NMR: Development and potential of an analytical method: An update. Journal of Natural Products, 75(4):834-851.

Pulat, H.F.; Yukselen-Aksoy, Y. & Egeli, I. (2014). The effect of soil mineralogy and pore fluid chemistry on the suction and swelling behavior of soils. Bulletin of Engineering Geology and the Environment, 73(1):37-42.

Qi, S.C. & Vanapalli, S.K. (2016). Influence of swelling behavior on the stability of an infinite unsaturated expansive soil slope. Computers and Geotechnics, 76:154-169.

Raja, P.S.K. & Thyagaraj, T. (2019) Effect of sulfate contamination on compaction and strength behavior of lime treated expansive soil. In: McCartney, J. & Hoyos, L. (eds) Recent Advancements on Expansive Soils. GeoMEast 2018. Sustainable Civil Infrastructures. Springer, Cham, pp. 15-27.

Rojvoranun, S.; Chavadej, S; Scamehorn, J.F. & Sabatini, D.A. (2012). Mechanistic studies of particulate soil detergency: II: Hydrophilic soil removal. Journal of Surfactants and Detergents, 15(6):663-677.

Schaumann, G.E. (2011). Proton Nuclear Magnetic Resonance (NMR) Relaxometry in Soil Science. Encyclopedia of Agrophysics, Landau, pp. 543-669.

Shein, E.V.; Torbik, E.A. & Abrosimov, K.N. (2017). Changes in the pore space of soil constructions in physical laboratory models. Moscow University Soil Science Bulletin, 72(1):31-34.

Signes, C.H.; Garzón-Roca, J.; Fernández, P.M.; de la Torre, M.E.G. & Franco, R.I. (2016). Swelling potential reduction of Spanish argillaceous marlstone Facies Tap soil through the addition of crumb rubber particles from scrap tyres. Applied Clay Science, 132-133:768-773.

Steiner, W. (1993). Swelling rock in tunnels: Rock characterization, effect of horizontal stresses and construction procedures. International Journal of Rock Mechanics and Mining Sciences and Geomechanics Abstract, 30(4):361-380.

Tahasildar, J. & Rao, B.H. (2016). Determination of swelling characteristics using soil water characteristic curve parameter. Indian Geotechnical Journal, 46(3):319-326.

Villar, M.V. & Lloret, A. (2008). Influence of dry density and water content on the swelling of a compacted bentonite. Applied Clay Science, 39(1-2):38-49.

Wang, D.Y.; Tang, C.S.; Li, J.; Luo, X.W. & Shi, B. (2016). An experimental study of penetration characteristics of expansive soil under wetting-drying cycles. Rock and Soil Mechanics, 37(1):57-65.

Xiao, H.B.; Zhang, C.S.; He, J. & Wang, Y.H. (2005). Study on the relationship between deformation and time of Nanning expansive soils. Journal of Railway Science and Engineering, 2(6):47-52.

Yu, P.J. & Chen, Y.J. (1965). The pore air-water configurations and their effects on the mechanical properties of partially saturated soils. Journal of Hydraulic Engineering, 1:16-23.

Zhang, J.R.; Xu, Q. & Sun D.A. (2014). Simulation of soil-water characteristic curves during drying and wetting cycles. Rock and Soil Mechanics, 35(3):689-695.

Residual Shear Strength of a Residual Soil of Granulite

M. Heidemann, L.A. Bressani, J.A. Flores

Abstract. This paper discusses the residual shear strength of a granulite residual soil that was involved in a large landslide in Brazil. The residual strength was investigated because of the great mobility achieved by the soil after failure. The experimental program comprised physical and mineralogical characterization and residual shear strength measurements. Direct shear tests show a progressive breakage of soil structure. In the tests the soil showed brittleness under the higher normal stresses. The residual friction angle measured in direct shear test is about 12.0°, remarkably smaller than 25.0° measured in peak. For ring shear tests a linear failure envelope indicates a friction angle of 7.7°. The mobilization of the residual condition imposes a severe fall in shear strength and may explain the mobility presented by the soil during the reported landslide. Particle size analysis indicated that the material becomes finer after more energetic sample preparation, but the shearing did not cause significant particle disintegration. Most of the published correlations between the residual friction angle and clay fraction or plasticity index do not apply to this material.

Keywords: direct shear, residual strength, residual soil, ring shear, structured soil.

1. Introduction

Residual shear strength is important in understanding the stability of old landslides, in the assessment of the engineering properties of soil deposits which contain pre-existing shear surfaces and for risk assessment of progressive failure in new and existing slopes (Lupini *et al.*, 1981; Skempton & Petley, 1967; Skempton, 1985). It is also important for the design of remedial measures (Stark & Eid, 1994) and for the understanding the role of residual strength in first time failures (Mesri & Shahien, 2003).

In problems associated with mobility of soil mass after instabilities due to liquefaction, some researchers use the term residual shear strength to describe the fully softened strength of soil (Norris *et al.*, 1997; Wang *et al.*, 2007; Dewoolkar *et al.*, 2015). In such cases, the concept of residual shear strength is taken as the drop of shear strength by changes in porosity and excess of pore pressure in an undrained failure rather than by the processes described in the former papers (e.g.: Skempton & Petley, 1967; Skempton, 1985).

In 2008, hundreds of landslides were reported in Southern Brazil after heavy rainfalls, many of them involving residual soils of granulite. In a specific case, the failure was triggered 14 days after the main rains ceased. The mobilized soil mass, detached from a 50 m high elevation, presented a high mobility and travelled about 500 m as a mudflow along a flat area until deposition.

One hypothesis is that after the landslide triggering the shear strength had dropped to residual values along the failure surface and inside the unstable soil mass, causing the acceleration and fluidization (with undrained conditions) of the soil. When the shear strains cause a decrease in the soil friction angle to values lower than the fully softened (critical value) and undrained conditions are created, the displacements necessary to reach equilibrium will be very large.

Considering this case, a study about residual shear strength of the soil involved in these landslides was conducted in order to investigate the validity of this hypothesis and to contribute to the understanding of the residual strength of tropical soils. This study was conducted in terms of drained residual shear strength and aimed to measure the shear strength parameters and assess the effects of the shearing process to the integrity of soil particles. Some observations concerning the influence of test type on the strength parameters measured, the form of sample preparation and the validity of correlations between residual friction angle and soil physical properties have been made. Drainage conditions during the movement of the unstable mass are not further discussed here.

Both direct shear device and ring shear device can be used to measure residual friction angle (ϕ'_r) as both allow unidirectional shearing of a soil specimen, but the second is considered the most reliable. But only the ring shear apparatus can apply large shear strains (or large displacements) without reversing the direction of the shearing process (Bishop *et al.*, 1971; Bromhead, 1979; Tika, 1999; Suzuki *et al.*, 2007; Skempton, 1985; Stark & Eid, 1994; Watry & Lade, 2000). Although ring shear apparatus are not commonly found, and many designers and researchers use direct shear tests results, Vithana *et al.* (2011) have shown that measurements of ϕ'_r from direct shear are almost 2

Marcelo Heidemann, D.Sc., Associate Professor, Department of Mobility Engineering, Federal University of Santa Catarina, Joinville, SC, Brazil. e-mail: marcelo.heidemann@ufsc.br.
Luiz Antônio Bressani, Ph.D., Full Professor, Department of Civil Engineering, Federal University of Rio Grande do Sul, Porto Alegre, RS, Brazil. e-mail: bressani@ufrgs.br.
Juan Altamirano Flores, D.Sc., Associate Professor, Department of Geology, Federal University of Santa Catarina, Florianópolis, SC, Brazil. e-mail: juan.flores@ufsc.br.
Submitted on September 5, 2018; Final Acceptance on February 14, 2020; Discussion open until August 31, 2020.
DOI: 10.28927/SR.431031

times higher than those obtained from ring shear in tuffaceous clay and mudstone samples; circa of 1.02 to 1.3 in loess, siltstone and alluvial loess samples. Chen & Liu (2013), on the other hand, measured similar values of ϕ'_r using both techniques.

Most studies related to residual shear strength are focused on sedimentary and artificial soils (Skempton & Petley, 1967; La Gatta, 1970; Bishop *et al.*, 1971; Townsend & Gilbert, 1973; Kenney, 1977; Lupini *et al.*, 1981; Skempton, 1985; Skempton & Vaughan; 1993; Stark & Eid, 1994; Tiwari & Marui, 2005; Wang *et al.*, 2007; Toyota *et al.*, 2009; Eid *et al.*, 2016). There is much less residual shear strength data from residual soils formed through rock alteration under tropical and sub-tropical environments (Tanaka, 1976; Wesley, 1977; Boyce, 1985; Simões, 1991; Lacerda & Silveira, 1992; Rigo *et al.*, 2006).

Since mineralogy can control residual shear strength, as suggested by Hawkins & Privett (1985), Skempton (1985), Stark & Eid (1994), Chattopadhyay (1972), Vaughan *et al.* (1978), Meehan *et al.* (2010) and Collotta *et al.* (1989), much of the knowledge about residual shear strength of sedimentary and laboratory mixed soils does not necessarily apply to tropical residual soils (Boyce, 1985). In addition, Rigo *et al.* (2006) showed that measured values of ϕ'_r in tropical soils from Southern Brazil are affected not only by soil mineralogy, effective normal stress and particle size distribution but also by particle weathering, parent rock and pedogenetic processes. That may be the reason why many authors have reported that largely used correlations between residual friction angle and simple physical indices, developed for sedimentary soils, do not apply to residual soils (Hayden *et al.*, 2018; Stark & Hussain, 2013; Wesley, 2003; Stark & Eid, 1994; Boyce, 1985).

Since the works of Charles & Soares (1984), Hawkins & Privett (1985) and Skempton (1985), many other researchers have shown that the shear strength envelopes of clayey and plastic soils are nonlinear, especially at a low effective normal stress (Stark & Hussain, 2013; Stark & Eid, 1994; Mesri & Shahien, 2003).

Particles of some residual soils can suffer disintegration by manipulation during the sample preparation or during the tests, as shown by Collins (1985), Silveira (1991) and Rigo (2005). Soils with partly altered minerals are prone to be crumbled. Thus, it is not simple to define precisely/definitely the amount of clayey or silty particles on these soils in order to predict the residual friction angle through a correlation and if the failure envelope will be linear or nonlinear.

Hoyos *et al.* (2014), Infante Sedano *et al.* (2007) and Merchán *et al.* (2011) showed the effects of suction on the residual strength of soils. Such results are important on soils that occur in unsaturated state and this condition is important in large areas of the world. For soils in tropical and humid areas and for failures preceded by rainy periods, the suction role does not seem significant considering that because of the high saturation degree the suction level tends to be low (but should be evaluated in each case).

2. Soil Description

The soil studied occurs in Vale do Itajaí, Santa Catarina state, South Brazil. The coordinates of the studied area are UTM 696995E and 7024013S. The elevation is around 58 m above the sea level. The material was mobilized in a landslide that occurred in 2008, 14 days after a main event of heavy rainfalls (more than 700 mm/4 days). Such heavy rainfalls occurred after a period of more than 60 rainy days. The landslide scar and the deposited soil are shown in Fig. 1, as well as the 500 m path followed by the soil after the failure.

The soil is a residual soil from granulite that regionally occurs in soil profiles of thickness larger than 50 m without lateritic features even at small depth. A careful field inspection confirmed that relict structures were absent in the scar. Its main soil physical properties are presented in Table 1.

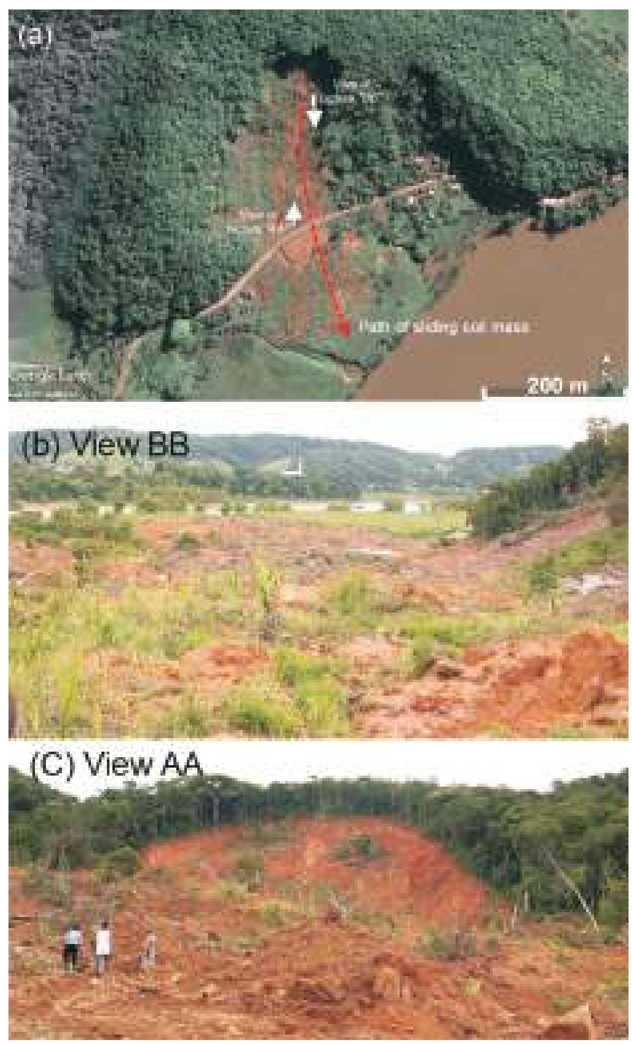

Figure 1 - Aerial view of studied area (a) and the mobilized soil after the landslide (b and c).

Table 1 - Summary of physical properties.

w_L [(1)]	47
w_P [(1)]	31
P_I [(1)]	16
G [(2)]	2.65
γ_d	11.9 kN/m^3
e	1.21
w_{nat} [(3)]	40.7 %
S_r [(3)]	87 %

[(1)]According to D4318/2010 (ASTM); [(2)]According to D854/2010 (ASTM); [(3)]Measured 8 months after the event.

The soil water characteristic curve (SWCC), previously determined in accordance with the recommendations of D5298/2010 (ASTM), revealed that for the range of saturation degree in which this soil was sampled the suction levels were lower than ~50 kPa. Considering the very wet period that preceded the landslide, the expected suction values should have been even lower. So, it is unlikely that suction had any significant role in the failure process and it was not taken into account.

In its natural state, the soil is composed mainly by silt as shown in the particle size curve (Fig. 2) obtained with the use of dispersive solution, according to procedures described in D422-63/2007 (ASTM). Before sieving, the crumbs of the soil were broken up using a mortar and rubber covered pestle. Care was taken to prevent disintegration or reduction of individual particles, using enough force as necessary to break up the aggregations without destroying the individual particles. The results revealed about 20 % of clays and the soil is classified as a silt of low plasticity (ML) by the Unified Soil Classification System - USCS (ASTM D2487/2011). Tests without the dispersive solution were

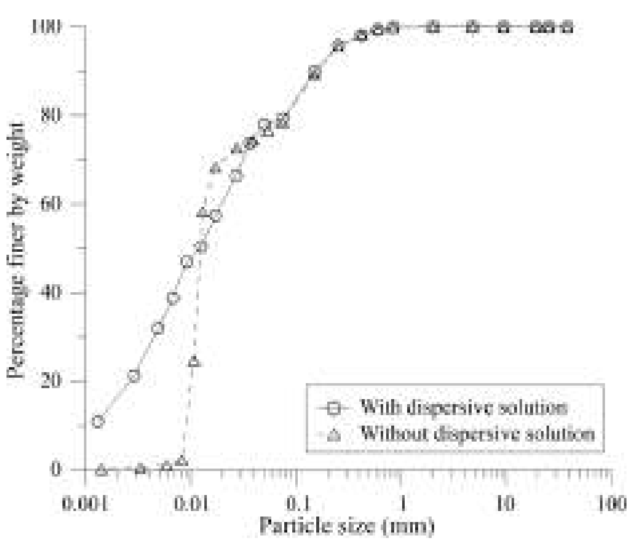

Figure 2 - Particle size curves of studied soil.

also carried out and the difference between them is shown in Table 2 with the clay fraction being the most affected.

The differences observed in Fig. 2 may be in part explained through the analysis with Scanning Electron Microscope (SEM). The images reproduced in Fig. 3 were made from crumbles carefully extracted from the inner part of an undisturbed sample. The crumbles had about 5 mm diameter and before the analysis they were air dried for 96 h and then oven dried for 24 h. Metallization of these samples was made by a first layer of carbon and a second layer of gold. SEM analysis was carried out in a SEM model JEOL JSM5800.

As shown in Fig. 3a some of the clay particles are grouped together forming clusters of silt and sand size. Other particles are adhered to larger particles (Fig. 3b). Feldspar crystals appear very altered and sometimes the cleavage planes are opened being susceptible to disintegration under mechanic actions (Fig. 3c).

In mineralogical terms, the soil is formed mainly by quartz, feldspars and kaolinite. Small amounts of illite and smectite were also found in X-ray diffractometry. These analyses were carried out in soil samples composed by particles smaller than 2 μm. With these fraction 4 pastilles were prepared: the first was analyzed in natural condition without orientation (powder), the second was analyzed in natural condition with orientation, the third was previously saturated with ethylene glycol (to find expansive minerals) and the last was previously heated at 550 °C for 2 h (for a better detection of kaolinite). The analyses were made using a diffractometer Siemens Bruker AXS, model D5000 with a goniometer θ - θ. The results were assessed with basis in the reference spectra of the JCPDS database.

3. Experimental Program

The soil was sampled in 15 cm edge blocks, in accordance with Brazilian Standard NBR 9604/1986 (ABNT). The blocks were extracted from the same location, in the middle of the landslide scar, which would represent around 6 m depth on the original profile. There was no visible heterogeneity in the exposed soil profile, except for the upper layer of organic topsoil.

Table 2 - Percentages of fractions obtained in the tests.

Fraction[(1)]	With dispersive solution	Without dispersive solution
Gravel	0	0
Coarse sand	0	0
Medium sand	1.92	1.73
Fine sand	18.75	19.81
Silt	63.87	78.09
Clay	15.46	0.37

[(1)]According to NBR 6502/1995 (ABNT).

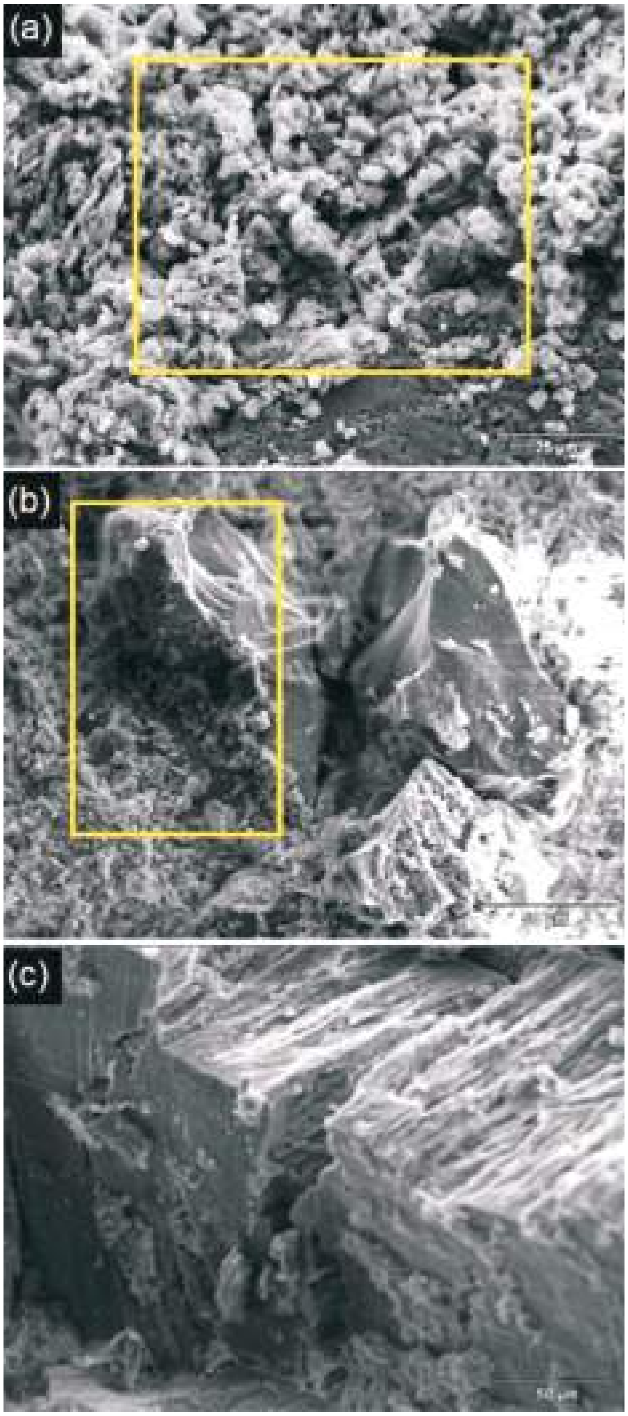

Figure 3 - Scanning electron microscopy images: (a) Detail in the box: silty size clusters formed by clays and fine silts; (b) Detail in the box: clays adhered to large quartz particle; (c) Cleavage of an altered feldspar crystal.

The position and orientation of the block samples were registered before moving them to the laboratory. Undisturbed specimens were trimmed from these blocks in order to guarantee that the shearing would occur in the same direction as the field failure. This was considered important as the original rock is metamorphic and the soil structure may preserve an anisotropic behavior. Direct shear tests have been carried on these undisturbed specimens according to general recommendations of D3080/2004 (ASTM).

The tests were carried out in saturated condition under effective normal stress of 50, 100, 200 and 380 kPa. Drained tests were chosen as they seem to represent the soil condition up to the onset of larger mass displacements. After the landslide triggering, the shear conditions probably changed to undrained conditions due to the dramatic rate increase (there is no field monitoring to support this assumption).

Computation of the shear rate based on values of t_{90} ($t = 11.6.t_{90}$) pointed out to a shear time of about 100 min. Considering the soil classification (ML) the authors decided to use a value 2 times larger than the 200 min suggested by the D3080/2004 (ASTM) for this kind of soil. The shear rate chosen was 0.016 mm/min that corresponds to ~400 min for a displacement of 7.5 mm. Each specimen was sheared 4 times: 3 reversal tests were carried out after the first one. To execute the reversals, normal stresses were reduced to 50 kPa and, after repositioning the specimen in the starting point, the required normal stress was applied again, and the new shearing stage started.

Ring shear tests were carried out following the D6467/2006 (ASTM) instructions in an equipment originally described by Bromhead (1979). This apparatus requires remolded specimens, which were prepared with the soil fraction passing in the #40 sieve. Before sieving, the crumbs of the soil were broken up using a mortar and rubber covered pestle. Care was taken to avoid disintegration or reduction of individual particles, using enough force as necessary to break up the aggregations without destroying the individual particles (as recommended in D6913/2009 (ASTM)). This procedure aimed to keep the microstructural features of the soil. Moisture content was corrected in order to reach the plastic limit (w_p = 31 %) as suggested by Stark & Vettel (1992) and Bromhead (1986). Distilled water was added to a soil sample of known dry mass and manually mixed and homogenized. The sample was kept hermetically closed in a bag for 48 h in order to obtain homogenization. The ring shear cell was filled manually, pressing the soil with a spatula until filling up the shear cell. The tests were performed with effective normal stress ranging from 25 to 600 kPa adopting a single stage technique (*i.e.* for each stress level one specimen was tested). Prior to the measuring test, a pre-shearing step was carried out to rapidly reach the residual strength condition (Anayi *et al.*, 1988; Stark & Vettel, 1992). The rate used during the tests was 0.12°/min (0.089 mm/min), which is considered slow enough to prevent the occurrence of excesses of pore pressure. The drainage occurs through the top and the bottom of the specimen where there are porous rings.

The granulometry of the soil used in one ring shear test (σ' = 200 kPa) was determined before the test after specimen assembling and after the test with the soil sample being taken from the region along the shear surface. As the amount of soil available was small, sieving and sedimentation procedures could not be used. Laser scanning was employed instead, using a CILAS 1180 apparatus without the use of dispersive agents. The analyses were made in a powder sample through the consideration of their light-scattering properties based on ISO 13320-1/2009 recommendations.

4. Results and Discussions

The initial physical characteristics of soil specimens used in direct shear tests are shown in Table 3. All the specimens presented almost the same unit weight, porosity and saturation degree with the exception of the specimen used in the test under effective normal stress of 380 kPa, which had lower void ratio and higher dry unit weight.

Figure 4 shows the direct shear results (stress-displacement curves) including the magnitude of shear strength parameters in (a) peak, (b) after the first shearing stage and (c) at large strain condition (end of test). Although a reduction of mobilized shear stress can be observed under all the normal stresses tested, this reduction is much clearer under 200 kPa and 380 kPa as a more brittle behavior can be observed. So, besides the shear displacement, the importance of higher normal stress is quite remarkable in the mobilization of residual strength.

Table 3 - Physical properties of specimens used in direct shear tests.

	50 kPa	100 kPa	200 kPa	380 kPa
w (%)	40.3	40.0	42.0	39.0
γ (kN/m^3)	16.3	16.2	16.4	16.6
γ_d (kN/m^3)	11.6	11.5	11.5	11.9
e	1.24	1.25	1.25	1.18
S_r (%)	86.3	84.7	89.7	87.6

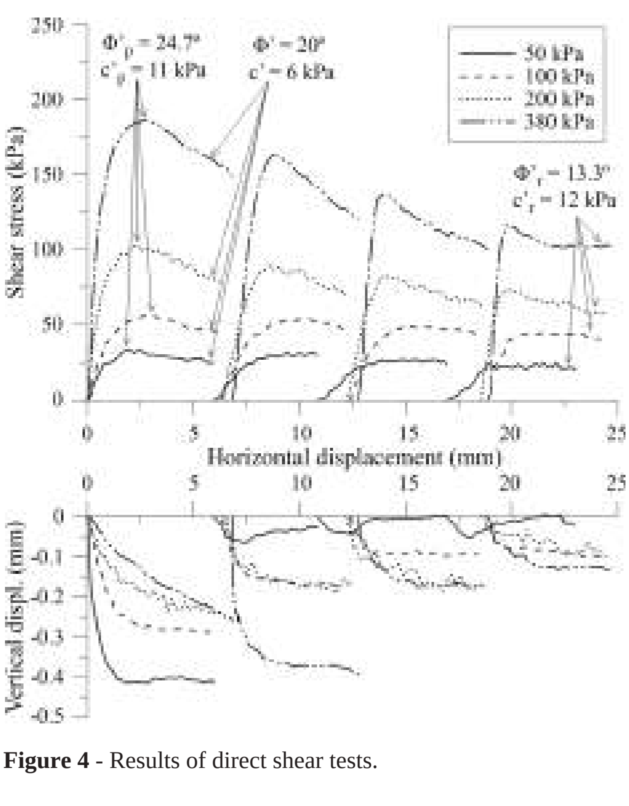

Figure 4 - Results of direct shear tests.

At the beginning of each shear reversal stage, the mobilized shear stress is higher than measured at the end of the previous stage. This is probably due to the partial disarrangement of the particle alignment caused by the reversal process itself, a common criticism of this technique (see Stark & Eid, 1994; Skempton & Petley, 1967; Skempton, 1985; Stark & Vettel, 1992; Hawkins & Privett, 1985), but the shearing stress dropped very quickly with the straining.

Except for the tests under σ' = 50 kPa, the behavior is typically contractive in all tests. The contraction in the first shear stage of the test under σ' = 50 kPa is probably due to voids reduction, which does not occur during consolidation with higher normal stresses. Unfortunately, due to limitations of the direct shear apparatus, such data cannot be examined quantitatively.

The peak shear strength parameters were derived from the highest shear stress measured in each test. The failure envelope for post peak shear strength was defined from a stable value of shear stress or from that for a displacement of 10 %. The failure criterion for residual conditions was defined from the final stable value of shear stress at the 4th stage.

Although large displacements are required for the mobilization of the (minimum) residual shear strength, considering the final mobilized shear stress of the 4th stages (4 tests), a linear failure envelope was obtained resulting in a residual friction angle (ϕ'_r = 13°) and cohesive intercept (c'_r ~ 12 kPa), which represent a remarkable drop from the peak strength.

The initial physical properties of the remolded specimens used on ring shear tests are presented in Table 4. These specimens were molded with higher density than undisturbed specimens to prevent that after the consolidation step the specimens become too thin.

The stress-displacement curves obtained from ring shear tests on remolded samples are shown in Fig. 5. The mobilized shear stress becomes stable when displacements exceeded about 20-30 mm. The tests with normal stresses

Table 4 - Physical properties of specimens used on ring shear tests.

w (%)	31.0
γ (kN/m^3)	16.7
γ_d (kN/m^3)	12.8
e	1.03
S_r (%)	79.4

of 400 and 600 kPa showed small shear strength peaks even after the pre-shear procedure (as reported by Lupini *et al.*, 1981).

Figure 6 shows the effective normal stress plotted against stress ratio (τ_r/σ') and friction angle derived for the end of the tests. The data indicate that the residual friction angle is affected by effective normal stress and the failure envelope is not linear. This is typical of soils in which sliding is the mechanism that controls the mobilization of residual strength, as high stress and/or displacement converts edge-to-face to face-to-face particle interactions, according to Stark & Eid (1994). In this soil, this is probably due to the high proportion of flatty particles, including some silts (as suggested by Anderson & Hammoud, 1988; Hawkins & Privett, 1985). Other authors such as Stark & Eid (1994) and Skempton (1985) report such non-normalization as caused by large amount of clay particles, which is not the case in this soil. The non-linearity of the failure envelope becomes clearer for effective normal stresses higher than 400 kPa (Fig. 7).

Shear strength parameters derived from these ring shear and direct shear tests are summarized in Table 5. The failure criterion adopted was the stabilization of mobilized shear stress at the test end.

The value of the residual friction angle (ϕ'_r ~ 7.7°) also indicates the occurrence of a sliding failure (Lupini *et*

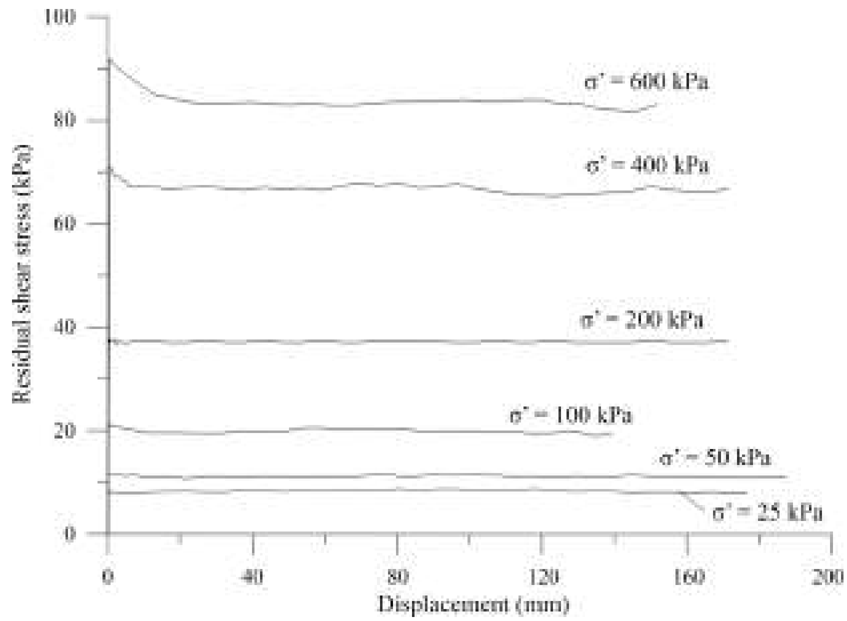

Figure 5 - Shear stress-displacement curves from ring shear tests.

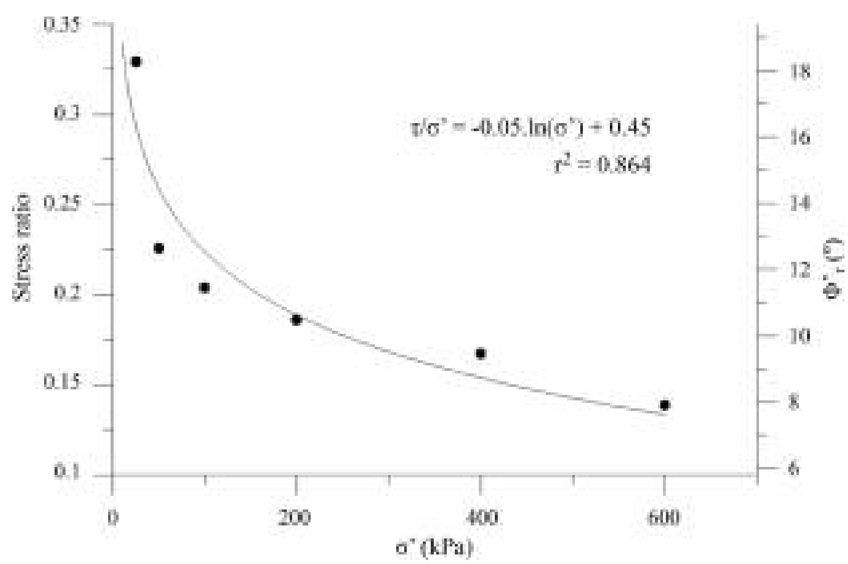

Figure 6 - Stress ratio and friction angle *vs.* effective normal stress.

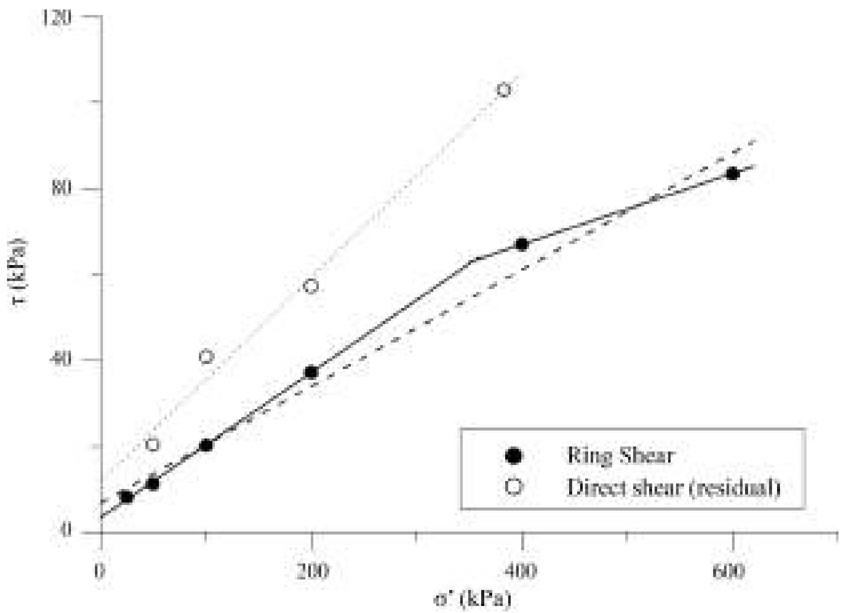

Figure 7 - Shear strength envelopes.

Table 5 - Summary of measured residual shear strength parameters.

Condition	ϕ'_r (°)	c'_r (kPa)	r^2
Ring shear (σ'_n = 25-600 kPa)	7.7	6.9	0.984
Ring shear (σ'_n = 25-600 kPa), c' = 0	8.6	0	0.957
Ring shear (σ'_n = 25-400 kPa), bilinear	9.0	4.3	0.999
Ring shear (σ'_n = 400-600 kPa), bilinear	4.7	34.0	1.000
Direct shear with reversals	13.3	12.0	0.988
Direct shear with reversals, c' = 0	15.7	0	0.939

al., 1981). On the other hand, according to the correlation developed by Mitchell (1993), the purely clayey fraction of this soil (computed from the test with dispersive solution) would lead to a turbulent shearing, without a smooth and well-defined shearing surface.

According to Kenney (1977), the sliding-like residual strength is strongly linked to the lamellar particle mineralogy. Lupini *et al.* (1981) associate low residual friction angles with the domain of montmorillonite clay minerals, while high residual friction angles would be linked to the presence of kaolinites and illites. And, although X-ray diffraction analyses indicate the predominance of kaolinite in the soil, it presented a low residual friction angle, contrary to the tendency presented by pure kaolinites studied by Tiwari & Marui (2005) and Lupini *et al.* (1981).

Adjusting linear envelopes to direct shear experimental data gives a ϕ'_r that is 1.7 times higher than that obtained from ring shear tests considering $c'_r > 0$ and 1.8 times if $c' = 0$. As residual friction angles are typically low, even small differences generate large percentage differences that reflects on the calculated stability safety factors.

Skempton (1985), Stark & Eid (1994) and Watry & Lade (2000) had already reported differences in this sense. Considering the more recent results presented by Vithana *et al.* (2011), the values measured in this work are consistent and fall between the observed by those authors in sedimentary clayey and sandy soils.

The process of sample preparation for ring shear test seems to cause some soil disaggregation, albeit small. Figure 8 shows particle size distribution curves of natural soil and of soil subjected to ring shear tests, obtained following D422-63/2007 (ASTM) recommendations. It is important to remember that particles larger than 0.42 mm had been removed from the specimens for the ring shear testing (< 2 %).

The soil manipulation during preparation of ring shear test specimens caused some soil aggregate disintegration mainly in the range between 0.04 and 0.3 mm. Probably such disintegration reaches sandy and silty clusters and partially altered feldspars. But the grading did not change significantly due to the shearing itself (see soil curves before and after testing - Figure 8). The testing did increase

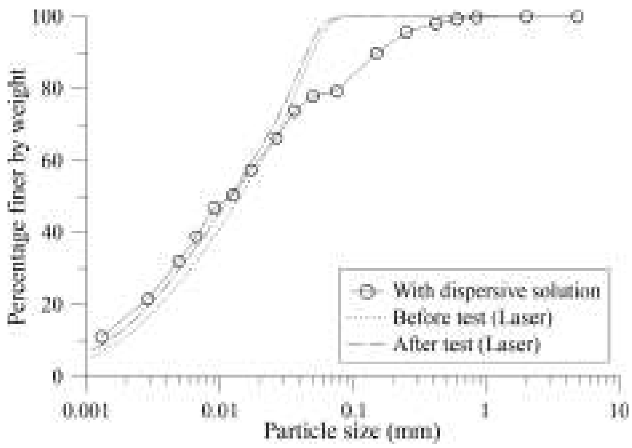

Figure 8 - Curves for the soils used in ring shear tests and reference grading curve.

the clay content (particles < 0.002 mm) by about 2.5 %. Consequently, the low residual shear strength of this soil seems to be associated to alignment of the particles parallel to the shear surface and some disintegration of soil clusters rather than individual soil particles breakage. On the other hand, the soil clustering may explain the large difference between peak and residual friction angle in direct shear tests.

None of the correlations between ϕ'_r (ring shear linear envelope with $c' > 0$ or $c' = 0$) and clay fraction or plasticity index, as proposed by Lupini *et al.* (1981), were able to successfully predict the behavior of this soil as shown in Fig. 9.

In contrast, the chart presented by Rigo *et al.* (2006), which shows the relationship between ϕ'_r and P_I found for quite a number of different soils, including various tropical soils, seems consistent with the results obtained here (Fig. 10). The soil studied here presents a similar behavior to soils tested by Rigo *et al.* (2006) with partially weathered minerals, also having a low friction angle and low P_I. According to those authors, such behavior is due to the disintegration of some minerals promoted by large displacements and subsequent particle reorientation. The same explanation appears to apply to the studied soil.

It is important to emphasize that this chart was not proposed by those authors to correlate the residual friction angle to P_I, but rather to state that, in some soils that are not sedimentary, this property can have a large variation compared to the observed results described by the classical work of Skempton and co-authors. Although volcanic ash soils have a large P_I and a much higher than expected value of ϕ'_r, the tropical soils with partly weathered minerals (most with clay particles inside them) have a low P_I and a very low value of ϕ'_r. So, Fig. 10 shows the importance of understanding that the expected behavior of soils is largely dependent on which group the soil belongs to (sedimentary clays and sands, lateritic soils, volcanic ash, residual soils with degradable minerals or micaceous).

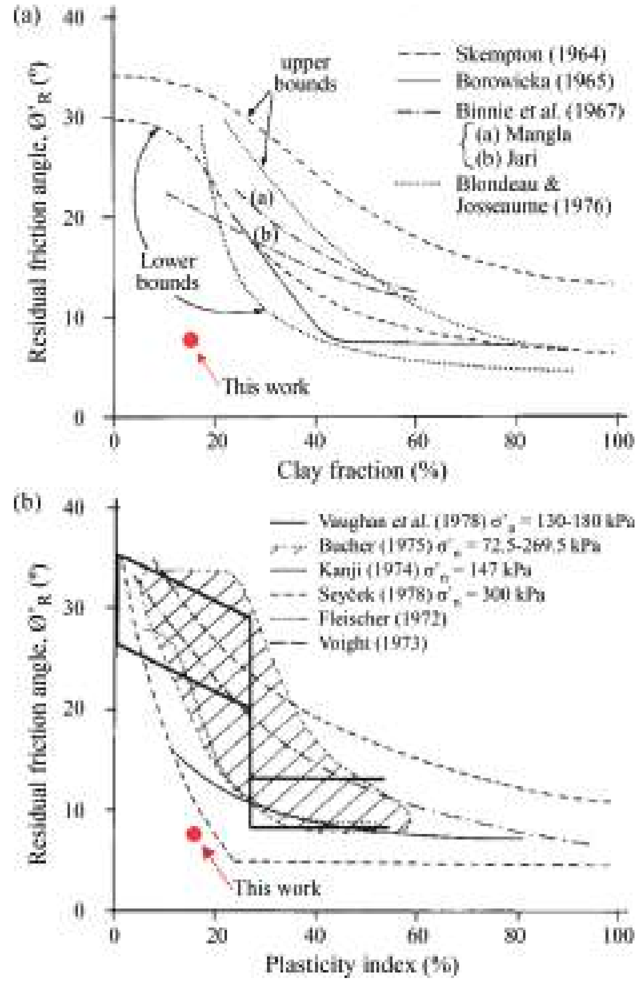

Figure 9 - Residual strength correlations with clay fraction (a) and plasticity index (b) (modified from Lupini *et al.*, 1981).

5. Conclusions

Ring shear tests on specimens of granulite residual soil resulted in an average residual friction angle of 7.7° associated to a sliding mode of failure, despite the small amount of clay minerals in its composition. Compared to data of sedimentary soils this value is quite low considering the small clay fraction in its composition. Reversal direct shear test results gave a higher 'residual' friction angle (12°) as the reversals cause particle misalignment. The obtained failure envelope was linear.

Specimen preparation for ring shear tests caused some disintegration of clusters of silt and fine sand size and increased the amount of free fine particles. In the laboratory tests, the shearing process does not seem to cause further disintegration as there are small differences between the pre and post-test particle size distribution curves (the clay fraction increased by 2.5 %).

The chart presented by Rigo *et al.* (2006) showed that the correlation between ϕ'_r and P_I is dependent on soil origin and composition. The soil tested presented a relation-

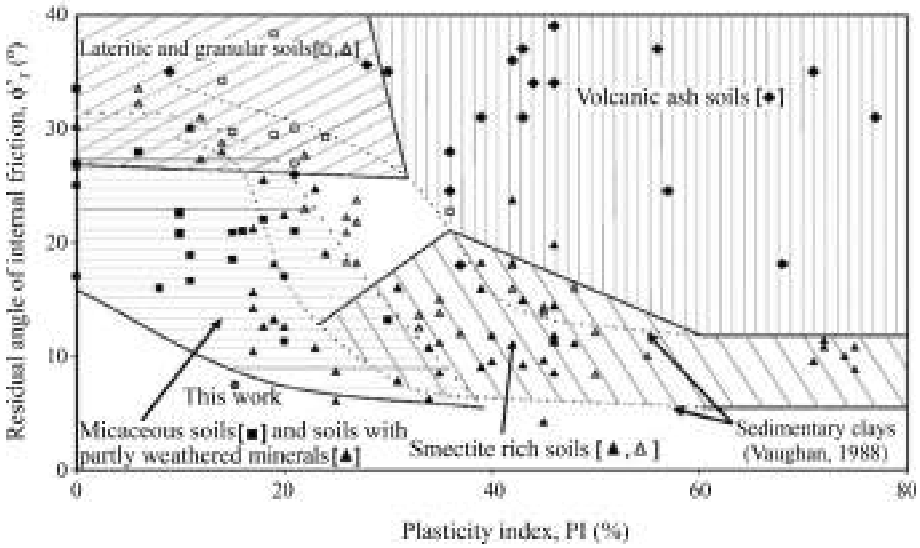

Figure 10 - Tropical soils grouped according to observed residual shear strength and P_I (modified from Rigo *et al.*, 2006).

ship between ϕ'_r and P_I that is in accordance with that found by those authors for soils with partly weathered minerals, and which has a very different behavior with P_I than that found previously by Skempton and co-workers.

This much lower than expected ϕ'_r found here seems to be associated with particle disintegration and its subsequent orientation by shearing. This disaggregation can be observed in the laboratory during manual specimen preparation. But the particle size distribution curves obtained before and after the shearing tests are very similar, thus implying that most of the soil clusters have been degraded during the test sample preparation. Ring shear tests have shown that effective normal stresses have some importance in the particle alignment mechanism: the residual friction angle reduces at larger normal effective stresses.

This data suggests that, as shearing displacements approach failure in the field, there will be soil aggregate disintegration and reduction of internal friction angle, as observed in reversal direct shear tests. There will be a strength reduction from peak to the fully mobilized residual shear strength (to values similar to ring shear test results). Accordingly, such behavior can explain the very fast landslide failure, as described by eyewitnesses, associated to a remarkably quick shear strength reduction from peak to fully mobilized residual strength (associated to cluster destruction and particle alignment).

References

ASTM (2003). Standard Test Method for Particle Size Analysis of Soils - D 422-63. ASTM International, West Conshohocken, Pennsylvania, USA, 8 p.

ABNT (1995). Rochas e Solos - NBR 6502. Associação Brasileira de Normas Técnicas. Rio de Janeiro, Brasil, 18 p.

ABNT (1986). Abertura de Poço e Trincheira de Inspeção em Solo, com Retirada de Amostras Deformadas e Indeformadas - Procedimento - NBR 9604. Associação Brasileira de Normas Técnicas, Rio de Janeiro, Brasil, 9 p.

Anayi, J.T.; Boyce, J.R. & Rodgers, C.D. (1988). Comparison of alternative methods of measuring the residual strength of a clay. Transportation Research Board (TRB), Washington, pp. 16-26.

Anderson, W.F. & Hammoud, F. (1988). Effect of testing procedure in ring shear tests. Geotechnical Testing Journal, 40(3):204-207.

ASTM (2011). Standard Practice for Classification of Soils for Engineering Purposes (Unified Soil Classification System) - D 2487-11. ASTM International, West Conshohocken, PA, USA, 12 p.

ASTM (2004). Standard Test Method for Direct Shear Test of Soils Under Consolidated Drained Conditions - D 3080-04. ASTM International, West Conshohocken, PA, USA, 7 p.

ASTM (2007). Standard Test Method for Particle-Size Analysis of Soils - D 422-63. ASTM International, West Conshohocken, PA, USA 8 p.

ASTM (2010). Standard Test Methods for Liquid Limit, Plastic Limit, and Plasticity Index of Soils - D 4318-10. ASTM International, West Conshohocken, PA, USA, 16 p.

ASTM (2010). Standard Test Method for Measurement of Soil Potential (Suction) Using Filter Paper - D 5298-10. ASTM International, West Conshohocken, PA, USA, 6 p.

ASTM (2006). Torsional ring shear test to determine drained residual shear strength of cohesive soils - D 6467-06. ASTM International, West Conshohocken, PA, USA, 6 p.

ASTM (2009). Standard Test Methods for Particle-Size Distribution (Gradation) of Soils Using Sieve Analysis - D 6913-04. ASTM International, West Conshohocken, PA, USA, 33 p.

ASTM (2010). Standard Test Methods for Specific Gravity of Soil Solids by Water Pycnometer - D 854-10. ASTM International, West Conshohocken, PA, USA, 7 p.

Bishop, A.W.; Green, G.E.; Garga, V.K.; Andresen, A. & Brown, J.D. (1971). A new ring shear apparatus and its application to the measurement of residual strength. Géotechnique, 21(4):273-328.

Boyce, J.R. (1985). Some observations on the residual strength of tropical soils. Proc. Int. Conf. Geomechanics in Tropical Lateritic and Saprolitic Soils, ABMS, São Paulo, pp. 229-237.

Bromhead, E.N. (1979). A simple ring shear apparatus. Ground Engineering, 12(5):40-44.

Bromhead, E.N. (1986). The Stability of Slopes. Chapman and Hall, London.

Charles, J.A. & Soares, M.M. (1984). The stability of slopes in soils with nonlinear failure envelopes. Can. Geotech. J., 21(3):397-406.

Chattopadhyay, P.K. (1972). Residual Shear Strength of Some Pure Clay Mineral. Ph.D. Thesis, University of Alberta, Edmonton, 340 p.

Chen, X.P. & Liu, D. (2013) Residual strength of slip zone soils. Landslides, 11(2):305-314.

Collins, K. (1985). Towards characterization of tropical soil microstructure. Int. Conf. Geomechanics in Tropical Lateritic and Saprolitic Soils, v. 1. ABMS, São Paulo, pp. 85-96.

Collotta, T.; Cantoni, R.; Pavesi, U.; Ruberl, E. & Moretti, P.C. (1989). A correlation between residual friction angle, gradation and the index properties of cohesive soils. Géotechnique, 39(2):343-346.

Dewoolkar, M.P.E.; Hargy, J.; Anderson, I.; Alba, P. & Olson, S.M. (2015) Residual and postliquefaction strength of a liquefiable sand. J. Geotech. Geoenviron. Eng., 142(2):04015068-1-04015068-11.

Eid, H.T.; Rabie, K.H. & Wijewickreme, D. (2016). Drained residual shear strength at effective normal stresses relevant to soil slope stability analyses. Engineering Geology, 204:94-107.

Hawkins, A.B. & Privett, K.D. (1985). Measurement and use of residual shear strength of cohesive soils. Ground Engineering, 18(8):22-29.

Hayden, C.P.; Purchase-Sanborn, K. & Dewoolkar, M. (2018). Comparison of site-specific and empirical correlations for drained residual shear strength. Géotechnique, 68(12):1099-1108.

Hoyos, L.R.; Velosa, C.L. & Puppala, A.J. (2014). Residual shear strength of unsaturated soils via suction-controlled ring shear testing. Engineering Geology, 172:1-11.

Infante Sedano, J.A.; Vanapalli, S.K. & Garga, V.K. (2007). Modified ring shear apparatus for unsaturated soils testing. Geotech. Test. J., 30(1):1-9.

ISO (2009). Particle Size Analysis - Laser Diffraction Methods - 13320. International Organization for Standardization, Geneva, Switzerland, 51 p.

Kenney, T.C. (1977). Residual strength of mineral mixtures. Proc. 9th International Conference in Soil Mechanics, Tokyo, pp. 155-160.

La Gatta, D.P. (1970). Residual Strength of Clays and Clay-Shales by Rotation Shear Tests. Harvard University, Cambridge, 220 p.

Lacerda, W.A. & Silveira, G.C. (1992). Características de resistência ao cisalhamento e de compressibilidade dos solos residuais e coluvionares da encosta do Soberbo, RJ. Proc. 1st Brazilian Symposium on Landslides, ABMS, Rio de Janeiro, pp. 445-461.

Lupini, J.F.; Skinner, A.E. & Vaughan, P.R. (1981). The drained residual strength of cohesive soils. Géotechnique, 31(2):181-213.

Meehan, C.L.; Brandon, T.L.; Duncan, J.M. & Tiwari, B. (2010). Direct shear testing of polished slickensided surfaces. Landslides, 7(2):157-167.

Merchán, V.; Romero, E. & Vaunat, J. (2011). An adapted ring shear apparatus for testing partly saturated soils in the high suction range. Geotech. Test. J., 34(5):433-444.

Mesri, G. & Shahien, M. (2003). Residual shear strength mobilized in first-time slope failures. J. Geotech. Geoenv. Eng., 129(1):12-31.

Mitchell, J.K. (1993). Fundamentals of Soil Behavior. 2nd ed. John Wiley and Sons, New York, 437 p.

Norris, G.; Siddharthan, R.; Zafir, Z. & Madhu, R. (1997). Liquefaction and residual strength of sands from drained triaxial tests. J. Geotech. Geoenviron. Eng., 123(3):220-228.

Rigo, M.L. (2005) Mineralogia, Intemperismo e Comportamento Geotécnico de Solos Saprolíticos de Rochas Vulcânicas da Formação Serra Geral. Tese de Doutorado, Universidade Federal do Rio Grande do Sul, Porto Alegre, 347 p.

Rigo, M.L.; Pinheiro, R.J.B.; Bressani, L.A.; Bica, A.V.D. & Silveira, R.M. (2006). The residual shear strength of tropical soils. Canadian Geotech. J., 43(4):431-447.

Silveira, G.C. (1991). Considerações sobre a granulometria dos solos residuais e coluvionares do escorregamento na estrada do soberbo - RJ. Solos e Rochas, 14(1):59-62.

Simões, P.R.M. (1991). Mecanismos de Instabilização em Taludes Naturais em Formações Expansivas da Bacia Sedimentar do Recôncavo Baiano. Tese de Doutorado, Universidade Federal do Rio de Janeiro, Rio de Janeiro, 277 p.

Skempton, A.W. & Petley, D.J. (1967). The strength along structural discontinuities in stiff clays. Proc. Geotechnical Conference on Shear Strength Properties of Natural Soils and Rock, NGI, Oslo, pp. 29-46.

Skempton, A.W. & Vaughan, P.R. (1993). The failure of Carsington dam. Géotechnique, 43(1):151-153.

Skempton, A.W. (1985). Residual strength of clays in landslides, folded strata and the laboratory. Géotechnique, 35(1):3-18.

Stark, T.D. & Eid, H.T. (1994). Drained residual strength of cohesive soils. J. Geotech. Eng., 120(5):856-871.

Stark, T.D. & Hussain, M. (2013). Empirical correlations: drained shear strength for slope stability analyses. J. Geotech. Geoenviron. Engineering, 139(6):853-862.

Stark, T.D. & Vettel, J.J. (1992). Bromhead ring shear test procedure. Geotechnical Testing Journal, 15(1):24-32.

Suzuki, M.; Tsuzuki, S. & Yamamoto, T. (2007) Residual strength characteristics of naturally and artificially cemented clays in reversal direct box shear test. Soils and Foundations, 47(6):1029-1044.

Tanaka, A. (1976) Algumas Considerações sobre a Resistência ao Cisalhamento do Solo Residual de Basalto de São Simão. Dissertação de Mestrado PUC-Rio, Rio de Janeiro, 145 p.

Tika, T.E. (1999) Ring shear tests on a carbonate sandy soil. Geotech Test Journal, 22(4):342-355.

Tiwari, B. & Marui, H. (2005). A new method for the correlation of residual shear strength of the soil with mineralogical composition. J. Geotech. Geoenviron. Engineering., 131(9):1139-1150.

Townsend, F.C. & Gilbert, P.A. (1973). Tests to measure residual strengths of some clay shales. Géotechnique, 23(2):267-271.

Toyota, H.; Nakamura, K.; Sugimoto, M. & Sakai, N. (2009). Ring shear tests to evaluate strength parameters in various remoulded soils. Géotechnique, 59(8):649-659.

Vaughan, P.R.; Hight, D.W.; Sodha, V.G. & Walbancke, H.J. (1978). Factors controlling the stability of clay fills in Britain. Proc. ICE Conf. on Clay Fills, Thomas Telford, London, pp. 205-217.

Vithana, S.B.; Nakamura, S.; Gibo, S.; Yoshinaga, A. & Kimura, S. (2011). Correlation of large displacement drained shear strength of landslide soils measured by direct shear and ring shear devices. Landslides, 9(3):305-314.

Voight, B. (1973). Correlation between Atterberg plasticity limits and residual shear strength of natural soils. Géotechnique, 23(2):265-267.

Wang, G.; Sassa, K.; Fukuoka, H. & Tada, T. (2007). Experimental study on the shearing behavior of saturated silty soils based on ring-shear tests. J. Geotech. Geoenv. Eng., 133(3):319-333.

Watry, S.M. & Lade, P.V. (2000). Residual shear strength of bentonites on Palos Verdes Peninsula, California. Proc. Slope Stability 2000, Geotechnical Special Publication n. 101, ASCE, Reston, pp. 323-342.

Wesley, L.D. (1977). Shear strength properties of halloysite and allophane clays in Java, Indonesia. Géotechnique, 27(2):125-136.

Wesley, L.D. (2003). Residual strength of clays and correlations using Atterberg limits. Géotechnique, 53(7):669-672.

List of Symbols and Acronyms

σ': effective normal stress
τ: shear stress
c': cohesive intercept
c'_r: residual cohesive intercept
c'_p: peak cohesive intercept
ϕ': friction angle
ϕ_r': residual friction angle
ϕ_p': peak friction angle
γ: unit weight
γ_d: dry unit weight
G: density of solid particles
w: moisture content
w_{nat}: natural moisture content
w_L: liquid limit
w_P: plastic limit
P_I: plasticity index
e: void ratio
S_r: degree of saturation
ABNT: Brazilian Association of Technical Standards
ASTM: American Society for Testing and Materials
ISO: International Organization for Standardization
JCPDS: Joint Committee on Powder Diffraction Standards
SUCS: Unified Soil Classification System

Triaxial Compression Test on Consolidated Undrained Shear Strength Characteristics of Fiber Reinforced Soil

T.S. Hou, J.L. Liu, Y.S. Luo, Y.X. Cui

Abstract. This study aims to experimentally analyze the effect of fiber length and fiber content on shear strength and deformation properties of fiber reinforced soil by consolidated-undrained triaxial shear tests. The best mechanical properties are presented by the samples with 1.0 % fiber content and 3.09 cm fiber length. The stress-strain relationship of fiber reinforced soil is strain hardening. The change laws of pore water pressure with the increasing of axial strain are affected by both confining pressure and the void ratio. The effective stress paths of fiber reinforced soil move to the left of the *p*'- *q* surface with the increase of fiber content, and the fiber length has no significant effect on effective stress paths. Reinforcement effect mainly improves the cohesion of soil samples, and three distribution patterns of flexible fibers in soil are proposed. The failure mode of saturated cotton fiber reinforced soil is bulging failure, radial deformation of soil is obviously restrained by fiber reinforcement.

Keywords: consolidated undrained shear characteristics, fiber content, fiber length, reinforced soil, stress-strain characteristics, shear strength.

1. Introduction

A composite geotextile made from a random and uniform mix of fiber materials into soil is called fiber reinforced soil. As for the technology of soil improvement, lime soil, cement soil, EPS (expanded polystyrene) particles light weight soil (Hou & Xu, 2009; Hou & Xu, 2010) and so on can be regarded as artificial composite soil. However, as the global community is turning to a more sustainable way of development, it encourages the stabilization technology that can replace or minimize the use of traditional cement and other curing agents. In this respect, the use of fibers has been favored by many scholars. In the rural areas of Northwest China, it is still possible to see the courtyard walls and houses built from the loess with straw and other natural fiber materials in it. It can be seen that fiber reinforced soil has already been used in production practice, but the theoretical research of fiber reinforced soil is far behind the practice. The problems such as reinforcement mechanism, reinforcement effect, strength parameters and so on remain to be studied.

The fiber materials used in the study are mainly composed of natural fibers such as wheat straw (Wei *et al.*, 2012), grass root (Wang *et al.*, 2015), sisal (Prabakar & Sridhar, 2002), cotton (Zhang *et al.*, 2005) and synthetic fiber such as polypropylene (Shao *et al.*, 2014), nylon (Estabragh *et al.*, 2011), polyester fiber (Chaduvul *et al.*, 2017) and so on. The study found that the fiber properties such as content, length, toughness, fineness and vertical and horizontal ratio, and soil properties such as water content, dry density, particle size distribution have an important influence on the strength of fiber reinforced soil (Chai & Shi, 2012; Krishna Rao & Nasr, 2012; Diambra & Ibraim, 2015; Tang *et al.*, 2016a; Tang *et al.*, 2016b). The effect of fiber content and fiber length on mechanical properties of fiber reinforced fine sand is studied through the California soil bearing ratio tests and direct shear tests by Krishna Rao & Nasr (2012). The test results show that the mechanical properties of fiber reinforced soil are optimal when the percentage of fiber mass to dry sand mass is 0.75 %. The tensile strength of polypropylene fiber reinforced soil is researched by Tang *et al.* (2016b), and the results show that the fiber reinforcement can significantly increase the peak strength of the soil, and the tensile strength increases with the increasing of fiber content and dry density, and decreases with the increasing of water content. Through the drying tests, it is found that the reinforcement of the fibers significantly reduces the cracking of the soil. Using the improved shear lag theory, the stress transfer mechanism between local fibers and soil particles is studied by Diambra & Ibraim (2015), and the effects of geometry of the fibers and particle size of the soil on the stress distribution along the fiber direction are clarified. Fiber reinforcement can not only effectively enhance the compressive strength, shear

Tian-shun Hou, Ph.D., Associate Professor, College of Water Resources and Architectural Engineering, Northwest A&F University, No. 23 Weihui Road, Yangling, Shaanxi, China. e-mail: houtianshunyx@sina.com.
Jian-long Liu, M.Sc. Student, College of Water Resources and Architectural Engineering, Northwest A&F University, No. 23 Weihui Road, Yangling, Shaanxi, China. e-mail: jianlong8903@163.com.
Ya-sheng Luo, Ph.D., Professor, College of Water Resources and Architectural Engineering, Northwest A&F University, No. 23 Weihui Road, Yangling, Shaanxi, China. e-mail: lyas1967@nwsuaf.edu.cn.
Yi-xiang Cui, M.Sc. Student, College of Water Resources and Architectural Engineering, Northwest A&F University, No. 23 Weihui Road, Yangling, Shaanxi, China. e-mail: 644139744@qq.com.
Submitted on December 23, 2018; Final Acceptance on February 13, 2020; Discussion open until August 31, 2020.
DOI: 10.28927/SR.431043

strength, tensile strength, plasticity and toughness of the soil (Anagnostopoulos *et al.*, 2013; Correia *et al.*, 2015; Diab *et al.*, 2016), but also improve the characteristics of special soils, such as expansive soil (Soltani *et al.*, 2018), frozen soil (Zaimoglu, 2010) and so on. In the action mechanism of reinforced soil, it is found that the enhancement effect of the fiber reinforced soil depends on the interfacial force between the fibers and the soil through single fiber pull-out tests and scanning electron microscope tests by Tang *et al.* (2009). For the modeling analysis of fiber reinforced soil, the function of fiber distribution in reinforced sand with random fiber distribution is given by Ibraim *et al.* (2012). The kinematic method of limit analysis is proposed by Michalowski (2008). The constitutive model of fiber reinforced sand based on triaxial tests is established by Diambra *et al.* (2013).

Most of the studies are based on sand, the research on cohesive soil is still less, and theoretical research of reinforced soil is still not systematic and mature. For the saturated clay ground, the soil is fully consolidated in the existing stress system. Due to the construction needs, the undrained condition is formed by the rapid loading on the ground. The ground stability and bearing capacity should be analyzed with the consolidated-undrained strength parameters under the condition above. The pore water pressure and effective stress parameters which are for ground stability analysis can be accurately measured by consolidated-undrained triaxial tests (CU), and consolidated-undrained tests can solve the problem of long drainage test time. With cotton fibers as reinforcing material and loess as raw material, the saturated cotton fiber reinforced soil with different fiber content and fiber length is tested by consolidated-undrained tests, and the consolidated undrained shear strength, deformation and pore pressure characteristics of the soil are studied. The research achievements can propose a new understanding for the consolidated undrained strength and deformation characteristics of reinforced soil, and it can also provide theoretical support for the application of fiber reinforcement technology, such as in ground improvement, slope treatment in the loess region, and so on.

2. Experimental Materials and Methods

2.1. Experimental materials

The fibers used in the tests are made of pure cotton. The basic physical and mechanical properties are given in Table 1.

The soil used in the tests is the loess of Yangling area in Shaanxi province of China, whose grain size distribution curve is shown in Fig. 1. The optimum water content of the soil is 19.4 % and the maximum dry density is 1.68 g/cm^3. The loess is a type of low liquid limit clay according to the plasticity chart. The other physical properties are shown in Table 2.

2.2. Sample preparation

The Yangling loess is air-dried and crushed into small particles, and then is passed through a 2 mm sieve to remove the debris and gravels. Some water is sprayed into the soil until the water content reaches the optimum water content 19.4 %. Then the wet soil is put into freshness protection packages for 24 h. After that, the target fiber mass is weighed, and then water is sprayed on the fibers. By keeping the mass of water and the mass of fibers the same, we make the water content of the fibers w_f = 100 %. Based on a lot of experimental results, when w_f > 100 %, fibers and soil are difficult to mix evenly, fibers are floating on mixed soil; when w_f < 100 %, bleeding phenomenon occurs during the compaction process of the fiber and soil mixture; only

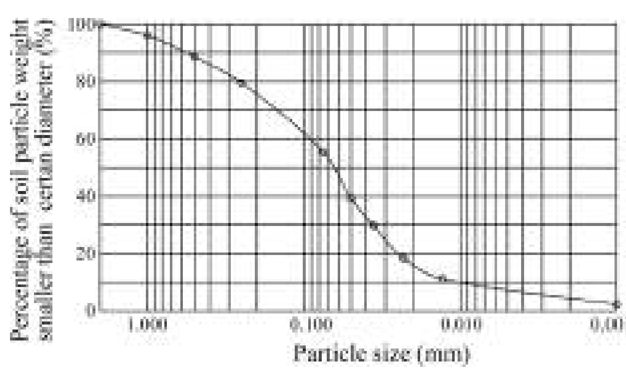

Figure 1 - Grain size distribution curve.

Table 1 - Physical and mechanical parameters of cotton fiber.

Density, ρ (gcm^{-3})	Diameter, D (mm)	Elongation (%)	Tensile strength (MPa)	Elasticity modulus (MPa)
1.54	0.8	37.0	8.2	40.0

Table 2 - Physical properties of Yangling loess in Shaanxi area.

Natural density, ρ (gcm^{-3})	Specific gravity, G_s	Natural water content, w (%)	Plastic limit, w_p (%)	Liquid limit, w_L (%)	Plasticity index, I_p	Liquidity index, I_L	Void ratio, e
1.69	2.72	19.1	20.6	34.2	13.6	-0.11	0.92

when w_f = 100 %, the compaction effect of fiber reinforced soil is the best. After a while, the fibers are fully stirred with the cured soil, so that the fibers are distributed in the soil randomly and evenly. After mixing evenly, the samples are prepared for light compaction tests. The size of soil samples is 61.8 mm in diameter and 125 mm in height. The compaction work is 592.2 kJ/m^3, the mass of hammer in the tests is 884.92 g, and the height of drop distance is 275 mm. The compaction of samples is divided into three layers, and the average compaction blows for each soil layer is 31 (Hou, 2012; Hou, 2014; Hou & Xu, 2011). In this way, the reinforced soil samples are prepared. In addition, the water content of unreinforced soil is the optimum water content (19.4 %), and the unreinforced soil samples are prepared using the same preparation methods as reinforced soil samples. After compaction, the wet density of unreinforced soil sample ρ_{wet} is 1.875 g/cm^3, dry density ρ_d is 1.57 g/cm^3, degree of compaction D_c is 93.47 %. Then the samples are saturated by the vacuum saturation method, the air-pumping time is not less than 1 h, and the soaking time is not less than 10 h. It is found through unconfined compression tests that the strength is optimum when the fiber content of the cotton fiber reinforced soil is 1.0 % and the fiber length is D/2 (D is the diameter of the sample) (Liu *et al.*, 2018). Thus, the sample preparation scheme of fiber reinforced soil samples and the wet density of fiber reinforced soil samples in the tests are shown in Table 3.

2.3. Experimental methods

The consolidated undrained triaxial test (CU) is used in the tests. The confining pressures are respectively 100 kPa, 200 kPa, 300 kPa and 400 kPa, and the shear rate is 0.1660 mm/min (shear strain rate is 0.13 % /min). The tests should be ended with shear failure or 20 % axial strain. The pore water pressure can be measured by sensors during the tests. The peak shear strength is chosen as the strength value. The shear strength of 15 % axial strain is chosen as the strength value when there is no peak shear strength.

3. Experimental results

3.1. Stress - strain - pore water pressure relation

(1) As can be seen in Fig. 2(a) to (j), the deviator stress of fiber reinforced soil increases rapidly at the initial stage of strain, and then slowly increases until the end of the tests. The stress-strain relationship of the reinforced soil is strain hardening. The stress-strain relationship curve of fiber reinforced soil is nonlinear, and the failure mode of the samples is bulging failure. Unreinforced soil also has the same change laws. (2) In Fig. 2(b) to (g), under the condition of 3.09 cm fiber length, when the confining pressure is the same, the deviator stress (when shear failure or 15 % axial strain) increases first and then decreases with the increasing of the fiber content. The deviator stress is maximum when the fiber content is 1.0 %. For example, under the condition of 200 kPa confining pressure and 3.09 cm fiber length, when the fiber content increases from 0 to 1.0 %, the deviator stress increases 6.6 %, from 334 kPa to 356 kPa. When the fiber content increases from 1.0 % to 3.0 %, and the deviator stress decreases 14.3 %, from 356 kPa to 305 kPa. (3) In Fig. 2(c) and (h) to (j), under the condition of 1.0 % fiber content, when the confining pressure is the same, the deviator stress (when shear failure or 15 % axial strain) increases first and then decreases with the increasing of fiber length. 3.09 cm is the optimal fiber length. For example, under the condition of 200 kPa confining pressure and 1.0 % fiber content, when the fiber length increases from 0 to 3.09 cm, the deviator stress increases 6.6 %, from 334 kPa to 356 kPa. When the fiber length increases from 3.09 cm to 6.18 cm, the deviator stress decreases 4.8 %, from 356 kPa to 339 kPa. (4) The improvement effect of fiber in soil is better at high confining pressure. Under the optimal reinforcement conditions (1.0 % fiber content and 3.09 cm fiber length), the deviator stress (when shear failure or 15 % axial strain) under the confining pressure of 100 kPa, 200 kPa, 300 kPa and 400 kPa increases by 3.1 %, 6.6 %, 17.1 % and 19.5 % respectively compared with the unreinforced soil. (5) In Fig. 2(a), the pore water pressure of unreinforced soil increases first and then decreases with the increasing of axial strain. In Fig. 2(b), (c) and (h), when the confining pressure is lower and the fiber content is smaller, the properties of reinforced soil are the same as those of unreinforced soil. (6) In Fig. 2(d) to (g), under higher confining pressure and bigger fiber content, the pore water pressure increases gradually with the increasing of axial strain, then tends to be stable.

To sum up, the optimal fiber content of fiber reinforced soil is 1.0 %, and the optimal fiber length is 3.09 cm. The stress-strain relationship of the reinforced soil is strain hardening. The stress-strain relationship curves of fiber reinforced soil are nonlinear, and the failure mode of the samples is bulging failure. Under lower confining pressure and lower void ratio, the mechanical properties of reinforced soil during the loading process are similar to those of unreinforced soil, and the pore water pressure increases first and then de-

Table 3 - Sample preparation scheme of reinforced soil samples.

Fiber length, L (cm)	Fiber content (mass ratio of dry fiber to dry soil), a_f (%)	Wet density of reinforced soil samples, ρ_{wet} (gcm^{-3})
3.09	0.5; 1.0; 1.5; 2.0; 2.5; 3.0	1.858; 1.840; 1.826; 1.810; 1.787; 1.760
1.55; 3.09; 4.64; 6.18	1.0	1.840

creases with increasing axial strain, which means that the interaction between fiber and soil is not obvious. Under higher confining pressure and higher void ratio, the interaction between fiber and soil is enhanced, the pore water pressure increases gradually with increasing axial strain, and then tends to be stable. The main cause of the stress-strain-pore water pressure relationship characteristics of fiber reinforced soil is shearing dilatancy or shearing shrinkage of the soil samples. In the drained tests of saturated soil, the water in the pore has sufficient time to squeeze out or breathe in, the shear dilatancy can be characterized using the macroscopic volume change. In the undrained tests of saturated soil, the wa-

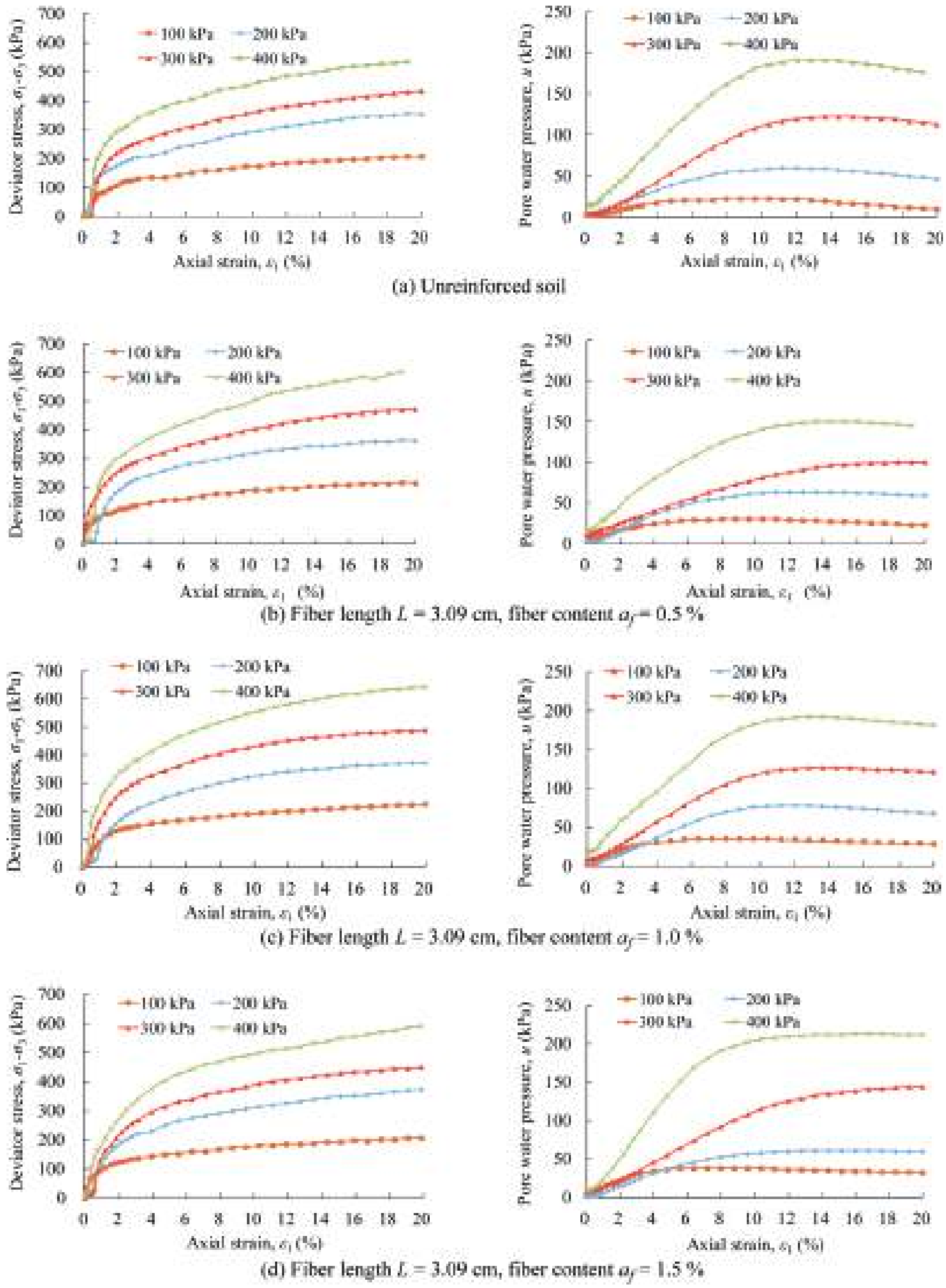

Figure 2 - Stress - strain - pore water pressure relation curves.

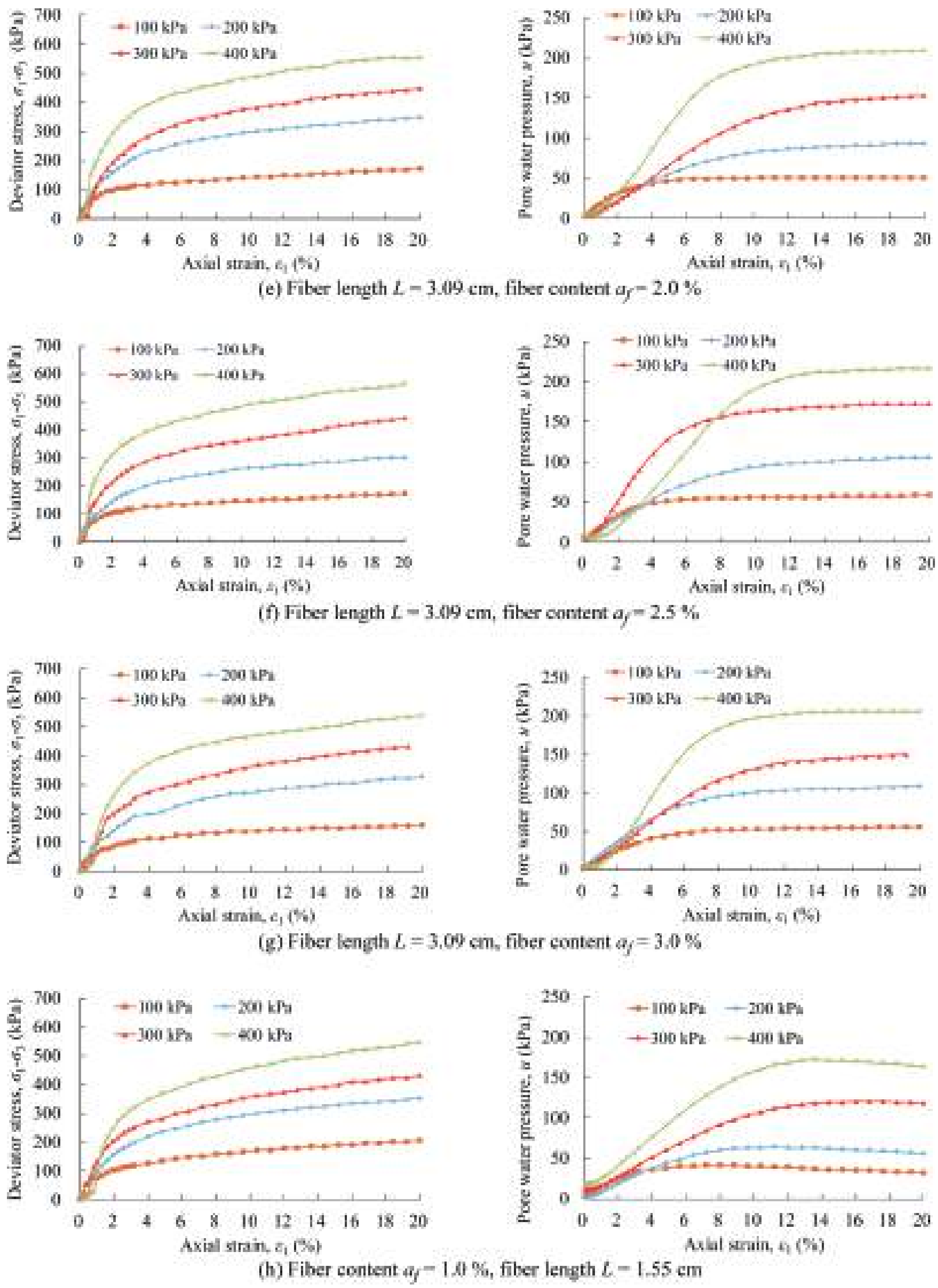

Figure 2 (cont.) - Stress - strain - pore water pressure relation curves.

ter in the pore cannot be squeezed out or breathe in, and the volume of saturated soil is constant during the shearing process, but the shear dilatancy still exists. Meanwhile, it is characterized as "body changing potential energy", which means the change of pore water pressure in the soil samples. When the samples have shear dilatancy tendency but the volume change is restricted, the pore water pressure decreases and the effective stress on the soil particles and fibers increases. However, the pore water pressure increases and the effective stress on the soil particles and fibers decreases when the samples have shear shrinkage tendency but the volume change is restricted.

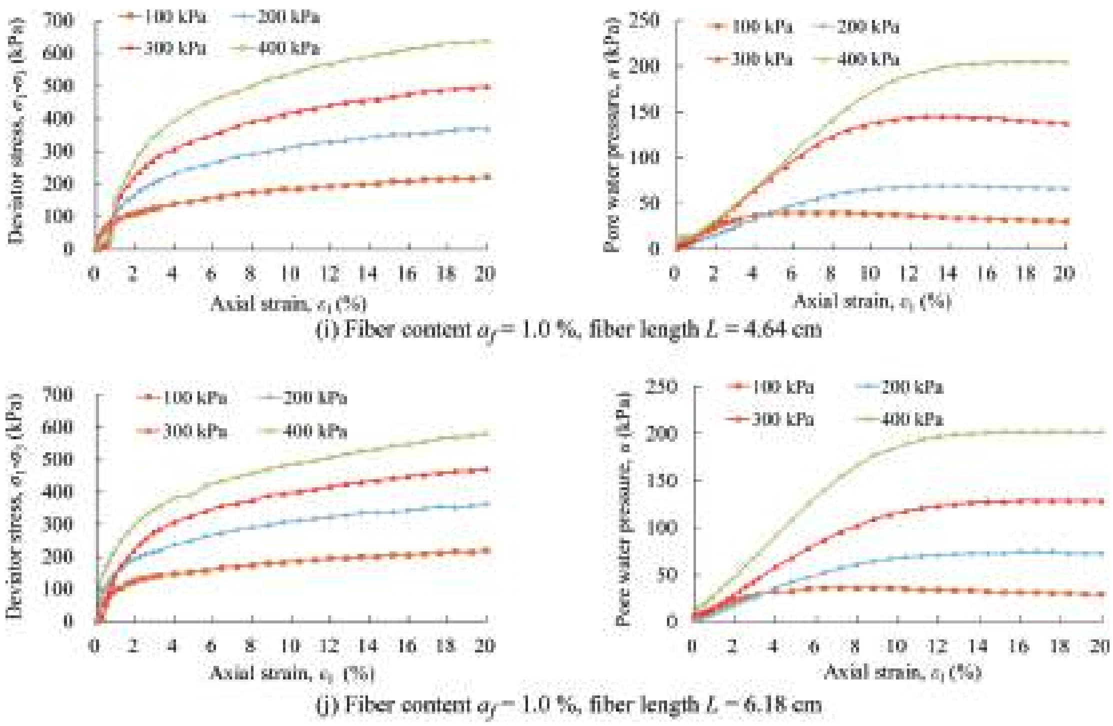

Figure 2 (cont.) - Stress - strain - pore water pressure relation curves.

3.2. Effective stress path

The effective stress of the fiber reinforced soil is assumed to be the stress shared by both the soil particles and the fibers under the external load, and is solved by the Terzaghi principle of effective stress. The effective stress paths of the fiber reinforced soil in the *p*' - *q* surface are shown in Fig. 3; the meanings of physical symbols in Fig. 3 are as follows: $p' = p - u = (\sigma_1 + \sigma_3)/2 - u$; $q = (\sigma_1 - \sigma_3)/2$. σ_1 is maximum principal stress; σ_3 is minimum principal stress; K'_f line is effective stress failure principal stress line. The effective stress path of the reinforced soil is a shape changing curve: it is a straight line when the strain is at the initial period, and then the curve begins to bend to the left. When the sample is near failure, the curve bends to the right and then develops along the failure principal stress line. With the increasing of fiber content, the stress path curve gradually moves to the left. When the fiber content is not more than 1.0 %, the effective stress path of the fiber reinforced soil is on the right side of that of the unreinforced soil. The stress path of the reinforced soil is on the left side of that of the unreinforced soil when the fiber content is more than 1.0 %. The main reason is that the space occupied by soil particles is replaced by fibers with the increasing of fiber content. Because the cotton fiber has loose structure, it increases the pore volume in the soil sample, resulting in the increasing of the void ratio. At the initial stage of strain, the average effective principal stress increases, the deviator stress increases, and the effect of the fiber content on the effective stress path is not obvious. With the increasing of strain, the average effective principal stress decreases significantly, and the deviator stress continues to increase. The greater the fiber content is, the more severe is the decrease of the average effective principal stress. With the further increase of strain, the average effective principal stress reaches a turning point and begins to increase, and the deviator stress increases along the failure principal stress line. The fiber length has no obvious effect on the effective stress path of fiber reinforced soil.

3.3. Pore water pressure coefficient

The relationship between the pore water pressure and the deviator stress (σ_1 - σ_3) of saturated fiber reinforced soil is shown in Fig. 4. (1) The pore water pressure increases with the increase of the deviator stress, and then eventually tends to a stable value. (2) The relationship between pore water pressure and deviator stress is nonlinear, and the curve is shown as “concave” first and then “convex”.

The British scholar A.W. Skempton pointed out that the pore water pressure caused by the deviator stress is $\Delta u_1 = AB(\Delta\sigma_1 - \Delta\sigma_3)$. The pore water pressure coefficient *B* is the coefficient related to saturation, and *B* is approximately equal to 1 for saturated soil. The pore water pressure coefficient *A* reflects shear dilatancy of the soil, it is not a constant but a function of the stress level in the experimental process. The pore water pressure coefficient $A = \Delta u_1/(\Delta\sigma_1 - \Delta\sigma_3)$ can be solved through the relationship curve between the pore water pressure and the deviator stress (σ_1 - σ_3). As is shown in Fig. 5, in that curve, there are

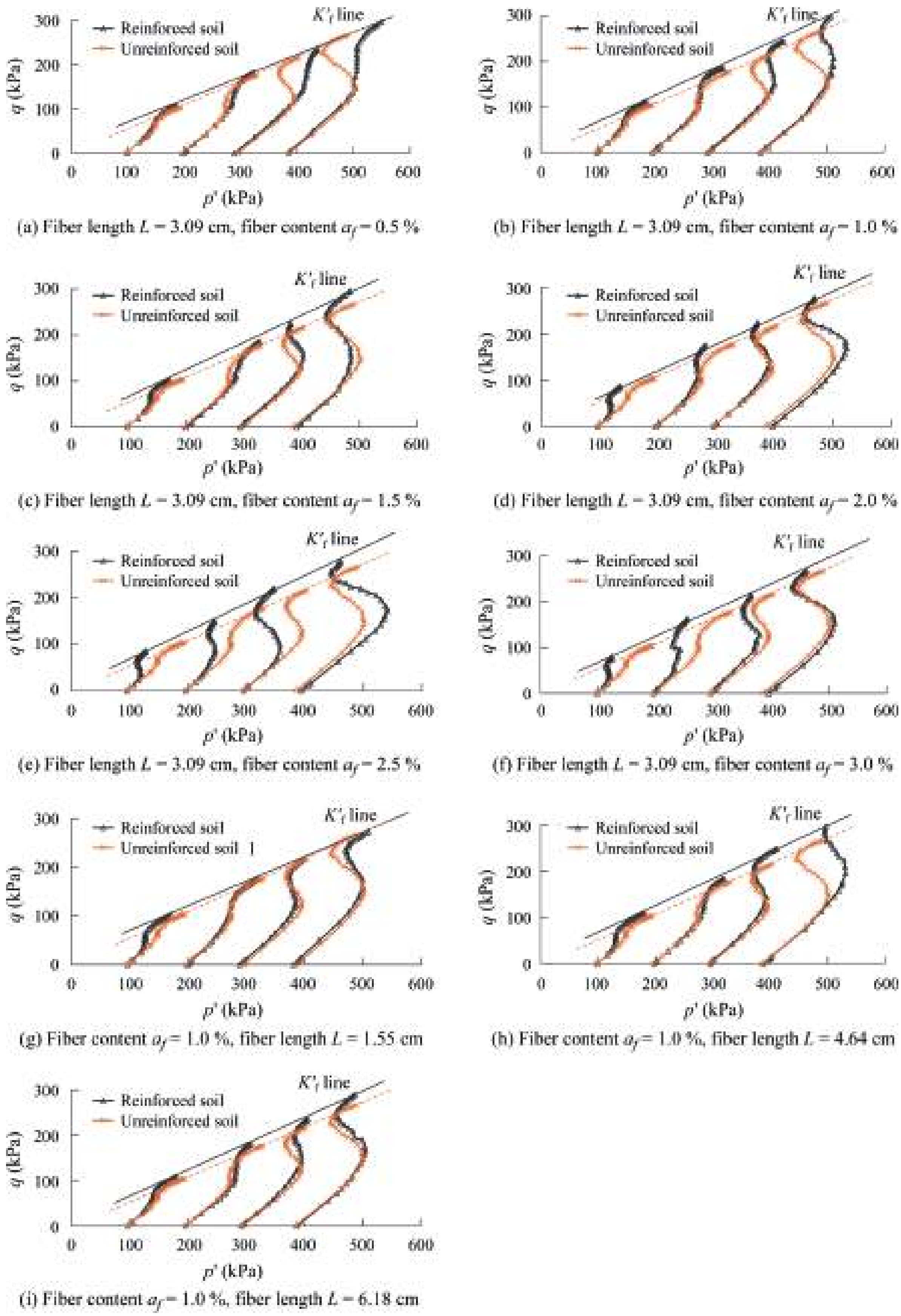

(a) Fiber length L = 3.09 cm, fiber content a_f = 0.5 %

(b) Fiber length L = 3.09 cm, fiber content a_f = 1.0 %

(c) Fiber length L = 3.09 cm, fiber content a_f = 1.5 %

(d) Fiber length L = 3.09 cm, fiber content a_f = 2.0 %

(e) Fiber length L = 3.09 cm, fiber content a_f = 2.5 %

(f) Fiber length L = 3.09 cm, fiber content a_f = 3.0 %

(g) Fiber content a_f = 1.0 %, fiber length L = 1.55 cm

(h) Fiber content a_f = 1.0 %, fiber length L = 4.64 cm

(i) Fiber content a_f = 1.0 %, fiber length L = 6.18 cm

Figure 3 - Effective stress paths for unreinforced soil and fiber reinforced soil.

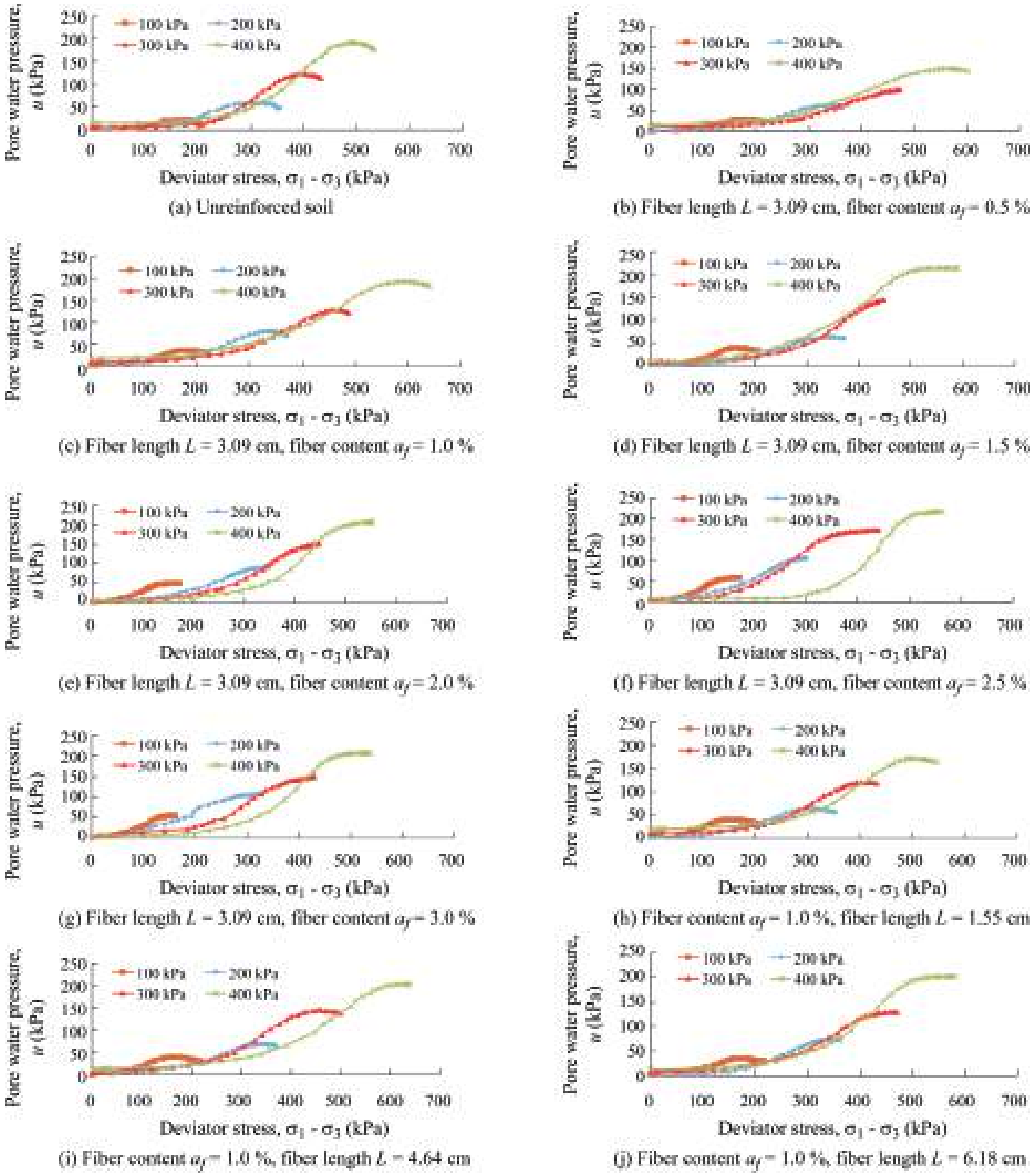

Figure 4 - Pore water pressure - deviator stress relation curves.

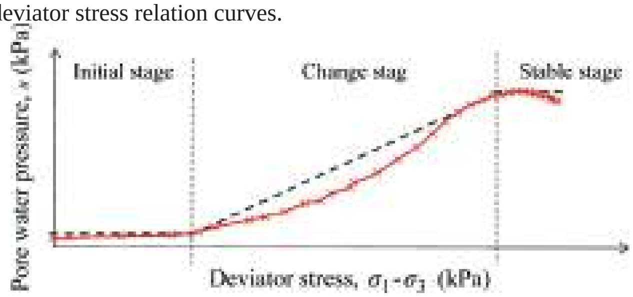

Figure 5 - A typical illustration of pore water pressure - deviator stress (σ_1 - σ_3) relation curves.

three obvious stages, which are defined as initial stage, change stage and stable stage. The average pore water pressure coefficient A_a can be solved by the secant slope of the curve during the change of stage. The average pore water pressure coefficients of the saturated compacted clay under 100 kPa, 200 kPa, 300 kPa, and 400 kPa confining pressure are 0.27, 0.33, 0.59 and 0.80, respectively. The average pore water pressure coefficients of the fiber reinforced soil with 1.0 % fiber content and 3.09 cm fiber length under 100 kPa, 200 kPa, 300 kPa, and 400 kPa confining pressure are 0.35, 0.43, 0.45 and 0.46, respectively. By calculating all the fiber reinforced soil samples' parameters, the value range of pore water pressure coefficient A of the compacted cotton fiber reinforced soil with 0.5 %~3.0 % fiber content and 1.55 cm~6.18 cm fiber length is 0.32~0.69. This demonstrates that the engineering properties of compacted cotton fiber reinforced soil are similar to those of slightly overconsolidated clay.

3.4. Shear strength parameters

The Mohr circles and shear strength envelopes of total stress and effective stress of saturated cotton fiber reinforced soil are shown in Fig. 6. (1) The total stress strength envelopes and effective stress strength envelopes of the fiber reinforced soil and the unreinforced soil are both a straight line approximately. The total stress strength envelopes are crossed with the effective stress strength envelopes, the effective cohesion is less than cohesion and the effective internal friction angle is larger than the internal friction angle. (2) The total stress strength envelopes of fiber reinforced soil and unreinforced soil with different reinforcement conditions are approximately parallel, and the effective stress strength envelopes are approximately parallel.

As is shown in Fig. 7, (1) The cohesion of fiber reinforced soil increases first and then decreases with the increase of fiber content, and the cohesion is the largest with 1.0 % fiber content. When the fiber length of the reinforced soil is 3.09 cm, the fiber content increases from 0.5 % to 1.0 %, and the cohesion increases 10.1 %, from 36.06 kPa to 39.71 kPa. The fiber content increases from 1.0 % to 3.0 %, and the cohesion decreases 63.5 %, from 39.71 kPa to 14.49 kPa. (2) The cohesion of fiber reinforced soil increases first and then decreases with the increase of fiber length, and the critical length or optimum length is 3.09 cm. When the fiber length reaches the critical length, the cohe-

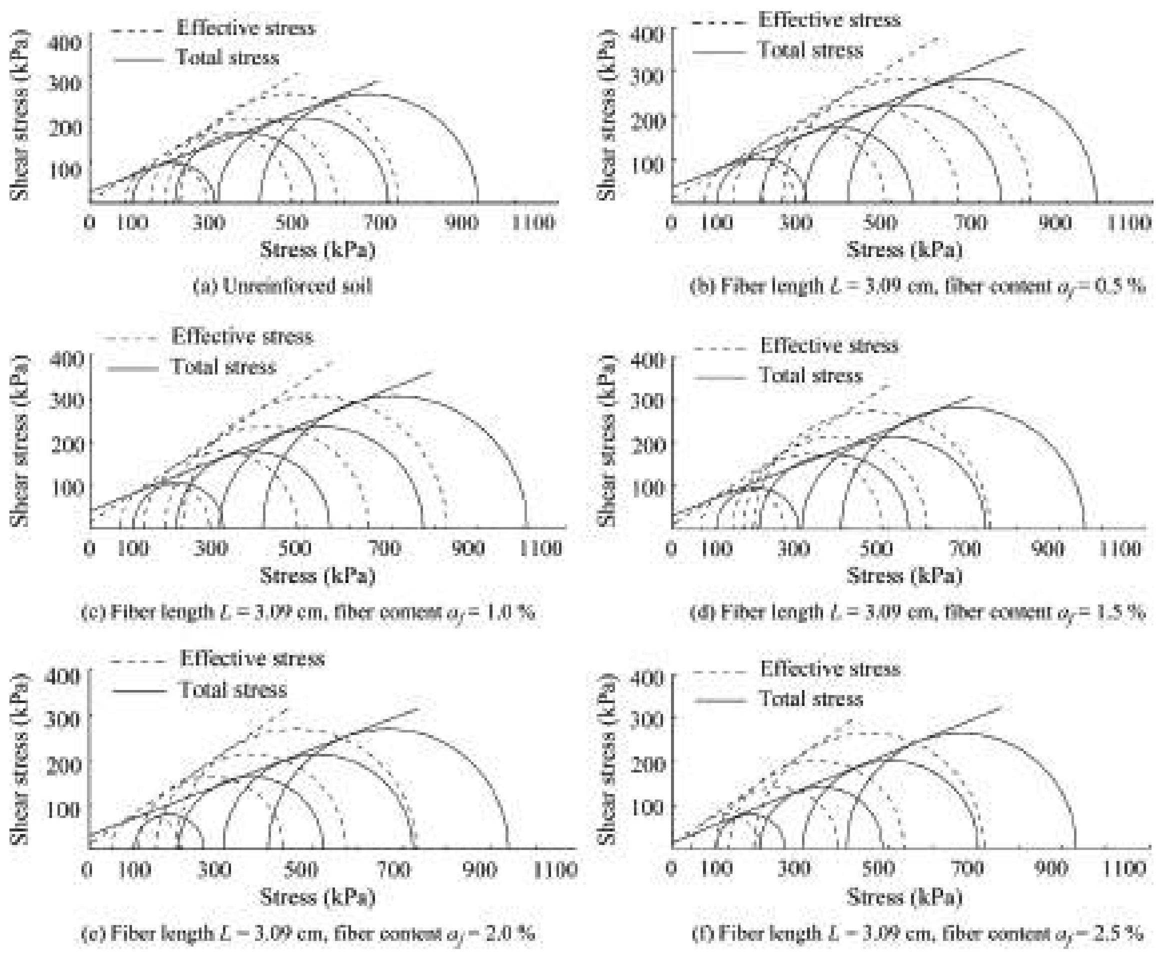

Figure 6 - Mohr circle and shear strength envelope of unreinforced soil and fiber reinforced soil.

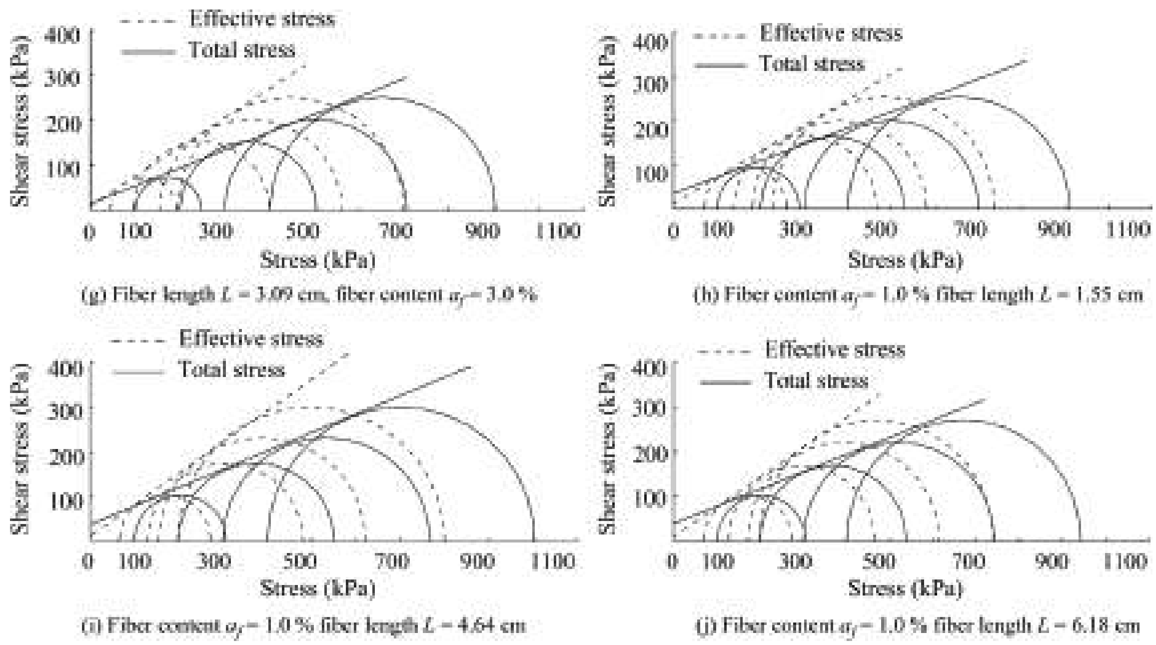

Figure 6 (cont.) - Mohr circle and shear strength envelope of unreinforced soil and fiber reinforced soil.

sion decreases with the increase of the fiber length, but the effect is not obvious. As for 1.0 % fiber content of fiber reinforced soil, the fiber length increases from 1.55 cm to 3.09 cm, and the cohesion increases 12.9 %, from 35.17 kPa to 39.71 kPa. The fiber length increases from 3.09 cm to 6.18 cm, and the cohesion decreases 0.9 %, from 39.71 kPa to 39.37 kPa. (3) The cohesion and effective cohesion of fiber reinforced soil with 3.09 cm fiber length and 1.0 % fiber content increase by 48.4 % and 112.3 %, respectively, compared with unreinforced soil.

As is shown in Fig. 8, the internal friction angle and the effective internal friction angle of the unreinforced soil are 20.96° and 31.53° respectively, the internal friction angle range of the reinforced soil with 3.09 cm fiber length and 0.5 %~3.0 % fiber content is 21.10°~22.24°, and the effective internal friction angle range is 31.16°~34.54°. The internal friction angle range of the reinforced soil with 1.0 % fiber content and 1.55 cm~6.18 cm fiber length is 20.31°~22.51°, and the effective internal friction angle range is 30.38°~35.16°. The internal friction angle of the fiber reinforced soil is basically the same as that of the unreinforced soil, and the reinforcement condition has no significant effect on the internal friction angle of the fiber reinforced soil.

The optimal fiber content is 1.0 %, and the optimum fiber length is 3.09 cm based on the analysis of the test results. According to the random distribution patterns of fibers in the samples by observation, summing up the existence form of flexible fibers in samples, the interaction modes between fibers and soil consists of three kinds: (1) Contact. The contact action between the fibers and soil particles provides the interfacial shear stress between the fibers and soil particles. (2) Bending. The fibers are bent in the soil, the soil particles are wrapped by fibers at the bend,

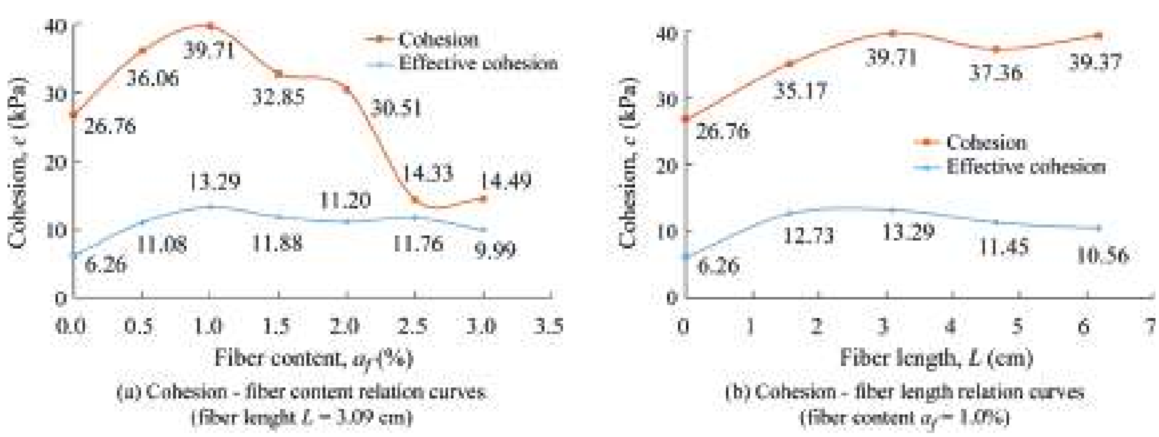

Figure 7 - Cohesion - fiber content, fiber length relation curves of fiber reinforced soil.

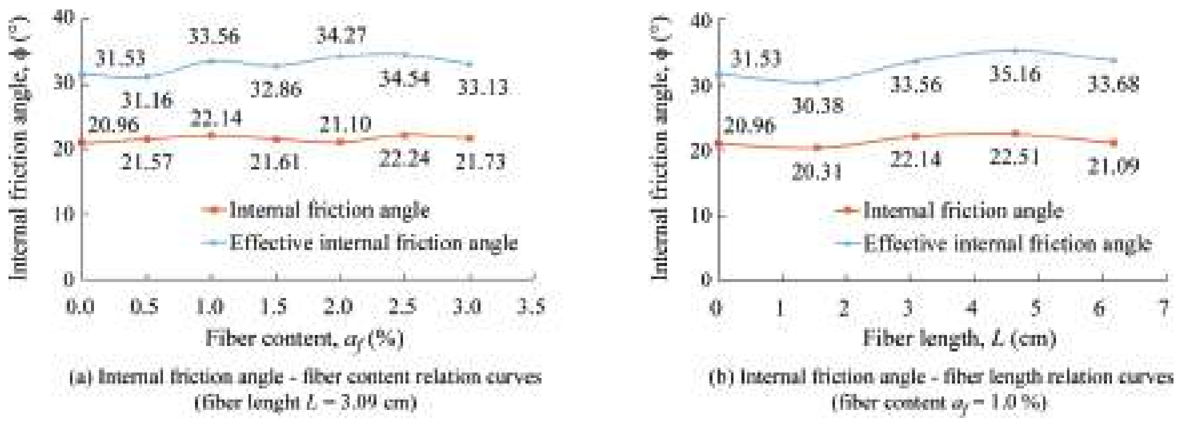

Figure 8 - Internal friction angle - fiber content, fiber length relation curves of fiber reinforced soil.

and tensile stress appears in the fibers because of the movement or movement tendency of soil particles under external load. (3) Interweaving. The fibers are a kind of network structure in the soil, and the three-dimensional network of the fibers can effectively restrict the movement of the soil particles. The movement difficulty of soil particles during the loading process of saturated soil has an important influence on the strength of soil. The results of the interaction between the fibers and soil particles can effectively restrict the movement of soil particles, thus the strength of the soil can be improved. The effect of the fiber content and the fiber length on fiber reinforced soil can be well explained by the interaction between the fibers and the soil particles (Liu *et al.*, 2018; Oliveira *et al.*, 2019; Xie *et al.*, 2019).

As to fiber content, the total contact area between the fibers and soil particles is limited when the fiber content is too low, and the fibers cannot be interwoven into the net, thus the increase of soil strength is limited. When the fiber content is too high, the fibers are stacked, thus the fibers and the soil particles cannot be in full contact. If the fibers are still in the “floating” state, the fibers are not anchored by the soil, or the anchorage is not enough, and the tensile property of the fibers cannot be fully used. As to fiber length, the contact area between the fibers and soil is small when the fibers are too short. The fibers are easily pulled out under load, the fibers cannot be effectively bent in the soil, and the fibers cannot be interwoven into a three-dimensional network. On one hand, when the fibers are too long, the fibers will be entangled with each other and they are not in full contact with the soil skeleton. On the other hand, the fiber length is too large, and a certain strain should be used to “wake up” the fibers in the soil. The strain of the specimens is not enough to induce the contribution of the fibers, which is one of the reasons for the decrease of the reinforcement effect.

In the laboratory tests, the influence of fiber length on the strength of the samples is related to the size of the samples. The unconfined compression tests of the cotton fiber reinforced soil with 100 mm height and 50 mm diameter were conducted, and the strength is the best with 1.0 % fiber content and 2.5 cm fiber length. The unconsolidated undrained triaxial tests (UU) of the cotton fiber reinforced soil with 125 mm height and 61.8 mm diameter were carried out, and the strength is best with 1.0 % fiber content and 3.09 cm fiber length. It can be seen that the results of unconfined compression tests, UU tests and CU tests are completely consistent, which means the optimum fiber length measured in the laboratory is $D/2$ (D is the specimen diameter). Therefore, the optimal fiber content and the optimum fiber length determined through the laboratory tests were 1.0 % and $D/2$, respectively.

3.5. Analysis of failure mode

The failure mode of the samples under different reinforcement conditions is shown in Fig. 9. (1) The failure mode of saturated cotton fiber reinforced soil is bulging failure. (2) The failure mode of the unreinforced soil samples is drum shaped, which is small at both ends, large in the middle, and the end effect is obvious. The radial deformation difference between the end and the middle of the fiber reinforced soil samples is reduced, and the end effect is weakened. The fiber reinforcement can restrain the movement of soil particles. The failure mode of the samples show that the fiber reinforcement can effectively restrain the radial deformation of the samples and improve the strength of the soil.

4. Conclusions

(1) The stress-strain relationship of the saturated cotton fiber reinforced soil is strain hardening. The change laws of the pore water pressure with the increasing of the axial strain are affected by confining pressure and void ratio.

(2) The fiber length has no obvious effect on the effective stress path of fiber reinforced soil. With the increase of fiber content, the effective stress path in p' - q surface of the reinforced soil gradually moves to the left side

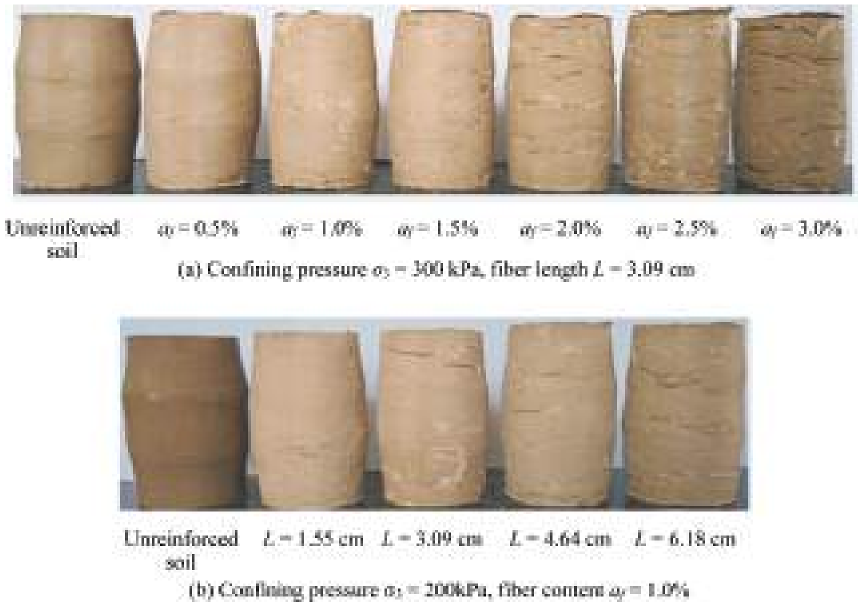

Figure 9 - Failure mode of fiber reinforced soil samples.

from the right side of that of unreinforced soil. The critical value of fiber content is 1.0 %.

(3) The relationship between pore water pressure and deviator stress is nonlinear, and it consists of three evident stages: initial stage, change stage and stable stage. The engineering properties of compacted cotton fiber reinforced soil are similar to those of slightly overconsolidated clay.

(4) There is an optimal fiber content and an optimum fiber length which are 1.0 % and 3.09 cm, respectively. Under the optimal fiber reinforced conditions, the effective cohesion of the fiber reinforced soil increases by 112.3 % compared with unreinforced soil. The internal friction angle of fiber reinforced soil is basically the same as that of the unreinforced soil, and the reinforcement condition has no significant effect on the internal friction angle of fiber reinforced soil.

(5) There are three fiber existing forms in fiber reinforced soil: contact, bending and interweaving. The failure mode of saturated cotton fiber reinforced soil is bulging failure. The reinforcement effect can effectively restrain the radial deformation of the samples.

References

Anagnostopoulos, C.A.; Papaliangas, T.T.; Konstantinidis, D. & Patronis, C. (2013). Shear strength of sands reinforced with polypropylene fibers. Geotechnical and Geological Engineering, 31(2):401-423.

Chaduvul, U.; Viswanadham, B.V.S. & Kodikara, J. (2017). A study on desiccation cracking behavior of polyester fiber-reinforced expansive clay. Applied Clay Science, 142(2):163-172.

Chai, S.X. & Shi, Q. (2012). Strength and deformation of saline soil reinforced with rice straw. Journal of PLA University of Science and Technology (Natural Science Edition), 13(6):646-650.

Correia, A.A.S.; Venda Oliveira, P.J. & Custódio, D.G. (2015). Effect of polypropylene fibres on the compressive and tensile strength of a soft soil, artificially stabilised with binders. Geotexiles and Geomembranes, 43(2):97-106.

Diab, A.A.; Sadek, S.; Najjar, S. & Daya, M.H.A. (2016). Undrained shear strength characteristics of compacted clay reinforced with natural hemp fibers. International Journal of Geotechnical Engineering, 10(3):263-270.

Diambra, A.; Ibraim E.; Russell, A.R. & Muir Wood, D. (2013). Fibre reinforced sands: from experiments to modelling and beyond. International Journal for Numerical and Analytical Methods in Geomechanics, 37(15):2427-2455.

Diambra, A. & Ibraim, E. (2015). Fibre-reinforced sand: Interaction at the fibre and grain scale. Géotechnique, 65(4):296-308.

Estabragh, A.R.; Bordbar, A.T. & Javadi, A.A. (2011). Mechanical behavior of a clay soil reinforced with nylon fibers. Geotechnical and Geological Engineering, 29(5):899-908.

Hou, T.S. (2012). Influence of expanded polystyrene size on deformation characteristics of light weight soil. Journal of Central South University, 19(11):3320-3328.

Hou, T.S. (2014). Model for compaction density and engineering properties of light weight soil. Chinese Journal of Geotechnical Engineering, 36(11):2127-2135.

Hou, T.S. & Xu, G.L. (2009). Experiment on triaxial pore water pressure-stress-strain characteristics of foamed particle light weight soil. China Journal of Highway and Transport, 22(6):10-17.

Hou, T.S. & Xu, G.L. (2010). Experimental study on the shear strength characteristics of foamed particle light weight soil. Journal of China University of Mining & Technology, 39(4):534-540.

Hou, T.S. & Xu, G.L. (2011). Optimum water content models and tests of light weight soil. Chinese Journal of Geotechnical Engineering, 33(7):1129-1134.

Ibraim, E.; Diambra, A.; Russell, A.R. & Muir Wood, D. (2012). Assessment of laboratory sample preparation for fibre reinforced sands. Geotextiles and Geomembranes, 34(3):69-79.

Krishna Rao, S.V. & Nasr, A.M.A. (2012). Laboratory study on the relative performance of silty-sand soils reinforced with linen fiber. Geotechnical and Geological Engineering, 30(1):63-74.

Liu, J.L.; Hou, T.S. & Luo, Y.S. (2018). Unconfined compressive strength of synthetic cotton fiber reinforced soil. Journal of Hydroelectric Engineering, 37(2):12-21.

Michalowski, R.L. (2008). Limit analysis with anisotropic fibre-reinforced soil. Géotechnique, 58(6):489-501.

Oliveira Júnior, A.I.; Jucá, J.F.T.; Ferreira, J.A. & Guilherme, L.C. (2019). Geotechnical behavior and soil-fiber interaction of clayey soil mixed with randomly dispersed coconut fibers. Soils and Rocks, 42(2):127-138.

Prabakar, J. & Sridhar, R.S. (2002). Effect of random inclusion of sisal fibre on strength behavior of soil. Construction and Building Materials, 16(2):123-131.

Shao, W.; Cetin, B.; Li, Y.D.; Li, J.P. & Li, L. (2014). Experimental investigation of mechanical properties of sands reinforced with discrete randomly distributed fiber. Geotechnical and Geological Engineering, 32(4):901-910.

Soltani, A.; Deng, A. & Taheri, A. (2018). Swell-compression characteristics of a fiber-reinforced expansive soil. Geotextiles and Geomembranes, 46(2):183-189.

Tang, C.S.; Shi, B.; Gao, W. & Liu, J. (2009). Single fiber pull-out test and the determination of critical fiber reinforcement length for fiber reinforced soil. Rock and Soil Mechanics, 30(8):2225-2230.

Tang, C.S.; Li, J.; Wang, D.Y. & Shi, B. (2016a). Investigation on the interfacial mechanical behavior of wave-shaped fiber reinforced soil by pullout test. Geotextiles and Geomembranes, 44(6):872-883.

Tang, C.S.; Wang, D.Y.; Cui, Y.J.; Shi, B. & Li, J. (2016b). Tensile strength of fiber-reinforced soil. Journal of Materials in Civil Engineering, 28(7):1-13.

Wang, Y.Z.; Liu, X.F.; Zhang, Z.K.; Ma, D.G. & Cui, Y.Q. (2015). Experimental research on influence of root content on strength of undisturbed and remolded grass-roots-reinforced soil. Chinese Journal of Geotechnical Engineering, 37(8):1405-1410.

Wei, L.; Chai, S.X.; Cai, H.Z. & Li, M. (2012). Triaxial shear strength and deviatoric stress-strain of saline soils reinforced with wheat straws. China Civil Engineering Journal, 45(1):109-114.

Xie, J.; Tang, C.S.; Yin, L.Y.; Lv, C. & Shi, B. (2019). Mechanical behavior of microbial-induced calcite precipitation (MICP)-treated soil with fiber reinforced. Chinese Journal of Geotechnical Engineering, 41(4):675-682.

Zaimoglu, A.S. (2010). Freezing-thawing behavior of fine-grained soils reinforced with polypropylene fibers. Cold Regions Science and Technology, 60(1):63-65.

Zhang, Y.M.; Zhang, X.D. & Zhang, H.R. (2005). Test research of geotechnique textile soil reinforcement mechanism and engineering application. Rock and Soil Mechanics, 26(8):1323-1326.

Mapping of Geological-Geotechnical Risk of Mass Movement in an Urban Area in Rio Piracicaba, MG, Brazil

L.E. Assis, E.A.G. Marques, C.A. Lima, S.J.M.C. Menezes, L.A. Roque

Abstract. The objective of this study is to create a geological-geotechnical risk map of mass movement for an urban perimeter of Rio Piracicaba city, state of Minas Gerais, MG, Brazil, by applying the methodology proposed by the Brazilian Ministry of Cities. Four neighborhoods were evaluated through works conducted in the field and with the aid of a GIS fed with aerial images obtained from an Unmanned Aerial Vehicle (UAV). In these neighborhoods, 29 points were categorized as risk-points, and 14 risk areas were delimited and hierarchized. Despite being considered a subjective evaluation, the methodology used is a simple and efficient qualitative method, which can contribute significantly to the preliminary identification of areas under risk of mass movements, indicating the nature of the predisposing factors. The areas classified as high-risk present significant physical and environmental problems, mainly due to non-compliance with current legislation regarding urban planning and land use. The outcomes of these surveys are valuable tools that will facilitate the planning and management of land use and occupation in the municipality.
Keywords: geotechnical cartography, geological-geotechnical risk, gis, mass movements, risk hierarchizing, UAV.

1. Introduction

Gravitational mass movements are important surface terrestrial phenomena and constitute a natural evolution of the slopes (Wolle, 1988). This type of events are related to the loss of shear strength of soils and/or rocks along a failure plane, intensified by the interference of other factors such as water, ice and air presence and slope (Bigarella & Passos, 2003). However, this phenomenon is no longer considered as only "natural", due to the numerous processes of anthropic intervention by the absence of planning and by degradation of the environment.

Disasters are considered inevitable and are directly related to the probability, intensity, danger and susceptibility of the factors involved, and which are related to environmental, social and economic conditions. However, they can be minimized through preventive actions, with the purpose of safeguarding communities at risk, based on monitoring and territorial planning (UNISRD, 2004). The International Decade for Natural Disaster Reduction (IDNDR) considers risk as the combination of the probability of a given event to occur and its likely negative consequences (UNISRD, 2009).

According to Tominaga (2007), the term "area of risk" is increasingly incorporated into the vocabulary of the Brazilian population, since accidents involving mass movements and floods during the rainy season have intensified and affected many communities that occupy slopes and urban areas with deficient infrastructure.

Vieira (2000) differentiates risk points from risk areas, by considering that risk points are imminent situations, which must be linked to a specific building or locality. Risk areas comprise situations that cover a larger proportion of space, with irregular shapes and sizes and encompass risk points that can, eventually, have different risk class.

The human actions that most interfere in the triggering of mass movements on slopes are related to deforestation, lack of drainage direction, inefficient natural drainages, cuts and landfill performed without technical support, poorly implemented engineering works, excavations and waste dump (Araújo, 2004).

Due to the numerous episodes of natural disasters recorded in recent years, mainly related to urban occupation of places susceptible to geological risks, Brazilian authorities were encouraged to take risk management measures. Based on interventionist practices and policies, these measures were established with the aim of contributing to the monitoring and a more ordered growth of the urban perimeter.

The Brazilian National Policy on Protection and Civil Defense - PNPDEC, created by Federal Law 12.608 / 2012 addresses, in its priority concepts, the necessity of mapping and preventive actions for the reduction of disasters. The purpose of this law is to enable municipalities susceptible to these types of events to produce a preventive and orderly land use plan (Diniz, 2012).

Laís Emily de Assis, M.Sc., D.Sc. Student, Universidade Federal de Viçosa, Viçosa, MG, Brazil. e-mail: laismily9@gmail.com.
Eduardo Antonio Gomes Marques, D.Sc., Full Professor, Universidade Federal de Viçosa, Viçosa, MG, Brazil. e-mail: emarques@ufv.br.
Cleverson Alves de Lima, D.Sc., Associate Professor, Universidade Estadual de Santa Cruz, Ilhéus, BA, Brazil. e-mail: clalima@uesc.br.
Sady Junior Martins da Costa de Menezes, D.Sc., Associate Professor, Universidade Federal Rural do Rio de Janeiro, Três Rios, Rio de Janeiro, Brazil. e-mail: sadymenezes@yahoo.com.br.
Leandro Antônio Roque, M.Sc., Universidade Federal de Viçosa, Viçosa, MG, Brazil. e-mail: leandroroque1@hotmail.com.
Submitted on March 13, 2019; Final Acceptance on November 6, 2019; Discussion open until August 31, 2020.
DOI: 10.28927/SR.431057

Among the changes in the regulatory framework proposed by PNPDEC, the Cities Statute designated by Federal Law 10.257 / 2001, which deals with urban policy guidelines, has undergone various alterations. These new obligations demand that all municipalities must present their susceptibilities to natural disasters through geotechnical charts and/or maps and identify and monitor major risk areas (occupied or not) (IPT, 2015).

Based on risk management works carried out by the Technological Research Institute of São Paulo (IPT), the Ministry of Cities has been supporting initiatives related to the monitoring and prevention of risks in precarious settlements in municipalities, by conducting direct actions and providing training through federal agencies (Brazil, 2007). According to Marques *et al.* (2011), this methodology is currently considered one of the most used for risk assessment in Brazil.

As observed by Marchiori-Faria *et al.* (2005), risk mapping performed to serve as a base for Civil Defense is considered one of the main forms of technical support provided to municipalities for their management and contingency planning. The identification and qualification of risks, based on field assessments, enables a rapid implementation of mitigating actions in areas considered susceptible to instabilities.

In recent years, along with several mapping methods, the use of tools such as remote sensing, aerial photogrammetry and other geotechnologies are considered fundamental instruments for mass movement risk management. The evaluation of risk scenarios based on the use of geotechnologies to acquire cartographic data has become a fundamental tool for the understanding of threats, for promoting an integrated management of contingency plans and for supporting management of disaster forecasting.

According to studies by Akgun (2012), Saito *et al.* (2015) and Shahabi & Hashim (2015), GIS is a necessary but still little explored technology in the recording of vulnerable communities and informal settlements for risk mapping. GIS is considered a satisfactory technique because it allows, through coordinates measured by GPS (Global Positioning System), to record points and to correlate them with images in GIS environments, acting as an aid in the estimation of monitoring and alert.

In this context, the present study aims to identify the processes responsible for the geological-geotechnical risk of mass movement in an urban perimeter composed by 4 neighborhoods in the city of Rio Piracicaba, MG, Brazil, by applying the methodology proposed by the Ministry of Cities, Brazil (2007). The focus was to identify points and areas based on field surveys, supported by a qualitative approach and field mapping. The identification was performed by using orthorectified aerial images obtained through the use of an UAV.

Risk assessment is a fundamental process for the prevention and monitoring of the study areas as they show an urban expansion involving irregular constructions, in a steep terrain and under unfavorable geological and geotechnical conditions. Even with these unfavorable characteristics, the majority of these risk areas do not have any registry in the municipal civil defense, as it will be demonstrated.

2. Materials and Methods

2.1. Characteristics of the study area

According to data from IBGE (2010) the municipality of Rio Piracicaba, located in the central part of the Minas Gerais State, has a total area of 373.4 km^2 and an estimated population of 14,149 inhabitants (Fig. 1).

Being part of the region known as Iron Quadrangle, the municipality is located mostly in a granite-gneiss domain and presents an extensive lithostratigraphic registry, and a northeast structural direction.

More recent surveys carried out by CPRM (2014) have shown that the main lithotypes found in Rio Piracicaba area are amphibolites, orthogneisses, shale and banded iron formations, presenting materials varying from very weathered to sound rock. Some other factors stimulate the occurrence of mass movements, such as: slope, thick weathering mantle, clay-silt rich soils, detrital cover (“canga” deposits) and presence of transition areas with soil-rock contacts and talus deposits at the foot of the slope. Climate is also a controlling factor, as there is a rainfall concentration, mainly between the months of November and January. According to Köppen classification, climate of Rio Piracicaba can be classified as Cwa, mesothermic climate with hot and rainy summers and dry winters, and average precipitation of 1462 mm (CPRM, 2010).

According to CETEC (1983) there are two predominant geomorphological units in the municipality, the Iron Quadrangle and the Dissected Plateaus, the Piracicaba river being the topographic divider between these units.

2.2. Modeling of the land of the municipality of Rio Piracicaba, MG, based on images generated by an UAV

A Sensefly Swinglet CAM Unmanned Aerial Vehicle (UAV) was used to survey the study area (Fig. 2). The UAV features a calibrated 12 MP Canon IXUS220HS RGB onboard camera that allows 7 to 30 cm/pixel spatial resolution (GSD) images. Its navigation system has sensors and GPS receivers with flight autonomy of up to 30 min and it is able to fly at a cruising speed of up to 36 km/h and resistance to winds of 5 m/s^{-1}.

A Garmin 60CSx GPS, with positioning accuracy ≤ 10.0 m, was used to collect the points. The takeoff area of the UAV was set at Point 1, from where the flight plan was executed (Fig. 3). The eMotion 2 software was used to control the UAV; it allows telemetry connection to the computer and transmits frequent correction signals, besides

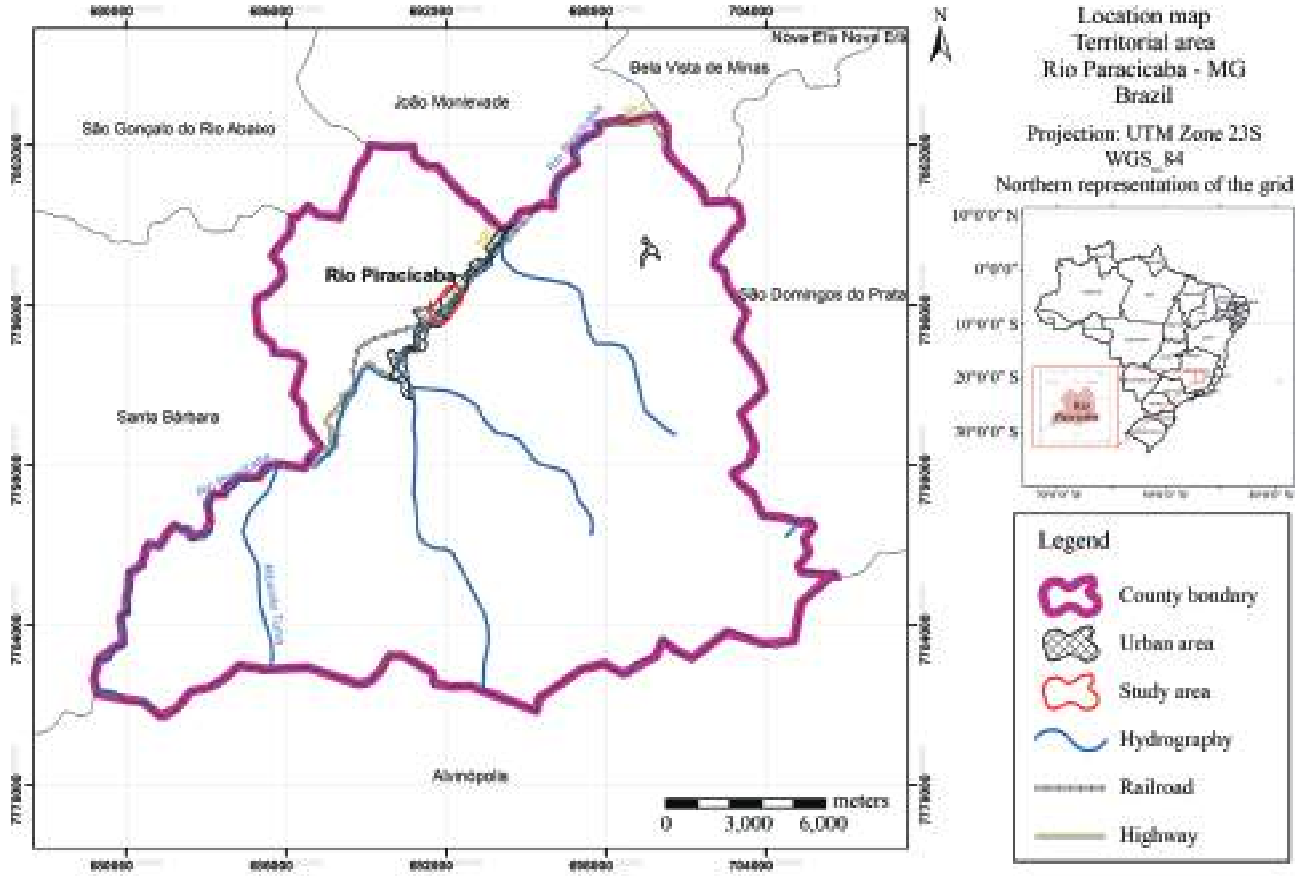

Figure 1 - Location Map of the Municipality of Rio Piracicaba, MG, Brazil.

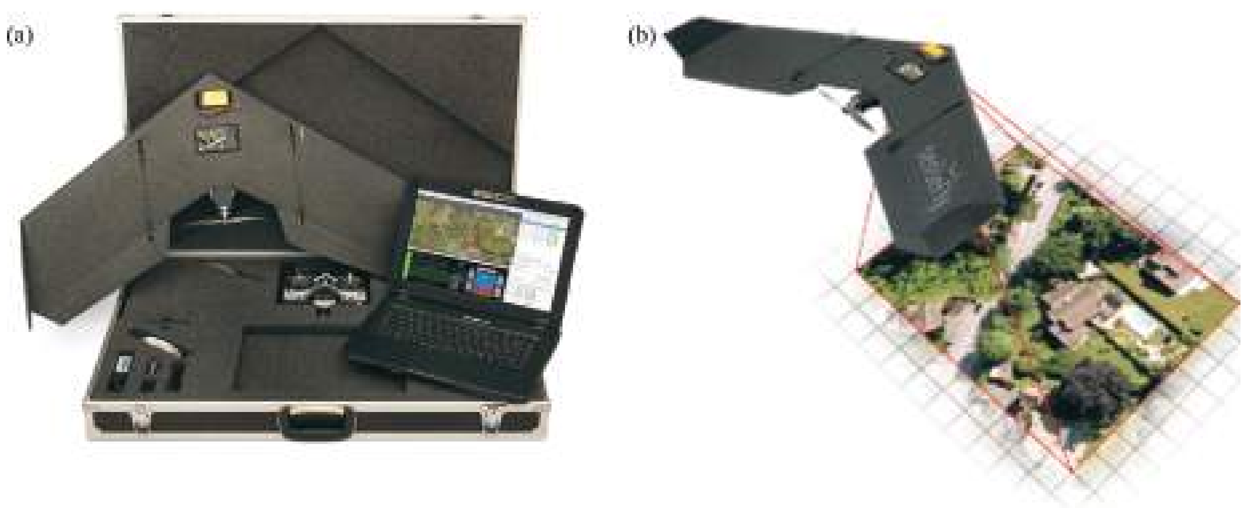

Figure 2 - UAV - Swinglet Cam Sensefly (Santiago & Cintra, 2015).

providing improvements in the ground/air resolution, increasing the safety of taking aerial photos.

The flight was carried out in favorable weather conditions to obtain data, with winds within the tolerance stated by UAV specifications and absence of precipitation and cloudiness. The survey covered an area of 124.06 ha and allowed capture of overlapping images (overlay) of 400 m x 300 m, for later use and preparation of cartographic digital bases. The processing was carried out at the Geotechnology Laboratory of Três Rios (GEO3R) - Institute of Federal Rural University of Rio de Janeiro. The computational programs used in the procedures were:

Figure 3 - Flight plan elaborated for the aerophotogrammetry of the study area. (Geographic Coordinate: Latitude: 691744,632; Longitude: 7796284,803).

Postflight Terra® 3D, Pix4UAV® Desktop and ArcGis® ESRI.

2.3. Modeling of thematic maps

Modeling of the thematic maps was performed at the Civil Engineering Department of the Federal University of Viçosa. The software ArcGis® 10.3.1 ESRI (Environmental Systems Research Institute) was used for the production of the following cartographic data:

- Terrain Modeling;
- Delimitation of study area and hydrography, complemented by identified drainage;
- Digital elevation model (DEM): made using Arctoolbox software, Topo to Raster interpolator, with the curves generated by the software Raster Surface - Contour as input data;
- Declivity: drawn from the Digital Elevation Model (DEM) and the level curves (Topographical Map) by way of geoprocessing in Slope software (3D analyst tool). The gradient (slope) analysis was subdivided into six classes, according to EMBRAPA (1979): 0-3 % (wavy), 8-20 % (gentle wavy), 20-45 % (wavy strong), 45-75 % (mountainous), > 75 % (steep)
- Interfaces with 3D thematic map, using ArcScene.

All the outcomes were organized from the orthomosaic obtained by the UAV survey, which contributed to the geomorphological analysis and characterization of the study area.

2.4. Processing and obtaining the database by the UAV

For the generation of the database collected from the flight and the junction of the 41 aerial photos, georeferencing and association of the geographic coordinates were performed using the Datum WGS84 UTM zone 23S system. Postflight Terra® 3D system and Pix4UAV® Desktop softwares were used to process the images and acquire the Orthomosaic and Digital Surface Model (DSM) (Fig. 4).

The data processed allowed to generate a GSD (Ground Sampling Distance) with 14 to 18 cm/pixel spatial resolution for the image-surveyed area. These data were essential for the production of the digital terrain model and contributed for the assessment of a good representation of the study area.

The presentation of the three-dimensional perspective (3D) (Fig. 5) was obtained by ArcGis® ESRI software in the ArcScene 10.3.1 extension. This information was an essential base for the modeling and for the understanding of events in the area.

2.5. Application of the methodology of the Ministry of Cities - Geological-geotechnical risk qualification

To determine the study area, meetings were held with the Civil Defense department of Rio Piracicaba Municipal-

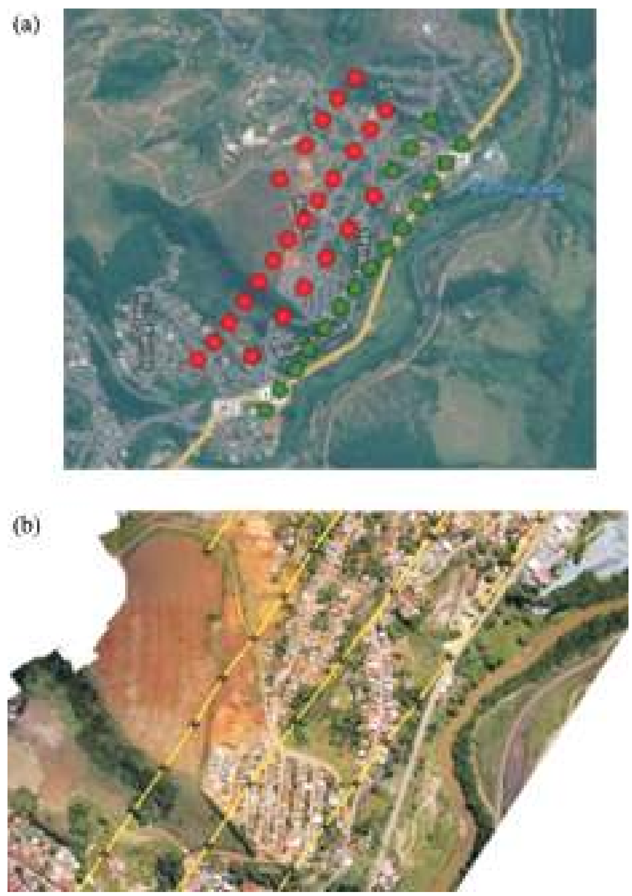

Figure 4 - (a) Element of Pix4UAV® Desktop Software in the study area after taking pictures (Geographic Coordinate: Latitude: 691744,632; Longitude: 7796284,803). (b) Component part of the processed Orthophoto showing the flight paths (trajectory) of the UAV over the studied area (Geographic Coordinate: Latitude: 691744,632; Longitude: 7796284,803).

Figure 5 - Three-dimensional perspective (3D) of the study area obtained with ArcScene®, version 10.3.1 (Geographic Coordinate: Minimum Latitude: 691341,000000, Maximum Latitude: 692625,813950; Minimum Longitude: 7795380,931400, Maximum Longitude: 7796856,871180) (Scale in 2D: XY Scale 1:7.000, Z Scale Elevation Factor: 1,5 ArcScene ®).

ity, and were supported by its historical collection on land use and occupation, landslide occurrences and social aspects. Geological-geotechnical mapping involved the complete evaluation of four neighborhoods (Córrego São Miguel, Padre Levy Housing Complex, Bom Jesus, Nossa Senhora da Conceição) in which the points and areas of geological-geotechnical risk associated with physical environment information were registered and georeferenced.

Points were collected by means of field surveys carried out in every street of the four evaluated neighborhoods using a GARMIN 60CSx GPS and photographic records. In these surveys, two different risk situations were identified and named: 1) current risk (situations of geological risks present in the urban area), and 2) potential risk (susceptibility in unoccupied areas). In the identification and mapping stage, geological/geomorphological diagnostic and land uses identification were performed, in which certain specific conditions were considered (see Table 1), for the classification of current and/or potential risk to mass movements within the study area.

The delimitation of the areas of risk (zoning) was carried out in the field through sectorization on the local cartographic base and the information of the previously identified risk points. The degree of risk for a given element was evaluated individually, mainly considering the typologies of the constructions for each sector and/or demarcated households, as well as its vulnerability to mass impact, in addition to the other observations related to the geologi-

Table 1 - Aspects for the classification of current/potential risk of mass movements in the study area. Adapted from Souza (2015).

Geological/geomorphological diagnosis	Use and occupation diagnosis	Identification of the main triggers
-Local geology (main lithotypes, structures, orientation of minerals, elements of discontinuity)	- Constructive standard of residences (cracks etc.)	- Disposal of trash and debris material on the slope
	- Poorly located constructions	- Drainage; Leakage of tubing/ Releasing of wastewater on the surface / Sanitary septic tanks
- Terrain (altimetry, declivities and orientations of slopes), identification of main triggers related to hydrological-climatic processes, natural changes in the inclination of layers	- Inefficient/nonexistent drainage system	- Identification of erosive features
	- Withdrawal of protection surface	- Mass movement scars
	- Removal of vegetation cover	- Cuts with inappropriate heights and inclinations; Released landfills; Execution of deficient landfills.
	- Deforestation.	

Table 2 - Risk hierarchy criteria (adapted from Brazil (2007) by Roque (2013).

Degree of probability	Description
(R0) No risk	1. The predisposing geological-geotechnical conditions (slope, type of terrain, etc.) and the level of intervention in the sector are of no potential for the development of landslides and undermining.
	2. Sign/feature/evidence(s) of instability is/are not observed. There is no evidence of development of drainage-margin or slope instability.
	3. If existing conditions are maintained, destructive events are not expected to occur in the period of a normal rainy season.
(R1) Low	1. The predisposing geological-geotechnical conditions (slope, type of terrain, etc.) and the level of intervention in the sector are of low potential for the development of landslides and undermining.
	2. There are of some signs/features/evidence of instability (slopes and drainage margins), although incipient. Process of instability at an early stage of development.

Table 2 - Cont.

	3. If the existing conditions are maintained, there is a low possibility of destructive events occurring during episodes of intense and prolonged rains in a rainy season.
(R2) Medium	1. The predisposing geological-geotechnical conditions (slope, type of terrain, etc.) and the level of intervention in the sector are of medium potential for the development of landslides and undermining.
	2. There are significant signs/features/evidence of instability (cracks in the ground, denudational landforms in slopes, etc.). The instability process is ongoing; however, it is still possible to monitor its evolution.
	3. If the existing conditions are maintained, it is quite possible that destructive events occur during episodes of intense and prolonged rains in the period elapsed by the rainy season.
(R3) High	1. The predisposing geological-geotechnical conditions (slope, type of terrain, etc.) and the level of intervention in the sector are of high potential for the development of landslides and undermining.
	2. There are signs/features/evidence of instability (cracks in the ground, denudational landforms in slopes, cracks in dwellings or retaining walls, tilted trees/poles, landslide scars, erosive features, proximity of dwellings in relation to banks of streams, etc.) and they are expressive and observed in great number or magnitude. Instability process at an advanced development stage.
	3. If the existing conditions are maintained, it is very likely that destructive events will occur during episodes of intense and prolonged rains in the period elapsed by the rainy season.

cal-geotechnical conditions and evidence of instability, according to Brazil (2007).

The data sheet used for risk mapping, with the results of the geological-geotechnical fieldwork evaluations, was adapted by Roque (2013) from the methodology proposed by the Ministry of Cities (Brazil, 2007) (see Table 2). Its main benefit is to standardize the criteria used to define the degree of risk of mass movements in the study area. The hierarchy of the degree of risk was based on the judgment and experience of the technical team (qualitatively), responsible for the survey. For zoning risk, a four-level probability hierarchy was set, adapted from the Ministry of Cities classification: (R0) No risk, (R1) Low Risk, (R2) Medium Risk and (R3) High Risk, being R3 considered as needing immediate intervention.

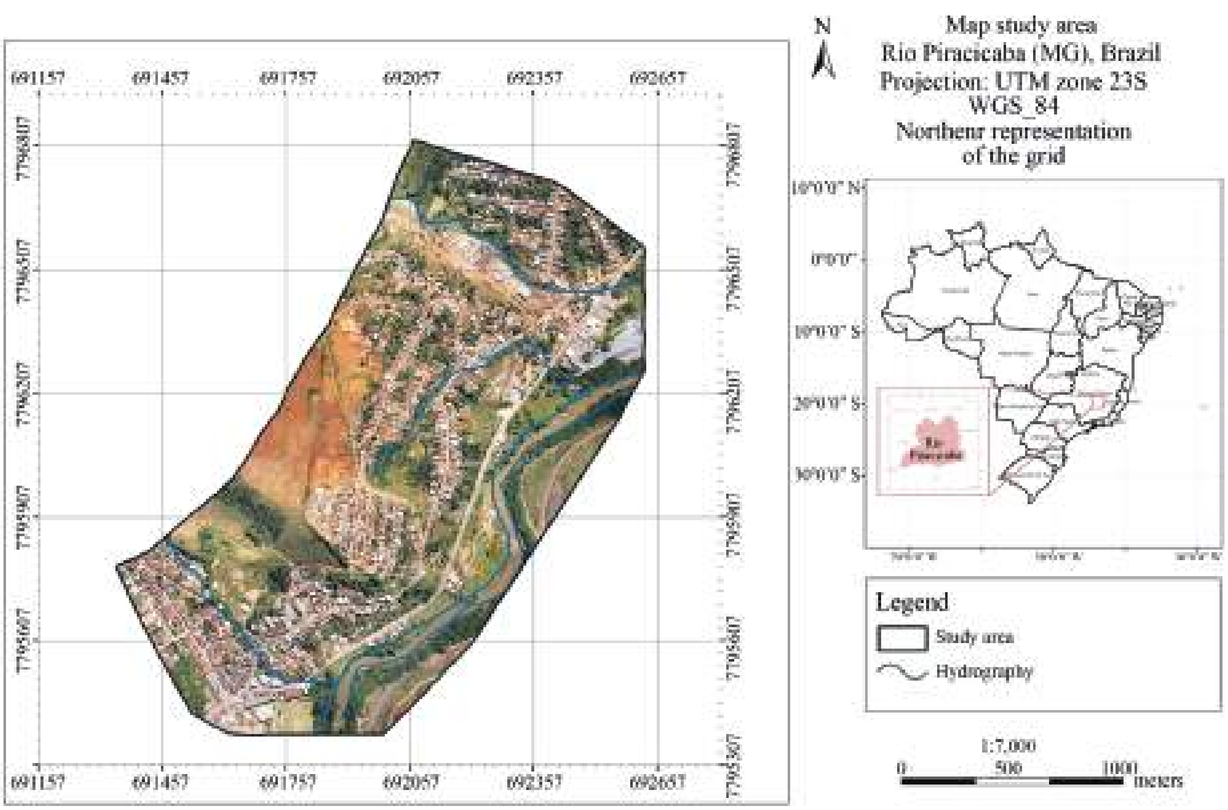

Figure 6 - Map of the study area in Rio Piracicaba, MG.

The points and areas mapped and the delimitation of risk sectors were plotted and organized in an RGB (3-2-1) orthomosaic (Fig. 6) obtained from the aerial photogrammetric survey by the Unmanned Aerial Vehicle (UAV) and processed with Postflight Terra® 3D and Pix4UAV® Desktop systems. This image has enabled to build the cartographic base in the GIS environment. This cartographic base, with scales varying from 1:7.000 to 1:800, aided the verification of points and the creation of the polygons of the georeferenced areas. The software used for the generation of scenarios and sectorization of risk was the ArcGis® 10.3.1, developed by ESRI (Environmental Systems Research Institute).

3. Results and Discussion

The classification of the degree of risk of the areas and points that were mapped in the four evaluated neighborhoods are shown in Table 3 and on the map presented in Fig. 7. As stated, the hierarchy was classified based on the type of use, pattern of settlement and other triggering aspects observed on the ground, in accordance with the methodology of the Ministry of Cities. Moreover, classification also took into account the diagnosis of the physical characteristics integrated into the digital cartographic data of the study area in GIS environment (digital terrain model, altimetry, slope, land use and occupation, and mass movement scars).

Table 3 - Number of points and areas by neighborhoods.

Neighborhoods	Points of risk			Areas of current risk			Areas of potential risk		
	R1 Low	R2 Medium	R3 High	R1 Low	R2 Medium	R3 High	R1 Low	R2 Medium	R3 High
Córrego São Miguel	1	6	13	4	2	2	1		1
COAHB	1	2	1					1	
Bom Jesus			3						1
Nossa Senhora da Conceição	1	1							1

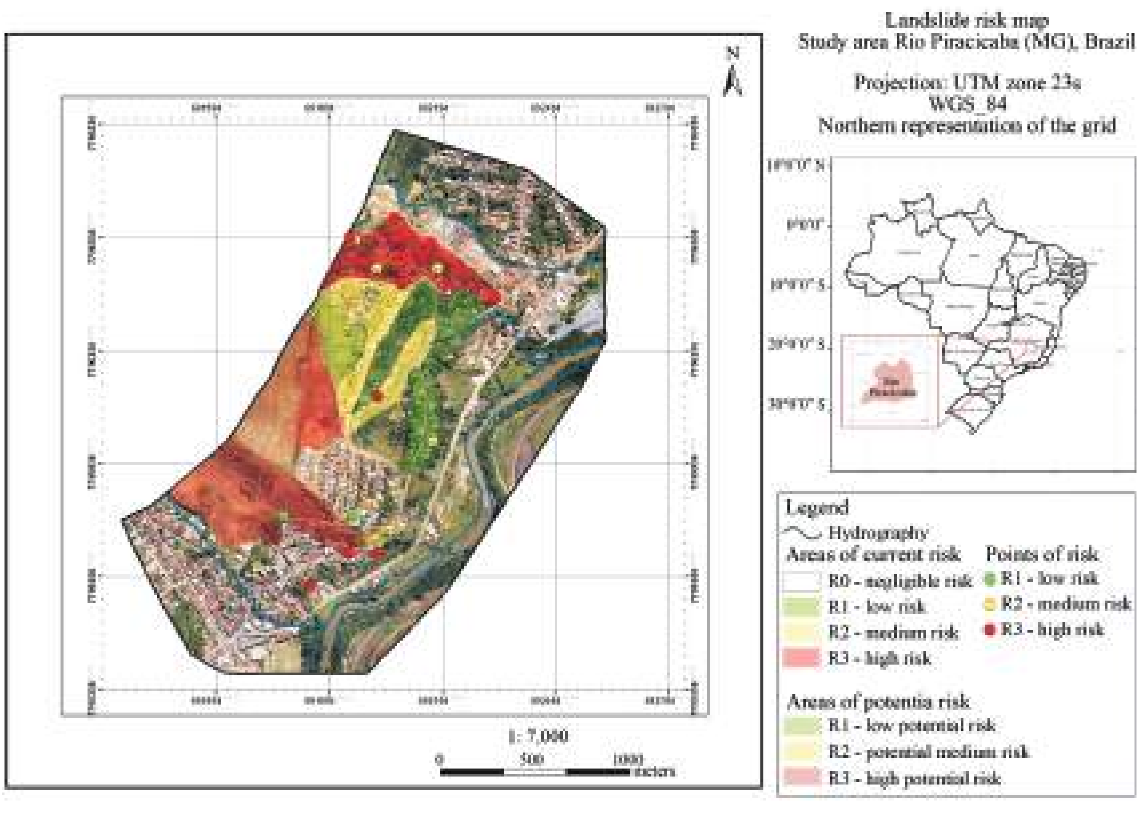

Figure 7 - Landslide risk map: areas of current risk, areas of potential risk (susceptibility) and points of risk - urban perimeter of Rio Piracicaba, MG.

To elucidate the situation of each neighborhood, the results were subdivided into 4 maps in larger scales, elaborated with the aim of a better representation of the urban and environmental diagnostic of the risk areas.

3.1. Córrego São Miguel neighborhood

The anthropic action, as a main environment modifier, in addition to the geotechnical, geological and geomorphological characteristics unfavorable to occupation, have allowed rating Córrego São Miguel neighborhood as the one with the greatest number of identified risk points (20), 8 areas of current risk and 2 of potential risk, which are considered priorities for immediate intervention and restructuring. It is suggested to prevent new occupations and reallocation of the population of the dwellings in the most critical situations and areas (Fig. 8).

The areas classified as high risk (R3) are marked by the presence of precarious and clandestine settlements, located at the top and at the base of cut slopes. There are a series of cuts and embankments carried out in a chaotic manner without any technical supervision, which result in the creation of zones of flow concentration and in large cutting heights and steep slopes. The neighborhood does not even have a sewage collection system and the residual effluents are launched *in situ* or directed to septic tanks; the drainage systems are non-existent or insufficient, and can

Figure 9 - Delimitation of High-risk points and area in the Córrego São Miguel neighborhood, precarious settlements, absence of rainfall drainage, erosive process in advanced stage and mass movements scars.

increase soil saturation, especially during periods of concentrated and intense rainfall. There are many banana trees whose roots promote water retention, along with dense vegetation on the slope, which may lead to vertical overload. This combination of factors increases the risks of mass movements (Fig. 9).

The predispositions observed in the medium-risk areas and points are related to the presence of exposed young residual soil, with formation of grooves and ravines due to concentrated surface runoff; cracks were also observed in the dwellings. Corrective measures must be taken for these situations, to prevent this degradation stage to progress.

Low-risk points and areas are situated on slopes varying from 3 to 45 %, in which the dwellings have better

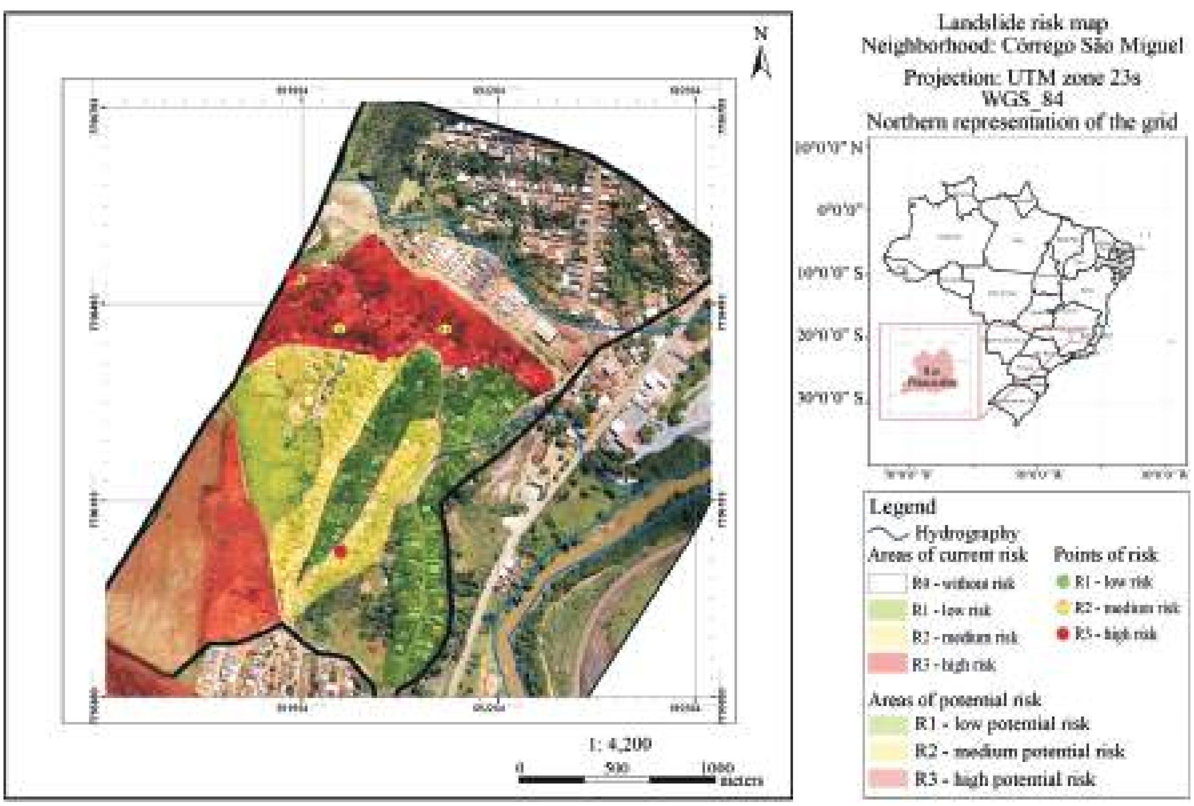

Figure 8 - Landslide risk map of Córrego São Miguel neighborhood, Rio Piracicaba, MG.

infrastructure conditions. However, damaged wastewater pipes were observed, with the effluents being disposed directly on roads. Although triggeringfactors are incipient, monitoring is necessary. For areas not yet occupied and categorized as with low potential risk, preliminary inspections should be carried out to assess geological-geotechnical characteristics and suitability for urbanization, in order to avoid cluttered occupations and cuts with inappropriate height and excessive slope

The area classified as potentially high-risk and the specified high-risk points described in slope of more than 45 % are related to the exposing of soil and rock and ferruginous soils compounds of strongly erodible lateritic (“cangas”). These materials impose a natural predisposition to morphodynamic deflagrations. It was observed that on erosive processes, the geometry of the slope favors the convergence of flows. According to the Civil Defense, this area has a history of mud runs in periods of heavy rainfall that affects residences located below. The municipality has already promoted some recovery attempts, but none has showed satisfactory results and, currently, the area is protected by wire fences. Occupations should be avoided.

As can be seen in the declivity map with the neighborhood limit (Fig. 10), the diagnosed points of risk are mostly located in the highly hilly terrains. On these points there are shallow soils (mostly silty sand) and rock outcrops in the base of the slopes, which present a natural predisposition for the action of the weather and, consequently, potentiate the risk of mass movements.

3.2. COAHB

The main risk-inducing factors on COAHB neighborhood are related to slopes with more than 30 % inclination, presence of soil/rock contacts and wastewater being disposed directly on lands and roads. This constant water flow in the soil causes increased saturation, decreases strength so increasing the risk of mass movements. The points classified as low risk require monitoring of the dynamic processes identified, related to the exposed soil and the absence of a drainage system. Drainage works are necessary to solve these problems; as well as planting, to restore the vegetation cover; and containment works, to prevent the degradation to progress (Fig. 11).

The area classified as medium potential risk is located at the base of a slope with inclination higher than 45 % (Fig. 12). The sparse vegetation still acts as a protective layer against water erosion, but the presence of shallow soils can control landslides during heavy rain periods. Thus, it is necessary to monitor the buildings that are located below this slope in order to avoid human and economic losses.

3.3. Bom Jesus neighborhood

In Bom Jesus neighborhood, 3 high-risk points were registered. The area demarcated as high potential risk (Fig. 13) corresponds to the face of a mountainous relief

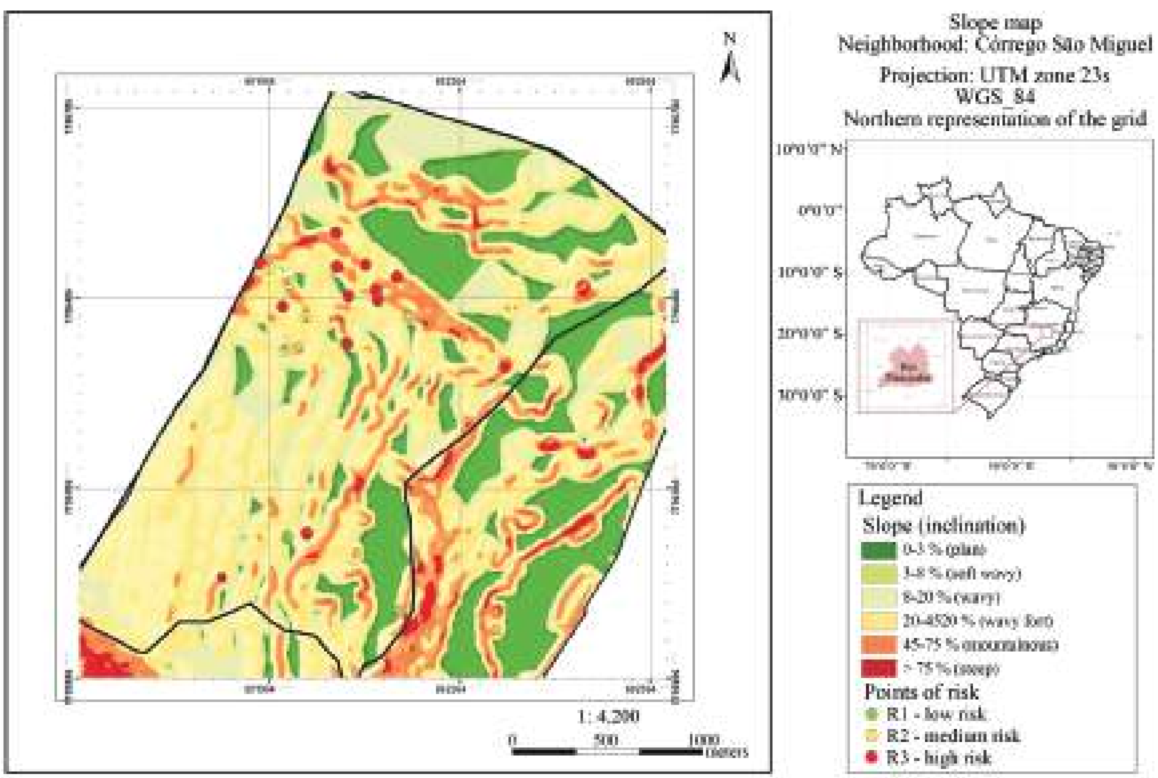

Figure 10 - Slope Map (inclination) (Córrego São Miguel Neighborhood, Rio Piracicaba, MG.

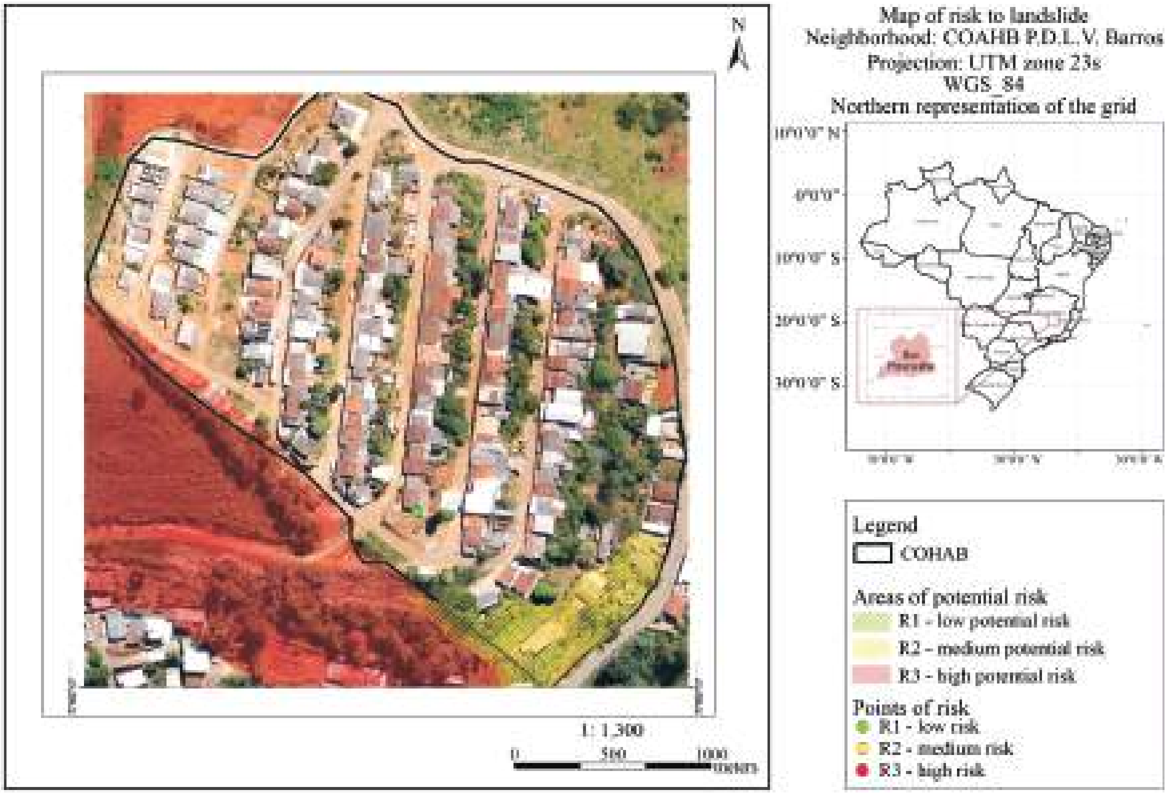

Figure 11 - Mass-movement risk map (neighborhood) COAHB Padre Levy, Rio Piracicaba, MG.

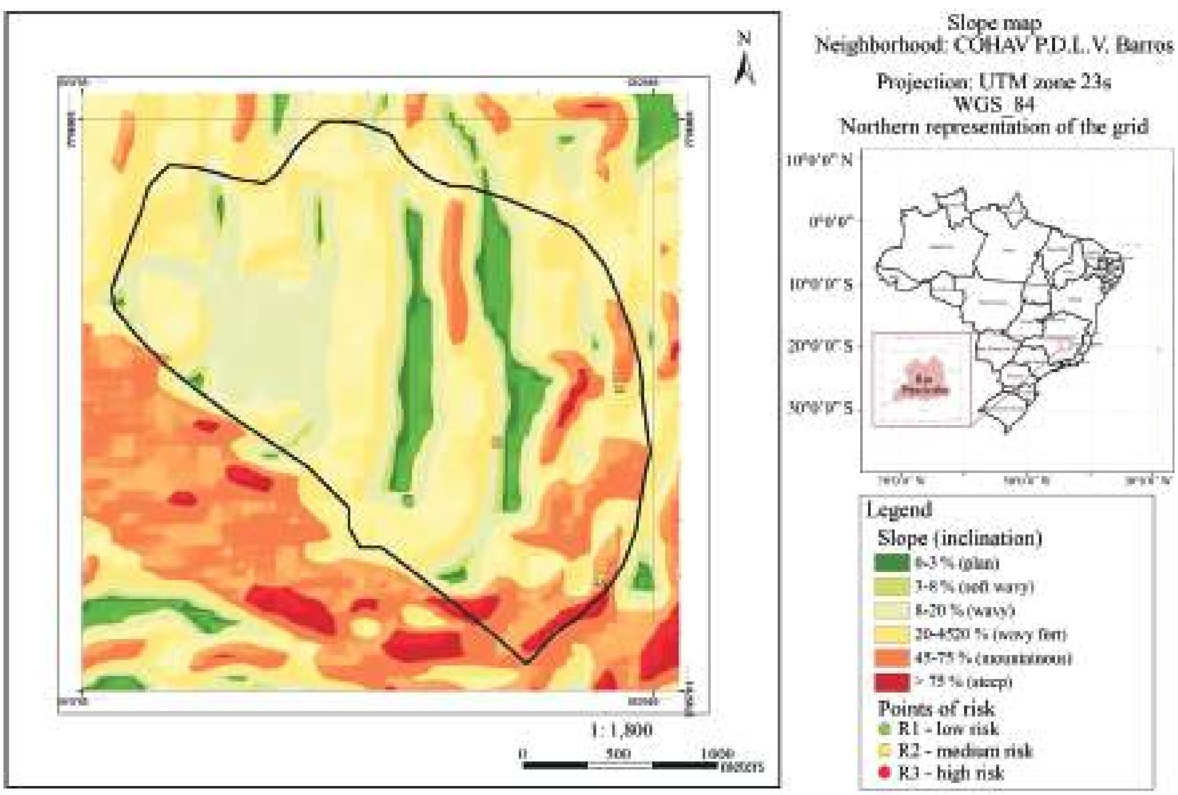

Figure 12 - Slope (inclination) map of COAHB neighborhood, Rio Piracicaba, MG.

slope, in which mass movement scars with recomposed crawling vegetation were identified; however, the dwellings below this slope should be monitored.

High-risk points are associated with landslides and presence of housing on the top. Unconsolidated materials and volumes of debris were identified at the talus deposit

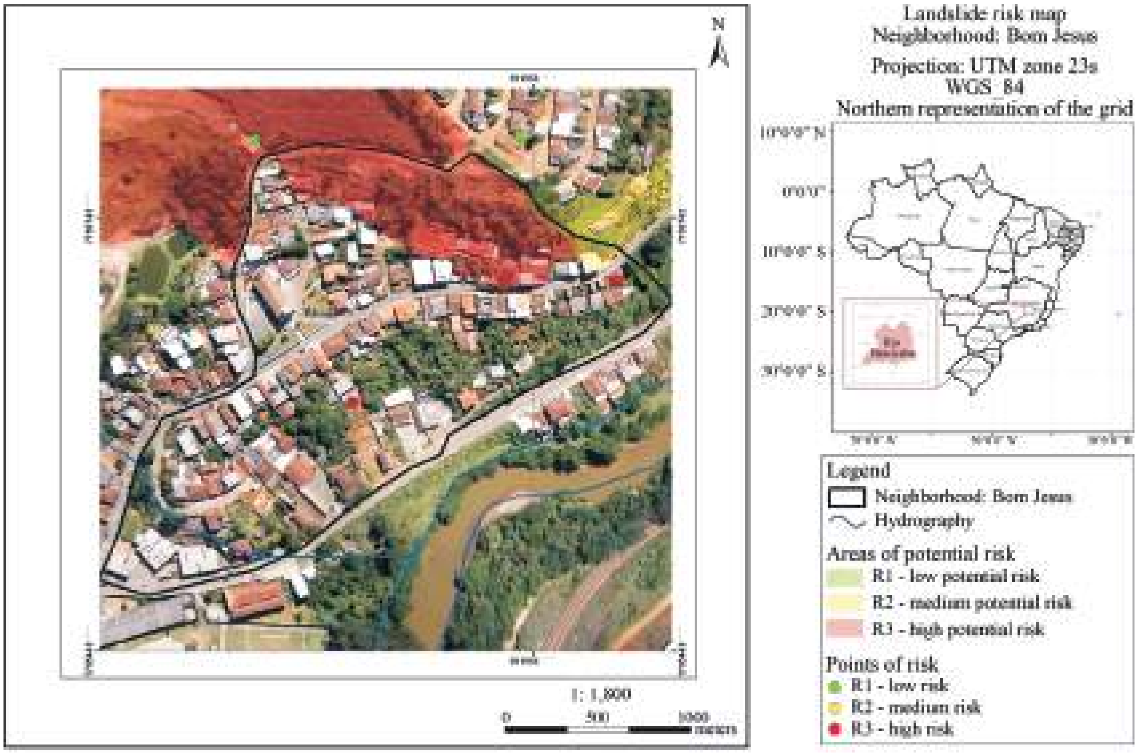

Figure 13 - Mass-movement risk map of Bom Jesus neighborhood, Rio Piracicaba, MG.

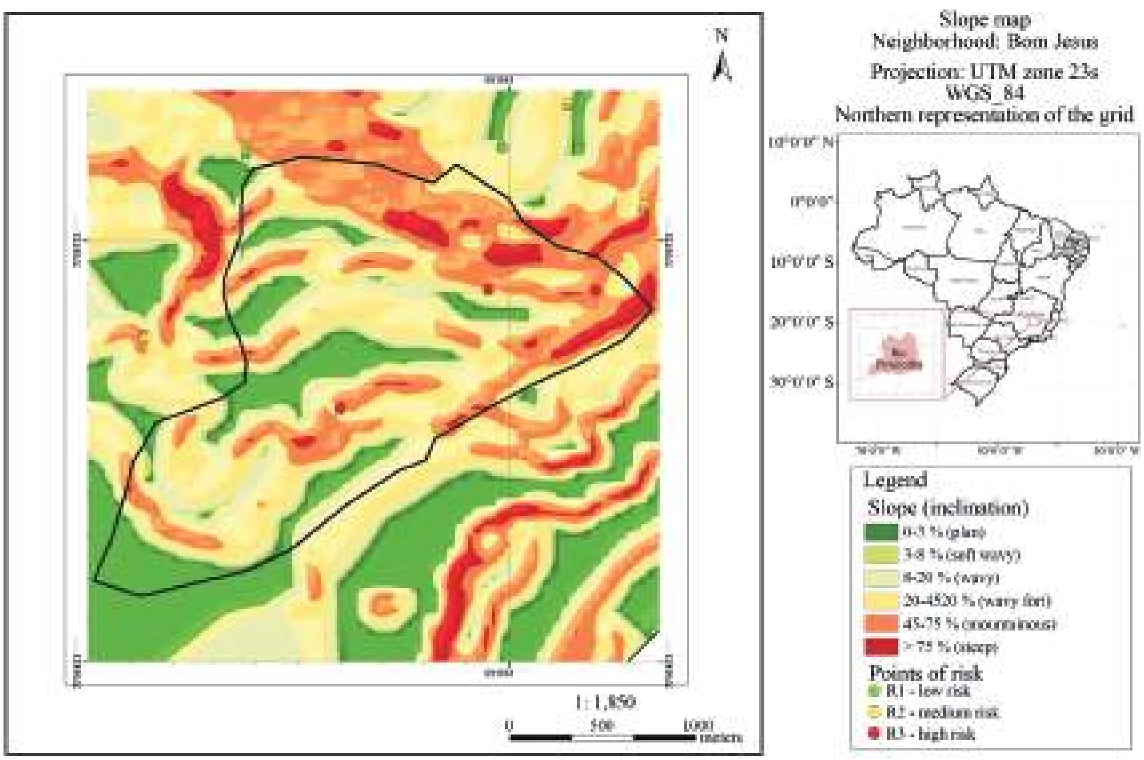

Figure 14 - Slope map (inclination) of Bom Jesus neighborhood, Rio Piracicaba, MG.

located at the foot of the hillside. Also, features such as apparent mass movements, inefficient retaining wall and absence of drainage increase the risk observed on these points.

These high-risk points must have a solution immediately, probably by a retaining wall. As can be seen in the declivity map (Fig. 14), this neighborhood is mostly located in an area of flat to highly undulating relief and presents a better constructive pattern. However, it should be monitored in order to avoid the emergence of risk-triggering agents.

3.4. Nossa Senhora da Conceição neighborhood

The neighborhood of Nossa Senhora da Conceição (Fig. 15) was the neighborhood that appeared to have better conditions of urban planning, despite the insufficiency of existing drainage systems. Only one medium-risk and one low-risk point were identified as presenting predisposing geological-geotechnical conditions. Erosive processes at an early stage of development were observed, as well as old mass-movement scars on a slope > 45 % with poor natural drainage, classified as high potential risk. In the municipality's master plan, these two listed sites are located in an environmental protection zone, which restricts their urban occupation and use, in order to protect and maintain its natural aspect.

According to the declivity map (Fig. 16), the dwellings are mostly located in areas of flat to highly undulating relief.

4. Conclusion

Mass movement risk assessment is an indispensable tool for the planning and monitoring of the urban environment and should be incorporated into the instruments of all Brazilian municipalities with the aim of minimizing the disasters caused by this type of event.

After the diagnosis made in the area of study in Rio Piracicaba, MG, it was possible to perceive the inefficiency of legislation and public policies related to the control of land use and occupation within the study area, mainly in the zones of social interest, such as Córrego São Miguel neighborhood.

After classification and integration of the results, it was observed that the points and areas classified as high risk are directly related to anthropic areas on slopes greater than 30 %, combined with the presence of dwellings of low constructive standard, with no engineering design, in which population lives in precarious conditions. Furthermore, there is insufficient rainfall drainage system and the disposal of sanitary sewage is absent and/or insufficient. All these aspects, together, intensify the process of soil saturation. In addition, there is a natural predisposition for geoenvironmental problems, such as a rugged topography and the presence of variable lithological units, earthy and rocky substrates of low strength, which are subject to frequent instability processes, by the natural action of gravity and the weather, mainly in periods of rainfall concentration. In this context, in which the risk scenario is imminent in relation to

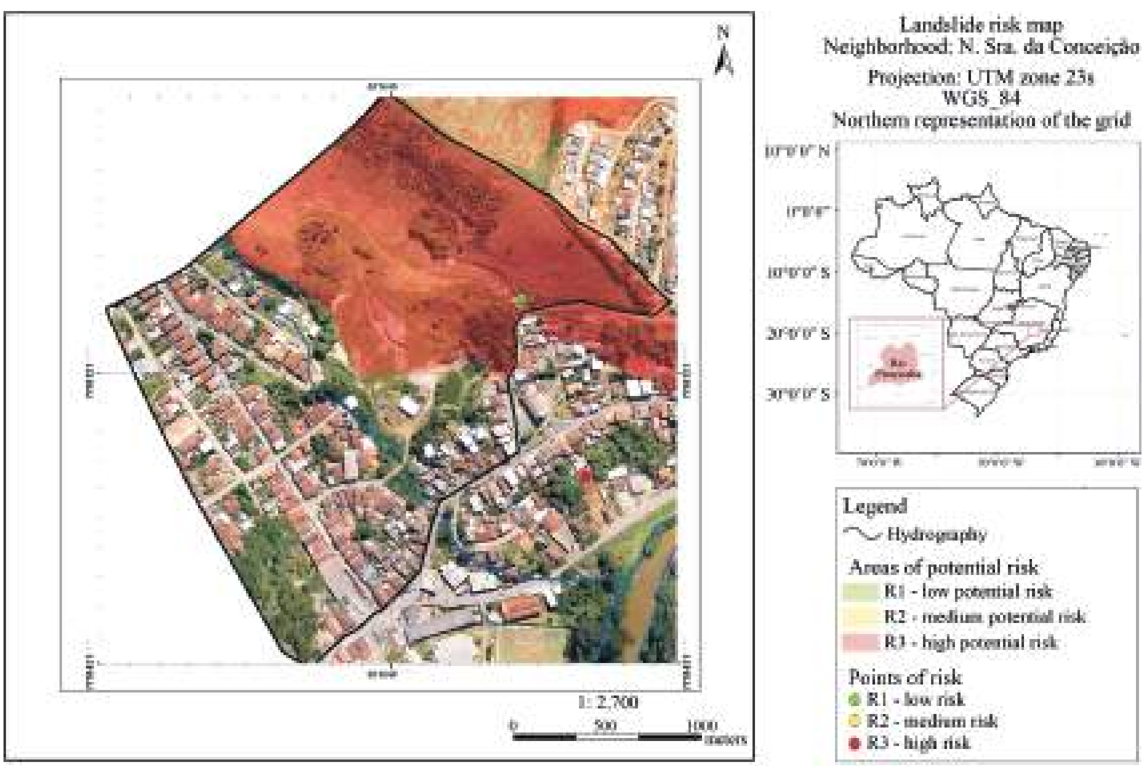

Figure 15 - Landslide risk map, Nossa Senhora da Conceição neighborhood, Rio Piracicaba, MG.

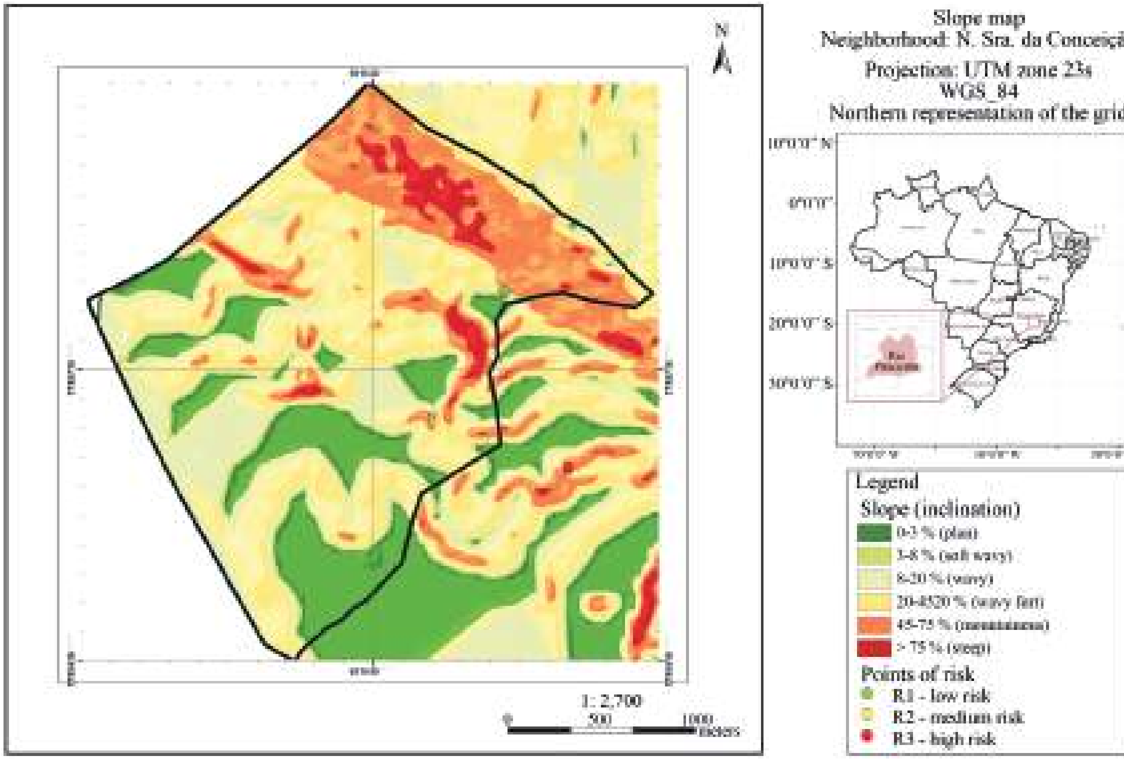

Figure 16 - Slope map (inclination) Nossa Senhora da Conceição neighborhood, Rio Piracicaba, MG.

the integration of the natural environment and the built environment, immediate interventions must be made by the Civil Defense, starting by withdrawing and relocating those dwellers in the most precarious situations, carrying out stabilization works, and promoting sustainable actions and educational activities to raise awareness within the population about the risks they are exposed to, so as to increase awareness and discipline to prevent future accidents.

The procedures used in this work through the application of the methodology of the Ministry of Cities have shown that, despite being considered a subjective evaluation by several authors, it is a low-cost process, effective as a preliminary identification of the main predisposing geological-geotechnical destabilization mechanisms. However, it is important to emphasize the importance of having professionals with experience and technical capacity to perform interpretations in the field, in order to coherently rank the risk level. It is worth stressing the need for these mappings to be updated annually, with the purpose of verifying the evolution of the risk frameworks in the municipality.

The use of the post-processing orthorectified image obtained from the survey of the Unmanned Aerial Vehicle-UAV, allowed the preparation of current maps with visual quality in detail scales, which ranged from 1:7.000 to 1:800, contributing to the integration of the data in the GIS environment. It can, therefore, be considered an excellent resource for obtaining, classifying, vectoring and plotting the specific areas of interest, besides being a suitable and agile support for geological-geotechnical mapping works. Thus, it may be of help for other projects involving environmental planning of the municipality.

Acknowledgments

To Brazil's CAPES Agency for the financial support, and to Civil Engineering Department of the Federal University of Viçosa and the Federal Rural University of Rio de Janeiro for technical support.

References

Akgun, A. (2012). A comparison of landslide susceptibility maps produced by logistic regression, multicriteria decision, and likelihood ratio methods: a case study at Izmir. Turk Landslides 9(1):93-106.

Araújo, P.C. de. (2004). Susceptibility Analysis to Landslides: A Probabilistic Approach. Doctoral Thesis in Geociências e Meio Ambiente, Instituto de Geociências e Exatas, UNESP, Rio Claro, 172 p (in Portuguese).

Bigarella, J.J. & Passos, E. (2003). Structure and Origin of Tropical and Subtropical Landscapes, v. 3. Editora da UFSC, Florianópolis (in Portuguese).

Brasil (2001). Law 10.257 (July 10th, 2001). Establishes general guidelines for urban policy and define other actions. Congresso Nacional, Brasília (in Portuguese).

Brazil (2001). City Statute Guide for Implementation by Municipalities and Citizens. Congresso Nacional, Brasilia, 273 p. (in Portuguese).

Brazil (2007). Ministry of Cities. Risk Mapping on Slopes and River Banks. Carvalho, S.C.; Macedo, S.E. & Ogura, T.A. (orgs). Instituto de Pesquisas Tecnológicas, Brasilia, Available in: http://www.cidades.gov.br/ (in Portuguese).

Brasi (2012). l. Law 12.608 (April 10th, 2012). Establishes the National Protection and Civil Defense System - SINPDEC and the National Council of Protection and Civil Defense – CONPDEC. Diário Oficial da República Federativa do Brasil, Brasília (in Portuguese).

CETEC (1983). Technological Center Foundation of Minas Gerais. Environmental Diagnosis of the State of Minas Gerais, Belo Horizonte, 148 p (in Portuguese).

CPRM (2010). Brazilian Pluviometric Atlas. CPRM - Mineral Resources Research Company Available in: http://www.cprm.gov.br (in Portuguese).

CPRM (2014). Emergency Action for Delimitation of Areas at High and Very High Risk to Floods and Mass Movements Rio Piracicaba - Minas Gerais. Rio Piracicaba, Minas Gerais, Brazil. CPRM - Mineral Resources Research Company. Available in: http://www.cprm.gov.br/publique/Gestao-Territorial/Geologia-de- Engenharia-e-Riscos-Geológicos/Setorização-de-Riscos-Geológicos 4138.html#minasgerais (in Portuguese).

Diniz, N.C. (2012). Cartografia geotécnica por classificação de unidades de terreno e avaliação de suscetibilidade e aptidão. Revista Brasileira de Geologia de Engenharia e Ambiental, 2(2):29-78.

EMBRAPA. (1979). National Land Survey and Conservation Service. EMBRAPA - Brazilian Agricultural Research Agency In: 10th Technical Land Survey Meeting, Rio de Janeiro. Proc. Rio de Janeiro, 83 p (in Portuguese).

IBGE. (2010). 2010 Census. IBGE - Brazilian Institute of Geography and Statistics. Available in: http://www.ibge.gov.br/home/estatistica/população/censo2010/default.shtm (in Portuguese).

IPT. (2015). Bitar, O.Y. (org.) Geotechnical Charts Guide: Basic Guidelines for Municipalities. Instituto de Pesquisa tecnológica do Estado de São Paulo. Available in: www.ipt.br/guia_cartas_geotecnicas.pdf (in Portuguese).

Marchiori-Faria, D.G.; Ferreira, C.J.; Rossini-Penteado, D.; Fernandes-da-Silva, P.C. & Cripps, J.C. (2005). Mapping of landslide and flood risk areas in housing areas of Diadema, SP. In: Annals XI Brazilian Congress of Engineering Geology, 2005, Florianópolis. ABGE, Florianópolis, CD-ROM (in Portuguese).

Marques, J.A.P.; Souza, J.H. & Maragon, M.A. (2011). Interference of landslides in traffic interruption in urban public roads in the city of Juiz de Fora - MG. In: 17th Urban Paving Meeting. Porto Alegre, RS. Anais. ABPV, Rio de Janeiro CD-ROM (in Portuguese).

Roque, L.A. (2013) Geological-Geotechnical Risk Areas Associated with Mass Movements in the Urban Core of Viçosa-MG. Master's Thesis em Engenharia Civil, Universidade Federal de Viçosa, Viçosa, 110 p (in Portuguese).

Saito, S.M.; Soriano, E. & Londe, L.R. (2015). Natural Disasters/Remote Sensing for Disasters. Oficina de Texto, São Paulo, 285 p (in Portuguese).

Shahabi, H. & Hashim, M. (2015). Landslide susceptibility mapping using GIS-based statistical models and Remote sensing data in tropical environment. Sci Rep 5:9899. doi:10.1038/srep09899.

Santiago & Cintra available in: https://www.santiagoecintra.com.br/.

Souza, L.A. (2015). Geoenvironmental Cartography and Progressive Geotechnical Cartography at Different Scales: Application in the Ribeirão do Carmo Watershed, Municipalities of Ouro Preto and Mariana, Minas Gerais. Doctoral Thesis, Escola de Minas, Universidade Federal de Ouro Preto, Ouro Preto, 456 p (in Portuguese).

Tominaga, L.K. (2007). The Evaluation of Different Methods Employed in Landslide Risk Analysis: The Application of a Methodological Proposal in Ubatuba, SP. Doctoral Thesis in Sciences, Physical Geography, Faculdade de Filosofia, Letras e Ciências Humanas, da Universidade de São Paulo, São Paulo, 240 p (in Portuguese).

UNISDR (2004). Living whit Risk. A Global Review of Disaster Reduction Initiatives. UNISDR United Nations International Strategy for Disaster Reduction. United Nations ISDR, Geneva, Switzerland.

UNISDR (2009). Terminology on Disaster Risk Reduction. UNISDR - United Nations International Strategy for Disaster Reduction. United Nations Strategy for Disaster Reduction, Geneva, Switzerland.

Vieira, V. (2000). Preliminary Characterization of the Geological Risk of the Urban Area of Viçosa - MG. Master's Thesis em Engenharia Civil, Universidade Federal de Viçosa. Viçosa, Minas Gerais, 92 p (in Portuguese).

Wolle, C.M. (1988). Analysis of Translational Landslides in the Serra do Mar in the Context of a Classification of Mechanisms of Slope Instability. Doctoral Thesis em Engenharia, Escola Politécnica, Universidade de São Paulo. São Paulo, 394 p (in Portuguese).

Landslide Susceptibility Mapping of Highway Slopes, Using Stability Analyses and GIS Methods

A.M.L. Craig, O. Augusto Filho

Abstract. The study presented in this paper aims to map landslide susceptibility on highway slopes and adjacent areas, using an approach based on stability analysis with deterministic methods considering semi-regional and detail work scales. The infinite slope method in a Geographic Information System (GIS) environment and a 1:10,000 scale topographic base (elevation intervals of 5 m) were used in the stability analysis at the semi-regional scale. Geological-geotechnical sections surveyed in the field with measuring tape and inclinometer (1:100 scale with 0.5 m vertical slope intervals) and the Bishop Simplified method were used in the detail scale. The geological-geotechnical materials present in the studied area are residual soils (sandstones, basalt and diabase), alluvial deposits and landfills. The slopes and marginal areas of the highway more susceptible to landslides were mapped based on quantitative models of analysis, reducing the subjectivity of the mapping. Limitations of the infinite slope method related to its physical-mathematical model were identified and analyzed. The approach used was efficient even considering the limitations of the infinite slope analysis method and the representativeness of the geomechanical parameters used in the stability analyses.

Keywords: Bishop Simplified, geological-geotechnical sections, infinite slope, residual soils, safety factor, slope susceptibility.

1. Introduction

During the execution of linear works a diversity of geological-geotechnical materials can be exposed, such as rock units and associated soils, as well as surface and underground water dynamics, which in turn, respond in different manners to the demands imposed by the system. In the case of highways, there are problems associated with the stability of the slopes and embankments.

Several studies have addressed this theme given its social, economic and environmental importance in highway management. Data from the Brazilian National Department of Transport Infrastructure shows that, only in 2011, about R$ 150 million were invested on the recovery of federal highways affected by landslides and erosion processes (DNIT, 2014).

The most recent studies dealing with landslide susceptibility mapping have used the combination of deterministic stability analysis models, such as the infinite slope method, with hydrological models in a Geographic Information System (GIS) environment. Following this research line, stand out the models SHALSTAB - Shallow Slope Stability Model (Montgomery & Dietrich, 1994); dSLAM - Distributed Slope Stability Model (Wu & Sidle, 1995; Dhakal & Sidle, 2003); SINMAP -Stability Index Mapping (Pack *et al.*, 1998; Pack *et al.*, 2005) and TRIGRS -Transient Rainfall Infiltration and Grid-Based Regional Slope-Stability Model (Savage *et al.*, 2004; Baum *et al.*, 2002; Baum *et al.*, 2008).

Some examples of the application of SHALSTAB and TRIGRS models are the studies of Ramos *et al.* (2002), Vieira (2007), Park *et al.* (2013), Rosniecek & Imai (2013) and Gioia *et al.* (2014). Wu & Abdel-Latif (2000), Augusto Filho (2006) and Silveira *et al.* (2012) used the infinite slope method in the elaboration of landslide susceptibility maps.

In this context, this paper proposes a landslide susceptibility mapping of the highway slopes and adjacent areas using an approach based on stability analyses with deterministic methods and considering semi-regional and detail work scales.

The infinite slope method in a GIS environment and a 1: 10,000 scale topographic base (elevation intervals of 5 m) were used in the stability analyses at the semi-regional scale. The Bishop Simplified method (available in the Slope/W module of the GeoStudio software) and geological-geotechnical sections surveyed in the field (1:100 scale with 0.5 m vertical slope intervals) were used in the detail scale.

The use of two simultaneous scales of analysis can be considered one of the differentials of the current study when compared to previous studies of landslide susceptibility mapping based on quantitative models. Another relevant aspect regards the identification and discussion of the limitations of the infinite slope method related to its physical-mathematical model. This method tends to produce anomalous results with the increase of safety factor (*SF*) rather than its reduction for failure surfaces with slopes greater than 60° and depths less than 1 m.

Ayla Margie de Leão Craig, M.Sc., Belo Horizonte, MG, Brazil. e-mail: aylaleao@gmail.com.
Oswaldo Augusto Filho, Ph.D., Associate Professor, Departamento de Geotecnia, Universidade de São Paulo, São Carlos, SP, Brazil. e-mail: oafilho@sc.usp.br.
Submitted on March 26, 2019; Final Acceptance on January 29, 2020; Discussion open until August 31, 2020.
DOI: 10.28927/SR.431071

The infinite slope method, developed by Skempton & DeLory (1957), assumes that the depth of failure is much less than the total extent of the slope and that the balance between the resistive and sliding forces on a single slope slice is sufficient to represent the level of stability of the entire slope. This simplification makes the method quite malleable for its application in various situations and presents a good compatibility with computer programs, especially those involving GIS (Ahrendt, 2005). The calculation of the *SF* in the infinite slope method is performed through the Eq. 1 below as proposed by Massad (2003).

$$SF = \frac{\mathbf{c}' + (\gamma_{nat} \times z \cos^2 i - \mathbf{u}) \tan \Phi'}{\gamma_{nat} \times z \sin i \cos i} \quad (1)$$

in which *SF* = safety factor; **c**' = effective cohesion; γ_{nat} = natural unit weight; ϕ': effective friction angle; *z* = depth of failure plane; *i* = slope angle; **u** = pore water pressure.

Bishop's method of analysis is a modification of the Fellenius method taking into account the balance of moments (resistant and acting) and the balance of forces acting on each coverslip (Fiori & Carmignani, 2009; Gaioto, 1992). The Bishop Simplified method considers the balance of forces and moments, initially proposed by Bishop, neglecting the lateral forces between the slices. In other words, the Simplified Bishop Method admits a circular failure surface and considers that the forces on the sides of the slices are horizontal, disregarding the tangential forces between them. This simplification results in a 1 % error on the exact calculation (Abramson *et al.*, 2002).

As it can be seen in Eqs. 2, 3 and 4 below, in the Simplified Bishop method the safety factor is obtained by an interative process.

$$SF = \frac{\sum [b \times \mathbf{c}' + (\mathbf{W} - \mathbf{u} \times b) \tan \Phi'] \times \frac{1}{\mathbf{M}(\alpha)}}{\sum \mathbf{W} \sin \alpha} \quad (2)$$

$$b = l \cos \alpha \quad (3)$$

$$\mathbf{M}(\alpha) = \cos \alpha \left(1 + \frac{\tan \Phi' \tan \alpha}{SF} \right) \quad (4)$$

in which *SF* = safety factor; *b* = slice thickness; **W** = slice weight; **c**' and ϕ' = effective cohesion and friction angle at the base of the slice center; **u** = pore water pressure at the base of the slice center; l = length of slice base.

2. Study Area

The study area covers a range of 500 m width on both sides of Luís Augusto de Oliveira highway (SP-215), between kilometers 170 to 192.2 (geographic coordinates Córrego Alegre datum: 48°17'29.657" W, 22°6'57.617" S; 48°4'33.742" W, 22°3'19.25" S). According to DER (2015), in 2014 the Average Daily Volume (ADV) of traffic on this highway reached 3,259 vehicles per day.

The studied section of the SP-215 highway crosses the municipalities of São Carlos, Ribeirão Bonito and Dourado, located in the center-west of the state of São Paulo, Brazil. The 1: 10,000 digital cartographic base was assembled on seven A3 sheets for printing (Fig. 1).

These areas are geologically composed of aeolian and fluvial sandstones (Botucatu and Adamantina formations,

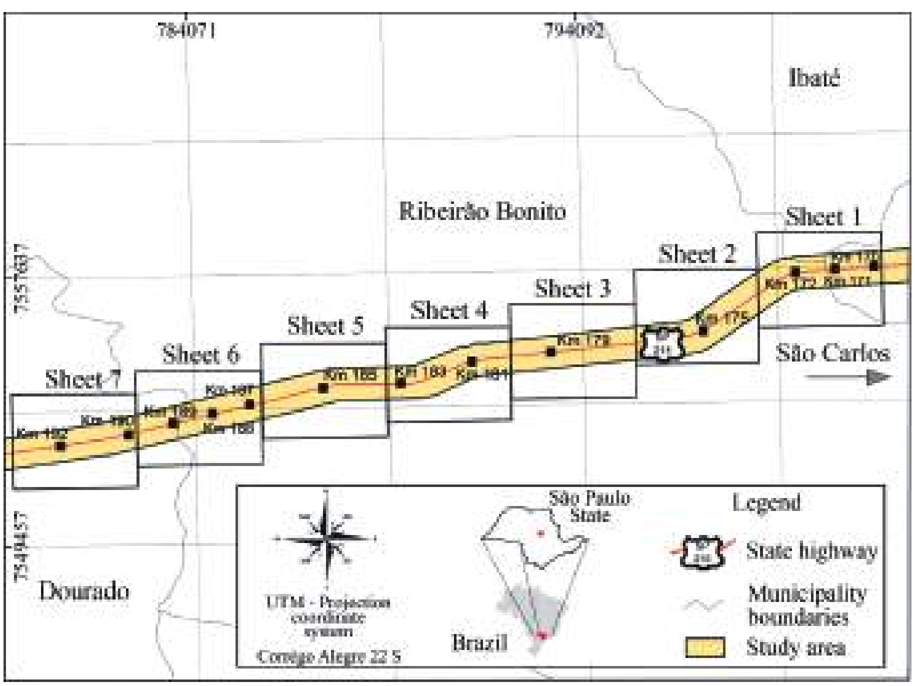

Figure 1 - Study area.

respectively), basalt and diabase rocks (Serra Geral Formation), and their respective residual soils, that together comprise the register of the Paraná Basin (Devonian-Cretaceous ages) in the State of São Paulo (IPT, 1981a). Subordinately, detrital slope deposits (colluvium) and alluvial deposits can occur in larger drainages. Geomorphologically the area mostly comprises hills, basaltic plateaus and escarpments (IPT, 1981b).

The rainy season runs from October to March, with the rainiest quarter from December to February. The driest period is from April to September, with the driest quarter between June and August.

Although the studied region does not present the same levels of natural susceptibility to the occurrence of landslides as the crystalline mountainous regions, these processes have occurred with a certain frequency, mainly in the highway cuts (Fig. 2).

3. Materials and Methods

The main materials and software used in the study were topographic maps at 1:10,000 scale, aerial images from Google Earth Pro and field survey equipment (geological hammer, measuring tape, inclinometer and compass), Arcmap (2010), Geoslope (2012) and Office (2010).

Initially, the subject of the research was defined, a bibliographic review was made and also the study area was chosen. Then, the research was developed according to the four major steps outlined below: Inventory; Landslide susceptibility mapping at 1:10,000 scale; Slope stability analyses at detail scale; and Synthesis.

3.1. Inventory

At this stage, the main geological and geotechnical information of interest for the study were collected and organized, and the digital cartographic base, the Digital Terrain Model (DTM) and the thematic maps necessary for the landslide susceptibility mapping of the surroundings and slopes of the highway at 1: 10,000 scale were produced. All maps produced in this step were elaborated using the GIS Arcmap/Arcgis spatial analysis tools.

The digital cartographic base at 1:10,000 scale included the topographical information (elevations contours every 5 m, elevation points, streams, highway cuts and landfills) and a mosaic of aerial images from Google Earth Pro. The thematic maps produced were: Shading, Hypsometric; Slope; and Geological Materials.

The DTM was produced with the top to raster command of the 3D Analyst Tools module. This tool performs a hydrologically correct interpolation of a surface starting from the input data related to the elevation contours, elevation points, streams, and boundaries of the digital cartographic base. A cell size of 2.5 m was defined as the

Figure 2 - Highway cut with shallow landslide in sandstone residual soil (Botucatu Formation).

interpolation grid, which is 50 % lower than the maximum permissible cartographic error at 1:10,000 scale (0.5 mm or 5 m).

The filter and the fill tools were applied to obtain the final hydrologically correct interpolated raster surface. The final DTM was qualitatively evaluated to ensure that it provided a realistic representation of the topographic surface. The qualitative evaluation created contours from the new surface with Contour tool and compared them to the input contour data.

These procedures are important because the accuracy of the shading, hypsometric and slope maps and of the landslide susceptibility mapping at 1:10,000 scale is largely associated with the quality of the DTM.

The map of geological materials was produced based on preexisting mappings and field surveys along the studied section of the highway.

3.2. Landslide susceptibility mapping at scale 1:10,000

The whole set of information obtained in the inventory stage allowed the accomplishment of a preliminary geological-geotechnical characterization of the study area and to carry out the landslide susceptibility mapping at 1:10,000 scale using the infinite slope method. This approach enabled the definition of landslide susceptibility by calculating the safety factor (*SF*) in all the cells of the terrain according to the characteristics of each one.

The safety factors (*SF*) were calculated using the infinite slope method (Eq. 1) and applying the raster calculator tool of the GIS considering a 2.5 m grid (same as the DTM). The operation was done using matrices with the data of the soil geomechanical parameters, slope, groundwater conditions and the depth of the failure surface (Fig. 3).

Three main scenarios were simulated taking into account the groundwater conditions and the failure plane. The objective of these simulations was to obtain the best fit between the model of landslide susceptibility mapping and the data collected in the field surveys.

Additional simulations were performed aiming to understand some anomalous results obtained related to limitations of the infinite slope stability analysis method not mentioned in previous studies. The conditions of *SF vs. slope angle* and failure surface depth, effective cohesion, friction angle and water level above the failure surface were simulated, taking as an example the geomechanical parameters of Botucatu Formation.

Due to limitations, infinite slope and the topography detail for 1:10,000 scale used for landslide susceptibility mapping, a modeling for the highway cuts and landfills was necessary to be performed separately.

In order to observe the most critical situation of analysis, the minimum values of cohesion and friction angle and maximum values of unit weight were adopted based on data found in the literature. The *SF* values obtained for each

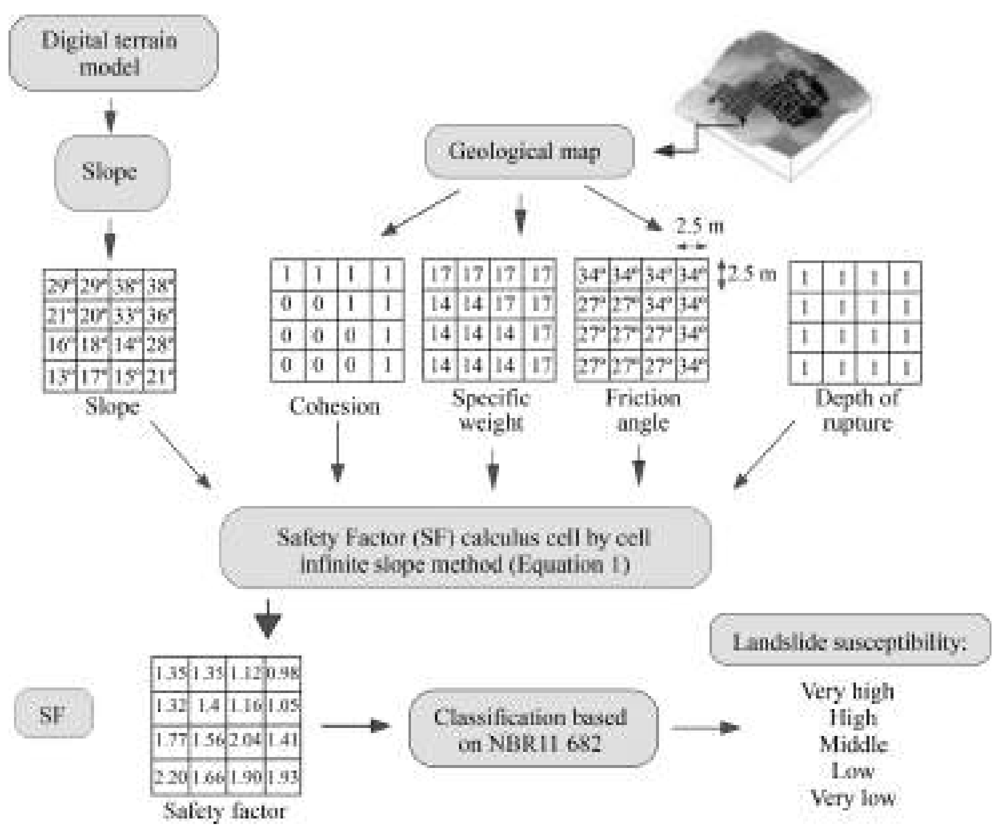

Figure 3 - Flow chart for landslide susceptibility mapping in GIS environment.

scenario simulated were classified into five classes of susceptibility considering the minimum safety increases of 15, 30, and 50 % for the low, medium, and high degrees of safety according NBR 11682 (ABNT, 2006) for mathematical models based on limit equilibrium (Table 1).

3.3. Slope stability analysis at detail scale

The detailed geological-geotechnical sections surveyed in the field were used for the slope stability analysis in this step. The stability analysis used the Bishop Simplified method (Eq. 2) and the SLOPE/W module of the GeoStudio software. The Bishop Simplified method was chosen because it provides intermediate results between the more and less conservative equilibrium methods of slope stability analysis (Krahn, 2004). The grid and radius method was used to research the critical failure surface. Four sections were selected to represent the most critical sectors and the main geological-geotechnical materials present in the highway slopes.

The geomechanical parameters used in these stability analyses were obtained from bibliography adjusted by the back analysis of landslides that occurred in the highway cuts sustained by residual soils of the three main geological formations present in the study area (Botucatu, Serra Geral and Adamantina Formations).

3.4. Synthesis

The results obtained in the previous steps were aggregated and analyzed resulting in the final map of landslide susceptibility in the slopes of the studied highway.

4. Results and Analyses

4.1. Thematic maps and characterization of the study area

The hypsometric map was sliced into six elevation intervals and the percentage areas of each class were calculated. The study area presents elevations ranging from 553 to 762 m. The elevations tend to increase from northeast to southwest. About 90 % and 100 % of the study area presented elevations between 550 and 650 m and 650 and 750 m on sheets 1 and 7, respectively. The elevations above 750 m occur only on sheets 4 and 5, comprising 3.6 and 6.2 % of their total areas respectively (Table 2).

The slope map was produced at continuous intervals of degrees and was subsequently reclassified into five classes expressed as percentages and related to erosion and landslide susceptibility (Table 3). Table 4 presents the percentage areas of each of these five slope classes in the study area.

The slope values varied from 0.1 to 180 % (0.006 to 60.9°), but there is a high predominance of slopes lower than 12 % throughout the study area (about 70 % of the total area in each of the seven sheets of the study area). Only the sheets 1, 4 and 5 present almost 11 % of their total area with slope between 20 % and 50 % (very high susceptibility to erosion and medium susceptibility to landslides) and only sheet 5 presents almost 5 % of its total area with slope over 50 % (very high susceptibility to erosion and high susceptibility to landslides, Tables 3 and 4).

Regarding the distribution of the geological formations in the study area (see Section 2), the presence of the

Table1 - Classes of safety factors (*SF*).

SF	Failure condition represented	Susceptibility
≤ 1	Failure	Very high
1.01 to 1.3	1 % to 30 % over the failure condition	High
1.31 to 1.5	31 % to 50 % over the failure condition	Middle
1.51 to 2	51 % to 100 % over the failure condition	Low
> 2	100 % over the failure condition	Very low

Table 2 - Percentage areas of hypsometric classes (source: hypsometric map).

Hypsometric classes (m)	Sheet 1	Sheet 2	Sheet 3	Sheet 4	Sheet 5	Sheet 6	Sheet 7
534-550	8.7	0	0	0	0	0	0
550-600	43.4	7.5	5.5	3.8	0	0	0
600-650	44.9	53.3	41.2	45.1	6.2	1.9	0
650-700	3	39.2	53.2	25.9	22.2	15.8	21.8
700-750	0	0	0	21.6	65.4	82.3	78.2
750-762	0	0	0	3.6	6.2	0	0

Table 3 - Slope classes (%) and erosion and landslide susceptibility.

Slope classes		Erosion and landslide susceptibility
(%)	(°)	
0-6	0-3.4	Low to erosion and very low to landslides
6-12	3.4-6.8	Medium to erosion and very low to landslides
12-20	6.8-11.3	High to erosion and low to landslides
20-50	11.3-26.6	Very high to erosion and medium to landslides
> 50	> 26.6	Very high to erosion and high to landslides

Adamantina Formation is noticed in a large percentage on sheets 5, 6 and 7, and the presence of the Botucatu Formation in high percentages on sheets 2 and 3 (Table 5).

Considering the distribution of slopes by the different geological formations present in the study area, only the Serra Geral/Basic Intrusive formation has almost 15 % and 4 % of its total area with slopes between 20 to 50 % and above 50 % respectively (Table 6).

The field surveys registered 33 control points. These control points were characterized considering their geological-geotechnical material (rocks, residual and transported soils, landfill), features of slope instability (landslide scars and erosive processes, cracks, springs) and the presence of drainage systems and other slope containment structures.

Only a few highway cuts that expose basalts and diabase of the Serra Geral Formation presented low weathered rock expositions, which have the potential to trigger rock falls and boulder rolling processes. Shallow landslides scars were identified on the highway slopes with residual soils of all geological formations present in the study area. Typically, these scars affect the total height of the highway cuts, presenting few meters width (2 to 5 m) and depths less than 2 m (Fig. 2). Features of slope instability were not identified on the highway landfills.

4.2. Landslides susceptibility mapping applying infinite slope model

The following three main scenarios were simulated based on the results of the thematic maps and geological-geotechnical characterization of the study area: 1 - Unsatured condition and failure surface 1 m deep; 2 - Unsatured condition and failure surface 2 m deep and 3 - Water level 0.5 m above the failure surface 1 m deep.

The map of geological and geotechnical units guided the bibliographic search for the geomechanical parameters of the formations found in the region. Similar geomechanical parameters were used for the residual soils of the diabase and basalt (Serra Geral Formation). The minimum values for each formation of Table 7 were considered for the simulations.

During the initial simulations for the calculation of *SF* using the infinite slope method and considering the boundary conditions described above, for slopes greater than about 60°, the *FS* values began to increase rather than decrease with increasing of slope value. Specific simulations were performed to understand these anomalous results related to limitations of the infinite slope stability analysis method not mentioned in previous studies.

Table 4 - Percentage areas of slope classes by (source: slope map).

Slope classes		Sheet 1	Sheet 2	Sheet 3	Sheet 4	Sheet 5	Sheet 6	Sheet 7
(%)	(°)							
0.1-6	0-3.4	15.4	27.1	67.0	24.9	41.5	41.3	51.3
6-12	3.4-6.8	51.5	49.5	25.9	44.8	31.9	41.7	38.0
12-20	6.8-11.3	20.5	20.1	6.0	15.6	10.7	11.4	8.6
20-50	11.3-26.6	11.8	3.4	1.0	11.7	11.1	4.5	2.1
50-180	26.6-60.9	0.7	0	0	3.0	4.8	1.2	0.1

Table 5 - Percentage areas of geological formations (source: geological units map).

Geological material	Sheet 1	Sheet 2	Sheet 3	Sheet 4	Sheet 5	Sheet 6	Sheet 7
Alluvial Deposit	3.4	1.8	0	0	0	0	0
Adamantina Fm.	0	0	0	11.4	46.3	72.8	96.1
Basic Intrusive	71.0	45.5	0	0	0	0	0
Serra Geral Fm.	0	0	0	55.3	52.4	27.2	3.9
Botucatu Fm.	25.6	52.7	100	33.3	1.4	0	0

Table 6 - Percentage areas of slope classes by geological formations (source: slope and geological units maps).

Slope classes		Geological formations			
(%)	(°)	Botucatu	Serra Geral/Basic Intrusive	Adamantina	Alluvial Deposit
0.1-6	0-3.4	51.0	15.9	50.3	66.3
6-12	3.4-6.8	38.6	44.2	39.0	25.8
12-20	6.8-11.3	8.5	21.6	8.9	6.1
20-50	11.3-26.6	1.8	14.6	1.7	1.9
50-180	26.6-60.9	0	3.7	0.1	0

Table 7 - Geological and geotechnical materials and geomechanical parameters.

Materials		**c**' (kPa)*	Φ' (°)*	γnat (kN/m^3)	References
Landfill		0	33.8	17.5	Magnani (2006)
Alluvial deposit		5	30	13.7	
Residual soils	Botucatu Fm.	2	28	15.32	Augusto Filho & Fernandes (2018)
		8	32	15.32	
		5	30	15.32	
	Serra Geral Fm.	13	31.5	14.9	Pinto *et al.* (1993)
		35	20	17.9	
		19	29	16.4	
	Adamantina Fm.	20	38.1	18.25	Queiroz (1986)

(*) In terms of effective stress.

These simulations considered the variation of the geomechanical parameters, the slopes, the failure surface depth and the saturation conditions. Tables 8 and 9 exemplify the results of these simulations for the residual soils of Botucatu Formation for unsaturated and saturated conditions respectively.

The results of Table 8 show that the shallower the failure surface and the greater the cohesion value of the soil, the smaller the maximum slope value that the infinite slope method will present coherent results (*FS* decreasing with increasing slope). The friction angle and water level height seem not to influence the slope value from which the *SF* inversion occurs (Table 9).

By differentiating the infinite slope equation with respect to the slope angle, we can find the slope from which *SF* inversion occurs for given values of cohesion, friction angle and failure surface depth of rupture. Equation 5 shows this process for the given parameters of Botucatu Formation **c**' = 8 kpa, γ_{nat} (kN/m^3) = 15,32 kN/m^3, Φ' = 32°, as Fig. 4 plots the equation. Table 10 shows the results of these analyses for each of the 3 main geological formations.

$$
\begin{aligned}
SF' = & -0.018227981744066105\mathrm{Csc}[°x]^2 \\
& +0.018227981744066105\mathrm{Sec}[°x]^2 \\
& -°\mathrm{Cs}[°x]^2 \ \tan[32°]
\end{aligned}
\qquad (5)
$$

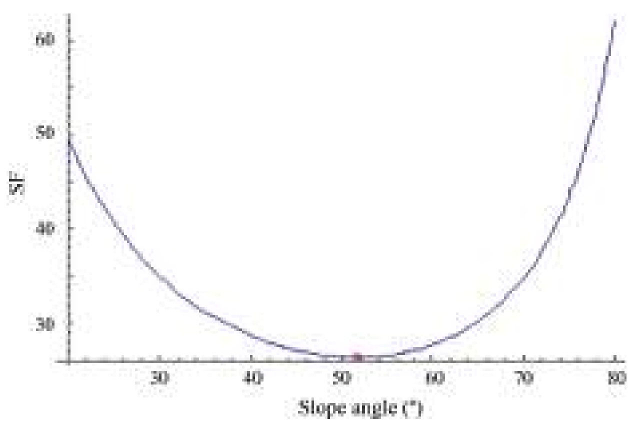

Figure 4 - Plot of Eq. 5.

After identifying the limitations of the infinite slope stability analysis method described above, the simulations were carried out to prepare the mapping of landslide susceptibility in the 1: 10,000 scale. Tables 11, 12 and 13 show the percentage areas of susceptibility classes in the study area considering the scenarios 1, 2 and 3.

The three simulated scenarios confirm that the section of the highway studied is located in sites with predominantly low susceptibility to landslides, as indicated by the data collected in the inventory step.

Table 8 - *SF vs.* slope, depth of failure and effective cohesion (residual soils of Botucatu Fm.). Lines 3, 9 and 14 show the slopes from which inversion of Safety Factor (*SF*) occurs.

ID	*SF*	Slope (°)	Depth of failure surface (m)*	*SF*	Slope (°)	**c'** (kPa)*
1	3.49	30	0.5	3.49	30	8
2	2.65	50		2.65	50	
3	2.77	60		2.77	60	
4	3.48	70		3.48	70	
5	6.22	80		6.22	80	
6	2.29	30	1	2.29	30	4
7	1.58	50		1.58	50	
8	1.57	60		1.57	60	
9	1.85	70		1.85	70	
10	3.16	80		3.16	80	
11	1.69	30	2	1.69	30	2
12	1.05	50		1.05	50	
13	0.96	60		0.96	60	
14	1.04	70		1.04	70	
15	1.64	80		1.64	80	

(*) θ' = 32° was adopted for these simulations.

Table 9 - *SF vs.* slope, friction angle and water level (residual soils of Botucatu Fm.). Lines 3, 8 and 13 show the slopes from which inversion of Safety Factor (*SF*) occurs.

ID	*SF*	Slope (°)	Friction angle (°)	*SF*	Slope (°)	Water level (m)
1	3.49	30	32	1.84	30	0.5
2	2.65	50		1.31	50	
3	2.77	60		1.32	60	
4	3.48	70		1.60	70	
5	6.22	80		2.78	80	
6	3.22	30	25	1.65	30	0.75
7	2.51	50		1.20	50	
8	2.68	60		1.22	60	
9	3.42	70		1.49	70	
10	6.19	80		2.62	80	
11	2.72	30	10	1.48	30	1
12	2.27	50		1.09	50	
13	2.51	60		1.13	60	
14	3.31	70		1.40	70	
15	6.14	80		2.47	80	

(*) Cohesion = 8 KPa and depth of failure surface = 0.5 m were adopted for these simulations.

Table 10 - Results of the analyses of the derivative of the infinite slope equation.

Residual soil	Angle for safety factor inversion (°)	Friction angle (°)	Cohesion (kPa)	Depth of failure surface (m)
Botucatu	51.65	32	8	0.5
Serra Geral/Basic Intrusive	50.77	20	13	1
Adamantina	52.63	38.1	20	1

The simulation of scenario 2 produced the highest percentage areas of medium and high susceptibility, concentrated in sheets 4 and 5, where also the highest slopes occur. Figure 5 illustrates the cartographic result for sheet 5. The increase of the failure surface depth (scenario 2) causes a significant decrease in the *SF* values but this decrease is not so significant when the water level increases (scenario 3).

Almost 100 % of the total area of Adamantina Formation, which occurs mainly in sheets 6 and 7 of the study area, presented very low susceptibility to landslides for the three scenarios simulated (Tables 14 to 16). These results indicate that the geomechanical parameters adopted for this formation are probably slightly above the actual values. A small landslide in the highway cut was identified in this formation in the field surveys.

Considering the data collected in the inventory step and especially in the field surveys, the landslides in the studied area should occur mainly in unsaturated conditions and be shallow (depths of 1 to 2 m), according to the boundary conditions simulated in scenarios 1 and 2.

4.3. Detail analysis of critical slopes

Stability analysis of the geological-geotechnical sections surveyed in the field were performed using the Bishop Simplified method and the software GeoStudio® (Slope/W) in order to detail the 1:10,000 mapping, especially the highway cuts and landfills. All these stability analyses considered the unsaturated condition (without water level).

Four sections were selected to represent the most critical sectors and the main geological-geotechnical materials present in the highway slopes, being three in cuts exposing residual soils (Botucatu, Serra Geral and Adamantina formations) and one in landfill.

All sections selected in the highway cuts present landslide scars, which made possible the accomplishment of a back analysis, that was executed in the Adamantina and Serra Geral Formations (Tables 17, 18 and Fig. 6). These formations were chosen in order to obtain most coherent geomechanical parameters, since the data used in the scenarios of semi-regional landslide susceptibility map were considered high.

Table 11 - Percentage areas of the susceptibility classes for scenario 1

Susceptibility classes	*SF*	Sheet 1	Sheet 2	Sheet 3	Sheet 4	Sheet 5	Sheet 6	Sheet 7
Very high	< 1.0	0	0	0	0	0	0	0
High	1.0 to 1.3	0	0	0	0	0	0	0
Medium	1.3 to 1.5	0	0	0	0	0	0	0
Low	1.5 to 2.0	0.1	0.2	0.1	0.2	0.6	0.2	0
Very low	> 2.0	99.9	99.8	99.9	99.8	99.4	99.8	100

Table 12 - Percentage areas of the susceptibility classes for scenario 2.

Susceptibility classes	*SF*	Sheet 1	Sheet 2	Sheet 3	Sheet 4	Sheet 5	Sheet 6	Sheet 7
Very high	< 1.0	0	0	0	0	0	0	0
High	1.0 a 1.3	0.16	0.02	0.001	0.28	1.08	0.33	0
Medium	1.3 a 1.5	0.29	0.05	0.012	1.56	2.02	0.50	0.005
Low	1.5 a 2.0	1.51	0.25	0.17	4.09	5.00	1.01	0.05
Very low	> 2.0	98.05	99.7	99.8	94.08	91.9	98.2	99.9

Table 13 - Percentage areas of the susceptibility classes for scenario 3.

Susceptibility classes	*SF*	Sheet 1	Sheet 2	Sheet 3	Sheet 4	Sheet 5	Sheet 6	Sheet 7
Very high	< 1.0	0	0	0	0.005	0	0	0
High	1.0 to 1.3	0.005	0.08	0.02	0.05	0.01	0	0
Medium	1.3 to 1.5	0.02	0.11	0.07	0.04	0.01	0	0
Low	1.5 to 2.0	0.33	0.53	0.3	0.7	1.66	0.5	0
Very low	> 2.0	99.6	99.3	99.6	99.2	98.3	99.5	100

Tables 17 and 18 show the cohesion/friction angle pair chosen in each back analysis. As might be expected, various combinations of cohesion and friction angle have FS close to 1.0. The Adamantina Formation residual soils,

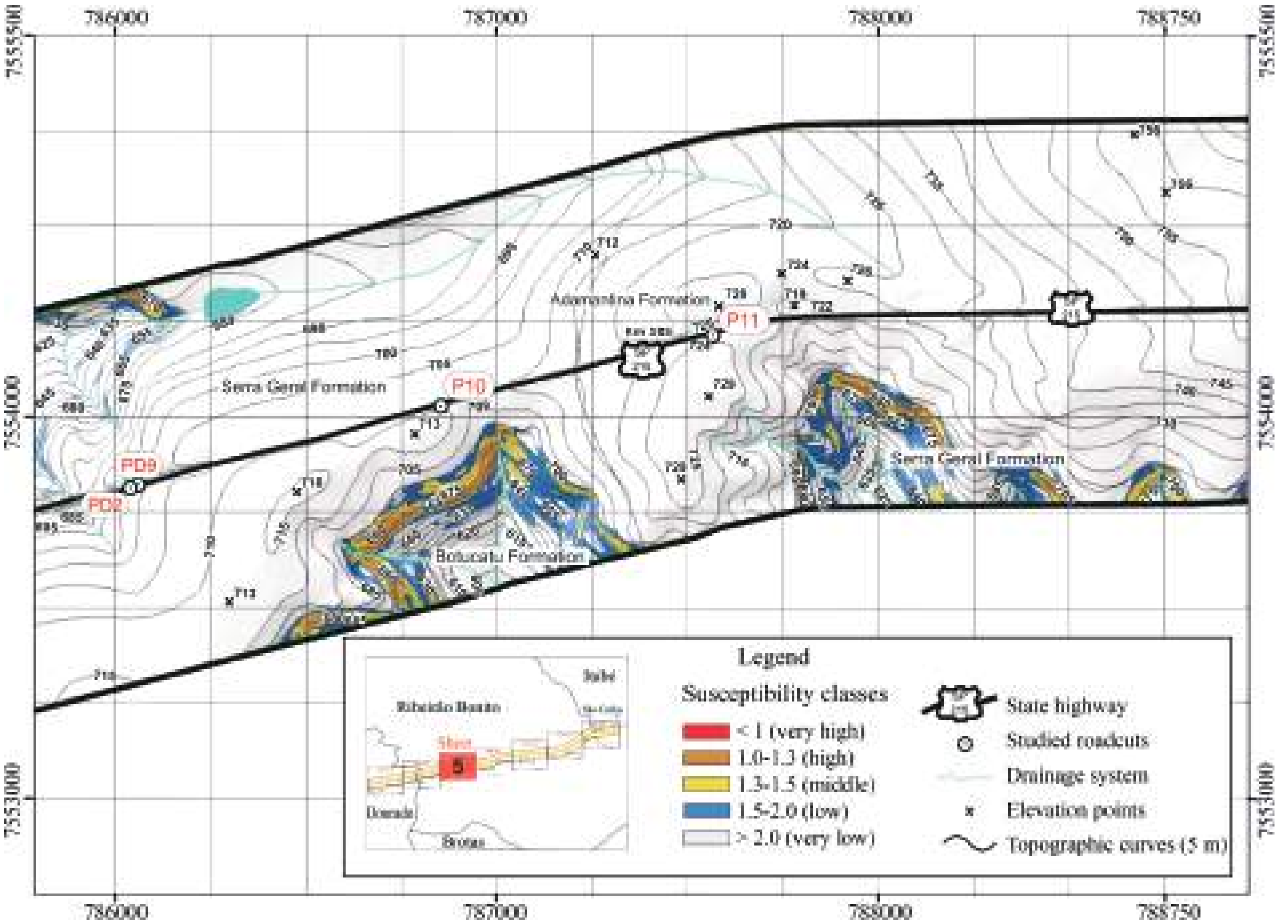

Figure 5 - Susceptibility mapping of sheet 5 considering scenario 2.

Table 14 - Percentage areas of geological materials per susceptibility classes of scenario 1.

Susceptibility classes	*SF*	Botucatu	Serra Geral/Basic Intrusive	Alluvial deposit	Adamantina
Very high	< 1.0	0	0	0	0
High	1.0 to 1.3	0.001	0	0	0
Medium	1.3 to 1.5	0.02	0	0	0
Low	1.5 to 2.0	0.18	0.38	0	0
Very low	> 2.0	99.8	99.6	100	100

Table 15 - Percentage areas of geological materials per susceptibility classes of scenario 2.

Susceptibility classes	*SF*	Botucatu	Serra Geral/Basic Intrusive	Alluvial deposit	Adamantina
Very high	< 1.0	0	0	0	0
High	1.0 to 1.3	0.02	0.70	0	0
Medium	1.3 to 1.5	0.05	1.66	0	0
Low	1.5 to 2.0	0.28	4.38	0.06	0.01
Very low	> 2.0	99.7	93.3	99.94	99.99

Table 16 - Percentage areas of geological materials per susceptibility classes of scenario 3.

Susceptibility classes	*SF*	Botucatu	Serra Geral/Basic Intrusive	Alluvial deposit	Adamantina
Very high	< 1.0	0.002	0	0	0
High	1.0 to 1.3	0.08	0	0	0
Medium	1.3 to 1.5	0.12	0	0	0
Low	1.5 to 2.0	0.59	1.05	0.1	0
Very low	> 2.0	99.2	98.95	99.9	100

although sandy, have significant percentages of fines (around 30 % at least) and Serra Geral Formation soils are clayey. Thus, it was used the pair with the highest cohesion and friction value that back analysis of the landslides affecting the residual soils of these formations resulted in FS close to 1.0.

The results clearly show that for the residual soils of Adamantina and Serra Geral Formations the values of effective friction angle and cohesion used in the semi-regional landslide susceptibility map are quite high for the reality of the site as shown by the back analysis (Tables 7, 17 and 18).

The stability analysis for the slope of Botucatu Formation using the parameters of semi-regional landslide susceptibility resulted in a *SF* value of 1.078 (Table 7 and Fig. 7a). The better fit for the strength parameters obtained from the bibliography for Botucatu Formation residual soils is due to the fact that, in this case, the parameters were obtained from shear strength (consolidated-drained triaxial compression test under saturated and unsaturated conditions) tests performed by Augusto Filho & Fernandes (2018) using soils of the same study area.

Table 18 - Back analysis of Serra Geral Formation. The values used in the new modelling are: **c**’ (kPa) = 5, Φ’ (°) = 14 and SF = 0.959.

c’ (kPa)	Φ’ (°)	*SF*
12	20	2.044
11	20	1.907
10	20	1.770
10	19	1.748
10	18	1.727
9	18	1.590
8	17	1.432
7	15	1.253
6	15	1.116
6	14	1.096
5	14	0.959
4	15	0.842

Table 17 - Back analysis of Adamantina Formation. The values used in the new modelling are: **c**’ (kPa) = 4, Φ’ (°) = 24.1 and SF = 1.077.

c’ (kPa)	Φ’ (°)	*SF*
0	36.1	1.074
0	34.1	0.997
1	32.1	1.028
0	32.1	0.924
2	30.1	1.061
3	28.1	1.097
3	26.1	1.032
4	24.1	1.077
4	22.1	1.017
5	20.1	1.068
5	18.1	1.013
5	16.1	0.959
6	16.1	1.07
6	14.1	1.019

The modeling for the landfill section resulted in a *SF* value of 1.065 (Fig. 7b). This value indicates that the parameters used for this material were slightly low, mainly related to the value of effective cohesion, since there were no signs of instability in the highway landfills in the studied section.

The results obtained in the stability analyses in the detailed geological-geotechnical sections were considered in the elaboration of the final landslide susceptibility map of the study area.

Finally, the results of the back analysis of the Adamantina and Serra Geral formations were used to calibrate the geotechnical parameters used previously in the susceptibility mapping of scenario 1 (Tables 17 and 18).

The results of the scenario 1 mapping using the calibrated parameters are described in Table 19. As expected, although areas of very low susceptibility (*SF* > 2) still predominate, there is a significant increase in areas of medium, high and very high susceptibility in the zones in which these two formations are present.

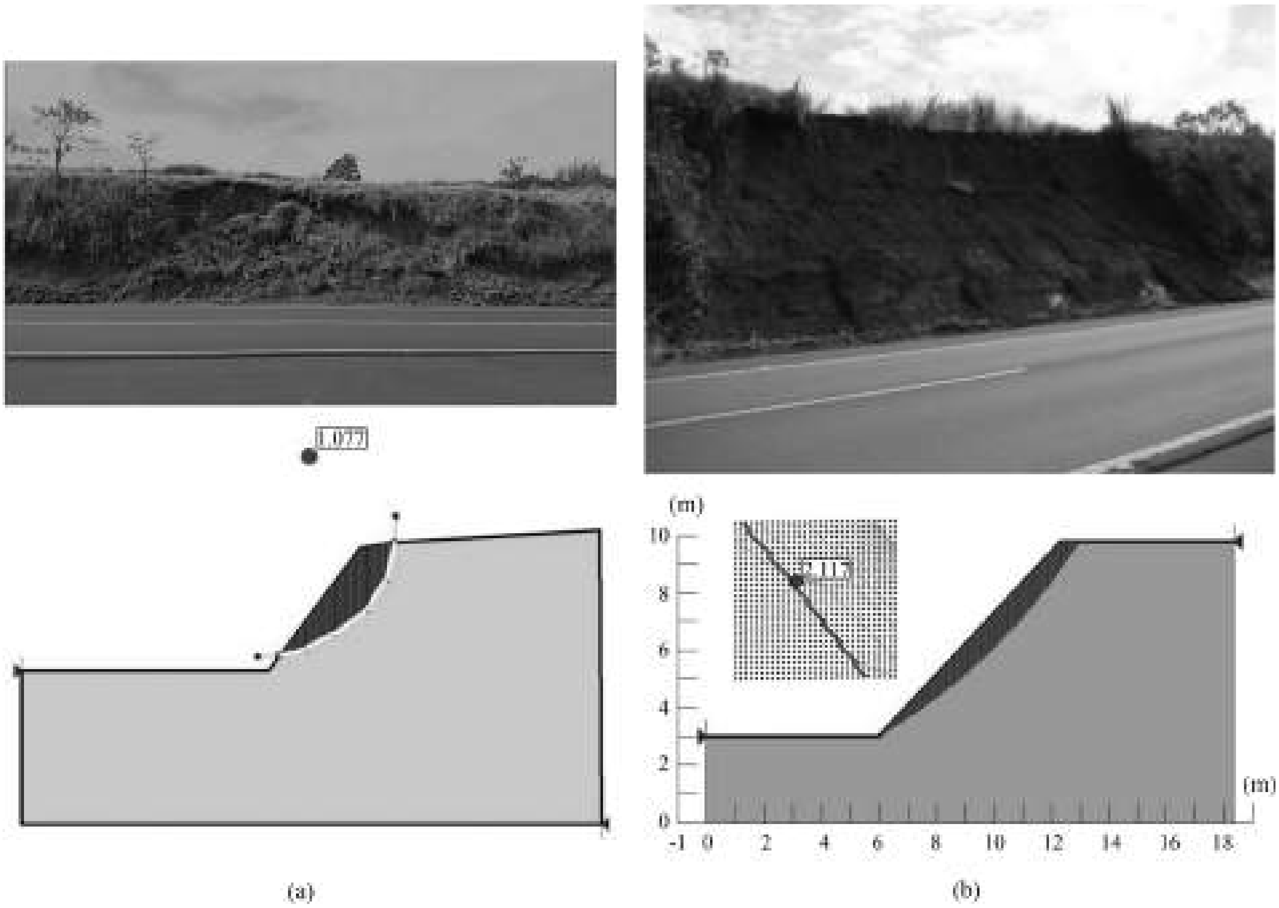

Figure 6 - Back analysis of the highway cut exposing residual soils of Adamantina (a) and slope stability analysis of Serra Geral (b) formations.

In sheet 3, no change occurs because there is no material from Serra Geral formation / diabase. In sheet 2 only a small increase occurs in the class of low susceptibility because, despite having the basic intrusive formation, soft slopes predominate in this area (Tables 11 and 19). The results are similar for scenario 2.

5. Conclusions

Stability simulations using the infinite slope method performed on the semi-detail scale (1: 10,000) allowed the identification of limitations not previously described associated with the physical-mathematical model of this method. These limitations can be overcome by calculating the angle from which *SF* inversion occurs, obtained by means of the derivative of the equation with respect to the slope angle.

The slope stability simulations using Bishop's simplified method in detailed geological-geotechnical sections produced in the field surveys allowed the adaption of the geomechanical parameters used in the semi-regional simulations, which made the mapping of susceptibility in the study area more realistic.

The approach used was efficient even considering the limitations of the infinite slope analysis method and the

Table 19 - Percentage area of the susceptibility classes for scenario 1 with adjusted geomechanical parameters.

Susceptibility classes	*SF*	Sheet 1	Sheet 2	Sheet 3	Sheet 4	Sheet 5	Sheet 6	Sheet 7
Very high	< 1.0	0.2	0	0	0.6	1.7	0.5	0
High	1.0 to 1.3	0.9	0	0	3.6	4.6	1.0	0.1
Medium	1.3 to 1.5	1	0	0	2.1	2.4	0.5	0.1
Low	1.5 to 2.0	3.4	0.4	0.1	4.2	3.7	1.3	0.4
Very low	> 2.0	94.5	99.6	99.9	89.5	87.6	96.7	99.4

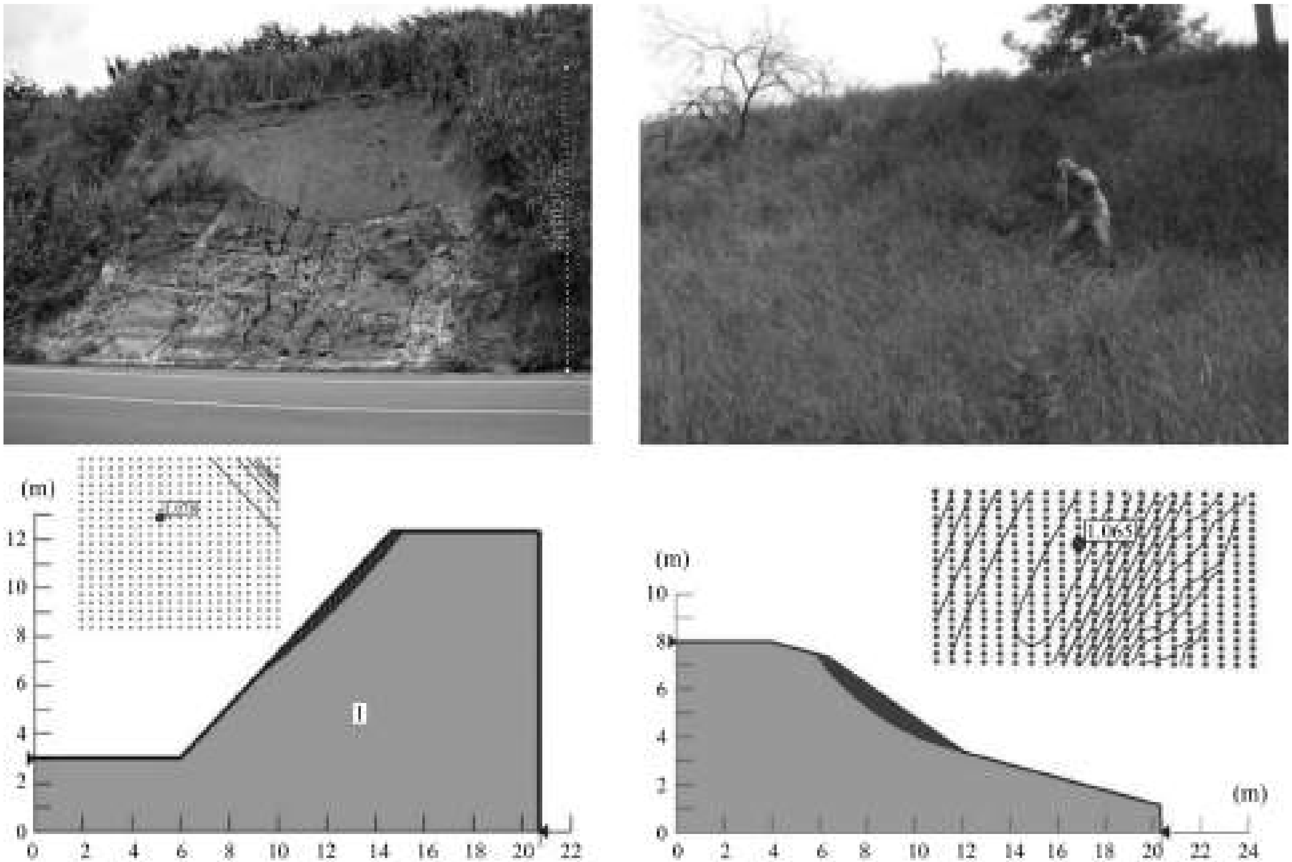

Figure 7 - a) Slope stability analysis in highway cut exposing residual soil of Botucatu Formation; b) Slope stability analysis in highway landfill (see Table 7 for geomechanical parameters used).

representativeness of the geomechanical parameters used in the stability analyses.

The slopes and marginal areas of the highway more susceptible to landslides were mapped based on quantitative models of analysis, reducing the subjectivity of the mapping. The use of deterministic stability analysis models in GIS environment and in geological-geotechnical sections results in great versatility and different scenarios can be simulated, adapting them to each situation analyzed.

Acknowledgments

The authors gratefully acknowledge the financial support of the Brazilian research funding agency CAPES (Coordenação de Aperfeiçoamento de Pessoal de Nível Superior).

References

ABNT (2006). Associação Brasileira de Normas Técnicas. NBR 11682: Estabilidade de Taludes e Encostas. Rio de Janeiro, Brazil, 33 p.

Abramson, L.W.; Lee, T.S.; Sharma, S. & Boyce, G.M. (2002) Slope Stability and Stabilization Methods. John Wiley & Sons, New Jersey, 649 p.

Ahrendt, A. (2005). Movimentos de Massa Gravitacionais - Proposta de um Sistema de Previsão: Aplicação Urbana na Área de Campos do Jordão, SP. Ph.D. Thesis, Escola de Engenharia de São Carlos, Universidade de São Paulo, 390 p.

ARCMAP (2010). Software available for Windows. ESRI.

Augusto Filho, O. (2006). Cartas de risco de escorregamentos e planos de seguro no Brasil: Um ensaio em Caraguatatuba (SP). Geotecnia (Lisboa), 108:197-214.

Augusto Filho, O. & Fernandes, M.A. (2018) Landslide analysis of unsaturated soil slopes based on rainfall and matric suction data. Bulletin of Engineering Geology and the Environment, 78:4167-4185.

Baum, R.L.; Savage, W.Z. & Godt, J.W. (2002). TRIGRS - A Fortran program for transient rainfall infiltration and grid-based regional slope-stability analysis. US Geological Survey Open-File Report, 424:38.

Baum, L.; Savage, W.Z. & Godt, J.W. (2008). TRIGRS - A Fortran program for transient rainfall infiltration and grid-based regional slope-stability analysis, version 2.0, US Geological Survey Open-File Report 2008-1159, available at: http://pubs. usgs. gov/of/2008/1159 and downloaded on September 4th 2018.

DER (2015). Departamento de Estradas de Rodagem. Volume Diário Médio das Rodovias (VDM) 2015. Available at: http://der.sp.gov.br/website/Acessos/MalhaRodoviária / VolumeDiario/ and Accessed in November 20, 2015.

Dhakal, A.S. & Sidle, R. (2003). Long-term modelling of landslides for different forest management practices. Earth Surface Processes and Landforms, 28(8):853-868.

DNIT (2014). Departamento Nacional de Infraestrutura de Transportes. Available at: http://www.dnit.gov.br/noticias/dnit-recupera-rodovias-federais-afetadas-por-chuvas. 011 and Accessed in July 14, 2014.

Fiori, A.P. & Carmignani, L. (2009). Fundamentos de Mecânica dos Solos e das Rochas. 2ª ed. Editora UFPR, Curitiba, 602 p.

Gaioto, N. (1992). Estabilidade de Taludes. Departamento de Geotecnia, Seção de Publicação da EESC-USP. [S.I:s.n].

GEOSTUDIO (2012). Software for Windows, GEOSLOPE INTERNATIONAL, available at http://www.geo-slope.com/support/downloads/2012 and downloaded on July 3rd 2018.

Gioia, E.; Speranza, G.; Ferretti, M.; Godt, J.W.; Baum, R.L. & Marincioni, F. (2014). Using the TRIGRS model to predict rainfall-induced shallow landslides over large areas. EGU General Assembly Conference Abstract, v. 16, EGU2014-14134

IPT, Instituto de Pesquisas Tecnológicas do Estado de São Paulo (1981a). Mapa Geológico do Estado de São Paulo, Escala 1:500.000. 2 v. São Paulo. Publicação IPT 1184.

IPT Instituto de Pesquisas Tecnológicas do Estado de São Paulo (1981b). Mapa Geomorfológico do Estado de São Paulo, Escala 1:1.000.000. 2 v. São Paulo. Publicação IPT 1185.

Krahn, J. (2004). Stability Modeling with SLOPE/W an Engineering Methodology. First edition. GEO-SLOPE/W International Ltd., Calgary, 396 p.

Magnani, H.O. (2006). Comportamento de Aterros Reforçados Sobre Solos Moles Levados à Ruptura. Ph.D. Thesis, COPPE, UFRJ, 507 p.

Massad, F. (2003). Obras de Terra: Curso Básico de Geotecnia. Oficina de Textos, São Paulo, 170 p.

Montgomery, D.R. & Dietrich, W.E. (1994). A physically based model for the topographic control on shallow landsliding. Water Resources Research, 30(4):1153-1171.

OFFICE (2010). Software for Windows. Microsoft.

Pack, R.T.; Tarboton, D.G. & Goodwin, C.N. (1998). The SINMAP approach to terrain stability mapping. In: 8th Congress of the International Association of Engineering Geology. Vancouver, British Columbia, v. 21, pp. 25.

Pack, R.T.; Tarboton, D.G.; Goodwin, C.N. & Prasad, A. (2005). SINMAP 2. A Stability Index Approach to Terrain Stability Hazard Mapping. Technical Description and Users Guide for Version 2. Canadian Forest Products Ltd, Utah, pp. 73.

Park, D.W.; Nikhil, N.V. & Lee, S.R. (2013). Landslide and debris flow susceptibility zonation using TRIGRS for the 2011 Seoul landslide event. Natural Hazards and Earth System Sciences, 13:2833-2849.

Pinto, C.S.; Gobara, W.; Peres, J.E.E. & Nader, J.J. (1993). Propriedades dos Solos Residuais. Solos do Interior de São Paulo. ABMS-NRSP, Depto. Geotecnia da EESC-USP, pp. 95-142.

Queiroz, R.C. (1986). Aplicação do Método de Retroanálise no Estudo da Estabilidade de Taludes de Estradas Situadas em Solos Oriundos da Formação Adamantina. Master Thesis, Escola de Engenharia de São Carlos, São Carlos, 98 p.

Ramos, V.A.; Guimarães, R.F.; Redivo, A.L.; Gomes, R.A.T.; Fernandes, N.F. & Carvalho júnior, O.A. (2002). Aplicação do modelo SHALSTAB, em ambiente Arcview, para o mapeamento de áreas suscetíveis a escorregamento raso na região do Quadrilátero ferrífero (MG). Espaço & Geografia, 5(1):49-67.

Rosniecek, A. & Imai, H.N. (2013). Mapeamento Geotécnico e Análise de Áreas Suscetíveis a Deslizamentos Rasos da Bacia do Rio Ratones - Aplicação do Modelo SHALSTAB. Conclusion of Course Work, Universidade Federal de Santa Catarina, Florianópolis, 155 p.

Savage, W.Z.; Godt, J.W. & Baum, R.L. (2004). Modeling time-dependent areal slope stability. In: Landslide: Evaluation and Stabilization. Balkema, Taylor and Francis Group, London, pp. 23-38.

Silveira, C.T.; Fiori, A.P.; Ferreira, A.M.; Felipe, R.S.; Kepel Filho, J.L.; Folador, R.M. & Costa, L.C. (2012). Análise do fator de segurança na estabilidade das vertentes na Bacia do Rio Jacareí, Serra do Mar Paranaense. Revista Brasileira de Geomorfologia, 13(3):287-297.

Skempton, A.W. & DeLory, F.A. (1957). Stability of natural slopes in London clay. Proc. 4th Int. Conf. On Soil Mechanics and Foundation Engineering, London, v. 2, pp. 378-381.

Vieira, B.C. (2007). Previsão de Escorregamentos Translacionais Rasos na Serra do Mar (SP) a Partir de Modelos Matemáticos em Bases Físicas. Ph.D. Thesis, Instituto de Geociências, Universidade Federal do Rio de Janeiro, Rio de Janeiro, 194 p.

Wu, T.H. & Abdel-Latif, M.A. (2000). Prediction and mapping of landslide hazard. Canadian Geotechnical Journal, 37(4):781-795.

Wu, W. & Sidle, R.C. (1995). A distributed slope stability model for steep forested basins. Water Resources Research, 31(8):2097-2110.

Pullout Testing of Soil Nails in Gneissic Residual Soil

A.C.N.B. Arêdes, E.A.G. Marques, A.H.C. Oliveira

Abstract. Soil nailing has proved to be an efficient and cost-effective stabilization technique, consisting in installing passive reinforcement in the soil that provides the material with tensile and shear strengths. The fundamental parameter in analyzing the mechanical behavior of this type of structure is the frictional resistance of the soil-nail interface, denominated q_s. This paper presents the results of pullout tests performed on a slope located on the campus of the Federal University of Viçosa, in Viçosa-MG, Brazil. Drilling boreholes enabled the identification of four different types of soil with predominant composition of fine sand and silt, all characterized as a gneissic residual soil. Different lengths and methodologies were studied in the pullout tests with the aim of assessing the impact these factors have on shear strength. The values of q_s obtained in the tests were similar to the ones reported by other authors. Even when running tests with low pressures, the results showed that the first grouting reinjection stage was able to provide a significant gain in the pullout resistance of the nails. Another point of observation was that, even though there are reasonable estimated values of q_s in the literature, the conduction of pullout tests is essential for the confirmation of the values to be used in each situation.

Keywords: gneissic residual soil, nail types, pullout test, reinjection grouting, shear resistance of the soil-nail interface, soil nailing.

1. Introduction

1.1. Principles of soil nailing

Among the techniques of soil stabilization, soil nailing is one that has been widely used for its efficiency, competitive cost-effectiveness, flexibility, and easy production. This method consists in inserting passive inclusions into the soil that provide it with additional tensile and shear strengths.

In the study of the mechanical behavior of soil nailing, it is assumed that the reinforced massif can be divided into an active zone, bounded by a failure surface, and a passive zone that is considered the resistant zone, where the nails are anchored.

The main mechanism of interaction between the nails and soil is associated with the mobilization of the frictional resistance of the soil-reinforcement interface, denominated q_s. Therefore, the pullout resistance is a fundamental parameter for the design of soil nail walls.

According to Ortigão (1997) and Hong *et al.* (2013), some factors can affect the value of q_s, such as ground conditions, effective overburden stresses of the soil nails (depth and overload), drilling method and hole cleaning, grout injection method and grout characteristics, as well as environmental factors, such as temperature and humidity.

The friction between the nail surface and surrounding soil can be determined through the application of empirical and theoretical methods, the elaboration of empirical correlations with results obtained in field trials, as well as through the conduction of field pullout tests.

Pullout testing is considered to be the most appropriate method to study soil-nail interaction, being widely employed for quality control in construction and performance evaluation of soil nail walls (Babu & Singh, 2010a and 2010b). The test consists in using a hydraulic jack to apply tensile loads to the nail anchored in the ground, then recording the displacement of the nail head for each applied load. The maximum axial tensile load exerted on the soil nail is obtained from the load-displacement curve.

There is no Brazilian standard that regulates the conduction of pullout tests, but several authors - such as Ortigão (1997), Ortigão & Sayão (2000), Zirlis *et al.* (2003), Springer (2006), Feijó (2007), and Beloni (2011) - have already presented recommendations for the procedure and how it should be controlled in soil nailing constructions.

The mobilization of shear strength upon the contact between the soil and the nail is not uniform. However, as a simplification, the value is assumed to be constant along the length of the reinforcement, resulting in a constant value of pullout resistance (q_s) that is calculated using Eq. 1. For nails larger than 10 m, the value of (q_s) varies in a non-linear manner along its length.

$$q_s = \frac{F_{\max}}{\pi D \cdot L_{anchored}} \quad (1)$$

where $F_{\max}$: maximum axial tensile load on the nail; D: drilling diameter; and $L_{anchored}$: anchored length of the nail.

Ana Carolina Nascimento de Barros Arêdes, M.Sc., Departamento de Engenharia Civil, Universidade Federal de Viçosa, Viçosa, MG, Brazil. e-mail: ana.aredes@ufv.br.
Eduardo Antonio Gomes Marques, D.Sc., Full Professor, Departamento de Engenharia Civil, Universidade Federal de Viçosa, Viçosa, MG, Brazil. e-mail: emarques@ufv.br.
Angelo Henrique Cruz Oliveira, M.Sc. Student, Departamento de Engenharia Civil, Universidade Federal de Viçosa, Viçosa, MG, Brazil. e-mail: angelo.cruz.oliveira@hotmail.com.
Submitted on April 10, 2019; Final Acceptance on October 1, 2019; Discussion open until August 31, 2020.
DOI: 10.28927/SR.431085

In this context, this paper presents results of pullout tests performed on a gneissic residual soil with the aim of determining the value of q_s. The objective of this study is to analyze the results of the tests, comparing them with values found in the literature, and to evaluate the variations in the nail's shear strength that result from the use of different nailing characteristics.

1.2. Values of q_s

Many studies present field pullout tests of soil nails conducted in Brazil and worldwide. Springer (2006) performed 25 pullout tests on a gneissic residual soil in Niterói - RJ, Brazil, obtaining results of q_s that ranged from 94 kPa to 240 kPa for nails without reinjection, and varied between 159 and 231 kPa for nails with 1 reinjection stage.

Beloni *et al.* (2017) conducted pullout tests with 12 nails without reinjection in a mature gneissic residual soil composed of sandy clay, located in Viçosa - MG (Brazil), obtaining values between 47 kPa and 82 kPa.

Seo *et al.* (2017) performed field pullout tests to analytically determine the shear behavior between the soils and grout, especially the soil-dilation effect that occurs during shearing. For this study, three experimental fields with different soil types were selected: colluvial soil, weathered granite soil, and fill soil. Two different construction methods were also analyzed: gravity grouting and pressure grouting. In the weathered granite soil, three different anchored lengths (2.0 m, 3.0 m, and 4.0 m) were used to verify the effect of the nail's length. All types of soil nails were installed in the vertical direction. After the pullout tests, the diameters of the soil nails were measured, being in around 13 cm with gravity grouting and 16 cm with pressure grouting. In this study, increased diameters were adopted to calculate the value of q_s.

According to Seo *et al.* (2017), the results for the colluvial soil (classified by the Unified Soil Classification System - USCS - as ML) showed values of q_s that varied from 96 to 120 kPa. In the weathered granite soil (USCS - SM), the pullout resistance observed ranged from 128 to 160 kPa, and, for the fill soil (USCS - SC), the average value of q_s was approximately 72 kPa.

Oliveira *et al.* (2017) presented a study of an area located in Ipatinga - MG, Brazil. In order to carry out this study, pullout tests were performed on 7 soil nails (1 without reinjection grouting, 3 with 1 stage of reinjection grouting, and 3 with 2 stages of reinjection grouting). All nails had 5 m of anchored length in a silty fine sand soil. The authors obtained mean q_s values of 53.36 kPa for nails without reinjection, 62.17 kPa for nails with 1 reinjection stage, and 79.77 kPa for nails with 2 reinjection stages.

Ghadimi *et al.* (2017) investigated the effects of overburden, injection pressure, and soil strength parameters on the bond strength of nails *in situ*. For this research, five different sites in Tehran, Iran, were studied, with a total number of 20 pullout tests of soil nails. The soils on all sites had a percentage of fine-grained soil < 10 %, a predominant composition of sand, gravel content > 37 %, and reached q_s values up to 600 kPa.

Hong *et al.* (2017) presented an analysis of the influence of a few parameters (overburden pressure, grouting pressure, and degree of saturation) on the pullout resistance of soil nails installed in a typical fully-decomposed granite or sand. Eight pullout tests of soil nails were conducted *in situ*. The authors presented the results obtained from laboratory and field tests, with a q_s value around 85 kPa.

Other researchers (França, 2007; Bhuiyan *et al.*, 2019) presented the results obtained from pullout tests carried out with a soil nail wall prototype built in a laboratory, which enabled the verification of conditions not often found *in situ*. França (2007) obtained values of pullout resistance of 145 kPa for medium-plasticity clayey-sand (USCS - SC). Bhuiyan *et al.* (2019), in turn, used Stockton Beach sand (silica sand) under varying conditions of overpressure and injection pressure, finding a maximum axial tensile load on the nail that ranged from 4.5 kN to 25 kN, with no specification of the exact diameter of the nails.

Silva (2018) used statistical analysis correlation to estimate the pullout resistance (q_s) in cohesive soils, based on results of percussion drilling (standard penetration test) and pullout tests. The research was carried out with 20 soil nails located in São Paulo - SP, Brazil, in 5 layers of different soils with lengths of 10 m, from which 7 m formed its free length and 3 m corresponded to the anchored length. The author proposed a correlation between N_{SPT} and q_s according to Eq. 2.

$$q_s = 65.80 + 1.68 N_{SPT} \tag{2}$$

Noor & Jamain (2019) based themselves on a case study to highlight the pullout and creep behavior of soil nailing. The soil nails were installed in three different construction sites, each consisting of a different type of soil (medium-stiff clayey silt, silty sand fill, and sandy silt set in rock). The selected nails underwent testing up to the point where the pre-determined working load reached 1.5 times its original value. According to the results, the silty sand fill generated a lower value of pullout resistance that ranged from 8.75 to 26.00 kPa. The medium-stiff clayey silt displayed values of pullout resistance of 50.40 kPa, while the soil nails installed in the sandy silt with rock yielded the highest value of pullout resistance, ranging from 127.32 kPa to 305.60 kPa.

2. Materials and Methods

2.1. Description of the location

This study was conducted in a cut slope in a gneissic residual soil, and was performed during the expansion of P. H. Rolfs avenue, located on the campus of the Federal University of Viçosa, in Viçosa, Minas Gerais, Brazil (Figs. 1 and 2). This research was brought about by the collapse of

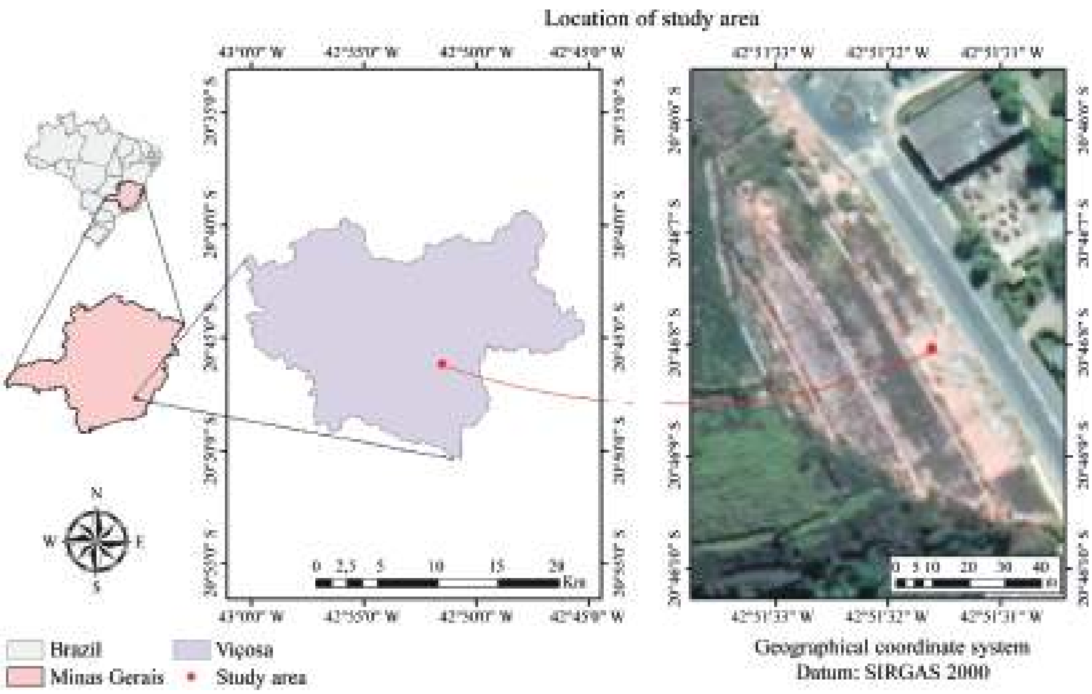

Figure 1 - Location of study area. Source: Google Earth.

Figure 2 - Front view of failure occurred in the studied area.

this slope that occurred during the dry season of 2015, between July 4th and 6th. At the time when the slope movement occurred, there were no drainage devices installed on the slope. A back analysis of this slope failure was presented by Arêdes *et al.* (2017).

The topography of the site was determined using a Terrestrial Laser Scanner (RIEGL VZ 400), a GNSS receiver (JAVAD) and a digital camera (Nikon 600D). Eight boreholes, with a maximum depth of 10 m, were drilled using a mechanical auger to identify the types of soil present in the geological-geotechnical cross-section that was built to perform slope stability analysis and to allow characterization of the site. Disturbed soil samples were collected at every 25 cm of drilling, and a visual-tactile examination was performed. The plan and cross-section were processed using Topograph (2012) and AutoCAD (2016) software.

2.2. Laboratory tests

Using PVC tubes (40 cm in height x 35 cm in diameter), four undisturbed samples were collected from the slope for laboratory tests. Following these tests, geotechnical characterization of the soils was performed to determine particle size distribution (ABNT, 2016d), particle unit weight (ABNT, 2016c), liquid limit (ABNT, 2016b), and plastic limit (ABNT 2016a).

The shear strength parameters of the soils were obtained from direct shear testing with natural water content, following the recommendations from ASTM (2011).

2.3. Pullout tests

The twelve holes drilled to install the nails were arranged in a single line with an average horizontal spacing of 1.5 m (Fig. 3). Among the twelve holes, six were drilled with 6 m length and an average diameter of 100 mm (nails 1 to 6 - Fig. 3), while the other six were drilled with 4 m length and the same average diameter (nails 7 to 12 - Fig. 3). Drilling of nails 2, 3, and 4 was done with a hydraulic drilling rig, while all other nails were drilled with a mechanical auger. After the drilling process, a PVC pipe was used to wash the holes until clean water came back through the orifices. The soil nails were installed at a 15° downward horizontal inclination.

To produce the nails, seven-meter-long CA-50 steel bars with 20 mm diameter were used in the holes that were 6 m in length, whereas five-meter-long bars were used for the ones with lengths of 4 m. Centralizers made of polyvinyl chloride (PVC) were installed along the length of each nail bar (spaced 1.5 m apart) to ensure that the nail bar was positioned in the center of the hole and that a minimum thickness of grout covered it completely.

In order to study the effect of the grout injection method on the shear resistance of the soil-nail interface, three types of nail were examined: without reinjection grouting (sleeve grout) and with 1 or 2 stages of reinjection grouting. The reinjection grouting was achieved with a tube-à-manchette attached to each steel bar. The tube-à-manchette used in this study consisted of a grout pipe that had 20 mm diameter and was perforated with small holes (grout injection points) at intervals of 1 m, which were enclosed by a sleeve of adhesive tape.

After the nail was prepared (Fig. 4a), it was inserted into the hole, leaving a gap of 1 m from the surface for the purposes of the pullout test. To prevent the cement grout from filling the first meter of the hole, the bar was wrapped with foam along this length.

The grout (cement CP-32 II-E), with a water/cement ratio of approximately 0.7, was released upwards at low pressure to perform the sleeve grout using the same PVC pipe used for washing the hole. The first stage of reinjection grouting was performed 24 h after the execution of the sleeve grout, and, during this step, the pressure grouting had a value of approximately 235 kPa. In this phase, a volume of grout corresponding to 4 bags of cement was injected for 5 min into the soil nails with 3 and 5 m of anchored length, respectively.

The first reinjection stage of the nails in which two reinjection stages would be carried out was not performed satisfactorily. During the course of the pressure grouting, in addition to the injection valves having ruptured and caused the valves that would be used in the second stage to break, too, part of the grout also came back through the hole. Thus, the applied pressure was relieved and the expected grout bulb was not formed. The test results for these nails (1, 4, 7, and 12) were considered incomplete reinjections and were disregarded in this study.

Table 1 summarizes the information related to each soil nail.

The setup (Figure 4b) of the pullout test was composed by the following equipment: pieces of wood (I), welded steel plate (II), hydraulic jack cast with a capacity of 50 tons (III), set for locking the steel bar (IV), steel plate for supporting extensometers (V), mechanical strain gauges

Figure 3 - Position of the soil nails.

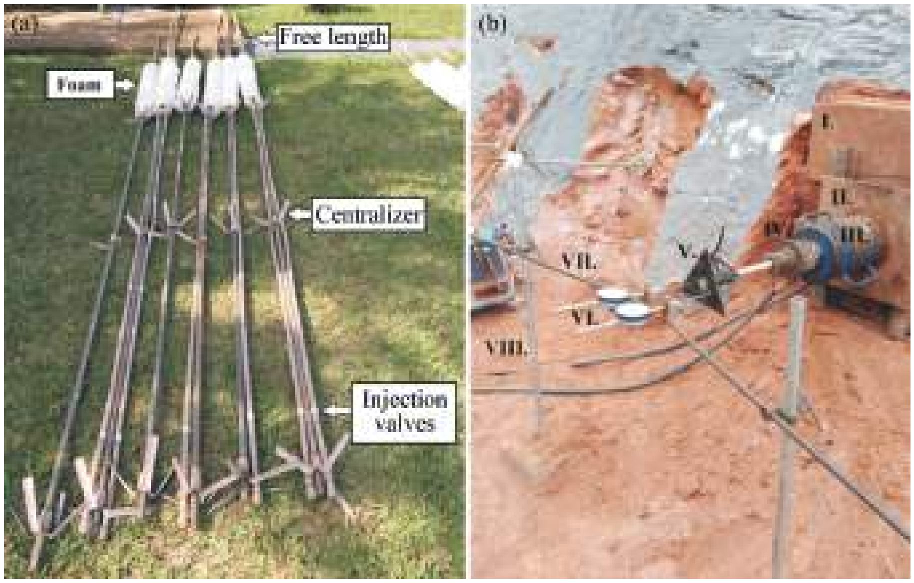

Figure 4 - Components of the pullout test: (a) Bar for insertion into the prepared hole. (b) Arrangement of the pullout test system.

Table 1 - Summary of nails information.

Soil nail	Total length of the steel bar (m)	Total length inserted into the hole (m)	Anchored length (m)	Diameter (mm)	Equipment used in drilling	Grouting method
1	7.00	6.00	5.00	100	Mechanical auger	Sleeve grout + 1 incomplete reinjection stage
2	7.00	6.00	5.00	100	Hydraulic drill	Sleeve grout + 1 reinjection stage
3	7.00	6.00	5.00	100	Hydraulic drill	Only sleeve grout
4	7.00	6.00	5.00	100	Hydraulic drill	Sleeve grout + 1 incomplete reinjection stage
5	7.00	6.00	5.00	100	Mechanical auger	Only sleeve grout
6	7.00	6.00	5.00	100	Mechanical auger	Sleeve grout + 1 reinjection stage
7	5.00	4.00	3.00	100	Mechanical auger	Sleeve grout + 1 incomplete reinjection stage
8	5.00	4.00	3.00	100	Mechanical auger	Only sleeve grout
9	5.00	4.00	3.00	100	Mechanical auger	Sleeve grout + 1 reinjection stage
10	5.00	4.00	3.00	100	Mechanical auger	Sleeve grout + 1 reinjection stage
11	5.00	4.00	3.00	100	Mechanical auger	Only sleeve grout
12	5.00	4.00	3.00	100	Mechanical auger	Sleeve grout + 1 incomplete reinjection stage

(VI), arms for pivoting and adjusting the position of the extensometers (VII), and a concrete-based fixed support for the pivot arms (VIII).

The pullout was carried out in stages, each corresponding to an additional application of load. During these stages, readings of the extensometers were taken at specific times: 0 s, 15 s, 30 s, 1 min, 2 min, 4 min, 8 min, 15 min and 30 min. After the thirty-minute reading, the stabilization of the displacement readings (Eq. 2) was checked. If this condition was satisfied, the end of the stage was characterized; otherwise, readings for 1 h, 2 h, and 4 h (and so on) were performed, doubling the value until stabilization was achieved. In Eq. 3, l_i represents the reading taken at each of the loading stages.

$$\frac{l_i - l_{i-1}}{\sum_{l=0}^{i} l} \times 100 \leq 5\,\% \qquad (3)$$

At the end of each stage, the procedure was repeated with a new application of load and another cycle of readings. In order to obtain sufficient data for the elaboration of the load-displacement curve, the increments for each loading step were estimated from the maximum pullout force expected for the soil. It was possible to notice that the frictional resistance in the soil-nail interface was overcome when the applied load did not stabilize and great displacements occurred.

3. Results and Discussion

3.1. Pluviometric data

The pluviometric information about the site, referring to this study's period of interest (July 4th to 6th, 2015), was obtained from the website of the Brazilian National Institute of Meteorology (INMET). Their data are generated daily in the weather station of Viçosa-MG, located on the campus of the Federal University of Viçosa, at a distance of 1.5 km from the slope site.

According to INMET (2016), there was 0 mm of rainfall in the city of Viçosa during this period, with the previous rainfall registered on June 16th with 4 mm, as shown in Fig. 5.

3.2. Geological and geotechnical site characterization

A visual-tactile examination of the disturbed samples was used to elaborate a representation of the geological-geotechnical cross-section of the slope, aligned with two boreholes, as shown in Fig. 6a. The field investigation revealed four different types of soil, all characterized as gneissic residual soil with many relict structures: faults, foliation (preserved), and manganese lenses. The mineralogy was mainly composed of quartz, feldspar, and mica. The groundwater table was not found during drilling.

Soil 1 was characterized as a fine silty sand and was dark red and purple in color; Soil 2 presented a silt-sandy texture and had an ochre color; Soil 4, which showed a lighter coloration that was rosier with grayish tones, displayed kaolinized levels and was classified as a silt with fine sand; finally, Soil 3, which was a mixture of soils 1 and 2, had variegated colors. Figure 5b shows the interface between Soils 2 (above) and 1 (below) displayed on the failure plane, with some relict faults planes transversal to the cut slope.

3.3. Laboratory tests

Table 2 presents a summary of the results of geotechnical characterization of four soil samples.

After fitting the linear Mohr-Coulomb failure envelope to the direct shear test results, the friction angle (ϕ) and cohesion intercept (c) were obtained for the envelopes containing the maximum values of shear stresses and the post-peak values, as shown in Table 3.

3.4. Pullout tests

During the testing routine, the hydraulic jack presented a deficiency that prevented the conduction of pullout tests on soil nails 4 (5 m, 1 incomplete reinjection) and 10 (3 m, 1 reinjection). As previously mentioned, the results of nails with 1 incomplete reinjection (nails 1, 4, 7, and 12) were disregarded in this study. Thus, only seven of the tests that were originally planned could be effectively considered valid. Figure 7 shows the results of the pullout tests, where unfilled markers represent the nails with 5 m of an-

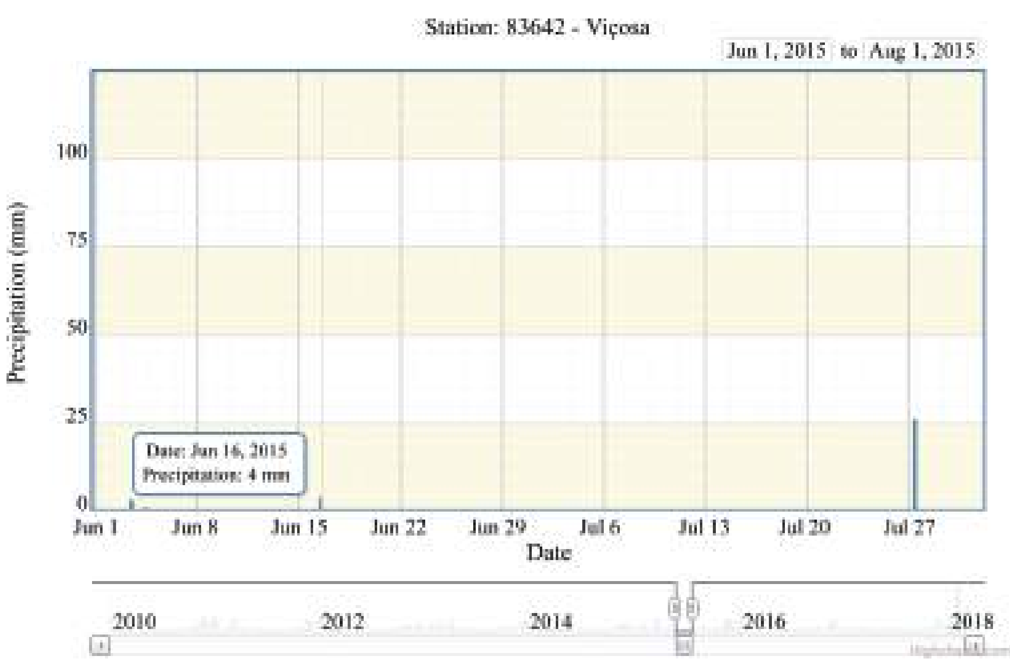

Figure 5 - Precipitation information about Viçosa between June 1st and August 1st. Source: INMET, 2019.

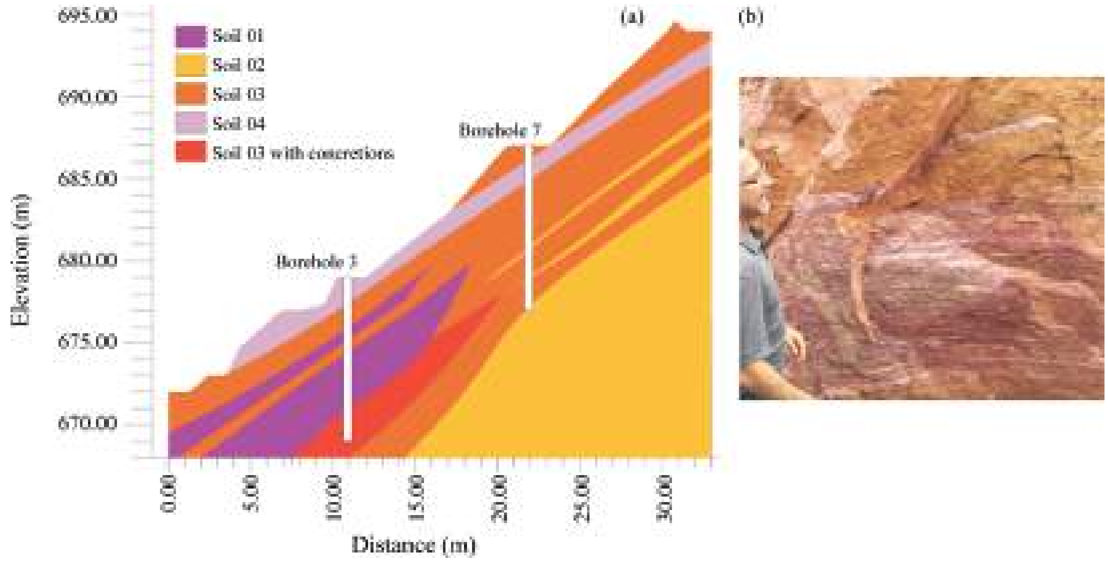

Figure 6 - Geotechnical characterization of the study area. (a) Geological-geotechnical cross-section. (b) Detail of the interface between the layers of Soils 03 (upper) and 01 (lower) and failures.

Table 2 - Results of geotechnical characterization of the samples.

Soil	Particle size distribution (%)			Atterberg limits (%)			γ_s (kN/m^3)
	Clay	Silt	Sand	LL	PL	PI	
1	3	23	74	38	21	17	26.61
2	9	49	42	55	30	25	27.58
3	5	33	62	44	28	16	27.34
4	3	35	62	39	27	12	26.41

chored length, and filled markers represent the tests with 3 m of anchored length.

A summary of the valid results is shown in Table 4. The maximum values of axial tensile load were obtained from the point of greatest curvature in the graphs of Fig. 7 that is, the maximum tensile force supported by the nail without excessive displacement.

When analyzing the results of the tests performed on soil nails with anchored length of 5 m, it is possible to see that, for soil nails without reinjection (3 and 5), the average maximum force was 108 kN. The two nails were placed with different drilling methods - one with a hydraulic drilling rig and the other with a mechanical auger -, but there was no significant difference in the maximum strengths. Nails with 1 reinjection (2 and 6), in turn, had an average pullout force of 148 kN. For soil nails 3 and 5, the drilling was performed differently and no effect of this procedure was observed on the maximum strengths.

During the testing of nails 2 and 6, due to deficiencies in the pullout support system, eccentric efforts were generated in the bar, which may have caused an increase in resistance. Nevertheless, the results of these tests were not excluded from the analysis, since their values were similar to the ones found in the literature for similar soils (Springer, 2006; Beloni, 2011; D'Hyppolito, 2017), and were consistent with the other tests performed in this study.

For soil nails with 3 m of anchored length, the load-displacement curves demonstrated that nails that used only sleeve grout (soil nails 8 and 11) had an average pullout force of 44 kN. Due to an overestimation of the maximum strength attributed to nail 11, its corresponding curve was obtained from a small number of stages. Even so, it was

Table 3 - Strength parameters.

Soil	Parameters	Maximum	Residual
1	Cohesion intercept (kPa)	29	21
	Friction angle (°)	26	24
2	Cohesion intercept (kPa)	79	1
	Friction angle (°)	34	44
3	Cohesion intercept (kPa)	41	23
	Friction angle (°)	20	21
4	Cohesion intercept (kPa)	25	19
	Friction angle (°)	16	12

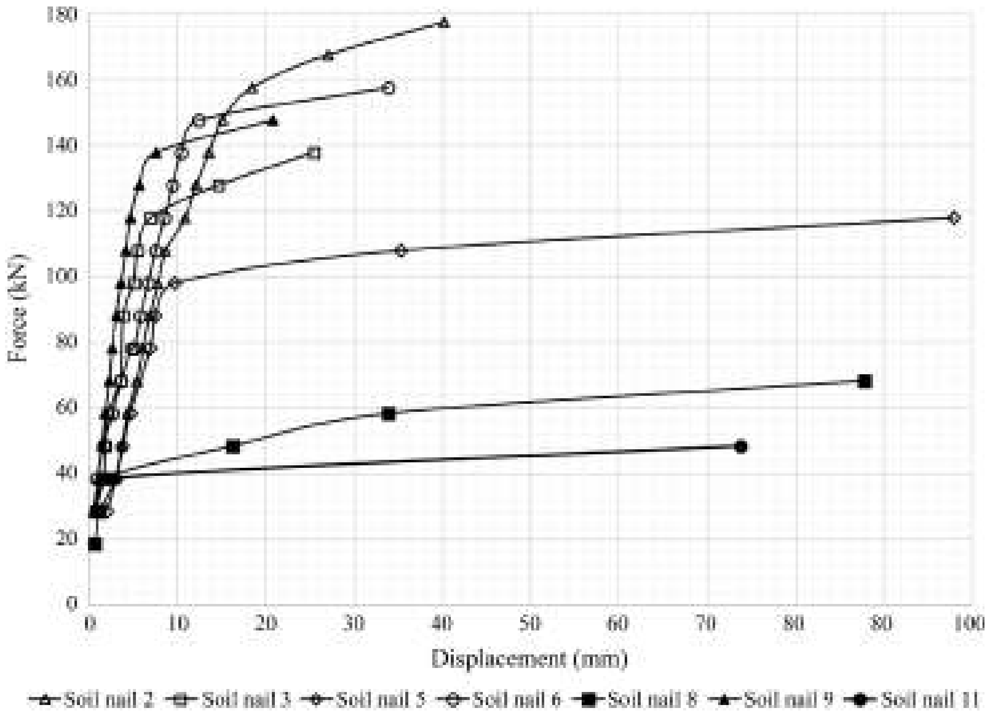

Figure 7 - Force *vs.* displacement of the soil nails.

Table 4 - Results of maximum load and corresponding displacement in the pullout tests of the soil nails.

Soil nails	$L_{anchored}$ (m)	Grout method	F_{max} (kN)	Displacement (mm)
2	5	1 reinjection	148	18.38
3	5	without reinjection	118	6.93
5	5	without reinjection	98	9.69
6	5	1 reinjection	148	12.38
8	3	without reinjection	48	16.27
9	3	1 reinjection	128	5.60
11	3	without reinjection	39	2.48

clear that the rupture occurred when this value of load was applied. With the execution of 1 reinjection, nail 9 showed a pullout force of 128 kN, a result that was not obtained for any of the other nails.

Table 5 lists the average maximum force values ($F_{max,\ mean}$) and the average pullout resistance ($q_{s,mean}$) grouped according to anchored length and grouting method (hole filling).

Based on the results shown in Table 5, a gain of approximately 200 % in strength can be observed in the nails with 1 reinjection and 3 m of anchored length. For the nails with 5 m of anchored length, this value was 37 % higher, as shown in Table 6. Thus, it is possible to notice a more sig-

Table 5 - Average pullout resistance results according to anchored length and grouting method.

Number of nails	$L_{anchored}$ (m)	Grouting method	$F_{max,\ mean}$ (kN)	$q_{s,mean}$(kPa)
2	5	1 reinjection	148	94
2	5	Without reinjection	108	69
1	3	1 reinjection	128	136
2	3	Without reinjection	44	47

Table 6 - Increase in pullout resistance in soil nails with 1 reinjection towards the staple without reinjection.

Anchored length (m)	Increased pullout resistance in relation to nails without reinjection grouting
3	193 %
5	37 %

nificant effect of the reinjection on the shorter soil nails, which can be justified by the higher volume of grout per meter inserted during the reinjection grouting.

Souza *et al.* (2005) reported that the increase in pullout resistance with the first-phase reinjection was equivalent to 78 % in pullout tests of soil nails with 6 m of anchored length, while Springer (2006), observed an increase of 50 % in nails with 3 m of anchored length. Hong *et al.* (2013) analyzed the effect of grouting pressure on the shear resistance of the soil-nail interface, registering an increase of approximately 47 % in nails injected with a pressure of 140 kPa (1.2 m of anchored length) when compared to the ones injected with zero pressure (gravity only). Seo (2017) observed that the maximum tensile forces obtained in the tests increased by almost 25 % in colluvium soils and weathered granite that underwent injection pressure, considering nails with 2 m of injection.

The tests performed in the present study with nails that had 3 m of anchored length showed a much higher increase when compared with the results reported by those authors, even though the results were lower for nails with 5 m of anchored length.

Despite the injected volume being the same for both nail lengths studied, which resulted in an injected volume per meter that was lower in nails with 5 m of anchored length, it was possible to observe that the five-meter soil nails with 1 reinjection had a strength that was 16 % higher than the three-meter nails (Table 5). For soil nails without reinjection grouting, this difference was around 45 %, also in favor of nails with a greater length. Such a behavior was expected, but this comparison is important to show the magnitude of the influence of nail size on pullout resistance.

Figure 8 shows a comparison between mean values of q_s for nails without reinjection (57.7 kPa) and nails with 1 stage of reinjection (115.0 kPa), using values presented in the literature and considering tests with 3 and 5 m of anchored length. The values observed in the present study were compared with results obtained from similar soils by the aforementioned authors. The values for soil nails without reinjection were closer to the ones reported in other studies, mainly those by Oliveira *et al.* (2017) and Noor & Jamain (2019).

The values of q_s obtained by Beloni *et al.* (2017), also in Viçosa-MG, were 25 % higher than those observed for nails without reinjection in this study. These authors found a mean q_s value of 75.5 kPa, and this variation can be justified by differences in the anchored length and by the variability of soil parameters.

3.5. Design aspects

The study of this site presented by Arêdes *et al.* (2017) attested to the overall stability of the slope, making it unnecessary to perform soil nailing to stabilize the slope. Therefore, a decision was made to implement a small concrete foot wall and to fill the spaces generated by the failure with rip-rap. In addition, a drainage system was installed on the berms.

Figure 9 shows the current lateral view of the slope.

4. Conclusions

In this research, we tried to evaluate the influence of nail length, and drilling and hole-filling methods on the

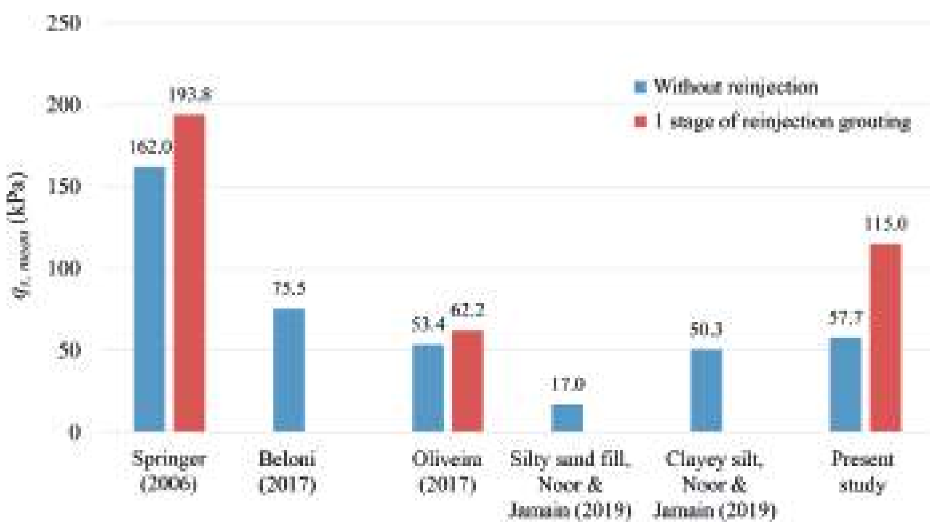

Figure 8 - Comparing values of $q_{s,mean}$ from this study with some results found on literature.

Figure 9 - Current lateral view of the slope.

frictional resistance of the soil-nail interface. The conclusions drawn from this study are summarized below:

a) Even having been performed at low pressure, the first reinjection phase was able to provide a significant gain in pullout resistance of around 200 % for three-meter nails and 37 % for five-meter nails. This increase can be explained by the filling of the voids caused by exudation of the cement grout and the formation of bulbs near the position of the valves. The difference between the three and five-meter nails arose from the lower grout volume applied per meter in the reinjection phases, compromising the comparison between nails of different lengths and same number of reinjection phases. In future studies and projects, it would be advisable to use volumes that are proportional to the lengths;

b) The methodology used to conduct two reinjections with the insertion of two tubes-à-manchette was not efficient. The adhesive tape used as sleeve did not provide adequate resistance, which resulted in its rupture during the first injection phase in both tubes, causing a return of part of the grout, a consequent pressure relief, and no formation of the expected bulb. A more resistant and flexible material, such as rubber, should be used for manufacturing the valves, which will cause them to open with the injection pressure and to close at the end of it, requiring only a tube-à-manchette;

c) The literature offers reasonable values for estimating q_s. However, it is essential for pullout tests to be performed before or during the evaluation of nailing work in order to validate these values and adjust them, if necessary;

d) Even if the pullout test is the method that provides values that are closest to reality, it is still a procedure that is very susceptible to errors in execution. The values obtained from it are very sensitive to the inexperience of operators, inaccuracy of the equipment, reading errors, poorly-supported reaction system, and many other factors. However, that does not make its conduction unnecessary, and it is only through good practice that these problems will be controlled.

Acknowledgments

This study was partially financed by the Coordination of Superior Level Staff Improvement - Brazil (CAPES) - Finance Code 001, and by the FACEV Foundation, through a partnership coordinated by Professor Eduardo Marques.

References

ABNT (2016a). Determination of Plastic Limit - NBR 7180. ABNT, Rio de Janeiro, Rio de Janeiro, Brazil, 3 p. (in Portuguese).

ABNT (2016b). Determining the Liquid Limit - NBR 6459. ABNT, Rio de Janeiro, Rio de Janeiro, Brazil, 6 p. (in Portuguese).

ABNT (2016c). Gravel Grains Retained on the 4,8 mm Mesh Sieve - Determination of the Bulk Specific Gravity, of the Apparent Specific Gravity and of Water Absorption - NBR 6458. ABNT, Rio de Janeiro, Rio de Janeiro, Brazil, 10 p. (in Portuguese).

ABNT (2016d). Soil - Grain Size Analysis - NBR 7181. ABNT, Rio de Janeiro, Rio de Janeiro, Brazil, 12 p. (in Portuguese).

Arêdes, N.B.C.A; Merlo, S.F.; Marques, E.A.G.; Candido, E.S. & Oliveira, A.H.C. (2017). Back analysis of a landslide in a residual soil of gneiss slope. Proc. XII Brazilian Conference on Slopes Stability, Florianópolis (in Portuguese) available at https://cobrae2017.websiteseguro.com/anais/index.php and downloaded on July 2th 2019.

ASTM (2011). Standard Test Method for Direct Shear Test of Soils Under Consolidated Drained Conditions - D 3080. ASTM International, West Conshohocken, Pennsylvania, USA, 9 p.

Babu, G.L.S. & Singh, V.P. (2010a). Soil nails field pullout testing: Evaluation and applications. International Journal of Geotechnical Engineering, 4(1):13-21.

Babu, G.L.S. & Singh, V.P. (2010b). Adequacy of field pullout testing of soil nails. Georisk: Assessment and Management of Risk for Engineered Systems and Geohazards, 4(2):93-98.

Beloni, M.L. (2011). Pullout Resistance of Nails in Gneiss Residual Soil. M.Sc. Dissertation, Departamento de Engenharia Civil, Universidade Federal de Viçosa, Viçosa, 126 p. (in Portuguese).

Beloni, M.L.; Souza, I.D. & Ferreira, R.D.S. (2017). Prediction of pullout resistance of nails through PMT test in a gneiss residual soil in Viçosa-MG. Proc. XII Brazilian Conference on Slopes Stability, Florianópolis (in Portuguese) available at https://cobrae2017.websiteseguro.com/anais/index.php and downloaded on July 2th 2019.

Bhuiyan, M.Z.I.; Wang, S.; Sloan, S.W.; Carter, J. & Raka, T.M. (2019). Effects of grout injection techniques in pressure grouted soil nail system. E3S Web Of Conferences, 92:1701. EDP Sciences.

D'Hyppolito, L.C.B.S. (2017). Empirical Relations to Estimate the Pullout Resistance of Anchorages. M.Sc. Dissertation, Departamento de Civil Engineering, Universidade Federal do Rio de Janeiro, Rio de Janeiro, 206 p. (in Portuguese).

Feijó, R.L. (2007). Monitoring of a Soil Nail Excavation in Residual Soil from Gneiss in Non Saturated Condition. D.Sc. Thesis, Departamento de Engenharia Civil, Universidade Federal do Rio de Janeiro, Rio de Janeiro, 176 p. (in Portuguese).

França, F.A.N. (2007). Pullout Tests in Soil Nailing Wall Built in Laboratory. M.Sc. Dissertation, Departamento de Engenharia Civil, Universidade de São Paulo, Escola de Engenharia de São Carlos, São Carlos, 123 p. (in Portuguese).

Ghadimi, A.S.; Ghanbari, A.; Sabermahani, M. & Yazdani, M. (2017). Effect of soil type on nail pull-out resistance. Proc. Institution Of Civil Engineers - Ground Improvement, 170(2):81-88.

Hong, C.; Liu, Z.; Zhang, Y. & Zhang, M. (2017). Influence of critical parameters on the peak pullout resistance of soil nails under different testing conditions. International Journal of Geosynthetics and Ground Engineering, 3(2):19-25.

Hong, C.; Yin, J.; Pei, H. & Zhou, W. (2013). Experimental study on the pullout resistance of pressure-grouted soil nails in the field. Canadian Geotechnical Journal, 50(7):693-704.

Instituto Nacional de Meteorologia (INMET) available at http://www.inmet.gov.br/portal/index.php?r=home/page&page=rede_estacoes_conv_graf and downloaded on July 2th 2019.

Noor, M.J.M. & Jamain, M.F. (2019). Pull out and creep behaviour of soil nailing - A case study. Journal of Mechanical Engineering, 16(1):189-211.

Oliveira, A.H.C.; Cândido, E.S.; Arêdes, A.C.N.B.; Beloni, M.L. & Souza, I.D. (2017). Analysis of correlations between the pullout resistance and the penetration resistance (N_{SPT}) in sandy soil. Proc. XII Brazilian Conference on Slopes Stability, Florianópolis (in Portuguese) available at https://cobrae2017.websiteseguro.com/anais/index.php and downloaded on July 2th 2019.

Ortigão, J.A.R. & Sayão, A.S.F.J. (2000). Soil nailing. Ortigão, J.A.R. & Sayão, A.S.F.J. (eds.), Geo-Rio - Technical Manual for Slopes - Anchorages and Nails, 2nd ed. Geo-Rio, Rio de Janeiro, pp. 39-55 (in Portuguese).

Ortigão, J.A.R. (1997). Pullout tests for soil nailing designs. Technical note. Soils & Rocks, 20(1):39-43 (in Portuguese).

Seo, H.; Pelecanos, L.; Kwon, Y. & Lee, I. (2017). Net load-displacement estimation in soil-nail pullout tests. Proc. Institution of Civil Engineers - Geotechnical Engineering, 170(6):534-547.

Silva, R.R.C. (2018). Determination of adhesion in soil nailing from correlations with SPT test. Revista Tecnologia, 39(2):1-12 (in Portuguese).

Souza, G.K.T.; Pitta, C.A. & Zirlis, A.C. (2005). Solo nailing - Nail executive's aspects. Proc. IV Brazilian Conference on Slope Stability, Salvador, pp. 835-844 (in Portuguese).

Springer, F.O. (2006). Pullout Tests of Nails in Gneissic Residual soil. D.Sc. Thesis, Departamento de Engenharia Civil, Pontifícia Universidade Católica do Rio de Janeiro, Rio de Janeiro, 310 p. (in Portuguese).

Springer, F.O. (2006). Pullout Tests of Nails in Gneissic Residual Soil. D.Sc. Thesis, Departamento de Engenharia Civil, Pontifícia Universidade Católica do Rio de Janeiro, 310 p. (in Portuguese).

Zirlis, A.C.; Pitta, C.A. & Souza, G.J.T. (2003). Soil nailing - Some executives details, tests, case studies. Workshop

Solo Nailing: Design, Implementation, Instrumentation and Behavior, São Paulo (in Portuguese).

List of Symbols

c: cohesion intercept
D: drilling diameter
PI: plasticity index
$F_{\max}$: maximum axial tensile load on the nail
$L_{anchored}$: anchored length of the nail
LL: liquid limit
PL: plastic limit
l_i: reading performed at each of the loading stages of the pullout test
$q_{s,\,mean}$: mean value of pullout resistance
q_s: frictional resistance of soil-reinforcement interface
γ_s: particle unit weight
ϕ: friction angle
USCS: Unified Soil Classification System

Sustainable Remediation:
A New Way of Thinking the Contaminated Sites Management

A.B. Braun, A.W.S. Trentin, C. Visentin, A. Thomé

Abstract. Within the evolution in the remediation field, the traditional approach to contaminated sites management, based almost exclusively on the risk, time, cost, and decontamination efficiency, is gradually being replaced by the concepts of sustainability. The most recent focus is the incorporation of the term "sustainable remediation (SR)", taking into account that application of a remediation technique can have its own impacts. Thus, this paper aims to present and analyze the characteristics and trends on the knowledge developed in the field of SR and its incorporation in the contaminated sites management context. Firstly, the background to the SR approach is presented. This discussion was carried out through a contextualization of the main changes that occurred in the contaminated sites management with insertion of SR. After that, the main characteristics and concepts of SR are presented and analyzed, and the different stakeholders involvement in this process is discussed. Finally, the main elements present in sustainability evaluation of remediation processes are discussed. It can be concluded that a consensus on the increasingly solid incorporation of a sustainable approach in remediation projects is emerging on the global scene with a view to reducing the process impacts and maximizing the long-term benefits of the contaminated site.

Keywords: environmental remediation, literature review, stakeholders involvement, sustainability evaluation, triple bottom line.

1. Introduction

Environmental issues for a long time did not receive due attention. Anthropogenic activities, such as inadequate and unregulated industrial and waste discharges, have resulted in contaminated sites around the world. These actions have led to a rapid increase in pollutant loads in air, water and soil, limiting the environment ability to absorb such contamination without causing adverse effects on natural ecosystems and human health. Thus, for the many contaminated sites that emerged and could no longer be corrected by natural processes alone, and thus generated some kind of risk, they needed to be managed, generally undergoing some remediation and rehabilitation process (Van Liedekerke *et al.*, 2014; Reddy & Adams, 2015).

The most important factor of a remediation process conduction is the fact that contaminated sites can bring serious consequences for human health and the environment (Bardos *et al.*, 2002; Hou *et al.*, 2017). The main goal of remediation is to reduce the harmful risks that contaminated sites may bring, in order to protect human health and the environment (Petruzzi, 2011; Anderson *et al.*, 2018; O'Connor & Hou, 2018). However, there is already a broad understanding that remediation is not inherently sustainable. The very implementation of remediation technology can result in other environmental, economic, and social secondary impacts both in the short and long term, and can even overcome the benefits of its application, producing a negative effect or reducing the overall net benefit of the remediation process (Forum, 2009; Petruzzi, 2011; Adams & Reddy, 2012; Hou *et al.*, 2014a; Bardos *et al.*, 2016a; Vidonish *et al.*, 2016; Yasutaka *et al.*, 2016; Favara & Gamlin, 2017; Anderson *et al.*, 2018; O'Connor & Hou, 2018).

Therefore, while society can benefit from new land use opportunities such as residences and recreation by contaminated site remediation, corrective actions can result in unintended consequences. These include atmospheric emissions of harmful pollutants, waste generation, significant natural resources consumption including fossil fuels and energy, materials using, ecosystems disruption and risks to workers and the community, among other negative impacts (Petruzzi, 2011; Harclerode *et al.*, 2015a; Rosén *et al.*, 2015). So, a tension comes up between protecting people from the environmental pollution risk and potentially damaging side effects from remediation activities, which may be associated with global damage (O'Connor & Hou, 2018).

In this sense, the approach, decision-making and how the management of contaminated sites is carried out has

Adeli Beatriz Braun, M.Sc., Ph.D. Student, Programa de Pós Graduação em Engenharia Civil e Ambiental, Universidade de Passo Fundo, Passo Fundo, RS, Brazil. e-mail: adelibeatrizbraun@hotmail.com.
Adan William da Silva Trentin, M.Sc., Ph.D. Student, Programa de Pós Graduação em Engenharia Civil e Ambiental, Universidade de Passo Fundo, Passo Fundo, RS, Brazil. e-mail: adan_trentin@hotmail.com.
Caroline Visentin, M.Sc., Ph.D. Student, Programa de Pós Graduação em Engenharia Civil e Ambiental, Universidade de Passo Fundo, Passo Fundo, RS, Brazil. e-mail: caroline.visentin.rs@gmail.com.
Antônio Thomé, Ph.D., Full Professor, Programa de Pós Graduação em Engenharia Civil e Ambiental, Universidade de Passo Fundo, Passo Fundo, RS, Brazil. e-mail: thome@upf.br.
Submitted on April 29, 2019; Final Acceptance on January 29, 2020; Discussion open until August 31, 2020.
DOI: 10.28927/SR.431097

been marked by some changes in recent years (Pollard *et al.*, 2004). Since the early 2000s, the interest in incorporating sustainability in this context of remediation has increased, through the dissemination of the term “sustainable remediation (SR)”. Its inclusion and dissemination are recent but gradually increasing, because it reflects the perception that remediation activities can bring positive and negative environmental, social and economic impacts, and that considering these aspects in isolation is no longer enough. It is necessary to establish effective balances between the benefits of remediation and the harmful emission of secondary pollutants (Rizzo *et al.*, 2016; O’Connor & Hou, 2018). Therefore, SR is intended to consider in a balanced way the three pillars of sustainability, and to implement sustainable measures and practices during the development of the entire remediation process (Forum, 2009).

However, although SR corresponds to a new paradigm shift within the management of contaminated sites, it is still an emerging approach in this context, and has evolved gradually over the past few years (Bardos *et al.*, 2011; Pollard *et al.*, 2004; Reddy & Adams, 2015; Hou *et al.*, 2016). This indicates there is scope for studies that review and deepen the knowledge of SR main characteristics, in order to assist researchers and professionals in the field of contaminated sites management and remediation to choose the best solutions available.

In view of the above considerations, this paper aims to present and analyze the characteristics and trends of the knowledge developed in the field of SR in contaminated sites management context. This discussion includes the background of the SR inclusion in the contaminated sites management field, as well as a contextualization of SR with the main concepts, the different stakeholders involvement approach and in what form the sustainability evaluation is carried out in the remediation.

2. Background and Contextualization of the Sustainability Insertion in the Management of Contaminated Sites

Corrective action selection systems created over 30 years have represented the best knowledge and practices available (Forum, 2009). Historically, contaminated land management has relied heavily on preventing unacceptable risks to human health and environment to ensure that a site is suitable for reuse (Bardos *et al.*, 2011; Hou & Al-Tabbaa, 2014).

Likewise, the decision-making process to select the contaminated site remediation technique has traditionally focused on the cost and ease of implementation of the remediation process, on the availability and viability of the technologies, on the time needed for remediation and on the efficiency for remediation to achieve decontamination goals and compliance with existing laws (Vik *et al.*, 2001; Pollard *et al.*, 2004; Forum, 2009; Harclerode *et al.*, 2015a).

Although these considerations are critical components in a conventional remedial options assessment, over the years practitioners and researchers have become aware that in many cases the contamination was not being destroyed but only transferred to a different environment (Adams & Reddy, 2012). Moreover, this traditional remediation approach does not assess atmospheric emissions, natural resource consumption, energy use, and worker safety during the remediation process, in addition to not fully balancing the environmental, social, and economic impacts of a project, since they generally focus on “internalities” of a project (correction objectives, system performance, and local impacts) and devote minor attention to its “externalities” (impacts at local, regional, and global level) (Forum, 2009).

Therefore, research in this context needs to go beyond simply determining the effect of treatment on contaminants and whether contaminant removal has been achieved (SuRF-UK, 2010; Vidonish *et al.*, 2016). A variety of other environmental factors, as well as economic and social aspects, play an increasing role in decision-making in contaminated sites management (Reinikainen *et al.*, 2016). The increase in the recognition of secondary adverse effects associated with remediation operations was one of the main driving forces that helped to change the context of managing contaminated sites (Forum, 2009; Huysegoms & Cappuyns, 2017).

Thus, the remediation industry has shown interest in including sustainability as a criterion of decision-making during the application of a remediation process (Bardos *et al.*, 2011; Rizzo *et al.*, 2016). The first perspectives for the insertion of sustainability in the remediation contexts arose through the dissemination of the green remediation concepts. At the beginning, a great deal of concern was focused on the primary impacts due to the contaminated sites and the environmental impacts of the remediation processes (Søndergaard *et al.*, 2017).

In this sense, green remediation is generally described as the practice that takes into account all the environmental effects and aspects of the remediation techniques application, seeking to use more ecological options and alternative/renewable sources of energy whenever possible, in order to maximize the environmental benefit (USEPA, 2008; Bardos *et al.*, 2013; Hadley & Harclerode, 2015). In addition to energy, green remediation relies on four other key elements to achieve its environmental objectives, such as: water; air and atmosphere; materials and waste; and land and ecosystems (USEPA, 2011). Therefore, green remediation is intended to improve environmental performance, reducing environmental impacts and conserving natural and ecological resources during remediation actions (Bardos *et al.*, 2013).

Green remediation was adopted by USEPA, in the United States, to regulate sustainability assessments in remediation projects. Some authors consider green remediation as a variant for SR (Hou *et al.*, 2014b). Others consider that SR can mean green remediation, when it is considered that reduced energy consumption minimizes greenhouse gas emissions; that lower environmental impacts are associated with cost reductions; and that green practices can lead to better and faster social acceptance, since stakeholders generally agree that the remediation process should be driven by the selection of green and environmentally friendly techniques (Baker *et al.*, 2009; Fortuna *et al.*, 2011).

However, most authors point out that the terms are not equivalent and there are differences in its approaches, since the application of green remediation may not achieve the sustainability goals, because alone it does not represent a complete and comprehensive approach, whereas it considers only the environmental aspects (Bardos *et al.*, 2013; Hadley & Harclerode, 2015; Bardos *et al.*, 2016a). Thus, with a view to a broader and holistic approach to sustainability, the two concepts are sometimes considered together as Green and Sustainable Remediation (GSR), addressing a range of environmental, social and economic impacts during all stages of remediation (Reddy & Adams, 2015). Yet, more recently and broadly, the term "sustainable remediation" has been used to express the balanced incorporation of the "Triple Bottom Line" in the context of contaminated sites management and remediation, as shown in Fig. 1, looking beyond the focus solely on risk control, but considering the overall environmental, economic and social benefits and impacts of remediation (Hou & Al-Tabbaa, 2014).

3. Characteristics and Concepts of SR

Sustainability and sustainable development represent complex, subjective and ambiguous concepts. The most commonly sustainability definition quoted internationally and widely accepted is that of the Report of the World Commission on Environment and Development - Brundtland Commission of 1987. Sustainable development is defined as meeting the needs of present generations without compromising the capacity of future generations to meet their own needs (Brundtland, 1987).

Since then, many have promoted adaptations and derivations of this definition to the most different fields, organizations, and specific sectors. SR applies the principles of sustainable development, since the latter has in essence the objective of promoting the balance between considerations of social, environmental and economic aspects, as well as between local and global needs (Bardos *et al.*, 2011; Virkutyte & Varma, 2014; Nathanail *et al.*, 2017).

Sustainable Remediation is an emerging study field and the growing interest and development of its concepts represent the advancement and maturity of contaminated sites remediation industry (Hou *et al.*, 2014b; Hadley & Harclerode, 2015). The understanding of what SR means as a whole has evolved in recent years, largely driven by the work of agencies and organizations working in the context, as well as studies developed by the scientific community (Hou *et al.*, 2014b), and different definitions are linked to the term (Cundy *et al.*, 2013). Table 1 provides the most common definitions used to represent the concept behind SR.

There is a high level of consensus among the definitions given in Table 1. It is clear the broad purpose of SR to reduce environmental, economic, and social impacts and to optimize and/or maximize long-term benefits of remediation projects, in a balanced decision-making process (Cundy *et al.*, 2013; Rizzo *et al.*, 2016). Therefore, the definitions tend to emphasize decision-making in a proportional and balanced way across all three elements/pillars of sustainability; the optimization of process benefits; the search

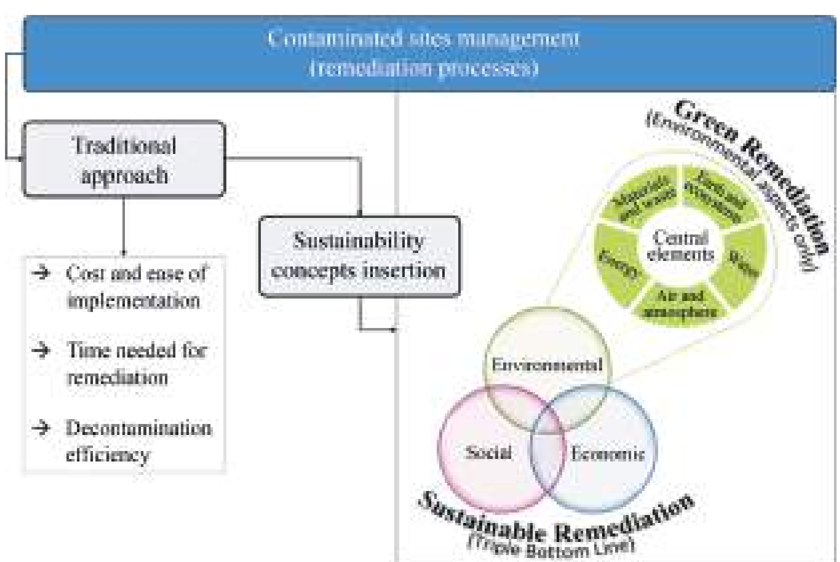

Figure 1 - Evolution of sustainability considerations in the context of contaminated sites remediation.

Table 1 - Examples of defining SR.

Reference	Definition
NICOLE (2010)	A SR project is one that stakeholders agree to represent the best solution considering environmental, social and economic factors, and where the benefits achieved outweigh the impacts.
SuRF-UK (2010)	SR is the practice of demonstrating, in terms of environmental, economic and social indicators, that the benefit of remediation is greater than its impact, and where the optimal solution is selected through a balanced decision.
ITRC (2011a, b)	SR refers to an integrated assessment of the environmental, economic and social impacts of corrective activities.
SuRF-US (Holland *et al.*, 2011)	SR can be defined as an alternative or combination of alternatives whose practice is to protect human health and the environment while maximizing the net environmental, social and economic benefits throughout the life cycle of the remediation project.
ISO (2017)	The practice of SR consists in eliminating and/or controlling the unacceptable risks of the remediation process in a safe and timely manner, optimizing the environmental, social and economic value of work.
Bardos (2014)	SR is a process of finding the ideal means to manage the risks associated with the remediation process. Therefore, in a generic sense it aims to achieve a global net benefit in the face of a series of environmental, economic and social concerns that are considered representative of sustainability.
Holland (2011); Hou *et al.* (2014c); Hadley & Harclerode (2015)	SR seeks to maximize benefits and reduce the overall environmental, economic and social impacts of remediation actions to ensure the protection of human health and the environment.
Bardos *et al.* (2016b)	SR is the process of effectively managing the risks to human health and the environment associated with the contaminated site and remediation processes, so as to minimize environmental footprint, maximize social benefits, and minimize the costs of such remediation activities. In addition, SR is the process that seeks to optimize the selection of remediation activities, promoting the use of more sustainable practices.

for the ideal means to find sustainable solutions; the management of risks and protection of human health and environment in general; the long-term vision; the identification of the best option among those available; the use of indicators to assess sustainability; and stakeholder involvement in the process (Rizzo *et al.*, 2016).

The balance between the three elements of the sustainability tripod has been a key factor in the approach to SR. Environmental elements go beyond soil and groundwater quality, but also include the use of non-renewable resources and the production of waste and air pollutants, for example by adopting *in situ* options that prevent truck driving through a neighborhood, producing exhaust smoke, consuming fuel and energy (Slenders *et al.*, 2017). Social elements are related to the deeper assessment of how the local community and global society are affected in a beneficial way and adversely by remediation activities, such as the nuisance due to dust, odor and noise from remediation work and the overall risk to human health, as well as the risk resulting from physical accidents to workers (Harclerode *et al.*, 2015b; Slenders *et al.*, 2017). The economic elements are associated with the full cost of the short- and long-term life cycle of the remediation process execution, and these must be evaluated in terms of risk reduction, increase in the site value and the resulting use, and improvement of ambience in general (Slenders *et al.*, 2017).

The net benefit has also been a central element of discussion in the conceptualization of SR. Reaching the net benefit is related to choosing alternatives, not only to reduce the risk to the health of site users but also to minimize costs, including both detrimental direct environmental, social and economic impacts during the remediation operation. Besides, this considers indirect harmful impacts during, for example, the acquisition of materials and energy and waste disposal associated with remediation (Forum, 2009; Hou *et al.*, 2017).

The SR approach also encourages the remediated sites reuse in order to achieve sustainable benefits from the entire system, including the brownfields redevelopment. SR in the context of site reuse involves finding the best balance between remediation and reuse options. SR increases value when associated with feasible reuse and increases long-term financial returns for investments. Locations can be reused in a conventional way (*e.g.*, for commercial, industrial or residential use), or require innovative forms of reuse (*e.g.*, for interim or ecological uses) (Bardos *et al.*, 2011; Holland, 2011; Holland *et al.*, 2013; Bardos, 2014; Mobbs *et al.*, 2019).

In general, the main mission of SR continues to be the reduction of the contamination risk, but its concept has brought greater attention to the side effects and contradictions often neglected in contaminated sites management and remediation (Hou & Al-Tabbaa, 2014; Anderson *et al.*, 2018). SR requires not only the identification of a technical solution, but an informed debate, discussion, negotiation and transparent decision-making (Mobbs *et al.*, 2019).

Sustainable Remediation provides a specific context to find the best solution by comparing different corrective alternatives, since there is no definitive sustainable solution (Hou *et al.*, 2018). In view of this, there is a variety of criteria which determine a SR process, and such criteria may include: that future benefits outweigh the cost of remediation; the environmental, social and economic impacts of implementing the remediation process are less than the impact of leaving the site untreated; the remediation process impacts are minimal and measurable; the time scale over which the consequences occur is part of the decision-making process; and the decision-making process includes an appropriate level of involvement of all stakeholders (Al-Tabbaa *et al.*, 2007).

As such, the adoption of SR presents specific benefits that make it an important approach and increasingly necessary in this environment, as well as clear drivers for its realization and fundamental objectives and characteristics (Forum, 2009; Bardos *et al.*, 2011; Fortuna *et al.*, 2011; Kalomoiri & Braida, 2013; Martino *et al.*, 2016; Slenders *et al.*, 2017), as can be seen in Fig. 2.

The importance of sustainability considerations in contaminated sites management is already prominent in political, organizational and business frameworks around the world. In recent years, a growing number of agencies and

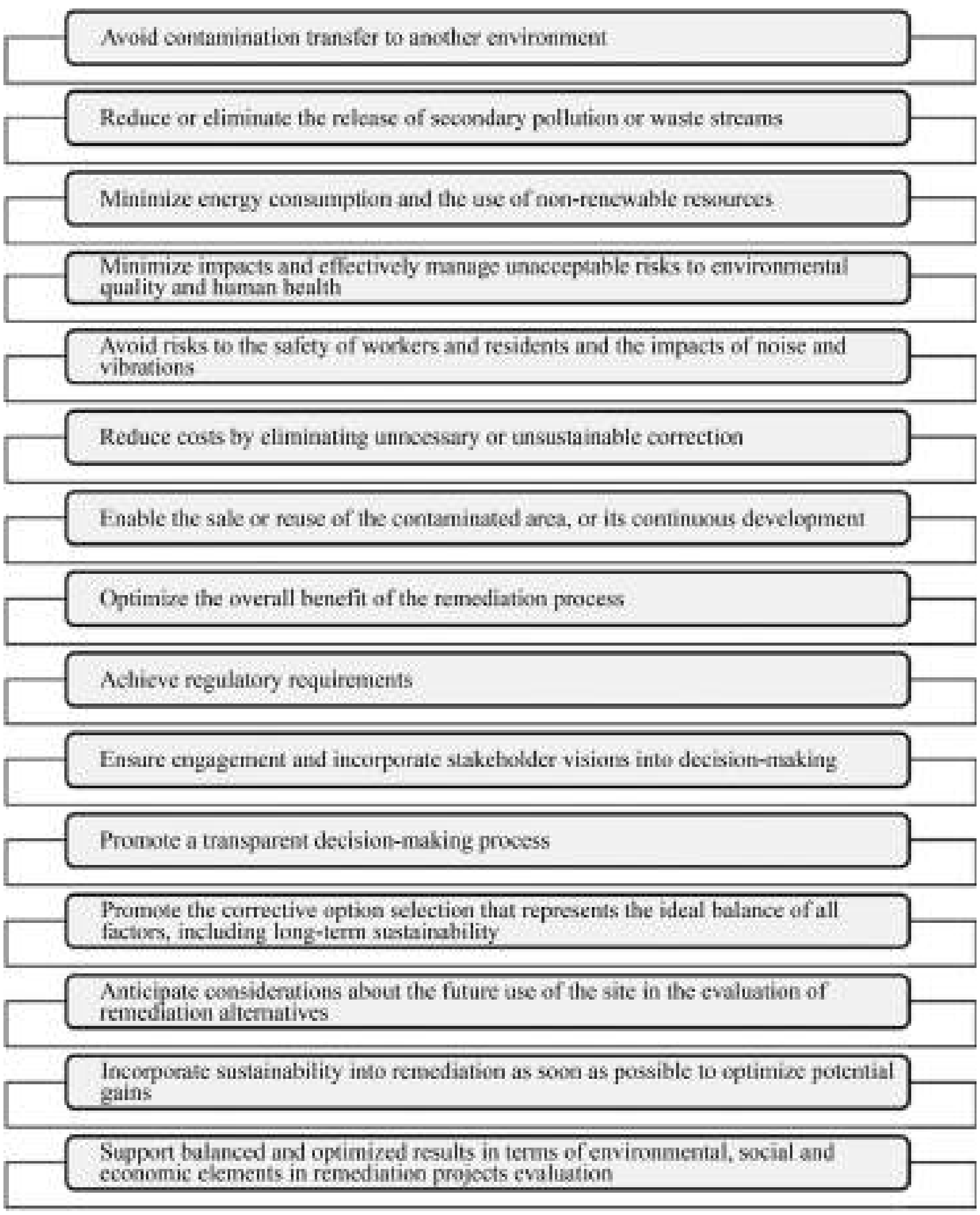

Figure 2 - Main objectives and characteristics of SR.

organizations from different countries have been debating SR and its approach in regulatory contexts (Hou & Li, 2018). These debates are followed by the adoption of SR procedures, publishing technical and normative guidelines, as well as guiding documents with structures, methods and tools to support evaluation and decision making (Holland, 2011; Sparrevik *et al.*, 2011; Huysegoms & Cappuyns, 2017; Anderson *et al.*, 2018; Song *et al.*, 2018).

The Sustainable Remediation Forum (SuRF), which began in the United States and was created in 2006 by professionals involved in remediation projects, researchers and industries, is the first coalition dedicated specifically to the promotion and application of remediation concepts (Bardos *et al.*, 2013; Hadley & Harclerode, 2015). Currently SuRF has partner organizations and groups also in the United Kingdom (SuRF-UK), Brazil (SuRF-Brazil), the Netherlands (SuRF-NL), New Zealand and Australia (SuRF-ANZ), Canada (SuRF-Canada), Italy (SuRF-Italy), China (SuRF-Taiwan), Japan (SuRF-Japan), and Colombia (SuRF-Colombia). These SuRFs share the progress, learning and work each group is carrying out in their different countries towards SR.

In addition to the SuRFs, other organizations are dedicated to developing initiatives for SR, including the United States Environmental Protection Agency (USEPA), the American Society for Testing and Materials (ASTM), the Interstate Technology & Regulatory Council (ITRC), the Network for Industrially Contaminated Land in Europe (NICOLE) and the United Kingdom Institution of Contaminated Land: Applications In Real Environments (CL:AIRE) (Bardos *et al.*, 2013; Hadley & Harclerode, 2015). The United Kingdom, where sustainability is widely recognized in regulation and used in practice, plays a leading role in promoting SR through the dynamic actions of CL:AIRE and SuRF-UK organizations (Hou *et al.*, 2014c; Rizzo *et al.*, 2016; Hou & Li, 2018).

These organizations produce several publications covering recommendations, guidelines, frameworks, standards and tools for evaluating SR, which fit in the context of different countries and regions and assist in its implementation in remediation activities (Hou *et al.*, 2016; Huang *et al.*, 2016). In the last decade, several events have been highlighted with the objective of promoting SR, some of which are presented in Fig. 3. One of the highlights is the publication of ISO 18504 in 2017, which is the first document with global coverage in the field of SR, consolidating the international state of practices on the approach and evaluation of sustainability in the context of remediation options (Rizzo *et al.*, 2016; ISO, 2017; Nathanail *et al.*, 2017; Bardos *et al.*, 2018).

This evolution in the approaches, orientations, structures and case studies focused on the discourse of sustainability in the contaminated sites remediation can also be perceived in the scientific production scenario. A survey of the Institute for Scientific Information (ISI) Scopus database indicates that the number of publications pertaining to SR has grown exponentially over the last decade (Fig. 3). According to Fig. 3, the first publications began in 1999, and since 2008 the total number of articles published began to grow, reaching its peak in 2014 and 2016. Besides this, according to our latest survey of the Scopus database (March 18, 2019), in 2019 there are already 29 publications, surpassing the year 2017 and with only two publications less than 2018. This shows that the concerns in this

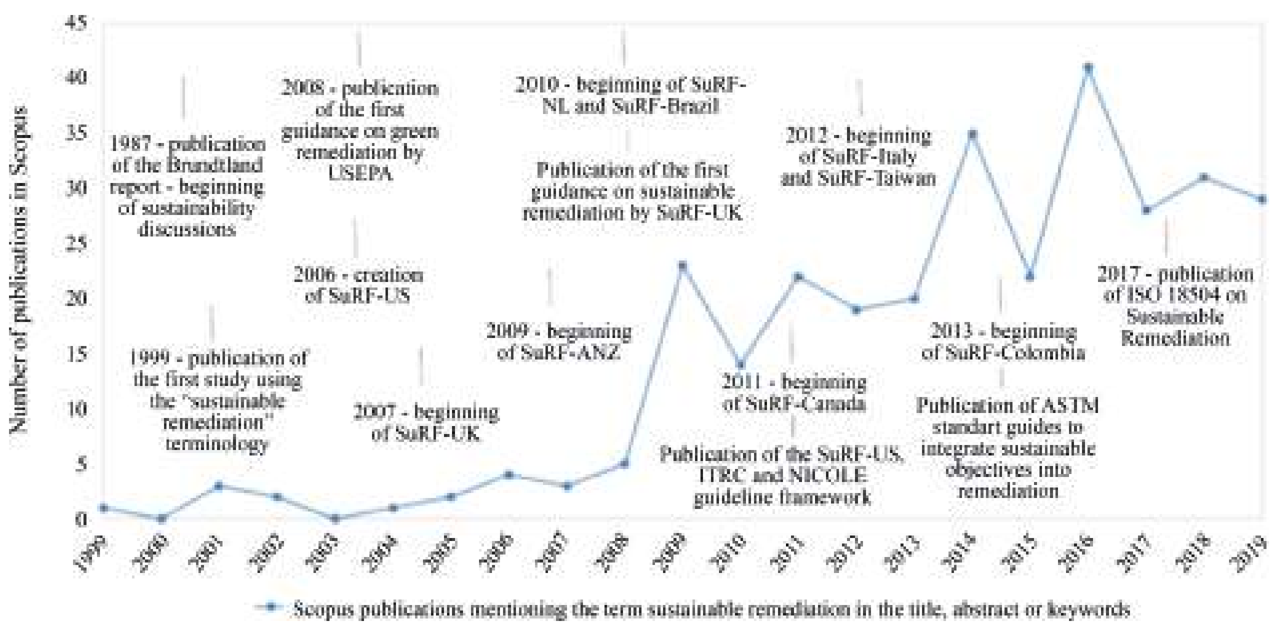

Figure 3 - Exponential growth of publications on SR and historical events. Source: Elaborated by the authors based on Bardos *et al.* (2013); Bardos (2014); Bardos *et al.* (2016b); Scopus (2018).

context tend to grow increasingly, since sustainability is at the peak of global discussions.

In this context, Brazil has only seven publications related to the subject. A situation that is due in large part to the fact that Brazil still does not have a concise approach towards SR in its regulatory context on the management of contaminated sites.

Taking into account all these approaches to SR, their incorporation can occur at all stages of the remediation processes life cycle, involving project stakeholders, principles, indicators, metrics, tools and methods to support the evaluation of potential sustainable correction alternatives (Petruzzi, 2011), as can be seen in Fig. 4.

3.1. Stakeholders involvement in SR processes

Involvement of stakeholders is an important practice of SR. It is widely recognized that decision-making and successful management and remediation of contaminated sites depends to a large extent on the interaction of a variety of stakeholders, each with its unique demand (Hou *et al.*, 2014a; Hou & Al-Tabbaa, 2014; Hou, 2016).

Stakeholders correspond to an organization, group or person that may potentially be directly or indirectly affected by some of the remediation project stages, or those that have an interest in solving the problem (Cundy *et al.*, 2013). Among the stakeholders who have the strongest influence on the sustainable practices adoption are: the owner of the site; federal, state, and local regulatory agencies; primary planners or consultants; the workers; local residents and neighboring sites affected by remediation actions; and researchers (Forum, 2009; Cundy *et al.*, 2013; Kalomoiri & Braida, 2013; Hou *et al.*, 2014a; Hou & Al-Tabbaa, 2014).

Site owners manage the costs of remediation and long-term administration of the property's environmental issues. Regulators, however, balance regulatory requirements with SR and reuse approaches. And finally, the involvement of the resident community and society in general increases their awareness of the risks associated with contamination and related remediation activities, and thus seeks to protect the environment and economic and quality-of-life improvements (Holland *et al.*, 2013; Harclerode *et al.*, 2016).

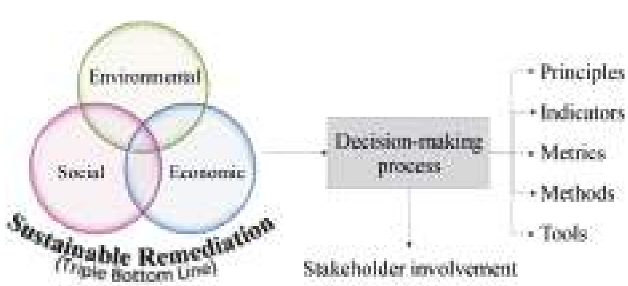

Figure 4 - Forms and stages of incorporation and evaluation of SR.

For the involvement of these stakeholders in remediation projects, some basic principles should be considered, such as: identifying and involving all stakeholders at the outset of the process; adopting a proactive approach; involve stakeholders at all stages of the process; planning long-term engagement; developing effective communication structures to enable reciprocal dialogue; ensuring that involvement is transparent and registered; recognizing that the criteria for assessing indicators may be subjective or objective; defining all assumptions clearly at the beginning of each step; and following a logical and gradual approach to avoid circular discussions and clearly address subjective issues (Cundy *et al.*, 2013). In addition, in order for this involvement to take place satisfactorily, stakeholders need to be aware of the limits of the remediation process and the objectives of SR (Kalomoiri & Braida, 2013).

Understanding the concepts of SR may not be the same for all these groups. O'Connor *et al.* (2019) observed that, on average, primary consultants gave higher scores for the environmental and social impacts analyzed than those given by regulators. However, across different perspectives, through transdisciplinary processes and communication or negotiation among stakeholders, consensus can be reached on a mutually beneficial and project-specific definition of sustainability and driving the adoption of sustainable practices (Forum, 2009; Hou, 2016). In addition, regulatory agencies play one of the most important roles among all stakeholders as they lead oversight of remediation activities and can act as mediators in disseminating sustainability concepts to other stakeholders in the process, as well as providing technical guidance to stakeholders. (Hou & Al-Tabbaa, 2014).

In general, stakeholder engagement is a vital SR practice to obtain useful feedback and identify the needs of all stakeholders and society at large (Harclerode *et al.*, 2016). In addition, it ensures that the uncertainties of sustainability assessment are minimized by allowing stakeholders to provide a balance of potential impacts and benefits (Cappuyns, 2016; NICOLE, 2010). Also, according to Harclerode *et al.* (2015b), stakeholder contributions already at the beginning of a remediation project can prevent conflicts, reduce unnecessary corrective measures, and help define the appropriate sustainability indicators acceptable to the context and acceptable to stakeholders.

However, since SR is still an emerging concept, stakeholders may not have enough knowledge to proactively stimulate and encourage sustainable practices, leading to divergent views and perceptions (Hou *et al.*, 2014a; Hou, 2016). In addition, dissemination and public engagement in remediation projects are still very limited, especially in developing countries, and greater incentives and improvements are needed to overcome these obstacles (O'Connor *et al.*, 2019). In this way, Hou *et al.* (2014a) have observed that although the involvement of different stakeholders affects behavior towards sustainability, their greatest influence is exerted through institutional forces, that is, in most cases, the institutionalization of specific environmental practices still precedes the influence stakeholders.

4. Sustainability Evaluation in Remediation

The sustainability evaluation in remediation is a key component of integrating diverse information to support decision making on SR (Rosén *et al.*, 2015). According to Hou *et al.* (2014d), the main objective of sustainability assessment in remediation is to collect information so that decision makers and stakeholders can manage complex systems with a holistic view. For Gibson *et al.* (2005), assessing sustainability while pursuing a general approach to sustainability contributes to defining the specificities of sustainability in particular circumstances.

Alternatively, assessing the sustainability of remediation is quite complex and usually involves a great deal of information from different sources, such as concrete data from on-the-spot investigations, environmental footprint analyzes, economic and social analyzes, as well as information that reflects views and preferences between those involved (Rosén *et al.*, 2015). Thus, the sustainability evaluation in remediation is a process that requires a set of individual criteria to be agreed upon by those who carry out the evaluation, defining what is relevant to the project perspectives and stakeholders (Bardos *et al.*, 2018).

The sustainability evaluation seeks to identify the impacts and benefits of a remediation project (Song *et al.*, 2018); to address and balance both local and regional/global dimensions, and to cover both short-term and long-term prospects (Hou *et al.*, 2014d; Hou *et al.*, 2018); and to manage, inform, compare, select, verify performance, and optimize appropriate remedial solutions and processes (Bardos *et al.*, 2018).

In general, the sustainability evaluation in remediation is facilitated by the use of principles, indicators, metrics, methods, and tools that can be used to ensure the practicality of SR.

The principles usually address a number of common issues, such as ecological integrity, social equity, the sustainability tripod, immediate and long-term sufficiency, and democratic processes (Ridsdale & Noble, 2016). The six principles of SR listed by SuRF-UK are often cited and used in this context (SuRF-UK, 2011). However, a number of agencies and organizations already provide lists of SR principles, new and/or complementary to those listed by SuRF-UK, to guide decision-makers (Department of Defence, 2010; ITRC, 2011a; NICOLE, 2012; ISO, 2017).

An indicator is a unique feature or a specific observable measure that expresses an environmental, social or economic aspect and results in a sustainability effect. These indicators can be measured to monitor and compare the performance of different remediation options according to criteria in question and to a specific site (NICOLE, 2012; Beames *et al.*, 2014; Virkutyte & Varma, 2014). In general, the indicators can be objective or subjective, with qualitative or quantitative approaches (Reddy & Adams, 2015; Tilla & Blumberga, 2018). And in this context, although there is no set of indicators standardized, the list of indicators for SR presented by SuRF-UK is the most well-known and frequently used in studies (SuRF-UK, 2011).

Indicators may not be easily measurable, requiring metrics to be integrated, so that they can be evaluated objectively and accurately. Sustainability metrics are numerical values that can be used to assess or determine the degree of success, performance or progress that a particular project or alternative can achieve in relation to sustainability dimensions (Reddy & Adams, 2015). As for indicators, there is also no commonly accepted set of metrics. SuRF presents an extensive list of metrics for SR in its metrics toolbox, which tabulates metrics for each phase of the remediation process. However, for the purpose of evaluating SR, the ITRC set provides a compilation of reasonably complete SR metrics, built from reputable sources and which can therefore be used as a basis in this context (ITRC, 2011a).

The methods or frameworks are conceptual and systematic forms of decision making that assist in the sustainability evaluation of a remediation project regarding environmental, social and economic aspects. In addition, they help evaluate the indicators and sustainability metrics of a remediation project (Reddy & Adams, 2015). A standardized and universally accepted method has not yet been developed. However, agencies and organizations in many countries have been active in developing structures to facilitate the sustainability assessment in contaminated sites remediation. This is especially perceived in regions where discussions on SR are in a more advanced process, such as the United States and Europe (Reddy & Adams, 2015; Ridsdale & Noble, 2016; Rizzo *et al.*, 2016; Slenders *et al.*, 2017).

In the world scenario, the developed methods correspond to: USEPA (US Environmental Protection Agency) (USEPA, 2012); ASTM (American Society for Testing and Materials) (ASTM, 2013); ITRC (Interstate Technology and Regulatory Council) (ITRC, 2011b); NICOLE (Network for Industrially Contaminated Land in Europe) (NICOLE, 2010); and four groups associated with the SuRF (Sustainable Remediation Forum) - United States (Holland *et al.*, 2011), United Kingdom (SuRF-UK, 2010), Australia and New Zealand (Smith & Nadebaum, 2016), and Taiwan (Huang *et al.*, 2016). At the Brazilian level, there are some initiatives aimed at SR, such as SuRF-Brazil and NICOLE Brazil, but the approach to sustainability issues and effective actions is still very limited. Therefore, no methods developed for the sustainability analysis in remediation are identified in the country.

The methods, as they are consisting in decision-making processes, often use tools during its stages to assist in the remediation project sustainability analysis. The Decision Support Tools (DSTs) comprise step-by-step approaches, which include qualitative, semi-quantitative or fully quantitative analyzes of remediation processes (Smith & Kerrison, 2013; Reddy & Adams, 2015; Anderson *et al.*, 2018).

In recent years a number of sustainability assessment tools have become available. These tools, of varying type and scope, may be in the public domain, sold as software for profit, or limited to use within a particular organization, which offer different levels of comprehensiveness, complexity and analysis (Holland *et al.*, 2011; Beames *et al.*, 2014; Reddy & Adams, 2015). In addition, tools can range from simple decision trees or spreadsheets, tables or graphs in Excel, to full life cycle assessments (Reddy & Adams, 2015; Huang *et al.*, 2016).

Many agencies, organizations, and studies categorize, list, and define the existing set of tools (Bardos *et al.*, 2002; Harclerode *et al.*, 2015b; Reddy & Adams, 2015; Cappuyns, 2016). Other studies aim to develop structures for sustainability evaluating of remediation projects, incorporating in decision-making the different tools already available (Halog & Manik, 2011; Kalomoiri & Braida, 2013; Yasutaka *et al.*, 2016; Hou *et al.*, 2017; Zheng *et al.*, 2019). In a more practical context, a considerable number of studies have already been carried out using different tools to analyze the impacts of remediation techniques, evaluating them and classifying for sustainability (Hou *et al.*, 2014b; Anderson *et al.*, 2018).

Therefore, there are already several evaluation and decision support tools for choosing more SR alternatives. However, more and more flexible instruments are needed to address the full range of indicators and metrics in the three dimensions of sustainability and to be applicable from project design to project reuse (Huysegoms & Cappuyns, 2017).

5. Conclusions

It is recognized in the academic world that sustainable remediation (SR), unlike traditional remediation and green remediation, presents a broader vision, bringing the incorporation of sustainability concepts in the management and remediation projects of contaminated sites. It may be noted that the main objective of SR is to consider both environmental, social and economic impacts and benefits that the application of a remediation technique can generate, always with a view to selecting the most sustainable option among those considered.

Great advances are observed in the SR field, especially with the creation of the Sustainable Remediation Forum (SuRF) in 2006 in the United States, in addition to the efforts of Agencies and Organizations in several countries to disseminate guidelines for the objective application of SR. In addition, the ISO 18504 publication, which comes to standardize the main outstanding issues regarding the orientation and implementation of SR concepts, represented a huge advance.

However, the practical application of SR in the remediation processes still needs to be improved. The concepts of SR are still very new in much of the world, as in the case of Brazil. The principles, indicators, metrics, methods and tools do not yet have standardization for worldwide use. In this way, the inclusion of sustainability in remediation should start from the dissemination of knowledge about SR, favoring the involvement of stakeholders in the decision-making processes.

Also, it is noted that, in order for the SR approach within the management of contaminated sites to continue to move forward, the SR should be seen as a new way of thinking about contaminated sites remediation, where the integration of economic, environmental, and social variables must be considered a fundamental factor in decision making.

Acknowledgments

The authors desire to express their gratitude to Research Group on Environmental Geotechnics and the Graduate Program in Civil and Environmental Engineering of University of Passo Fundo, and to the Coordination for the Improvement of Higher Education Personnel (CAPES) and Foundation for Research Support of the State of Rio Grande do Sul (FAPERGS) for funding the research group.

References

Adams, J.A. & Reddy, K.R. (2012). State-of-the-Practice of Characterization and Remediation of Contaminated Sites. Geotechnical Engineering State of the Art and Practice, pp. 423-442.

Al-Tabbaa, A.; Harbottle, M. & Evans, C. (2007). Robust Sustainable Technical Solutions. Sustainable Brownfield Regeneration, pp. 203-236.

Anderson, R.; Norrman, J.; Voltar, P.E.; Söderqvist, T. & Rosen, L. (2018). What's the point? The contribution of a sustainability view in contaminated site remediation. Science of The Total Environment, 630:103-116.

ASTM (2013). Standard Guide for Integrating Sustainable Objectives into Cleanup - E2876-13. ASTM International, West Conshohocken, Pennsylvania, USA.

Baker, C.B.; Smith, L.M. & Woodward, D.S. (2009). The Sustainable Remediation Forum. Remediation Journal, 9(4):135-139.

Bardos, P.; Lewis, A.; Nortcliff, S.; Matiotti, C.; Marot, F. & Sullivan, T. (2002). Review of Decision Support Tools for Contaminated Land Management, and their Use in Europe. Final report. Austria: Umweltbundesamt - Federal Environment Agency, on behalf of Contaminated Land Rehabilitation Network for Environmental Technologies (CLARINET), 192 p.

Bardos, P.; Bone, B.; Boyle, R.; Ellis, D.; Evans, F.; Harries, N.D. & Smith, J.W.N. (2011). Applying sustainable development principles to contaminated land management using the SuRF-UK framework. Remediation Journal, 21(2):77-100.

Bardos, P.; Bakker, L.; Darmendrail, D.; Harries, N.; Holland, K.; Mackay, S.; Pachon, C.; Slenders, H.; Smith, G.; Smith, J. & Wiltshire, L. (2013). Sustainable and green remediation - Global update. Proc. 12th AquaConSoil: ThS E3 Sustainable use of the subsurface, Barcelona.

Bardos, P. (2014). Progress in sustainable remediation. Remediation Journal, 25(1):23-32.

Bardos, R.P.; Cundy, A.B.; Smith, J.W.N. & Harries, N. (2016a). Sustainable remediation. Journal of Environmental Management, 184:1-3.

Bardos, R.P.; Bone, B.D.; Boyle, R.; Evans, F.; Harries, N.D.; Howard, T. & Smith, J.W.N. (2016b). The rationale for simple approaches for sustainability assessment and management in contaminated land practice. Science of the Total Environment, 563-564:755-768.

Bardos, R.P.; Thomas, H.F.; Smith, J.W.N.; Harries, N.D.; Evans, F.; Boyle, R.; Howard, T.; Lewis, R.; Thomas, A.O. & Haslam, A. (2018). The development and use of sustainability criteria in SuRF-UK's sustainable remediation framework. Sustainability, 10(6):1781-1803.

Beames, A.; Broekx, S.; Lookman, R.; Touchant, K. & Seuntjens, P. (2014). Sustainability appraisal tools for soil and groundwater remediation: How is the choice of remediation alternative influenced by different sets of sustainability indicators and tool structures? Science of The Total Environment, 470-471:954-966.

Brundtland, G.H. (1987). Report of the World Commission on Environment and Development: Our Common Future. Oslo, 300 p. Available at: http://www.un-documents.net/wced-ocf.htm and downloaded on March 15th 2019.

Cappuyns, V. (2016). Inclusion of social indicators in decision support tools for the selection of sustainable site remediation options. Journal of Environmental Management, 184:45-56.

Cundy, A.B.; Bardos, R.P.; Church, A.; Puschenreiter, M.; Friesl-Hanl, W.; Müller, I.; Neu, S.; Mench, M.; Witters, N. & Vangronsveld, J. (2013). Developing principles of sustainability and stakeholder engagement for "gentle" remediation approaches: The European context. Journal of Environmental Management, 129:283-291.

Department of Defence (2010). Guidelines for Consideration of Sustainability in Remediation of Contaminated Sites. Australian, 29 p. Available at: http://www.defence.gov.au/estatemanagement/Governance/Policy/Environment/Contamination/Docs/SustainabilityRemediationGuidelines.pdf and downloaded on March 15th 2019.

Favara, P. & Gamlin, J. (2017). Utilization of waste materials, non-refined materials, and renewable energy in in situ remediation and their sustainability benefits. Journal of Environmental Management, 204:730-737.

Fortuna, M.E.; Simion, I.M. & Gavrilescu, M. (2011). Sustainability in environmental remediation. Environmental Engineering and Management Journal, 10(12):1987-1996.

Forum, U.S. (2009). Sustainable remediation white paper - Integrating sustainable principles, practices, and metrics into remediation projects. Remediation Journal, 19(3):5-114.

Gibson, B.; Hassan, S.; Holtz; S.; Tansey, J. & Whitelaw, G. (2005). Sustainability Assessment: Criteria and Processes. Earthscan, London, 268 p.

Hadley, P.W. & Harclerode, M. (2015). Green remediation or sustainable remediation: moving from dialogue to common practice. Remediation Journal, 25(2):95-115.

Halog, A. & Manik, Y. (2011). Advancing integrated systems modelling framework for life cycle sustainability assessment. Sustainability, 3(2):469-499.

Harclerode, M.A.; Lal, P. & Miller, M.E. (2015a). Quantifying global impacts to society from the consumption of natural resources during environmental remediation activities. Journal of Industrial Ecology, 20(3):410-422.

Harclerode, M.; Ridsdale, D.R.; Darmendrail, D.; Bardos, P.; Alexandrescu, F.; Nathanail, P.; Pizzol, L. & Rizzo, E. (2015b). Integrating the social dimension in remediation decision-making: State of the practice and way forward. Remediation Journal, 26(1):11-42.

Harclerode, M.A.; Lal, P.; Vedwan, N.; Wolde, B. & Miller, M.E. (2016). Evaluation of the role of risk perception in stakeholder engagement to prevent lead exposure in an urban setting. Journal of Environmental Management, 184:132-142.

Holland, K.S.A. (2011). Framework for sustainable remediation. Environmental Science & Technology, 45(17):7116-7117.

Holland, K.S.; Lewis, R.E.; Tipton, K.; Karnis, S.; Dona, C.; Petrovskis, E.; Bull, L. P.; Taege, D. & Hook, C. (2011). Framework for integrating sustainability into remediation projects. Remediation Journal, 21(3):7-38.

Holland, K.; Karnis, S.; Kasner, D.A.; Brandt, P.B.; Hadley, P.W.; Nathanail, P.; Ryan, J.; Smith, L.M. & Wice, R. (2013). Integrating remediation and reuse to achieve whole-system sustainability benefits. Remediation Journal, 23(2):5-17.

Hou, D. & Al-Tabbaa, A. (2014). Sustainability: A new imperative in contaminated land remediation. Environmental Science & Policy, 39:25-34.

Hou, D.; Al-Tabbaa, A.; Chen, H. & Mamic, I. (2014a). Factor analysis and structural equation modelling of sustainable behavior in contaminated land remediation. Journal of Cleaner Production, 84:439-449.

Hou, D.; Al-Tabbaa, A. & Luo, J. (2014b). Assessing effects of site characteristics on remediation secondary life cycle impact with a generalized framework. Journal of Environmental Planning and Management, 57(7):1083-1100.

Hou, D.; Al-Tabbaa, A. & Guthrie, P. (2014c). The adoption of sustainable remediation behaviour in the US and UK: A cross country comparison and determinant analysis. Science of The Total Environment, 490:905-913.

Hou, D.; Al-Tabbaa, A.; Guthrie, P.; Hellings, J. & Gu, Q. (2014d). Using a hybrid LCA method to evaluate the sustainability of sediment remediation at the London Olympic Park. Journal of Cleaner Production, 83:87-95.

Hou, D. (2016). Divergence in stakeholder perception of sustainable remediation. Sustainability Science, 11(2):215-230.

Hou, D.; Guthrie, P. & Rigby, M. (2016). Assessing the trend in sustainable remediation: A questionnaire survey of remediation professionals in various countries. Journal of Environmental Management, 184:18-26.

Hou, D.; Qi, S.; Zhao, B.; Rigby, M. & O'Connor, D. (2017). Incorporating life cycle assessment with health risk assessment to select the `greenest' cleanup level for Pb contaminated soil. Journal of Cleaner Production, 162:1157-1168.

Hou, D.; Ding, Z.; Li, G.; Wu, L.; Hu, P.; Guo, G.; Wang, X.; Ma, Y.; O'Connor, D. & Wang, X. (2018). A sustainability assessment framework for agricultural land remediation in China. Land Degradation & Development, 29(4):1005-1018.

Hou, D. & Li, G. (2018). Green and sustainable remediation movement in the new millennium and its relevance to China. Luo, Y. & Tu, C. (eds), Twenty Years of Research and Development on Soil Pollution and Remediation in China. Science Press and Springer, China, pp. 39-53.

Huang, W.-Y.; Hung, W.; Vu, C.T.; Chen, W.-T.; Lai, J.-W. & Lin, C. (2016). Green and sustainable remediation (GSR) evaluation: framework, standards, and tool. A case study in Taiwan. Environmental Science and Pollution Research, 23(21):21712-21725.

Huysegoms, L. & Cappuyns, V. (2017). Critical review of decision support tools for sustainability assessment of site remediation options. Journal of Environmental Management, 196:278-296.

ISO (2017). Soil Quality e Guidance on Sustainable Remediation - ISO/DIS 18504. International Standards Organization, Geneva, Switzerland, 23 p.

ITRC (2011a). Green and Sustainable Remediation: State of the Science and Practice. Interstate Technology & Regulatory Council, Washington, D.C., EUA, 84 p.

ITRC (2011b). Green and Sustainable Remediation: a Practical Framework. Interstate Technology & Regulatory Council, Washington, D.C., EUA, 135 p.

Kalomoiri, A. & Braida, W. (2013). Promoting decision making through a Sustainable Remediation Assessment Matrix (SRAM). International Journal Innovation and Sustainable Development, 7(3):252-270.

Martino, L.E.; Dona, C.L.; Dicerbo, J.; Hawkins, A.; Moore, B. & Horner, R. (2016). Green and sustainable remediation practices in Federal Agency cleanup programs. Environmental Earth Sciences, 75(21):3-13.

Mobbs, S.; Orr, P. & Weber, I. (2019). Strategic considerations for the sustainable remediation of nuclear installations. Journal of Environmental Radioactivity, 196:153-163.

Nathanail, C.P.; Bakker, L.M.M.; Bardos, P.; Furukawa, Y.; Nardella, A.; Smith, G.; Smith, J.W.N. & Goetsche, G. (2017). Towards an international standard: The ISO/DIS 18504 standard on sustainable remediation. Remediation Journal, 28(1):9-15.

NICOLE (2010). NICOLE Road Map for Sustainable Remediation. Network for Industrially Contaminated Land in Europe, Rotterdam, Netherlands, 4 p.

NICOLE (2012). How to Implement Sustainable Remediation in a Contaminated Land Management Project? NICOLE Sustainable Remediation Work Group 2012 Report. Network for Industrially Contaminated Land in Europe, Rotterdam, Netherlands, 61 p.

O'Connor, D. & Hou, D. (2018). Targeting cleanups towards a more sustainable future. Environmental Science: Processes & Impacts, 20(2):266-269.

O'Connor, D.; Müller-Grabherr, D. & Hou, D. (2019). Strengthening social-environmental management at contaminated sites to bolster green and sustainable remediation via a survey. Chemosphere, 225:295-303.

Petruzzi, N.M. (2011). A case study on the evaluation and implementation of green and sustainable remediation principles and practices during a RCRA corrective action cleanup. Ground Water Monitoring & Remediation, 31(2):63-71.

Pollard, S.J.T.; Brookes, A.; Earl, N.; Lowe, J.; Kearney, T. & Nathanail, C.P. (2004). Integrating decision tools for the sustainable management of land contamination. Science of the Total Environment, 325(1-3):15-28.

Reddy, K.R. & Adams, J.A. (2015). Sustainable Remediation of Contaminated Sites. Momentum Press, New York, 268 p.

Reinikainen, J.; Sorvari, J. & Tikkanen, S. (2016). Finnish policy approach and measures for the promotion of sustainability in contaminated land management. Journal of Environmental Management, 184:108-119.

Ridsdale, D.R. & Noble, B.F. (2016). Assessing sustainable remediation frameworks using sustainability principles. Journal of Environmental Management, 184:36-44.

Rizzo, E.; Bardos, P.; Pizzol, L.; Critto, A.; Giubilato, E.; Marcomini, A.; Albano, C.; Darmendrail, D.; Döberl, G.; Harclerode, M.; Harries, N.; Nathanail, P.; Pachon, C.; Rodriguez, A.; Slenders, H. & Smith, G. (2016). Comparison of international approaches to sustainable remediation. Journal of Environmental Management, 184:4-17.

Rosén, L.; Back, P.E.; Söderqvist, T.; Norrman, J.; Brinkhoff, P.; Norberg, T.; Volchko, Y.; Norin, M.; Bergknut, M. & Döberl, G. (2015). SCORE: A novel multi-criteria decision analysis approach to assessing the sustainability of contaminated land remediation. Science of The Total Environment, 511:621-638.

Scopus (2018). Document Search. Available at: https://www.scopus.com/home.uri and downloaded on March 18th 2019.

Slenders, H.L.A.; Bakker, L.; Bardos, P.; Verburg, R.; Alphenaar, A.; Darmendrail, D. & Nadebaum, P. (2017). There are more than three reasons to consider sustainable remediation, a Dutch perspective. Remediation Journal, 27(2):77-97.

Smith, J.W.N. & Kerrison, G. (2013). Benchmarking of decision-support tools used for tiered sustainable remediation appraisal. Water, Air & Soil Pollution, 224(1706):1-11.

Smith, G. & Nadebaum, P. (2016). The evolution of sustainable remediation in Australia and New Zealand: A storyline. Journal of Environmental Management, 184:27-35.

Søndergaard, G.L.; Binning, P.J.; Bondgaard, M. & Bjerg, P.L. (2017). Multi-criteria assessment tool for sustainability appraisal of remediation alternatives for a contaminated site. Journal of Soils and Sediments, 18(11):3334-3348.

Song, Y.; Hou, D.; Zhang, J.; O'Connor, D.; Li, G.; Gu, G.; Li, S. & Liu, P. (2018). Environmental and socio-economic sustainability appraisal of contaminated land remediation strategies: A case study at a mega-site in China. Science of the Total Environment, 610-611:391-401.

Sparrevik, M.; Saloranta, T.; Cornelissen, G.; Eek, E.; Fet, A.M.; Breedveld, G.D. & Linkov, I. (2011). Use of life cycle assessments to evaluate the environmental footprint of contaminated sediment remediation. Environmental Science and Technology, 45(10):4235-4241.

SuRF-UK (2010). A Framework for Assessing the Sustainability of Soil and Groundwater Remediation. Sustainable Remediation Forum UK and Contaminated Land: Applications in Real Environments (CL:AIRE), London, United Kingdom, 63 p.

SuRF-UK (2011). Annex 1: The SuRF-UK Indicator Set for Sustainable Remediation Assessment. Sustainable Remediation Forum UK and Contaminated Land: Applications in Real Environments (CL:AIRE), London, United Kingdom, 18 p.

Tilla, I. & Blumberga, D. (2018). Qualitative indicator analysis of a sustainable remediation. Energy Procedia, 147:588-593.

USEPA (2008). Green Remediation: Incorporating Sustainable Environmental Practices into Remediation of Contaminated Sites. U.S. Environmental Protection Agency, Washington, D.C., EUA, 56 p.

USEPA (2011). Introduction to Green Remediation. U.S. Environmental Protection Agency, Washington, D.C., EUA, 2 p.

USEPA (2012). Methodology for Understanding and Reducing a Project's Environmental Footprint. U.S. Environmental Protection Agency, Washington, D.C., EUA, 135 p.

Van Liedekerke, M.; Prokop, G.; Rabl-Berger, S.; Kibblewhite, M. & Louwagie, G. (2014). Progress in Management of Contaminated Sites in Europe. European Union, Luxembourg, 72 p.

Vidonish, J.E.; Zygourakis, K.; Masiello, C.A.; Sabadell, G. & Alvarez, P.J.J. (2016). Thermal treatment of hydrocarbon-impacted soils: A review of technology innovation for sustainable remediation. Engineering, 2(4):426-437.

Vik, E.A.; Bardos, P.; Brogan, J.; Edwards, D.; Gondi, F.; Henrysson, T.; Jensen, B.K.; Jorge, C.; Mariotti, C.; Nathanail, P. & Papssiopi, N. (2001). Towards a framework for selecting remediation technologies for contaminated sites. Land Contamination and Reclamation, 9(1):119-127.

Virkutyte, J. & Varma, R.S. (2014). Greener and Sustainable Remediation Using Iron Nanomaterials. ACS Symposium Series, pp. 1-21.

Yasutaka, T.; Zhang, H.; Murayama, K.; Hama, Y.; Tsukada, T. & Furukawa, Y. (2016). Development of a green remediation tool in Japan. Science of The Total Environment, 563-564:813-821.

Zheng, Z.J.; Lin, M.Y.; Chiueh, P.T. & Lo, S.L. (2019). Framework for determining optimal strategy for sustainable remediation of contaminated sediment: A case study in Northern Taiwan. Science of The Total Environment, 654:822-831.

Prediction of Compression Index of Soft Soils from the Brazilian Coast Using Artificial Neural Networks and Empirical Correlations

A.G. Oliveira Filho, L.B. Totola, K.V. Bicalho, W.H. Hisatugu

Abstract. This paper aims to explore the potential use of artificial neural networks (ANNs) to predict the compression index (C_c) of soft soils from the Brazilian coast. Results from 225 standard consolidation (oedometer) tests and the corresponding soil index properties (*i.e.*, initial void ratio, natural water content and Atterberg limits) of a wide variety of fine-grained soils reported in the literature were compiled and investigated herein. The ANN prediction performance is compared with linear empirical correlations created from the database investigated. In addition, correlations presented in the literature are also used and evaluated through different statistical techniques. Overall, for the organized dataset, the ANN outperformed the empirical correlations, highlighting the fragility and limitations of single and multiple variable linear empirical correlations.

Keywords: artificial neural network, compression index, empirical correlations, soft soils, statistical analysis.

1. Introduction

The idealized linear relationship between void ratio and log of effective consolidation pressure of a normally consolidated clay that applies over a range of stresses and void ratios defines the compression index (C_c). The C_c obtained from the consolidation test on clay may be a useful engineering approximation for predictions of consolidation settlement of normally consolidated natural clays. At a given value of effective consolidation pressure, the void ratio of a normally consolidated natural clay depends on the nature and amount of clay minerals present, as indicated by the liquid limit (Skempton, 1970). The greater the liquid limit, the higher the void ratio in a soil. Moreover, previous published empirical relationships between C_c and soil index properties are often used during preliminary investigation of suitability of a foundation site during planning stages.

While conducting the laboratory test is indispensable, it is also relatively time-consuming. In addition, sufficient undisturbed field samples are often difficult and costly to obtain. For these reasons, numerous studies have been made to predict the C_c from soil index properties, obtained from tests more easily carried out (Djoenaidi, 1985). Many researchers have published empirical correlations estimating C_c from soil index properties around the world (*e.g.* Terzaghi & Peck, 1967; Azzouz *et al.*, 1976; Ozer *et al.*, 2008; Kalantary & Kordnaeij, 2012; McCabe *et al.*, 2014; and Kootahi & Moradi, 2016) and for Brazilian soft soils (Futai *et al.*, 2008; Coutinho & Bello, 2014; Baroni & Almeida, 2017). However, empirical correlations may not be applied to soils elsewhere without consideration of soil origin, and the multiplicity of existing empirical correlations indicates the need of evaluation criteria for their use.

The artificial neural networks (ANNs) technique has been used in geotechnical engineering for prediction of engineering properties of soils based on previously known index properties of these soils. The work of Rumelhart *et al.* (1986) on the backpropagation algorithm is a milestone in the use of ANN in civil engineering studies. Further studies on the application of ANN in geotechnical engineering include the prediction of properties like the hydraulic conductivity in clays (Goh, 1995), the optimum water content and the corresponding maximum dry density of the soil (Najjar *et al.*, 1996) and the residual friction angle prediction of clays (Das & Basudhar, 2008). ANNs were also used for soils settlement estimation (Nejad *et al.*, 2009; Benali *et al.*, 2013) and shear strength parameter prediction (Khanlari *et al.*, 2012).

Due to their learning capacity, ANNs are less influenced by the natural variability of C_c and therefore are a potential tool in estimating the parameter. The use of ANN for the C_c prediction is presented in some studies (Ozer *et al.*, 2008; Park & Lee, 2011; Kalantary & Kordnaeij, 2012; Kurnaz *et al.*, 2016) and all of them presented satisfactory results.

This paper aims to explore the potential use of a computer-based modelling technique namely ANN to predict

Amandio Gonçalves de Oliveira Filho, M.Sc., Departamento de Engenharia Civil, Universidade Federal do Espírito Santo, Vitória, ES, Brazil. e-mail: amandio.oliveira@aluno.ufes.br.
Lucas Broseghini Totola, M.Sc., Departamento de Engenharia Civil, Universidade Federal do Espírito Santo, Vitória, ES, Brazil. e-mail: lucas.totola@aluno.ufes.br.
Kátia Vanessa Bicalho, Ph. D., Full Professor, Departamento de Engenharia Civil. e-mail: katia.bicalho@ufes.br.
Willian Hiroshi Hisatugu, D.Sc., Full Professor, Departamento de Computação e Eletrônica. e-mail: wilian.hisatugu@ufes.br.
Submitted on June 1, 2019; Final Acceptance on Januray 29, 2020; Discussion open until August 31, 2020.
DOI: 10.28927/SR.431109

C_C using measured index soil properties. A collected database containing results of 295 standard oedometer laboratory tests and corresponding soil index properties, carried out on a wide variety of fine-grained soils from Brazilian coast and reported by different researchers was compiled by the authors. Thus, a wide range of soils and soil properties, including low and high plasticity soils from the Brazilian coast, are investigated. The ANN ability to overcome limitations of single and multiple variables linear correlations is evaluated by comparing ANNs predictions performances with single empirical correlations created for the database investigated. In addition, results of correlations presented in the literature are also evaluated through different statistical techniques. These empirical correlations use simple or multiple variables to predict C_C from index properties such as natural water content (w_n), initial void ratio (e_0) and liquid limit determined by the Casagrande method (LL_{CUP}).

2. Material and Methods

2.1. Database soil description

The results of standard consolidation (or oedometer) tests and the corresponding index properties of 295 soft soils from different deposits of the Brazilian coast are investigated. The dataset reported by different researchers (Table 1) and compiled in this paper are derived from academic studies providing a high-quality database of laboratory consolidation tests. The data include test results on low and high plasticity soils from six Brazilian coastal states, up to 3000 km away from each other: Espírito Santo (ES), Santa Catarina (SC), Pernambuco (PE), Rio de Janeiro (RJ), Rio Grande do Sul (RS) and São Paulo (SP). The standard oedometer test in Brazil is carried out according to ABNT NBR-12007 (ABNT, 1990).

The predictive model capacity is highly dependent on experimental database quality. Laboratory data may contain inaccuracies associated with experimental laboratory errors. For this reason, and assuming the oedometer tests are performed on fully saturated samples (S = 100 %), some of the soils presented data inconsistency and were removed from the investigation. In addition, Tukey's Rule was applied for identification and exclusion of systematic bias or outliers. The outliers are values below Q1 - 1.5*(Q3 - Q1) or above Q3 + 1.5*(Q3 - Q1), where Q3 and Q1 are the first and third quartile of the dataset, respectively.

From the mentioned preprocessing, 70 out of 295 samples were removed. Table 2 presents the statistical properties of the 225 remaining samples from the dataset. Besides C_C, the soil index properties examined are the natural water content (w_n), the initial void ratio (e_0), the plasticity index (PI) and the liquid limit determined by the Casagrande method (LL_{CUP}).

The fine-grained particles of a soil govern the compressibility, constituting, mainly, the silt and clay fractions, with particle sizes range smaller than about 200 mesh sieve size (0.074 mm). From liquid limit (LL_{CUP}) and plasticity index (PI) values, it is possible to classify these fines through the Casagrande plasticity chart, which is used by the Unified Soil Classification System (USCS) as shown in Fig. 1. The chart analysis shows the heterogeneity of Brazilian coast fine-grained soils with a wide range of LL_{CUP} values. These values suggest large variability of clay mineral groups within the investigated database. Most of the investigated soils (*i.e.*, 88 %) are classified either as high plasticity clays (CH) or as high plasticity silts and organics soils (MH-OH).

Table 2 - Statistical description of the selected 225 experimental results.

Variable	Minimum	Maximum	Mean	Standard deviation
LL_{CUP} (%)	25	211	94.46	43.18
PI (%)	4	136.1	54.92	29.55
w_n (%)	29	221.34	97.5	41.53
e_0	0.73	5.66	2.54	1.03
C_c	0.09	3.27	1.3	0.71

Table 1 - References sources and location of the soil samples investigated from Brazilian coast.

Reference	Location	n**
Baran (2014)	Araranguá, Florianópolis, Itajaí, Palhoça, Penha and Tubarão (SC), Recife (PE) and Rio Grande (RS)	109
Kootahi & Moradi (2016)	Juturnaíba, Macaé and Rio de Janeiro (RJ), Recife (PE)	50
UFES* Geotechnical Laboratory	Grande Vitória (ES)	56
Póvoa (2016)	Macaé (RJ)	6
Queiroz (2013)	Itaguaí (RJ)	8
Silva (2013)	Duque de Caxias (Sarapuí and REDUC) and Queimados (RJ), Recife and Suape (PE), Florianópolis (SC) and Santos (SP)	66

*Federal University of Espírito Santo.
**Number of soil samples.

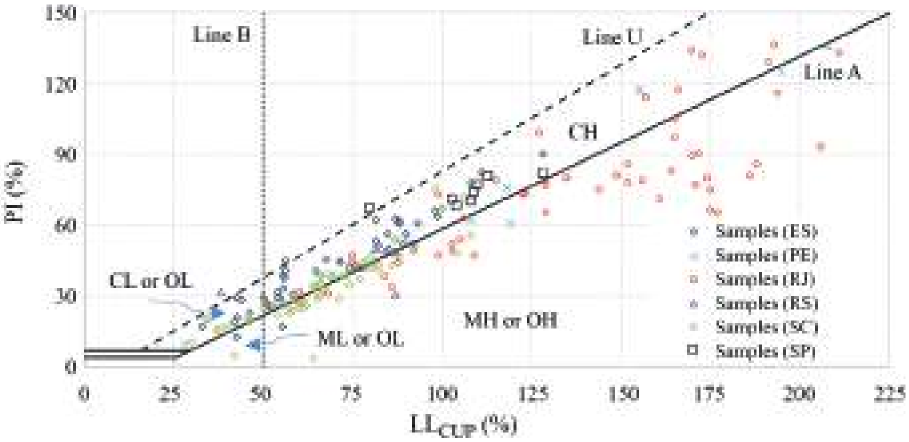

Figure 1 - Casagrande plasticity chart of investigated soil samples.

Table 3 presents a statistical summary of C_C for each soil class. As expected, the soils within the high plasticity classes have the higher values of C_C. These classes also present a wide range of C_C values (*i.e.* from 0.17 to 3.08 and 0.44 to 3.27, respectively).

The Pearson correlation coefficient was used to evaluate the correlation among the used properties. From Table 4, w_n and e_0 showed relatively strong correlation with C_C (*i.e.*, 0.87 and 0.86, respectively). In addition, the pairs w_n - e_0 and LL_{CUP}-PI showed strong correlations which may affect ANN performance.

Table 4 - Correlation among the properties investigated.

	C_C	LL_{CUP}	PI	w_n	e_0
C_C	1				
LL_{CUP}	0.82	1		Symmetrical	
PI	0.79	0.93	1		
w_n	0.87	0.71	0.71	1	
e_0	0.86	0.70	0.70	0.99	1

2.2. Existing correlations investigated

As presented in Table 5, several empirical correlations have been previously published by different investigators for estimating C_C values from different local sites. Most of these equations estimate C_C from single-variable regressions with w_n (C1-C4), LL_{CUP} (C6-C8) or e_0 (C10 - C12). Multiple regression correlations (C14-C15) are also presented and account for both mineralogical composition and soil structure influence on C_C. It should be noted that all these correlations are in linear form and show a direct and positive relationship between C_C and the input properties investigated.

2.3. Artificial neural networks

ANNs are characterized as artificial intelligence (AI) techniques inspired by the structure of the human brain to simulate its operation in computational systems in a simplified way. The neural networks are distinguished by performing three essential operations: learning and storing knowledge; applying the knowledge acquired in solving proposed problems; as well as acquiring new knowledge from constant learning (Khanna, 1990).

The artificial neuron is the basic processing element of an ANN. A neuron model is formed by a set of input connections (x_j), synaptic weights (w_{kj}), where k is the number of input neurons and j corresponds to the input stimulus; and the bias (b_k), a weighting parameter which can increase or decrease the value of the linear combination of inputs of the neuron activation function (f.). Figure 2 presents a simplified model of an artificial neuron, where (u_k) represents the linear combination of input signals, and (y_k) corresponds to the output value of the neuron, adapted from Haykin (2001). Thus, the input weighting process represents the learning rate acquired by an ANN. The weights are adjusted as the input dataset is presented to the network. The supervised learning process in an ANN is based on the

Table 3 - C_C Statistical summary by USCS Division of investigated soil samples.

USCS	Samples	Minimum	Maximum	Average	Standard deviation
CH	108	0.17	3.08	1.25	0.62
CL	25	0.09	1.31	0.47	0.29
MH-OH	90	0.44	3.27	1.62	0.69
ML-OL	2	0.25	0.38	0.32	0.09

Table 5 - Selected empirical correlations and their references used to estimate compression index from index properties.

Independent variable(s)	ID	References	Equations	Region
w_n	C1	Azzouz *et al.* (1976)	$C_c = 0.0100w_n - 0.05$	Greek and North-American Clays
	C2	Castello & Polido (1986)	$C_C = 0.014w_n - 0.17$	Brazilian Coast soft clays (ES)
	C3	Coutinho & Bello (2014)	$C_C = 0.014w_n - 0.094$ ($w_n < 200$) $C_C = 0.004\, w_n + 1.738$ ($w_n > 200$)	Brazilian Coast Marine clays (PE)
	C4	Kootahi & Moradi (2016)	$C_C = 0.012(w_n - 7.75)$	Marine fine-grained soils worldwide
LL_{CUP}	C6	Terzaghi & Peck (1967)	$C_C = 0.009(LL_{CUP} - 10)$	All clays
	C7	Castello & Polido (1986)	$C_C = 0.01(LL_{CUP} - 8)$	Brazilian Coast Marine clays (ES)
	C8	Kootahi & Moradi (2016)	$C_C = 0.012(LL_{CUP} - 8)$	Marine fine-grained soils worldwide
e_0	C10	Azzouz *et al.* (1976)	$C_C = 0.400\, e_0 - 0.100$	Greek and North-American Clays
	C11	Castello & Polido (1986)	$C_C = 0.228\, e_0 + 0.22$	Brazilian Coast Marine clays (ES)
	C12	Kootahi & Moradi (2016)	$C_C = 0.510(e_0 - 0.33)$	Marine fine-grained soils worldwide
e_0, LL_{CUP}, w_n	C14	Azzouz *et al.* (1976)	$C_C = 0.37(e_0 + 0.003LL_{CUP} + 0.0004w_n - 0.34)$	Greek and American Clays
e_0, LL_{CUP}	C15	Kootahi & Moradi (2016)	$C_C = 0.374(e_0 + 0.01LL_{CUP} - 0.47)$	Marine fine-grained soils worldwide

adjustment of the synaptic weights so that the output value is the closest possible to the expected value.

The activation function (*f.*) has the objective of limiting the input signals of the network in a specific range, usually between [0;1] or [-1;1], to generate the output neuron from the input values x_i of the network and the adjusted weights. The most used functions in geotechnical research are log-sigmoid, tan-sigmoid and linear. The ANN architecture is the way the network presents the arrangement of its neurons (Fig. 2). The structure can be in a single hidden layer or in several layers. The layers located between the entry and exit layers are called intermediate or hidden layers.

2.3.1. Backpropagation algorithm

The multilayer perceptron (MLP) is a multilayered artificial neural network composed of sigmoidal activation functions in the hidden layers. In this type of architecture, the hidden layer uses a non-linear activation function, such as the sigmoidal function, giving the network a genuinely non-linear model. For MLP, unlike simple Perceptron, the error *e* is not obtained simply from the difference between the desired output and the output calculated by the network because there are now intermediate layers. Hence, for the training stage, Rumelhart *et al.* (1986) proposed the backpropagation algorithm, one of the most used in practical applications of ANN.

The algorithm principle is to estimate the error of the intermediate layers by estimating the effect caused in the output layer error, using the descending gradient. The error is thus backpropagated in the network to correct the synaptic weights of the hidden layers. For this reason, the activation functions need to be continuous, differentiable, such as logistic functions, and hyperbolic tangent (Braga *et al.*, 2001). The Levenberg-Marquardt (LM) algorithm, an optimization of the backpropagation algorithm, is an iterative numerical optimization technique capable of locating the minimum of a function expressed as the sum of squares of other nonlinear functions and is widely used in ANN studies.

The LM backpropagation is an adaptive network, where each node in the network has the same node function. LM function uses the Jacobian matrix for calculations that assume the performance as a mean or sum of squared error (Kannaiyan *et al.*, 2019). The LM algorithm can be better explained in Hagan & Menhaj (1994) and Raina *et al.* (2009).

2.3.2. Proposed ANN models

The potential of ANN to estimate the compression index (C_C) is investigated by developing different ANNs models. The simulations in this study have been carried out in the *MATLAB* environment. Using the toolbox *nftool*, the ANNs were trained with the Levenberg-Marquardt (LM) training algorithm.

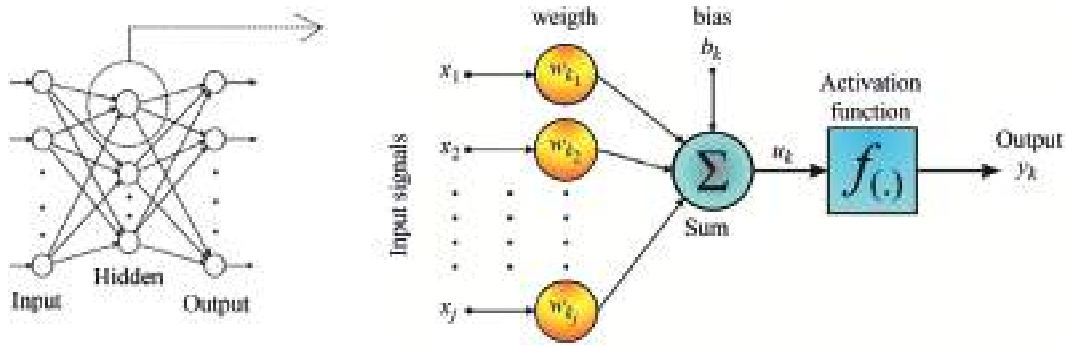

Figure 2 - ANN Architecture and Non-linear neuron model adapted from Haykin (2001) and Shahin *et al.* (2001).

Shahin (2013) points out that in most geotechnical problems, the architecture of an ANN is usually obtained through trial and error. Hornik *et al.* (1989) demonstrated a single hidden layer as sufficient to approximate any continuous function. Caudil (1988) points out that the number of hidden neurons (H) in a network with a single layer is a function of the number of input variables (I), as shown in Eq. 1.

$$H < (2I + 1) \quad (1)$$

On this hand, the networks in this study were trained with a single hidden layer, with the number of neurons in the hidden layer varying (2, 4, 6 and 10), and using four input parameters: LL_{CUP}, PI, e_0 and w_n. The log-sigmoid activation function in the hidden layer and the linear function in the output layer were used. In the training stage, 80 % of the total soil samples were used (177 selected experimental data). From these, 70 % were used for training, 15 % for validation and 15 % for testing. It is important to highlight that in *nftool toolbox*, these three steps make up the network training. Overall, in the first step, the network adjusts the synaptic weights minimizing the error function (*i.e.*, the mean squared error, MSE, Eq. 2). The validation samples are used to measure the generalization of the networks, and their errors are used to correct the synaptic weights and stop the training process. The testing samples are independent measures of the ANN. The remaining soil samples (20 %) were reserved for the cross-validation test (48 selected data). In this stage, the generalization capacity of the model is evaluated. The soil samples used for the cross-validation test were not included in the training stage.

$$MSE = \frac{1}{n}\sum_{i=1}^{n}(C_{c,\,measured} - C_{c,\,predicted})^2 \quad (2)$$

The selection of samples for training and cross-validation subsets followed the representativeness criteria including different domains of variation of C_C, a strategy distribution of the samples as discussed by Fortin *et al.* (1997). Thus, all the ranges of the histogram shown in Fig. 3 are represented in both training and cross-validation sets.

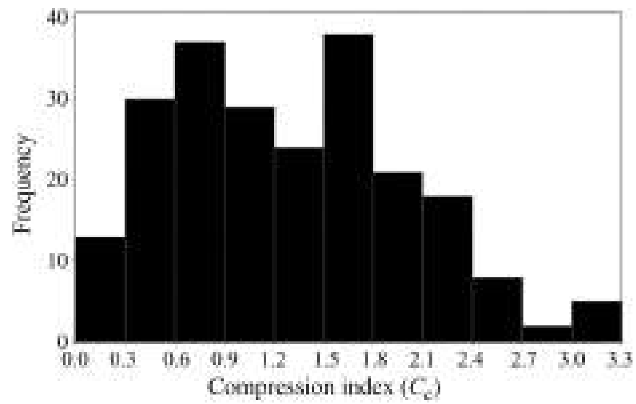

Figure 3 - Compression index histogram of the selected experimental results.

3. Results

3.1. Statistical evaluation methodology

It is not easy to choose the best estimation method to use, requiring criteria in its selection, which suggests the use of statistical techniques to evaluate the different methods used in geotechnical investigations. As a methodology to evaluate the estimation capacity of empirical correlations and ANNs, some statistical criteria are assessed: (i) the root mean square error (*RMSE*), (ii) the estimated and measured compression index ratio (*K*), (iii) the ranking index (*RI*) and (iv) the ranking distance (*RD*). The methodology is based on previous publications (Briaud & Tucker, 1988; Giasi *et al.*, 2003; Ozer *et al.*, 2008; Onyejekwe *et al.*, 2015; Güllü *et al.*, 2016).

The *RMSE* is the root mean square error of the difference between the estimated and measured values, which consequently attributes greater weight to the largest errors. Values close to zero indicate better model performance. The *RMSE* is calculated as follows:

$$RMSE = \sqrt{\frac{1}{n}\sum_{1}^{n}(C_{c,\,estimated} - C_{c,\,measured})^2} \quad (3)$$

where n is the number of observations, $C_{C,\ estimated}$ is the value predicted by the empirical correlations or ANNs, and $C_{C,\ measured}$ is the experimental C_C value obtained from the oedometer test.

The average and standard deviation of $C_{C,\ estimated}$ and $C_{C,\ measured}$ ratio (K) assesses how an equation underestimates or overestimates a value and compose accuracy and precision measurement parameters of the *RI* and *RD* methods. K is calculated as:

$$K = \frac{C_{c,\ estimated}}{C_{c,\ measured}} \tag{4}$$

Briaud & Tucker (1988) point out that the accuracy of K in evaluating the predictive capacity of a method is represented by the average of K. The precision of the method, is given by the scatter of the estimated values around the average of K, which is measured by the standard deviation of K. Theoretically, the factor K varies between zero and infinity, with an optimal value equal to one (Briaud & Tucker, 1988). Values of ($K < 1$) and ($K > 1$) indicate if results are underestimated or overestimated, respectively (Abu-Farsakh & Titi, 2004). The best estimated results are associated with the average (μ) of K close to one and standard deviation (*SD*) of K close to zero (Abu-Farsakh & Titi, 2004; Güllü *et al.*, 2016).

The ranking index (*RI*) was proposed by Briaud & Tucker (1988) to alleviate the problem of non-symmetric distribution of K values. The *RI* is a general index that relates μ and *SD* of all the K values of a group of estimates of a variable and provides a judgment of the accuracy and precision of the estimation. For the evaluation, low values of *RI* indicate good performance of the prediction model. The *RI* is determined by the formula:

$$RI = \left|\mu(\ln[K])\right| + SD(\ln[K]) \tag{5}$$

The ranking distance (*RD*) is an alternative general index proposed for assessing the quality of a calculation method, assessing the accuracy and precision of an estimation. As *RI*, *RD* also considers μ and *SD* of all the K values of the analyzed data (Giasi *et al.*, 2003). For assessment, low *RD* values indicate high accuracy and precision in the estimated values. The *RD* is determined as follows:

$$RD = \sqrt{(1-\mu_{[k]})^2 + (SD_{[k]})^2} \tag{6}$$

The performance is also evaluated through the coefficient of correlation for equations (R^2). In general, R^2 value has the objective of evaluating the relationship between two variables, from "n" observations of those variables, indicating how much the independent variable can be explained by the fixed variable. The R^2 values close to 1 indicate a better correlation between two variables:

$$R^2 = 1 - \frac{\sum_{i=1}^{n}\left(C_{c,\ estimated,\ i} - C_{c,\ measured,\ i}\right)^2}{\sum_{i=1}^{n}\left(C_{c,\ measured,\ i} - \overline{C}_{c,\ measured}\right)^2} \tag{7}$$

where $C_{C,\ measured}$ = input value, $C_{C,\ estimated}$ = estimated output value, $\overline{C}_{c,\ measured}$ = average input values and n = number of variables.

3.2. New empirical correlations proposed

Based on Pearson correlation values, Table 4, there is a strong relationship between C_C and index properties w_n, e_0 and LL_{CUP}. For this reason, three new single linear empirical correlations have been developed to estimate C_C from these properties for the Brazilian coast soft soils. The correlations have been created in the statistical software *Minitab*. The same 177 samples used for ANN training were used to create the empirical correlations. The remaining 20 % (48 samples) will be used as cross-validation test for both ANNs models and correlations created.

The Kolmogorov-Smirnov hypothesis test has been used to evaluate the residuals normality and homoscedasticity diagnosis has been performed to ensure empirical correlations validity. At the time the normality hypothesis was denied, points outside the 95 % interval have been removed (outliers) and the analysis has been repeated (Berger & Zhou, 2014). After statistical analysis, three new simple adjustment empirical correlations were determined for investigated Brazilian coast soft soils as follows (Table 6). All of them present a p-value (> 0.05) which indicates a good adherence to normal distribution.

Figures 4a, 4b and 4c present graphically the empirical correlations created and those from Table 5, with C_C as a function of w_n, e_0 and LL_{CUP}, respectively. It is noticed that empirical correlations could yield to the different results in a wide range of variability, which shows the particularity of the correlations with the local geological sites of the selected soil samples for the modelling.

3.3. Trained ANN performance

The C_C prediction capacity for Brazilian coast soft soils of the trained ANNs were evaluated by different statistical parameters (*i.e.*, *RMSE*, *K*, *RI*, *RD* and R^2). The predicted C_C values are compared to the measured C_C values determined from laboratory oedometer test. The results obtained by the four trained ANNs are summarized in the Tables 7 and 8 for the training and cross-validation sets,

Table 6 - Correlations proposed for the investigated database.

ID	Variable(s)	Equation	R^2
C5	w_n	$C_C = 0.01601w_n - 0.3209$	0.83
C9	LL_{CUP}	$C_C = 0.6155e_0 - 0.3521$	0.55
C13	e_0	$C_C = 0.01581LL_{CUP} - 0.138$	0.83

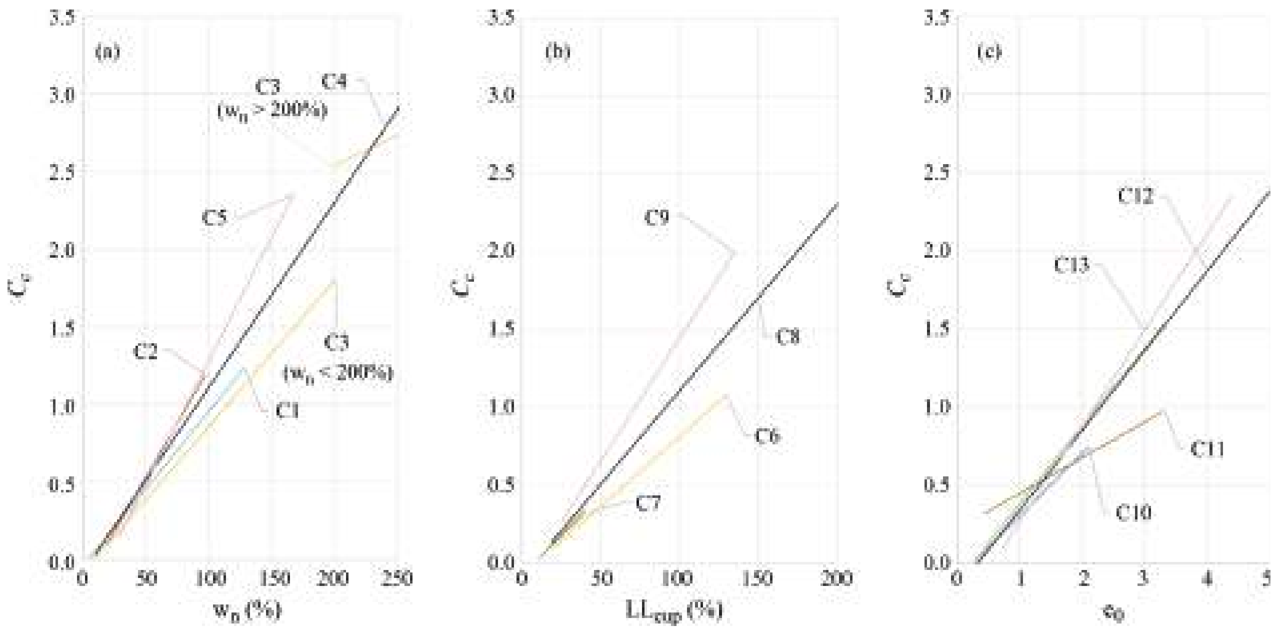

Figure 4 - Graphical representation of empirical correlations for C_C prediction using (a) w_n, (b) LL_{CUP}, and (c) e_0.

Table 7 - Statistical measurements for ANNs performances (training set).

ID	Input parameters	Hidden neurons	RMSE	*K*				*RI*	*RD*	R^2
				% < 1	% > 1	μ	*SD*			
ANN1	PI, e_0, LL_{CUP}, w_n	2	0.31	46.3	53.7	1.13	0.45	0.38	0.47	0.80
ANN2		4	0.262	46.9	53.1	1.10	0.41	0.34	0.43	0.86
ANN3		6	0.30	46.9	53.1	1.15	0.44	0.40	0.46	0.82
ANN4		10	0.28	52.0	48.0	1.07	0.38	0.32	0.38	0.84

Table 8 - Statistical measurements for ANNs performances (cross-validation set).

ID	Input parameters	Hidden neurons	*RMSE*	*K*				*RI*	*RD*	R^2
				% < 1	% > 1	μ	*SD*			
ANN1	PI, e_0, LL_{CUP}, w_n	2	0.28	52.1	47.9	1.10	0.35	0.33	0.36	0.88
ANN2		4	0.26	45.8	54.2	1.14	0.33	0.34	0.35	0.90
ANN3		6	0.30	45.8	54.2	1.15	0.43	0.40	0.46	0.87
ANN4		10	0.29	54.2	45.8	1.07	0.29	0.28	0.30	0.87

respectively. Each ANN was trained varying the number of neurons in the hidden layer.

The high values of R^2 associated with low *RMSE* values are evidence of good statistical performance of the ANNs trained for C_C prediction. The R^2 values range between 0.80-0.90 and *RMSE* values range between 0.26-0.30 considering the cross-validation sets. The cross-validation set results prove the ANN ability to generalize the acquired knowledge.

In terms of precision, assessed by the *K* values, a balance between the percentage values of ($K > 1$) and ($K < 1$) is observed for the trained ANNs, with a slight tendency to overestimate the C_C for most of the models ($\mu > 1$).

Overall, the increase in number of neurons in the hidden layer has not provided significant improvement in the C_C prediction ability for the investigated experimental dataset. It is suggested that the use of 4 neurons is enough. Thus, in this study, good prediction performance was reached using a number of hidden neurons equal to the number of inputs of the model, which agrees with the work of Ozer *et al.* (2008).

3.4. Empirical correlations performance

The C_C prediction capacity for Brazilian coast soft soils of both empirical correlations developed from this study and the correlations presented in the literature also were evaluated by statistical parameters (*i.e.*, *RMSE*, *K*, *RI*, *RD* and R^2). The cross-validation set is used to illustrate and compare the behavior of empirical correlations and ANN models. Table 9 shows the results.

The common behavior for the empirical correlations was a tendency of underestimate C_C ($\mu_{[k]} < 1$), especially those correlating C_C and LL_{CUP}. Also, the empirical correlations tended to underestimate C_c for soil samples of more compressible soils (higher C_c values). The LL_{CUP} values are strongly affected by clay mineralogy. Thus, there are limitations in the application of the investigated empirical correlations to soils from different geological origin or to soils with a C_C range outside the limits of the data from which the correlation was created.

For the reason cited, the empirical correlations proposed for this study database C5 and C13 (with w_n and e_0, respectively) presented the lower *RMSE*, *RI* and *RD* values. These two soil index properties have the strong correlation with C_C, which explains how they better explain C_C variation. In the same way, the multi-variable correlation C15, proposed by Kootahi & Moradi (2016) (for marine soils around the world and similar to soils in this study database) had a reasonable statistical performance. Also, the correlation was not extrapolated.

From Tables 7, 8 and 9, none of the correlations have satisfied all the evaluation criteria concomitantly and the trained ANNs presented statistical performance more consistent than the empirical correlations. For a general assessment, low values of *RI and RD* close to each other correspond to higher accuracy estimation, which is observed for ANNs and empirical correlations C5, C13 and C15, as shown in Fig. 5. Even though the ANN results regarding *RI* and *RD* are similar with these 3 correlations (two of them proposed for this study database), the *RMSE* for the ANNs can be up to 35 % lower.

The results reinforce the need for using more than one statistical parameter in the evaluation of different estimation methods. Analyzing only one parameter alone can lead to erroneous and meaningless conclusions. However, in this specific study, the values of *RD* and *RI* did not add conclusions and the analysis could be limited to *RMSE* and the values of *K* and $\mu_{[K]}$. Even though Güllü *et al.* (2016) point out that the *RD* index assigns equal weight to both accuracy and precision of estimation and provides more information than the *RI* index and *RMSE*, a crescent linear variation of both $SD_{[K]}$ with *RD* index and *RMSE* and $\mu_{[K]}$ with *RI* index is observed. That said, they seem to indicate the same behavior.

Figures 6 and 7 present the results when the performance by soil class is evaluated according to USCS. As shown in Table 3, there is limited data for ML-OL and CL samples, so only the CH, MH-OH samples are analyzed.

Table 9 - Statistical summary of the C_C estimated from empirical correlations cross-validation set.

Variable(s)	ID	*RMSE*	*K*				*RI*	*RD*	R^2
			% < 1	% > 1	μ	*SD*			
w_n	C1	0.56	79.2	20.8	0.83	0.37	0.60	0.41	0.85
	C2	0.33	58.3	41.7	1.04	0.42	0.35	0.42	
	C3	0.55	77.1	22.9	0.86	0.41	0.59	0.44	
	C4	0.41	75.0	25.0	0.95	0.41	0.45	0.41	
	C5	**0.32**	**58.3**	**41.7**	**1.03**	**0.37**	**0.33**	**0.37**	
LL_{CUP}	C6	0.73	89.6	10.4	0.67	0.25	0.82	0.42	0.77
	C7	0.63	87.5	12.5	0.77	0.30	0.69	0.38	
	C8	0.48	64.6	35.4	0.92	0.36	0.51	0.37	
	C9	0.40	31.3	68.8	1.20	0.47	0.48	0.51	
e_0	C10	0.57	79.2	20.8	0.82	0.36	0.38	0.40	0.82
	C11	0.78	79.2	20.8	0.81	0.53	0.80	0.56	
	C12	0.39	68.8	31.3	1.00	0.41	0.41	0.41	
	C13	**0.35**	**60.4**	**39.6**	**1.02**	**0.37**	**0.36**	**0.38**	
e_0, LL_{CUP}, w_n	C14	0.54	79.2	20.8	0.83	0.33	0.58	0.38	0.84
e_0, LL_{CUP}	**C15**	**0.36**	**62.5**	**37.5**	**0.99**	**0.36**	**0.36**	**0.36**	**0.86**

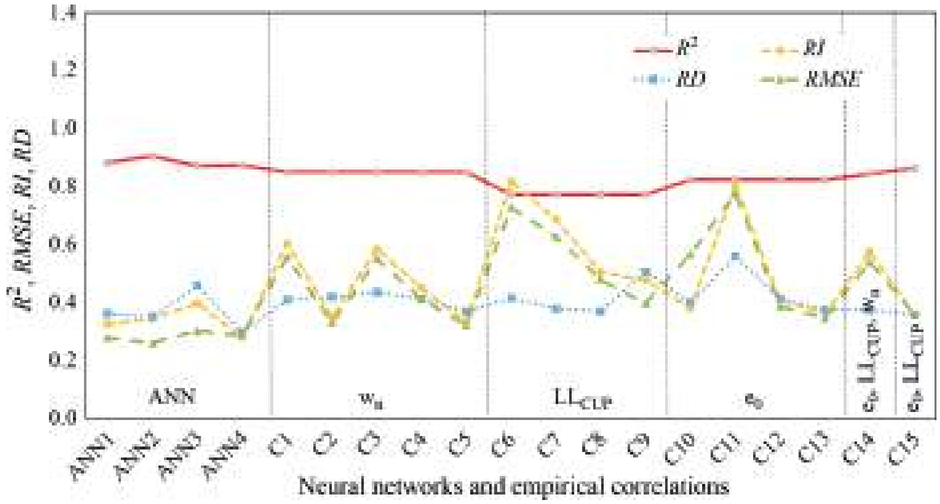

Figure 5 - Results of R^2, RMSE, RI and RD evaluation for each empirical correlation and ANNs for cross-validation set.

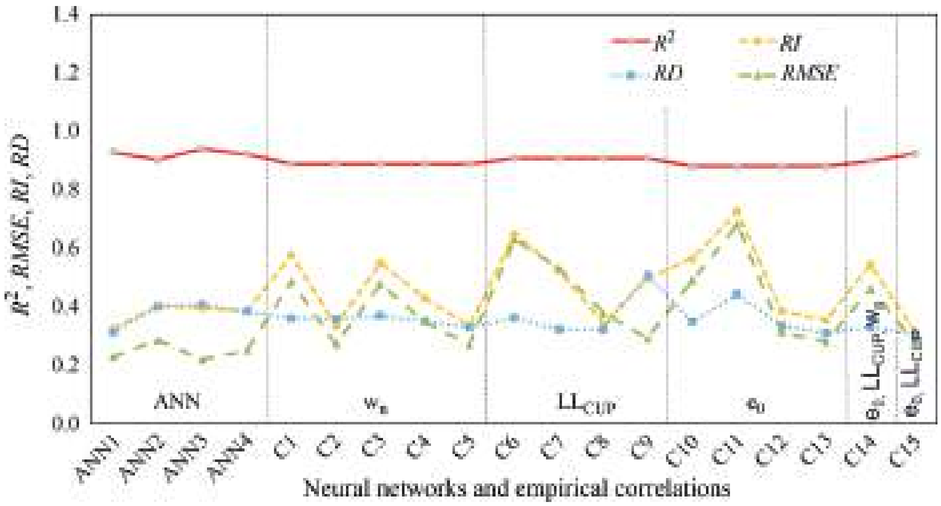

Figure 6 - Results of R^2, RMSE, RI and RD by each empirical correlation and ANNs for CH soils for cross-validation set (n = 26).

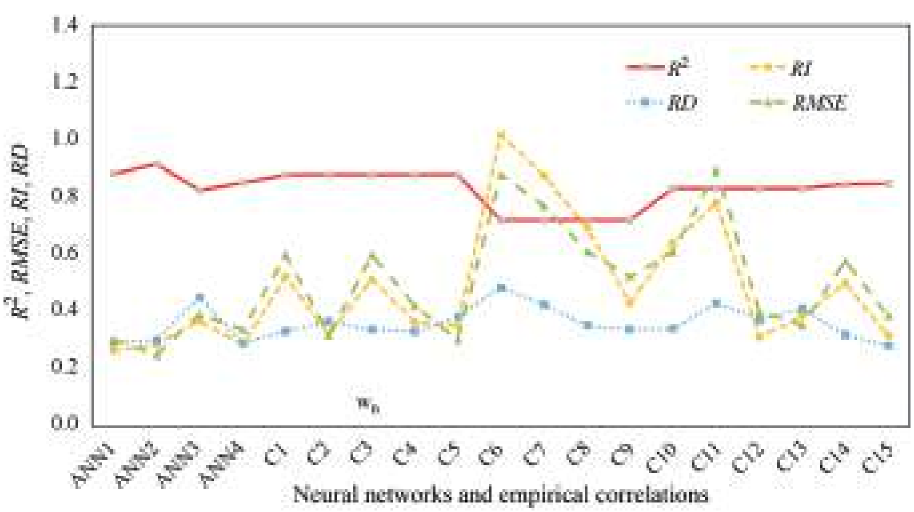

Figure 7 - Results of R^2, RMSE, RI and RD by each empirical correlation and ANNs for MH-OH soils for cross-validation set (n = 16).

Overall, both CH and MH-OH show similar results when analyzed by ANNs, however, the MH-OH class presented best precision and accuracy, as reveled by lower *RI* and *RD* values. The empirical correlations seem to follow the same tendency of the ANNs. Again, C5 and C15 are the correlations which better approximate the minimum values of *RMSE*, *RI* and *RD*, for both soil sample classes.

The ANN results grouped by Brazilian states are shown in Fig. 8. Due to the reduced number of cross-validation samples for SP, RS and PE Brazilian states, a statistical evaluation for these geological sites was not possible. In terms of *RMSE*, *RD* and *RI*, the best minimum adjustments between the curves occurred for soil samples from RJ and SC, indicating highest accuracy and precision

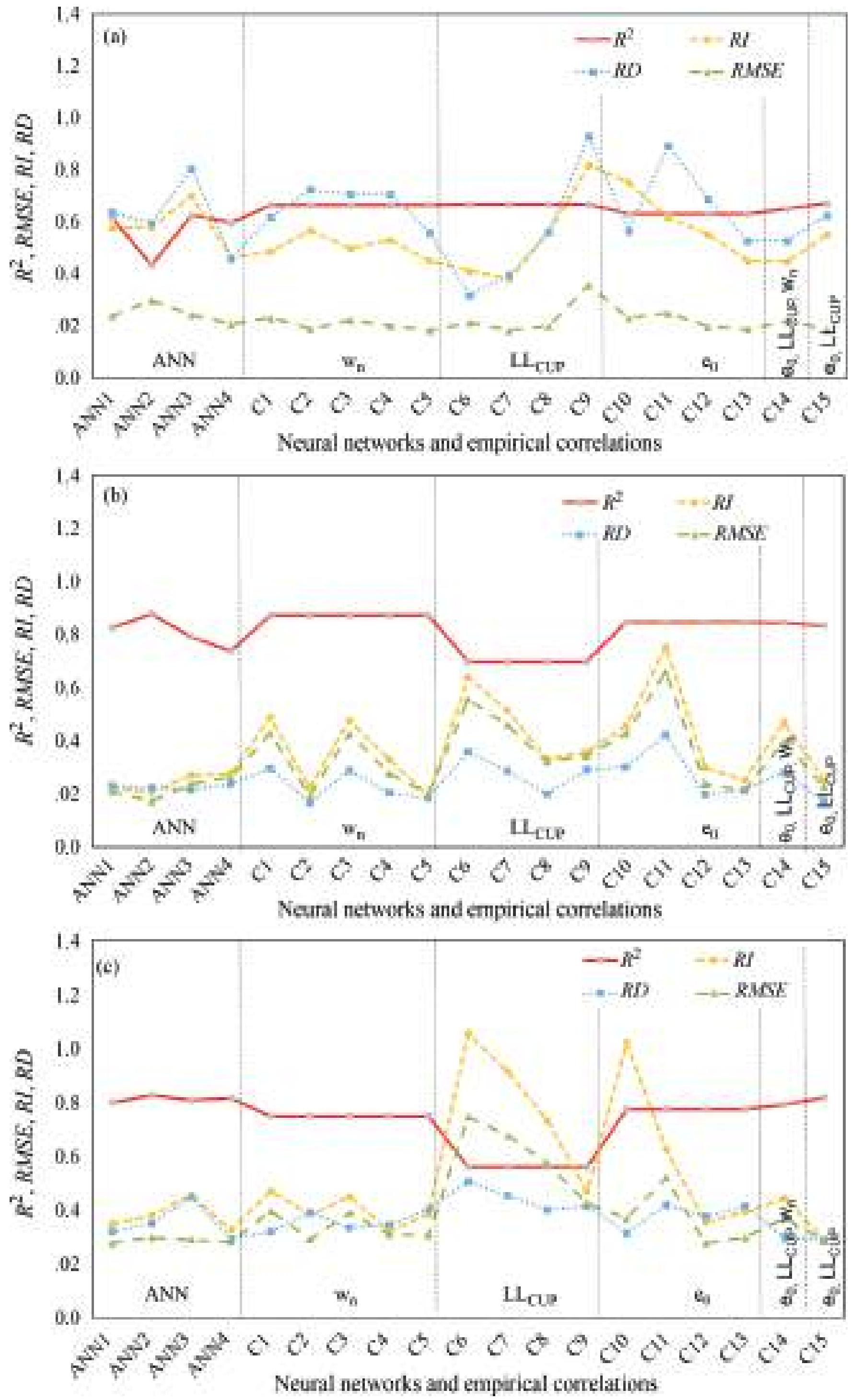

Figure 8 - Results of R^2, RMSE, RI and RD by empirical correlations and ANNs for cross-validation samples by (a) ES (n = 10), (b) RJ (n = 13) and (c) SC (n = 15).

of the predicted C_C values, especially for the network ANN2. The C_C interval variation for ES soil samples is 0.13-1.53, against 0.29 - 3.08 for RJ and 0.09 - 2.20 for SC samples. These observations indicate best performances of the ANN estimations for soils with higher compressibility.

In addition, Fig. 9 compares measured and estimated C_C for the empirical correlations and trained ANNs with the best and worst statistical performance for cross-validation sets. It is possible to notice that ANN results are close to each other, while greater divergence is noted for empirical correlations. Overall, both, empirical correlations and ANNs tend to underestimate higher C_C values ($C_C > 1$). According to the calculated statistical parameters, the best distribution of the C_C estimated by the ANNs around the equal line for any value of C_c can be graphically observed in all cases. The C_C empirical correlations with w_n present results closer to the equal C_C measured line than correlations with e_0 and LL_{CUP}, corroborating the statistical parameters previously evaluated.

4. Conclusions

In this paper, the performance of ANNs and widely used single and multi-variable empirical equations for compression index estimation was evaluated using a dataset of 225 fine-grained soils with a wide range of soil properties (*i.e.*, LL_{CUP} values ranging from 25 up to 200 %) from six Brazilian coastal states. Different networks have been trained with 2, 4, 6 and 10 neurons in a single hidden layer. The ANN training used the Levenberg-Marquardt algorithm (LM), the log-sigmoid activation function in the hidden layer and the linear function in the output layer. In addition, new empirical correlations were proposed for Brazilian coast soft soils using the least squares regression and residual analysis test techniques. The performance of both empirical correlations and ANNs have been evaluated through statistical techniques that include: (i) the root mean square error (*RMSE*), (ii) the ratio of the estimated to measured compression index (*K*), (iii) the ranking index (*RI*) and (iv) the ranking distance (*RD*).

Overall, the proposed ANN models outperformed the empirical correlations investigated, which is proved by the statistical parameters used. The minimum *RMSE* was 0.26 for the trained ANNs, 0.32 for the single empirical correlations created and 0.36 for the empirical correlations from the literature. The main reason for that is the underestimation of C_C for samples of more compressible soils by the empirical correlations. Among the input properties, the empirical correlations proposed in this study correlating C_C with w_n (C5) and e_0 (C13) showed the best estimation results. Also, the better performance of proposed correlations over those from the literature proves the influence of soil geological origin on the prediction capacity performance.

It is noteworthy that the empirical correlations are usually better applied to the modelling soil sample sites, and several standard oedometer tests using different soil samples in an investigated site are required for determination of C_C due to the observed heterogeneity of Brazilian coast fine-grained soils. By their ability to learn, adapted ANNs are less influenced by the site natural spatial variability. Moreover, the ANN method can always be updated by presenting new training soil examples as new data with measured C_C and corresponding index properties become available. Thus, these presented results reveal that the adapted ANNs created for estimation of soft soils C_C from the Brazilian coast have potential application as an alternative to the empirical correlations during preliminary investigation of suitability of a foundation site during planning stages.

In addition, the authors propose to send to readers the *MATLAB .mat* file, which contains the synaptic weights from the trained ANN4, which can be used in *MATLAB* environment, for prediction of compression index from Brazilian soil samples in preliminary investigation studies.

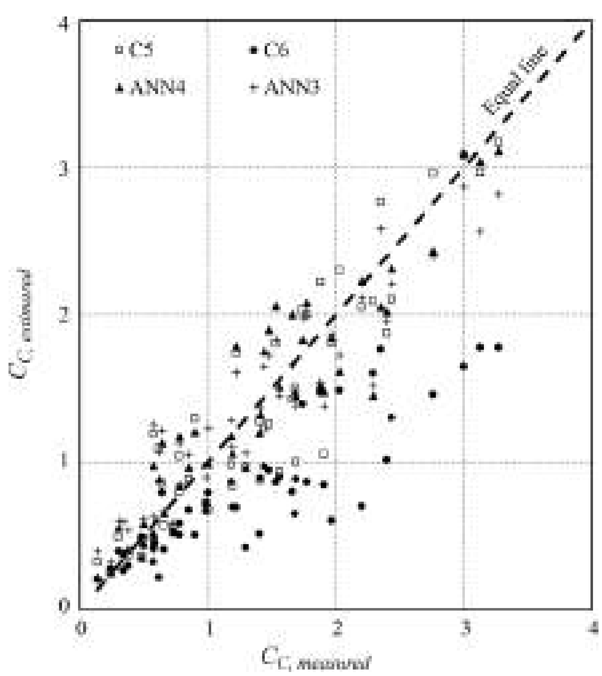

Figure 9 - Comparison between measured and estimated C_C for empirical correlation and ANN for cross-validation set (n = 48) by best (C5-ANN4) and worst (C6-ANN3) performances.

Acknowledgments

The first author is grateful to Petrobras for their support. The second author is grateful to CAPES for financial support. The third author is grateful to CNPq for financial support. The authors are grateful to the editor and reviewers for their interest in our research and for helpful comments that considerably improved our manuscript.

References

ABNT (Associação Brasileira de Normas Técnicas) NBR 12007, (1990). Soil - Unidimensional Consolidation

Test - Procedure. ABNT, Rio de Janeiro, Brazil, 15 p. (in Portuguese).

Abu-Farsakh, M.Y. & Titi, H.H. (2004). Assessment of direct cone penetration test methods for predicting the ultimate capacity of friction driven piles. Journal of Geotechnical and Geoenvironmental Engineering, 130(9):935-944.

Azzouz, A. S.; Krizek, R. J. & Corotis, R. B. (1976). Regression analysis of soil compressibility. Tokyo. Soils Foundations, 16(2):19-29.

Baran, K.R., (2014). Compressibility Geotechnical Properties of a Soft Clay From Itajaí-SC. Master Dissertation, Department of Civil Engineering, Technological Center, Federal University of Santa Catarina, Santa Catarina, 335 p.

Baroni, M. & Almeida, M.S.S. (2017). Compressibility and stress history of very soft organic clays. Proceeding of Institution of Civil Engineers - Geotechnical Engineering, 170(2):148-160. Thomas Telford Ltd.

Berger, V.W. & Zhou, Y.Y. (2014). Kolmogorov-Smirnov Test: Overview. Wiley Statsref: Statistics Reference Online. John Wiley & Sons, Ltda, New York, pp. 1-5.

Benali, A.; Nechnech, A. & Bouzid, A. (2013). Principal Component Analysis and Neural Networks for Predicting the Pile Capacity Using SPT. International Journal of Engineering and Technology, 5(1):162-169.

Braga, A.P.; Carvalho, A.P. & Ludermir, T.B. (2001). Neural Networks: Theory and Applications, 2nd ed. LTC, Rio de Janeiro, 226 p.

Briaud, J.L. & Tucker L.M. (1988). Measured and predicted axial load response of 98 piles. J Geotech Eng (ASCE), 114(9):984-1001.

Castello, R.R. & Polido, U.F. (1986). Some characteristics of consolidation of marine clays from Vitória, ES. In. VIII Brazilian Congress of Soil Mechanics and Foundation Engineering, Rio Grande do Sul, pp. 149-159.

Caudil, M. (1988). Neural networks primer, Part III. AI Expert, 3(6):53-59.

Coutinho, R.Q. & Bello, M.I.M.C.V. (2014). Geotechnical characterization of Suape soft clays, Brazil. Soils and Rocks, 37(3):257-276.

Das, S.K. & Basudhar, P.K. (2008). Prediction of residual friction angle of clays using artificial neural network. Engineering Geology, 100(3-4):142-145.

Djoenaidi, W.J. (1985). Compendium of Soil Properties and Correlations. Doctorate Thesis, The School of Civil and Mining Engineering, University of Sydney, Sydney, 788 p.

Fortin, V.; Ouarda, T.B.M.J. & Bobée, B. (1997). Comment on “The use of artificial neural networks for the prediction of water quality parameters” by HR Maier and GC Dandy. Water Resources Research, 33(10):2423-2424.

Futai, M.M., Almeida, M.S.S.; Lacerda, W.A. & Marques, M.E.S. (2008). Laboratory behavior of Rio de Janeiro soft clays. Index and compression properties- part 1. Soils and Rocks, 3(2):69-75.

Giasi, C.I.; Cherubini, C. & Paccapelo, F. (2003). Evaluation of compression index of remoulded clays be means of Atterberg limits. Bulletin of Engineering Geology and the Environment, 62(4):333-340.

Goh, A.T.C. (1995). Modeling soil correlations using neural networks. Journal of Computing in Civil Engineering, ASCE, 9(4):275-278.

Güllü, H.; Canakci, H. & Alhashemy, A. (2016). Use of ranking measure for performance assessment of correlations for the compression index. European Journal of Environmental and Civil Engineering, 22(5):578-595.

Hagan, M.T. & Menhaj, M.B. (1994). Training feedforward networks with the Marquardt algorithm. IEEE transactions on Neural Networks, 5(6):989-993.

Haykin, S. (2001). Neural Networks. A Comprehensive Foundation, 2nd ed. Pearson Education, McMaster University, Hamilton, Ontario, Canada, 823 p.

Hornik, K.; Stinchcombe, M. & White, H. (1989). Multilayer feedforward networks are universal approximators. Neural networks, 2(5):359-366.

Kalantary, F. & Kordnaeij, A. (2012). Prediction of compression index using artificial neural network. Scientific Research and Essays, 7(31):2835-2848.

Kannaiyan, M.; Govindan, K. & Raghuvaran, J.G.T. (2019). Prediction of specific wear rate for LM25/ZrO2 composites using Levenberg-Marquardt backpropagation algorithm. Journal of Materials Research and Technology, 9(1):530-538.

Khanlari G.R.; Heidari, M.; Momeni, A.A. & Abdilor, Y. (2012). Prediction of shear strength parameters of soils using artificial neural networks and multivariate regression methods. Engineering Geology, 131-132(1):11-18.

Khanna, T. (1990). Foundations of Neural Networks. Addison-wesley Publishing Company, New York, 196 p.

Kootahi, K. & Moradi, G. (2016). Evaluation of compression index of marine fine-grained soils by the use of index tests. Marine Georesources & Geotechnology, 35(4):548-570.

Kurnaz, T.F.; Dagdeviren, U.; Yildiz, M. & Ozkan, O. (2016). Prediction of compressibility parameters of the soils using artificial neural network, 5(1801):1-11.

McCabe, B.A.; Sheil, B.B.; Long, M.M.; Buggy, F.J. & Farell, E.R. (2014). Empirical correlations for the compression index of Irish soft soils. Geotechnical Engineering, 167(6):510-517.

Najjar, Y.M.; Basheer, I.A. & Naouss, W.A. (1996). On the identification of compaction characteristics by neuronets. Computers and Geotechnics, 18(3):167-187.

Nejad, F.P.; Jaksa, M.B.; Kakhi, M. & McCabe, B.A. (2009). Prediction of pile settlement using artificial neural networks based on standard penetration test data. Computers and Geotechnics, 36(7):1125-1133.

Onyejekwe, S.; Kang, X. & Ge, L. (2015). Assessment of empirical equations for the compression index of fine-grained soils in Missouri. Bulletin of Engineering Geology and the Environment, 74(3):705-716.

Ozer, M.; Isik, N.S. & Orhan, M. (2008). Statistical and neural network assessment of the compression index of clay-bearing soils. Bull Eng Geol Environ., 67(4):537-545.

Park, H.I. & Lee, S.R. (2011). Evaluation of the compression index of soils using an artificial neural network. Computers and Geotechnics, 38(4):472-481.

Póvoa, L.M.M. (2016) Geotechnical Characterization of a Soft Soil Deposit in Lowland Area Located in Macaé-RJ. Master Degree Dissertation, Civil Engineering, Federal University of Norte Fluminense Darcy Ribeiro (UENF). Campos dos Goytacazes, Rio de Janeiro, 156 p.

Queiroz, C.M. (2013). Geotechnical Properties of a Soft Clay Deposit in the Region of Itaguaí-RJ. Master Degree Dissertation, Geotechnics and Transprotation Course, Federal University of Minas Gerais, Belo Horizonte, Minas Gerais, 118 p.

Raina, R.; Madhavan, A. & Ng, A.Y. (2009). Large-scale deep unsupervised learning using graphics processors. Proc. 26th annual international conference on machine learning. ACM, pp. 873-880.

Rumelhart, D.E.; Hilton, G.E. & Williams, R.J. (1986). Learning representation by back-propagation errors. Nature, 323(6088):533-536.

Shahin, M.A.; Jaksa, M.B. & Maier, H.R. (2001). Artificial neural network applications in geotechnical engineering. Australian geomechanics, 36(1):49-62.

Shahin, M.A. (2013). Artificial intelligence in geotechnical engineering: Applications, modeling aspects, and future directions. In: X.S. Yang *et al*., Metaheuristics in Water, Geotechnical and Transport Engineering. 1st ed. Elsevier, Amsterdan, pp. 169-204.

Skempton, A.W. (1970). The consolidation of clays by gravitational compaction. Q. J. Geol. Sot. 125(1-4):373- 411.

Silva, D.M. (2013). Estimation of the Compressive Index of Soft Clays of the Brazilian Coast From Characterization Tests, Master Dissertation, Department of Civil Engineering, COPPE, Federal University of Rio de Janeiro, Rio de Janeiro, 182 p.

Terzaghi, K. & Peck, R.B. (1967). Soil Mechanics in Engineering Practice. 2nd ed. Wiley, New York, 512 p.

Tunnel Misalignment with Geostatic Principal Stress Directions in Anisotropic Rock Masses

O.P.M. Vitali, T.B. Celestino, A. Bobet

Abstract. Rock masses may present pronounced stress anisotropy, and so it is likely that a tunnel is misaligned with the geostatic principal stress directions. As a consequence, anti-symmetric axial displacements and axial shear stresses are induced around the tunnel due to the presence of far-field axial shear stresses. Limited research has been conducted on the effects of-far-field axial shear stresses on tunnel behavior. This paper investigates the effects of tunnel misalignment with the geostatic principal stresses in anisotropic rock masses. 3D FEM modeling of a tunnel misaligned 45° with the principal horizontal stresses is conducted. An anisotropic geostatic stress field is considered, with the major horizontal stress two times larger than the vertical stress and the minor horizontal stress equal to the vertical stress. The anisotropic behavior of the rock mass is represented by a transversely anisotropic elastic model, with properties typical of anisotropic rock masses. Tunnels in horizontally and vertically-structured rock masses are assessed. Unsupported and supported tunnels are investigated. The results show that asymmetric deformations and asymmetric stresses are induced near the face of the tunnel as a result of the tunnel misalignment with the geostatic principal stresses and with the rock mass structure. These asymmetric deformations near the face affect the ground-support interaction such that the internal forces in the liner are also asymmetric.

Keywords: 3D face effects, anisotropy, far-field shear stress, geostatic stress anisotropy, rock anisotropy, tunnel, tunnel misalignment.

1. Introduction

The literature shows that rock masses are likely to present pronounced geostatic stress anisotropy and anisotropic mechanical properties. This is a consequence of the rock complex formation processes. According to Brady & Brown (2006), the main factors affecting rock mass properties and geostatic stresses are: topography (elevations and valleys); residual stresses (due to cooling, for instance); tectonic movements; fracturing and jointing; and inclusions. Thus, geostatic stresses and mechanical properties are expected to be complex as well. In-situ stress measurements in rock masses show large horizontal stresses and significant horizontal stress anisotropy (Gysel, 1975; Brown & Hoek, 1978; McGarr & Gay, 1978; Evans *et al.*, 1989; Martin, 1997; Haimson *et al.*, 2003; Wileveau *et al.*, 2007; Zhao *et al.*, 2013, 2015; Park *et al.*, 2014; Perras *et al.*, 2015; Soucek *et al.*, 2017). For instance, Martin (1997) reported a highly anisotropic stress field in a massive granitic rock mass in Canada. The average stresses were: $\sigma_1/\sigma_2 = 1.2 \pm 0.1$ and $\sigma_1/\sigma_3 = 3.9 \pm 0.5$. Gysel (1975) presented the geostatic stress field measured in two sections along the Sonnerberg tunnel (Lucerne, Switzerland), in sandstone. The stress ratios were $\sigma_1/\sigma_3 = 2.33$, $\sigma_1/\sigma_2 = 2.10$ on one of the sections and $\sigma_1/\sigma_3 = 4.29$, and $\sigma_1/\sigma_2 = 1.70$ on the other. Haimson *et al.* (2003) and Park *et al.* (2014) evaluated the geostatic stress field of granitic and gneissic rock masses in South Korea, near Seoul, in an active seismic area. The measured horizontal stresses showed large stress anisotropy and were consistently larger than the vertical stress. An extensive compilation of 77 geostatic stresses was conducted by McGarr & Gay (1978), where the interval, with 95 % confidence, for each principal stress ratio was: $\sigma_1/\sigma_2 = 1.45 \pm 0.80$ and $\sigma_1/\sigma_3 = 2.42 \pm 2.28$. These data show that the expected stress anisotropy in rock is indeed high and quite variable.

The importance of tunnel alignment with the geostatic principal stress directions is recognized in the literature. Goodman (1989) recommends aligning the tunnel or cavern with the major principal stress to minimize stress concentrations around the opening. Convergence measurements of tunnels constructed in the Underground Research Laboratory (URL) in France showed the importance of the tunnel orientation with respect to the geostatic principal stress directions. These tunnels were excavated in an anisotropic claystone rock mass at 490 m depth, with average principal stress ratios $\sigma_h/\sigma_v = 1$ and $\sigma_H/\sigma_v = 1.3$ (Wileveau *et al.*, 2007). Because of the sedimentation process, the rock had an oriented structure (horizontal bedding), and thus anisotropic mechanical properties, with E_1/E_3 varying from 1.2 to 2 (Armand *et al.*, 2013). Experimental tunnels were

Osvaldo Paiva Magalhães Vitali, MSc, Ph.D. Candidate, Lyles School of Civil Engineering, Purdue University, West Lafayette, IN, USA. e-mail: ovitali@purdue.edu.
Tarcisio Barreto Celestino, Ph.D., Professor Doctor, São Carlos School of Engineering, University of São Paulo, São Carlos, SP, Brazil. e-mail: tbcelest@usp.br.
Antonio Bobet, Ph.D., Edgar B. and Hedwig M. Olson Professor, Lyles School of Civil Engineering, Purdue University, West Lafayette, IN, USA. e-mail: bobet@ecn.purdue.edu.
Submitted on September 28, 2019; Final Acceptance on February 13, 2020; Discussion open until August 31, 2020.
DOI: 10.28927/SR.431123

excavated parallel and perpendicular to σ_H. A supported circular tunnel of radius 2.6 m, aligned with σ_H, showed horizontal convergence of 37 to 58 mm and vertical convergence of 24 to 30 mm. A similar tunnel aligned with σ_h showed horizontal convergence of 19 mm to 34 mm and vertical convergence of 112 mm to 158 mm (Armand *et al.*, 2013).

Tunnel design is commonly conducted assuming that the tunnel is aligned with one of the geostatic principal stress directions and yet, as previously discussed, the assumption is unrealistic. When the tunnel is misaligned with the geostatic principal stress directions, far-field axial shear stresses are present. These axial shear stresses induce anti-symmetric axial displacements and axial shear stresses far-behind the tunnel face (Vitali *et al.*, 2018; 2019a; 2019b; 2019c). On shallow tunnels in isotropic ground, Vitali *et al.* (2019b) observed that the far-field axial shear stress induced asymmetric deformations and stresses near the face and that ground-support interaction and yielding around the tunnel, if any, were affected by the asymmetric deformations near the face. Vitali *et al.* (2019c) investigated the effects of tunnel misalignment on the progressive failure around the well-documented experimental tunnel at the URL in Canada (Martin, 1997). They found that no plastic deformations at the tunnel walls occurred when the tunnel was aligned with the minor principal stress, but asymmetric spalling would occur if the tunnel was not aligned with the geostatic principal stresses.

Asymmetric deformations of the tunnel walls have been observed on tunnels in structured rock masses, such as phyllites and slates. For instance, asymmetric radial displacements at the tunnel wall, horizontal displacements at the crown and axial displacements at the springline are often measured on the shotcrete support of NATM tunnels in anisotropic rock masses (Schubert & Budil, 1995; Goricki et al., 2005; Schubert et al., 2005; Schubert & Moritz, 2011; Klopcic & Logar, 2014; Lenz *et al.*, 2017). Those asymmetric deformations are commonly associated with the anisotropic properties of the rock mass and with localized heterogeneities. Button *et al.* (2006) observed that the asymmetric deformation patterns observed in the field could be partially reproduced numerically in tunnels not aligned with the rock mass structure. Tonon and Amadei, (2002, 2003) and Fortsakis *et al.* (2012) highlighted the importance of considering the anisotropic properties of the rock mass in numerical models to obtain more accurate ground deformation predictions (they assumed, however, that the tunnel was aligned with the geostatic principal stresses). In this paper, the influence of the tunnel misalignment with the geostatic principal stresses in anisotropic rock masses is assessed, for unsupported and supported tunnels, through 3D FEM modeling. Horizontally- and vertically-structured rock masses are considered. A transversely anisotropic elastic model is adopted to represent the rock mass.

2. 3D FEM Model

3D FEM modeling was conducted to investigate tunnels misaligned with the geostatic principal stresses in anisotropic rock masses. A tunnel misaligned 45° with the major principal horizontal stress, in a transversely anisotropic rock mass, is assumed. The rock mass is assumed elastic with the following properties: Young modulus perpendicular to the structural planes (E_1), 1 GPa; Young modulus parallel to the structural planes ($E_2 = E_3$), 3 GPa; in-plane Poisson ratio (ν_{23}), 0.333; out-of-plane Poisson ratio ($\nu_{13} = \nu_{12}$), 0.25; in-plane Shear modulus (G_{23}), 1.125 GPa; and out-of-plane Shear modulus ($G_{23} = G_{13}$), 0.667 GPa. These properties are typical of highly anisotropic rock masses, such as phyllites and slates. According to Worotnicki (1993), more than 50 % of highly structured rock masses present a E_1/E_2 ratio larger than 2. For the simulations, horizontal and vertical structural planes are considered (*i.e.* dip angles 0° and 90°, respectively). The geostatic principal stresses are: vertical stress (σ_v), 5 MPa (the vertical stress is assumed as a principal stress), minor horizontal stress (σ_h), 5 MPa and major horizontal stress (σ_H), 10 MPa. This is not an unusual anisotropic stress field, according to *e.g.* Gysel, 1975; Evans *et al.*, 1989; Haimson *et al.*, 2003; Wileveau et al., 2007; Park et al., 2014; Soucek et al., 2017. Two directions for the major horizontal stress are evaluated: σ_H perpendicular to the strike and σ_H parallel to the strike of the rock structure (*i.e.* perpendicular or parallel to the rock bedding; note that the direction of the horizontal stresses for a tunnel parallel to the rock structure does not change the results due to the symmetry of the problem).

Figure 1 shows the FEM mesh built for the investigation. The tunnel is circular with radius (r_0) 5 m. 2nd order hexahedron elements are used. The mesh refinement and the size of the model (Fig. 1a) are selected to ensure the results accuracy, following the recommendations provided by Vitali *et al.* (2017). Figure 1b illustrates the plan view of the mesh with the boundary conditions, where $\Psi = 45°$ is the angle that the tunnel makes with the principal horizontal stresses. The geostatic stress field is generated by applying a load pressure at the boundaries with the same magnitude as the geostatic principal stresses. Given the anisotropic rock masses investigated (*i.e.* horizontally- and vertically-structured rock masses) and that the vertical axis is a principal stress direction, it is possible to take advantage of the symmetry of the problem and use only half the discretization. The mesh consists of a refined structured grid at the center of the model, where the results are extracted, linked to the boundaries by an unstructured grid, as shown in Figs. 1c and 1d.

Supported and unsupported tunnels are considered. The 3D FEM simulation follows the excavation sequence of the tunnel by deactivating the elements inside the excavation and activating the elements that represent the tunnel support, if present. The simulations are run in two steps: the first step generates the geostatic stress field, and the second, the excavation and support, if present. The liner is represented by shell elements with thickness 0.5 m ($0.1r_0$). No slip between ground and liner is allowed. Figure 2 illustrates the mesh near the face of a supported tunnel. The liner, if included, is installed immediately after the excavation; that is, the unsupported span is zero. In Fig. 2, position 1 indicates a location far-ahead of the face of the tunnel and represents the region not affected by the tunnel excavation; position 2 is at the face of the tunnel; and position 3, far-behind the face of the tunnel, where stresses and displacements are independent of the distance from the face of the tunnel.

3. Tunnel in Horizontally Structured Rock Mass

Horizontal stratification is not uncommon in sedimentary and even metamorphic rock masses. The effects of such structure on tunnels misaligned with the geostatic principal stresses are analyzed through a number of simulations where the tunnel is horizontal and, thus, aligned with the rock mass structure. Two cases are studied: (1) far-field stresses $\sigma_{xx,ff} = \sigma_{zz,ff} = 7.5$ MPa, $\sigma_{yy,ff} = 5$ MPa, $\tau_{xz,ff} = 2.5$ MPa (tunnel oriented at $\Psi = 45°$ with the far-field principal stresses) and (2) same far-field stresses, but no far-field shear, *i.e.* $\sigma_{xx,ff} = \sigma_{zz,ff} = 7.5$ MPa, $\sigma_{yy,ff} = 5$ MPa, $\tau_{xz,ff} = 0$, to investigate the influence of the far-field axial shear.

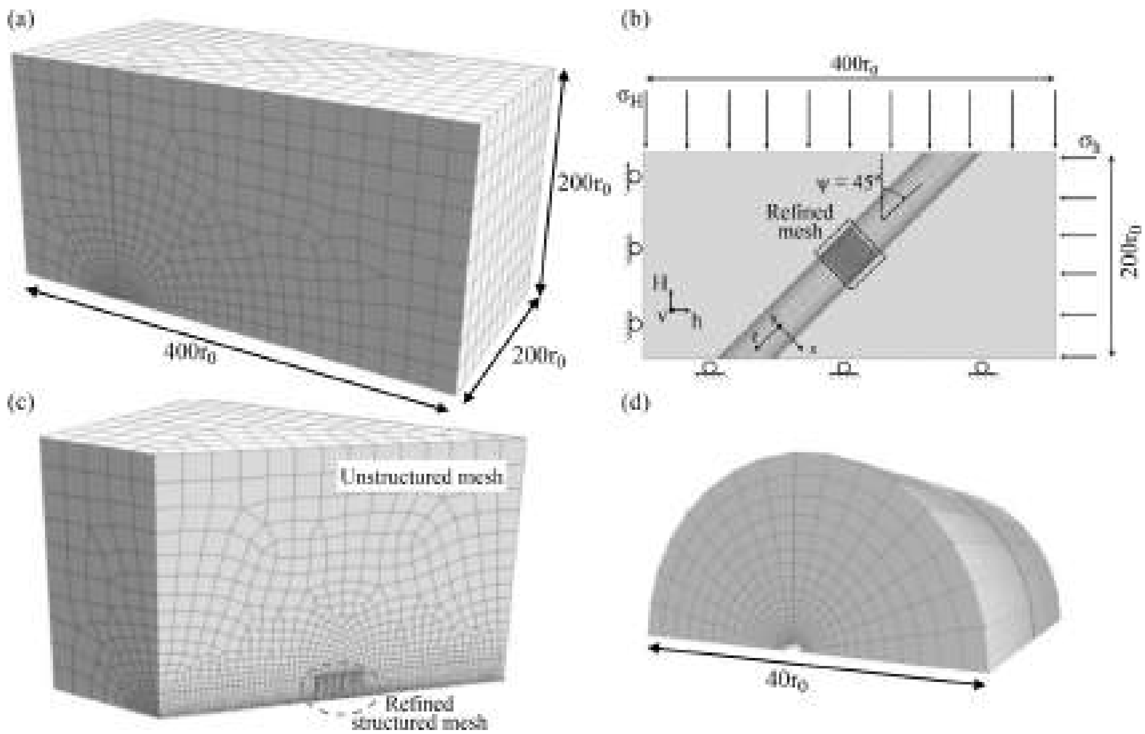

Figure 1 - FEM mesh. (a) Model dimensions; (b) plan view and boundary conditions; (c) vertical cross section along the tunnel and; (d) refined mesh at the center of the model. r_0 is the tunnel radius and is 5 m.

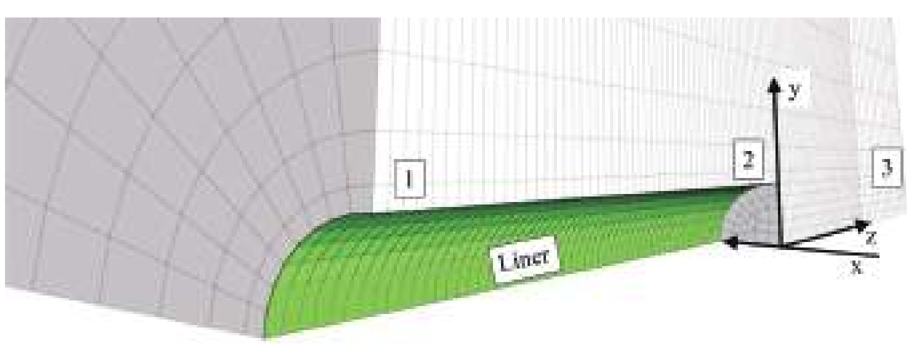

Figure 2 - Mesh near the face of the supported tunnel, with the coordinate system XYZ attached to the tunnel. Position (1) represents a point far ahead of the face; (2), at the face (*i.e.* Z = 0); and (3), far-behind the face.

Figure 3 shows the horizontal and vertical tunnel convergence, normalized with the tunnel radius, with the distance from the face, normalized also with the tunnel radius, for the two cases. Displacements start to increase at $4r_0$ ahead of the face, abruptly increase at the face and increase further behind the face until they are constant at about $4r_0$ behind the face. Tunnel deformations are identical in both cases, which indicates that the far-field axial shear stress has no influence on the results. It is interesting to note that the vertical and the horizontal tunnel deformations are similar, despite the fact that the far-field horizontal stress is larger than the vertical. The reason for this is that the stiffness of the ground parallel to the rock mass structure is the largest and the stiffness perpendicular to the structure is the smallest. So, in the simulations, the (larger) horizontal stress is parallel to the stiffest rock mass direction and the (smaller) vertical stress is parallel to the softest rock mass direction, and so the two effects compensate each other.

Figure 4 shows the normalized radial displacements and the deformed cross-section at the face and far behind the face. For Case 2, with no far-field axial shear stress, the deformations are symmetric at the face and far-behind the

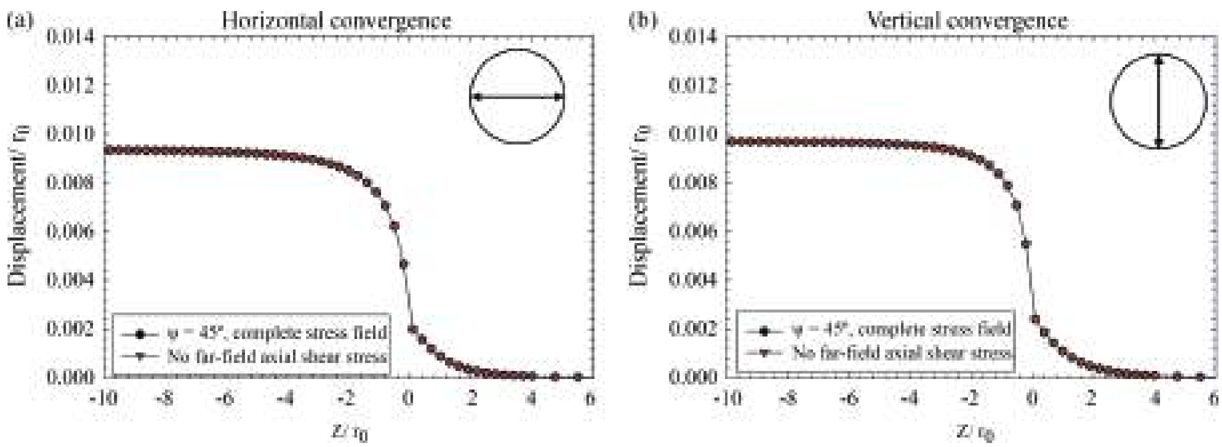

Figure 3 - Tunnel convergence *vs.* distance from the face (both normalized with respect to the tunnel radius) for unsupported tunnel. (a) horizontal convergence, (b) vertical convergence. Z is the distance from the face of the tunnel (Fig. 2); r_0, the tunnel radius, is 5 m. The circles represent the tunnel cross section and the arrows indicate the direction and location of the displacements plotted.

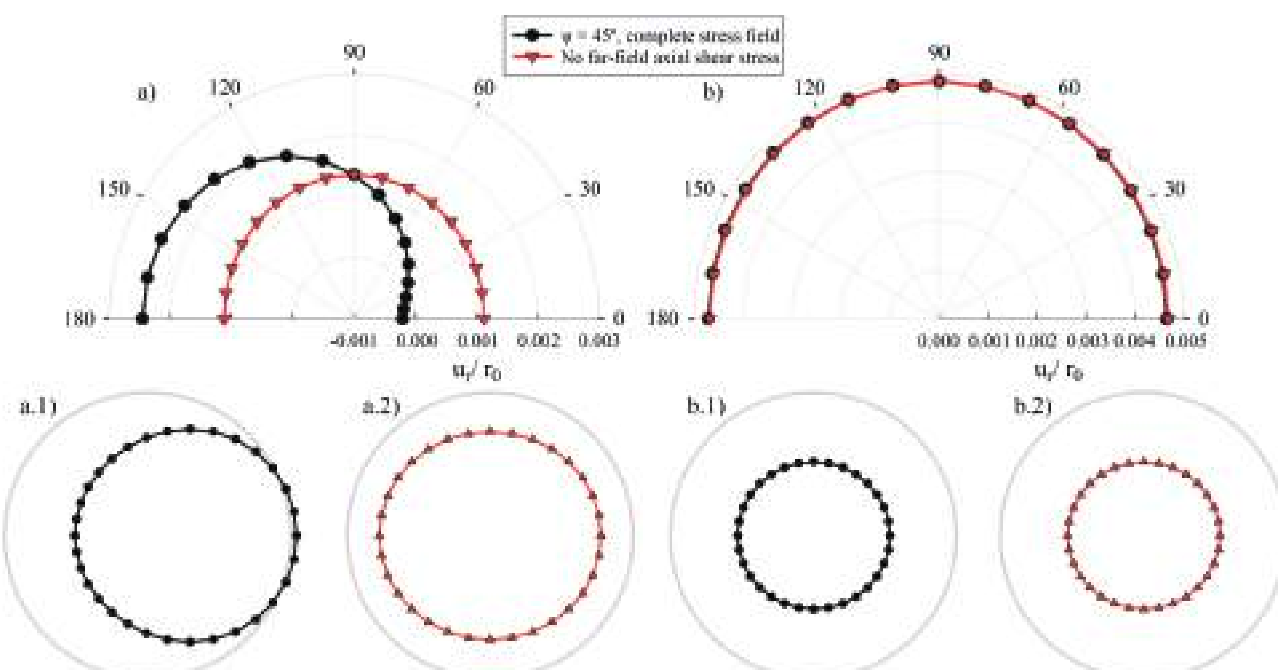

Figure 4 - Normalized radial displacemets at the tunnel perimeter with respect to the tunnel radius and deformed tunnel cross-section, for unsupported tunnel. (a) at the face; (b) far-behind the face. Deformations are magnified 200 times at the face and 100 times far-behind the face. u_r is the radial dsplacement and r_0, the tunnel radius, is 5 m.

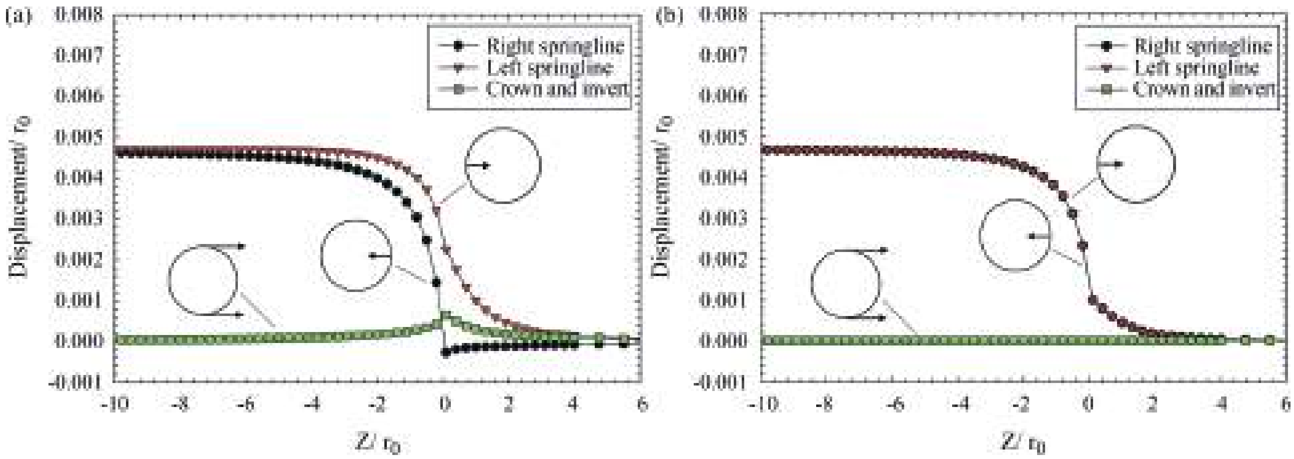

Figure 5 - Displacements *vs.* distance from the face (both normalized with respect to the tunnel radius). (a) Case 1, complete stress field; (b) Case 2, no far-field axial shear. Z is the distance from the face (Fig. 2); r_0, the tunnel radius, is 5 m. The circles represent the tunnel cross section and the arrows indicate the direction and location of the displacements plotted.

face. For Case 1, with the complete stress field, the deformations at the tunnel perimeter are symmetric far-behind the face, but asymmetric at the face, where the tunnel cross section translates towards the right. Far-behind the face, the deformed cross section in both cases is exactly the same, which shows that the far-field axial shear stress does not affect the radial displacements far-behind the face. This is because, when the tunnel axis is aligned with one of the principal material directions, in-plane and out-of-plane deformations are decoupled (Vitali *et al.*, 2020).

The normalized radial displacements at the springline, on the right and left, and the tunnel cross section translation are presented in Fig. 5. For Case 1, complete stress field, the radial displacements are asymmetric from a distance of $4r_0$ ahead of the face to about $6r_0$ behind the face. A translation of the tunnel cross section occurs near the face, which is maximum at the face (*i.e.* at Z = 0). For Case 2, the radial displacements at the springline do not change with the distance from the face; that is, no translation of the tunnel cross section occurs. Thus, the presence of the far-field axial shear stress induces asymmetric deformations near the face. Figure 6 shows the normalized "corrected" radial displacements with the normalized distance from the face, for Case 1. The corrected radial displacement is the radial displacement without the translation of the tunnel cross section, as indicated in Fig. 6. The corrected radial displacements are asymmetric near the face, which is consistent with Vitali *et al.* (2019b). The authors observed that the far-field axial shear stress caused asymmetric radial deformation near the face of a shallow tunnel in isotropic ground. Those asymmetric radial displacements could be decomposed into a rigid body displacement of the tunnel cross section and anti-symmetric radial displacements.

The stress paths, normalized with respect to the vertical stress, at points near the tunnel perimeter (*i.e.* at right and left springline and at the crown) are shown in Fig. 7

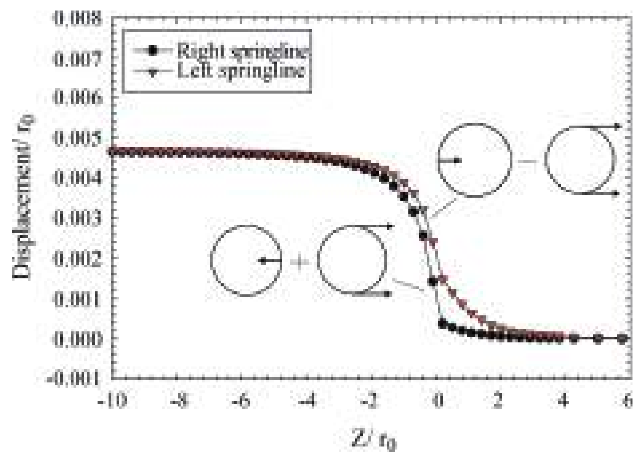

Figure 6 - Displacements *vs.* distance from the face (both normalized with respect to the tunnel radius). Case 1, complete stress field. Z is the distance from the face (Fig. 2); r_0, the tunnel radius, and is 5 m. The circles represent the tunnel cross section and the arrows indicate the direction and location of the displacements plotted.

(see Fig. 2 for location of points 1, 2, 3). The stresses were computed at a distance of $0.1r_0$ from the tunnel perimeter, to minimize the disturbance due to the corner between face and tunnel. For Case 1 (complete stress field), on the right-hand side of the springline, the rock stresses increase towards the face of the tunnel, *i.e.* both mean stress and maximum shear stress increase; close to the face, the stresses abruptly increase, while they steadily decrease behind the face until they reach a constant value. On the left-hand side, the opposite is observed; that is, unloading ahead of the face and loading behind the face. Note that far behind the face of the tunnel, the two stress paths yield the same results. The asymmetry of the stress paths is consistent with the asymmetric deformations near the face discussed previously. Indeed, there is a horizontal translation

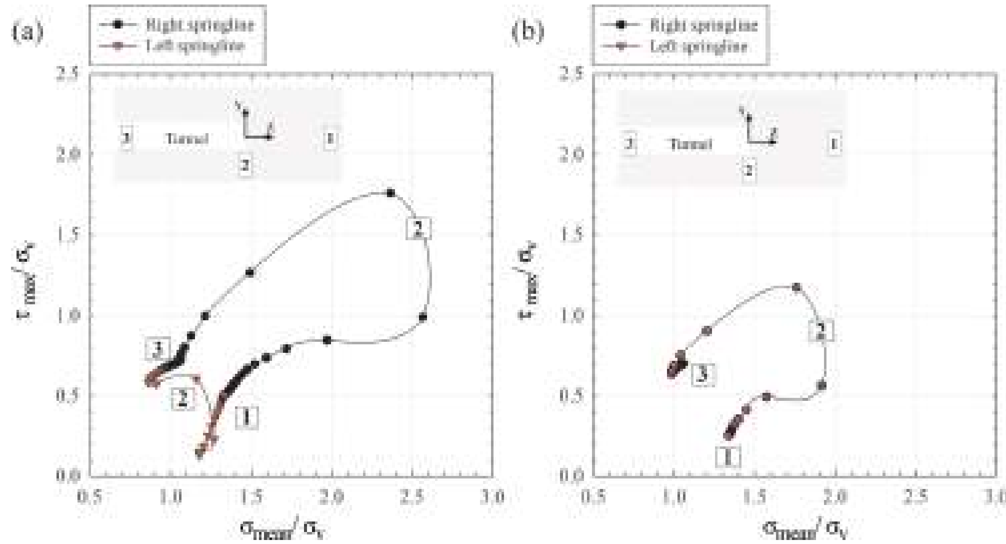

Figure 7 - Normalized stress paths with respect to the vertical stress. (a) Case 1, full stress field; (b) Case 2, no far-field axial shear. Position (1) represents a point far ahead of the face of the tunnel; (2), at the face (*i.e.* Z = 0); and (3), far-behind the face.

of the tunnel cross section towards the right near the face, as shown in Fig. 4, that results in compression of the rock at the right springline, while the rock at the left springline is unloaded. For Case 2, no far-field axial shear stress, the two stress paths are exactly the same. There is loading ahead of the face and unloading behind the face. Note that unloading ahead of the face was observed only when the far-field axial shear stress was present. Figure 8 presents the normalized stress paths at the crown for Case 1 (complete stress field) and Case 2 (no far-field axial shear). The stresses at the crown and at the invert are the same because of the symmetry of the problem. The stress paths for the two cases follow a loading path ahead and behind the tunnel face, with an increase of the mean effective stress near the face. The shear stresses are larger for Case 1 than for Case 2 because of the presence of the far-field axial shear stress.

Figure 9 shows the normalized axial displacements at the tunnel perimeter, for Case 1 (complete stress field; for Case 2, no axial displacements were induced far-behind the face). As one can see in the figure, anti-symmetric axial displacements are induced far-behind the face. The axial displacements are maximum at the springline and zero at the crown; those are produced by the far-field axial shear stress. At the face, the axial displacements are asymmetric due to the constraints produced by the tunnel face (Fig. 4).

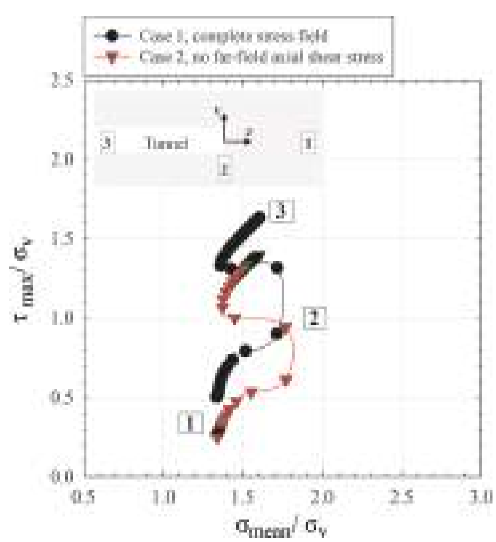

Figure 8 - Stress paths at the crown. Position (1) represents a point far ahead of the face of the tunnel; (2), at the face (*i.e.* Z = 0); and (3), far-behind the face.

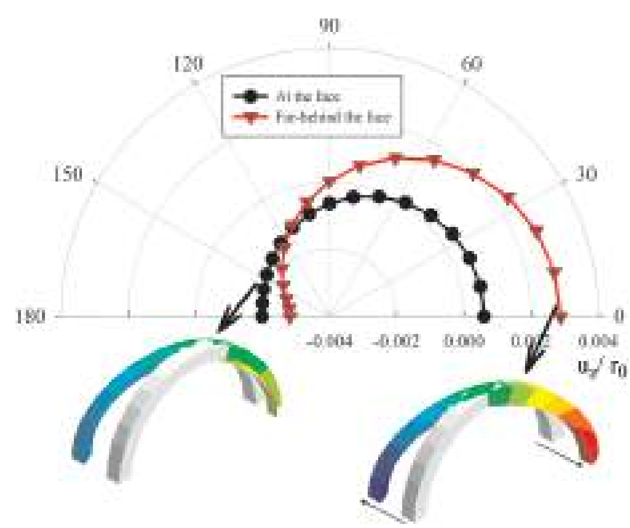

Figure 9 - Normalized axial displacements with respect to the tunnel radius along the tunnel perimeter for Case 1, complete stress field. Unsupported tunnel. The colors of the deformed tunnel cross-section are associated with the magnitude of the axial displacements and are shown to help with the visualization (the colors legend is not included for clarity, but the magnitude of the displacements is given in the plot).

For Case 2, where the far-field axial shear stress is neglected, no anti-symmetric axial displacements are induced and so, no asymmetric radial deformations occur near the face.

If a liner is installed near the face, the asymmetric radial deformations may affect the stresses in the support. To investigate the influence of the far-field axial shear stress on supported tunnels in a horizontally structured rock masses, the two cases previously discussed are analyzed again, but with a liner placed close to the face (Fig. 2). Figure 10 shows the normalized radial displacements with the normalized distance from the face. For Case 1, complete stress field, the radial displacements at the springline are asymmetric near the face and far behind the face. For Case 2, no far-field axial shear, the radial displacements at the springline are always symmetric. Consistent with the findings from the unsupported tunnel, the asymmetric deformations are caused by the anti-symmetric axial displacements induced by the far-field axial shear stress.

Figure 11 shows the normalized radial stresses at the tunnel perimeter, with respect to the vertical stress, with the normalized distance from the face. For Case 1, complete stress field, on the right-hand side of the springline, the radial stresses increase at the face and abruptly decrease behind the face; then, they slightly increase with the distance from the face until they are constant. On the left-hand side of the springline, the radial stresses decrease ahead of the face as the distance from the face decreases and then, behind the face, they increase with distance until they are constant. The radial stresses on the right are larger than on the left springline, which is consistent with the asymmetric deformations near the face. Note that there is a translation of

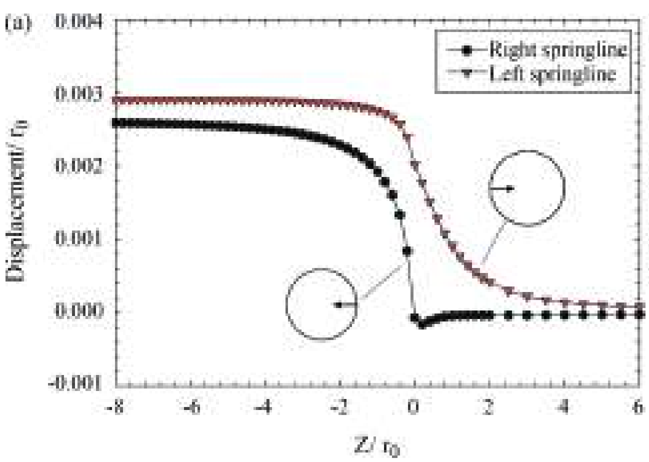

Figure 10 - Radial displacements *vs.* distance from the face (both normalized with respect to the tunnel radius), for supported tunnel. (a) Case 1, complete stress field and, (b) Case 2, no far-field axial shear. Z is the distance from the face of the tunnel (Fig. 2); r_0, the tunnel radius, is 5 m. The circles represent the tunnel cross section and the arrows indicate the direction and location of the displacements plotted.

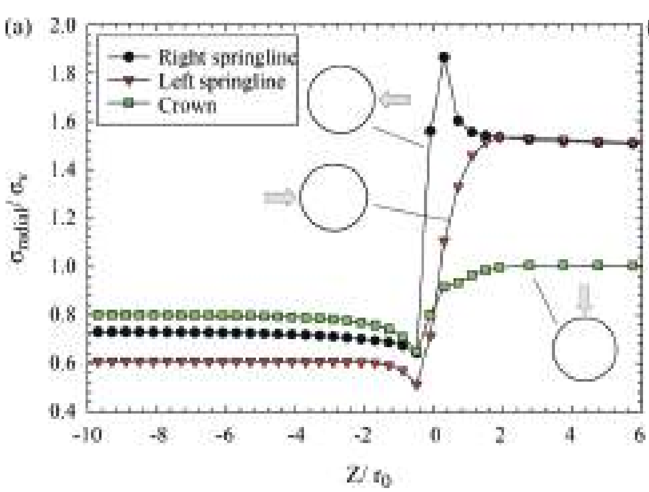

Figure 11 - Normalized radial stresses with respect to the far-field vertical stress *vs.* the normalized distance from the face with respect to the tunnel radius, for supported tunnel. (a) Case 1, complete stress field; (b) Case 2, no far-field axial sher stress. Z is the distance from the face of the tunnel (Fig. 2); r_0, the tunnel radius, is 5 m . The circles represent the tunnel cross section and the arrows indicate the direction and location of the radial stresses plotted.

the tunnel cross section towards the right (Fig. 4.a.1), which compresses the right springline and unloads the left. For Case 2, the radial stresses are the same (*i.e.* both abruptly decrease at the face and slightly increase behind the face until they are constant far-behind the face). It is interesting to note that the radial stresses at the crown are similar in both cases. At the crown, the radial stresses decrease ahead of the face and increase behind the face until they reach a constant value. Note that, behind the face, the radial stresses at the crown are larger than at the springline. Figure 12 shows the internal forces in the liner, normalized with respect to the vertical stress and the tunnel radius. The internal forces (*i.e.* thrust forces and bending moments) are symmetric for Case 2 (no far-field axial shear) and asymmetric for Case 1 (complete stress field), where they are larger on the right than on the left. This observation is consistent with the asymmetric radial displacements that occur at the tunnel perimeter. Note also that Case 1 produces the largest internal forces.

4. Tunnel in Vertically-Structured Rock Mass

In this analysis, the tunnel is inclined 45° with the strike of the rock structure and with the geostatic principal horizontal stresses, as shown in Fig. 13. The figure also shows the boundary conditions of the FEM model, which are analogous to those in Fig. 2. Three cases are investigated: (1) major horizontal stress (σ_H) perpendicular to the strike; (2) no far-field axial shear stress; and (3) major horizontal stress (σ_H) perpendicular to the strike. The far-field horizontal and axial stress are the same in all three scenarios (*i.e.* $\sigma_{xx,ff} = \sigma_{zz,ff} = 7.5$ MPa). When σ_H is perpendicular to the strike (Case 1), the far-field axial shear stress ($\tau_{xz,ff}$) is

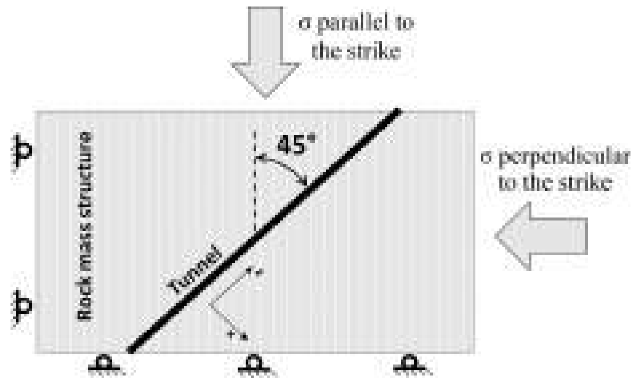

Figure 13 - Plan view of the tunnel misaligned with the vertically structured rock mass and boundary conditions.

2.5 MPa, and when parallel to the strike (Case 3), $\tau_{xz,ff} = -2.5$ MPa. Case 2 assumes $\tau_{xz,ff} = 0$.

The axial displacements at the tunnel perimeter, normalized with respect to the tunnel radius, are presented in Fig. 14, for an unsupported tunnel. In all cases, axial displacements are induced far behind the face. The axial displacements are asymmetric at the face and anti-symmetric far-behind the face. The axis of anti-symmetry far-behind the face is the vertical axis in all three cases, so the maximum axial displacements are at the springline and there are no axial displacements at the crown or invert. This is because of the presence of the far-field axial shear stress and because of the tunnel misalignment with the rock mass structure. It is interesting to note that the axial displacements for Case 2, no far-field shear, are larger than for Case 3, σ_H parallel to the strike, but smaller than for Case 1, σ_H perpendicular to the strike. The reason for this is that, when σ_H is perpendicular to the strike, the axial distortions produced by the far-field axial shear stress and by the rock

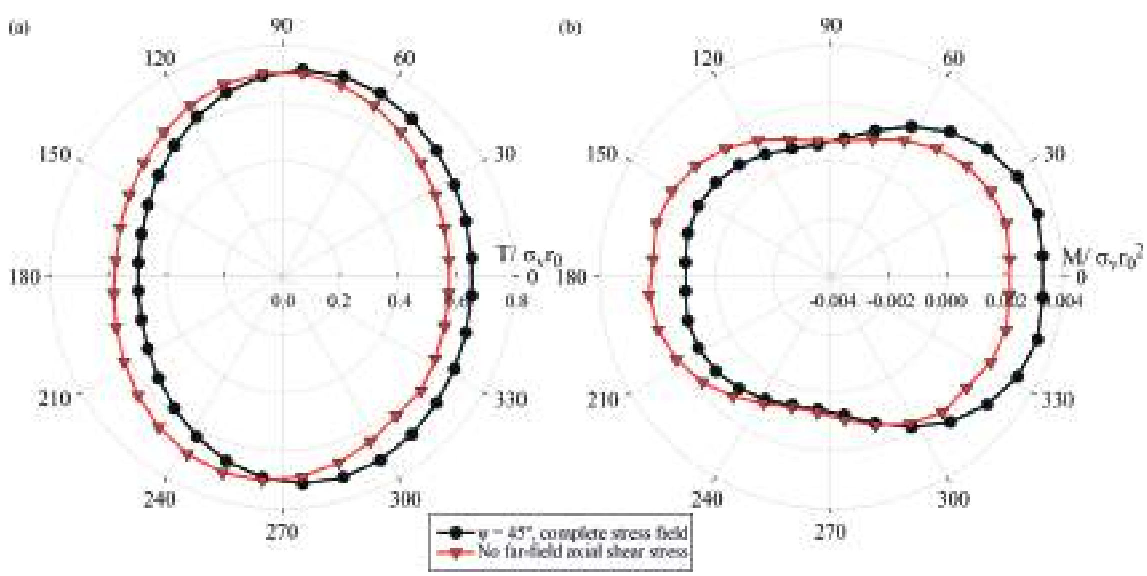

Figure 12 - Normalized internal forces with respect to the vertical stress and tunnel radius. (a) Thrust (b) Bending moment.

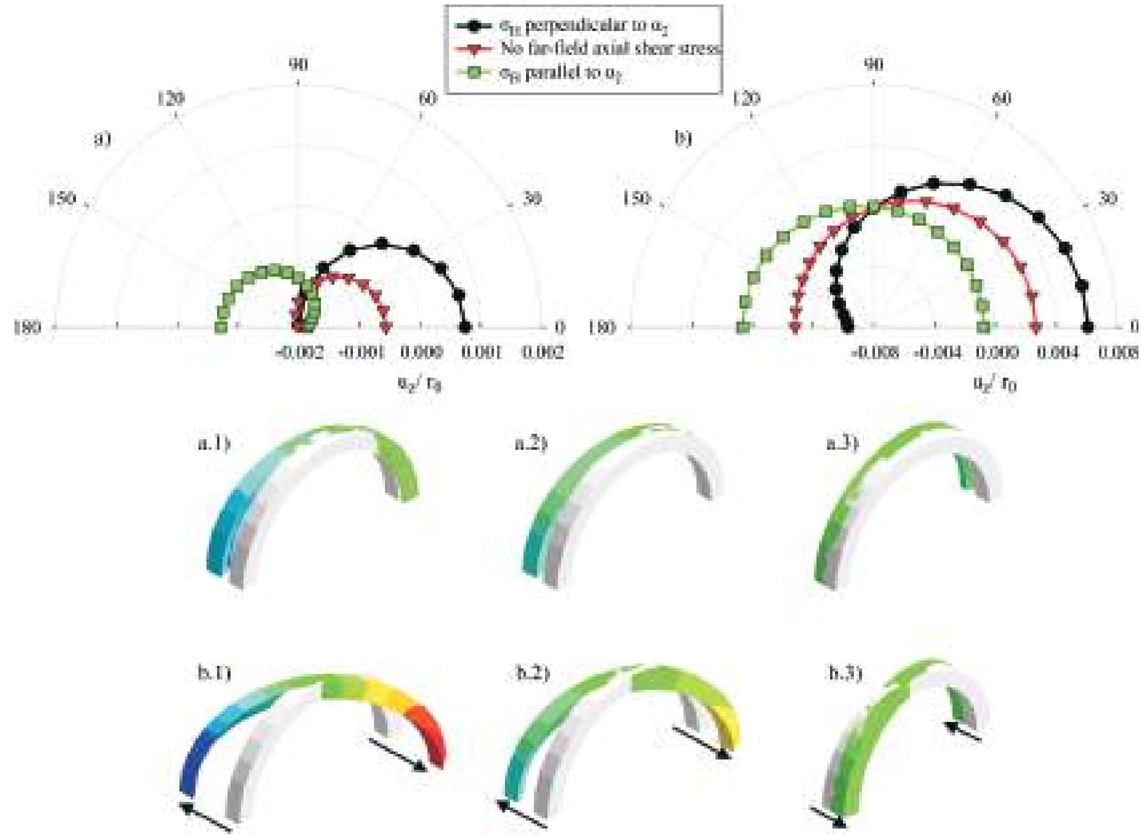

Figure 14 - Normalized axial displacements of the tunnel: (a) at the face; (b) far-behind the face. The colors of the axially deformed tunnel cross-sections are associated with the magnitude of the axial displacements and are used for visualization purposes (the colors legend is not included for clarity, but the magnitude of the displacements is given in the plot).

mass anisotropy complement each other, while when σ_H is parallel to the strike, they have opposite effects.

Figure 15 shows the normalized horizontal and vertical tunnel displacements with the normalized distance from the face of the tunnel. The displacements of Case 1 with horizontally structured rock mass are plotted for comparison. The vertical displacements are similar in all three cases with vertically structured rock mass and are smaller than those with horizontally structured rock mass. The reason for this is because the rock stiffness in the vertical direction is the largest for vertically structured rock mass and the smallest for horizontally structured rock mass. For verti-

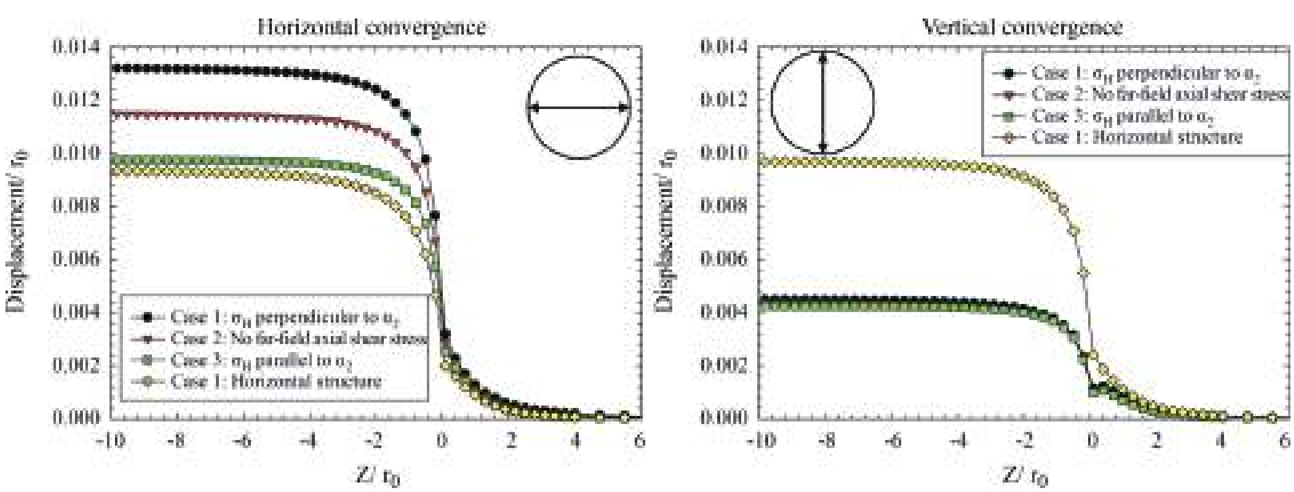

Figure 15 - Horizontal and vertical tunnel convergence *vs.* distance from the face (both normalized with respect to the tunnel radius), for unsupported tunnel. Z is the distance from the face of the tunnel (Fig. 2); r_0, the tunnel radius, is 5 m. The circles represent the tunnel cross section and the arrows indicate the direction and location of the displacements plotted.

cally structured rock mass, the horizontal displacements are larger for Case 1 (σ_H perpendicular to the strike) and smaller for Case 3 (σ_H parallel to the strike). This is due to the compliance matrix of the transversely anisotropic elastic model, which is fully populated when the tunnel is misaligned with one of the principal axes of material anisotropy. Thus, in-plane and out-of-plane stresses and deformations are coupled. As a consequence, radial displacements are affected by the far-field axial shear stresses. Note that when the tunnel is aligned with one of the principal axes of the material anisotropy, in-plane and out-of-plane deformations are decoupled. As a consequence, the far-field axial shear stress has no influence on the radial displacements far-behind the face (see *e.g.* Figs. 4 and 5 for horizontally-structured rock mass). The horizontal convergence for Case 1 with horizontally structured rock mass is smaller than with vertically structured rock mass, because the rock mass stiffness is the largest in the horizontal direction than when the rock mass structure is horizontal.

Figure 16 shows the normalized radial displacements and the deformed tunnel cross-section for the cases with vertically structured rock mass and for Case 1, with horizontally structured rock mass, which is included for comparison. At the face of the tunnel, the radial displacements are always asymmetric, but they are symmetric far-behind the face. As explained before, the asymmetric deformations near the face occur because the anti-symmetric axial displacements are constrained by the face of the tunnel. Note that the asymmetric deformations at the face and the symmetric deformations far-behind the face are larger when σ_H is perpendicular to the strike (Case 1) and smaller when σ_H is parallel to the strike (Case 3). At the face, a horizontal translation of the tunnel cross section occurs for all cases. The translation is towards the right for Case 1 (σ_H perpen-

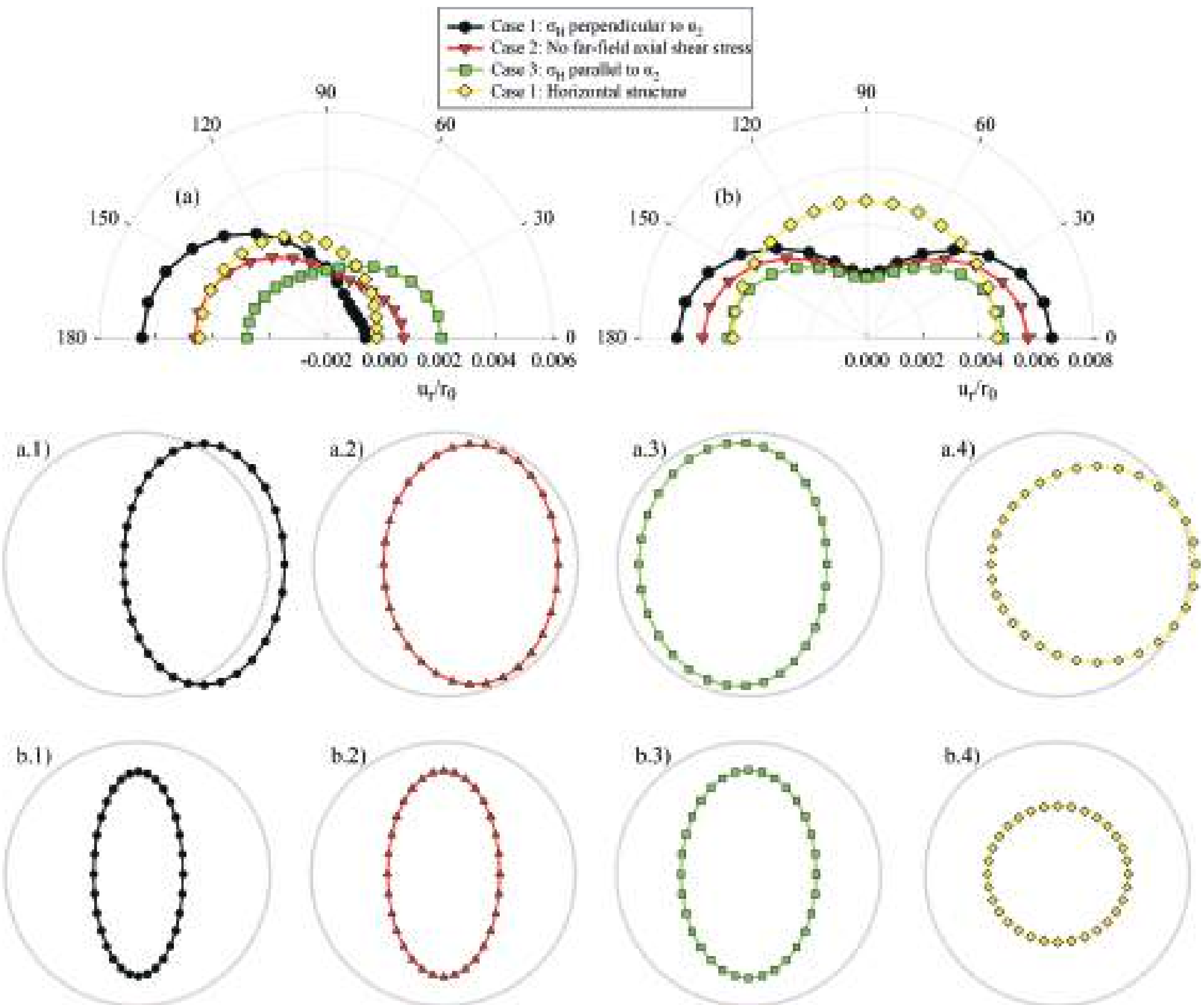

Figure 16 - Normalized radial displacements at the tunnel perimeter with respect to the tunnel radius and deformed tunnel cross-section, for unsupported tunnel. (a) at the face; (b) far-behind the face. Deformations are magnified 200 times at the face and 100 times far-behind the face.

dicular to the strike, Fig. 16.a.1), Case 2 (no far-field axial shear stress, Fig. 16.a.2) and for Case 1 with horizontally structured rock mass (Fig. 16.a.4), but it is towards the left for Case 3 (σ_H parallel to the strike, Fig. 16.a.3). As one can see in Fig. 16, the deformed tunnel cross-section has a pronounced ellipsoidal shape far-behind the face when the rock structure is vertical (Cases 1 to 3). This is the result of a far-field horizontal stress larger than vertical, and the fact that the larger horizontal stress is applied in the direction of the smaller stiffness of the rock. The opposite happens in the horizontally structured rock mass, as discussed in the previous section.

Figure 17 shows the normalized radial displacements at the springline and the horizontal translation of the tunnel

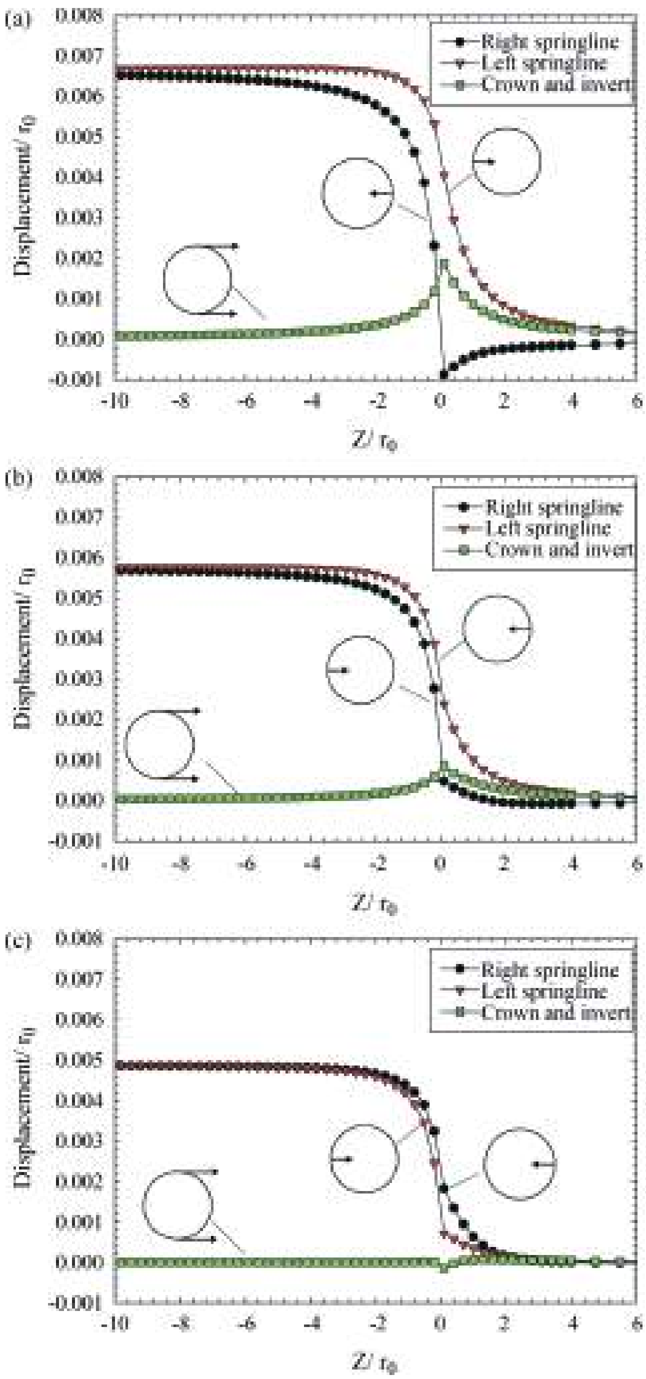

Figure 17 - Normalized radial and horizontal translation of the tunnel cross section with respect to the tunnel radius *vs.* the normalized distance from the face with respect to the tunnel radius, for unsupported tunnel. (a) Case 1, σ_H perpendicular to the strike; (b) Case 2, no far-field axial shear stress and; (c) Case 3 σ_H parallel to the strike. Z is the distance from the face of the tunnel (Fig. 2); r_0, the tunnel radius, is 5 m. The circles represent the tunnel cross section and the arrows indicate the direction and location of the displacements plotted.

cross section with the normalized distance from the face of the tunnel. The radial displacements on the left and right at the springline are different near the face but are the same far-behind the face. The horizontal translation of the tunnel cross section occurs near the face in all three scenarios; it is maximum at the face and reduces to zero far behind the face. Figure 17 also shows the "corrected" radial displacements, which are the radial displacements without the translation, as indicated in the graphs. For Case 2, no far-field axial shear stress, the corrected radial displacements are the same (within numerical approximation) on both sides of the springline. For Cases 1 and 3, where the far-field axial shear stress is not zero, the corrected radial displacements near the face are asymmetric. Thus, the horizontal translation observed in Case 2, no far-field axial shear, is in reality a horizontal rigid body displacement of the tunnel cross section, while in Cases 1 and 3, where the far-field axial shear stress is present, the deformations are more complex. The combination of rock anisotropy and far-field axial shear produces a response of the rock around the tunnel quite different (and more complex) than when the rock is isotropic. Indeed, in isotropic elastic ground, Vitali *et al.* (2019b) observed that the asymmetric radial deformations near the face due to a far-field axial shear stress could be decomposed into a rigid body displacement of the tunnel cross-section and anti-symmetric radial displacements, which is not always the case in anisotropic rock.

Figure 18 shows the stress paths at the springline, normalized with respect to the vertical stress. The labels (1, 2 and 3) shown in Fig. 18 refer to positions far-ahead of the face (1), at the face (2), and far-behind the face (3), as indicated in Fig. 2. The stresses are extracted at a distance of $0.1r_0$ from the tunnel perimeter, to avoid the mathematical singularity at the corner formed between the tunnel face and the excavation. As a consequence of the asymmetric deformations near the face, the stress paths are asymmetric near the face as well. For Case 1, σ_H perpendicular to the strike, the rock on the right-hand side of the springline takes load ahead of the face, the stresses increase near the face, and then they decrease behind the face. On the left, the stresses decrease ahead of the face and increase behind the face. Note that the stresses on the right and left springlines far-behind the face are the same. The stress paths are consistent with a horizontal translation of the tunnel cross section towards the right, which compresses the rock at the springline, to the right, and unloads to the left. The opposite is observed for Case 3, σ_H parallel to the strike. On the right, there is unloading ahead of the face and loading behind the face; on the left springline, there is loading ahead of the face and unloading behind. Note that the tunnel translation in Case 3 is towards the left. For Case 2, no far-field axial shear stress, both sides of the springline follow the same stress path. The stresses near the face are larger at the right springline, which is consistent with the observed horizontal translation towards the right. It is interesting to note that the unloading stress path ahead of the face is only observed when the far-field axial shear stress is present. Figure 19 shows the normalized stress paths at the crown with respect to the vertical stress, for the three cases with vertically structured rock mass, and for Case 1, with horizontally structured rock mass, which is included for comparison. As one can see, all the stresses increase near the face. The shear stresses are smaller for Case 2, no far-field axial shear stress, than for the other cases. Far-behind the face, the stress state for Case 1, σ_H perpendicular to the strike, and Case 3, σ_H parallel to the strike, are the same and slightly different than for Case 1, with horizontally structured rock mass. This finding suggests that the orientation of the rock structure with respect to the tunnel strongly affects the ground deformations around the tunnel, particularly near

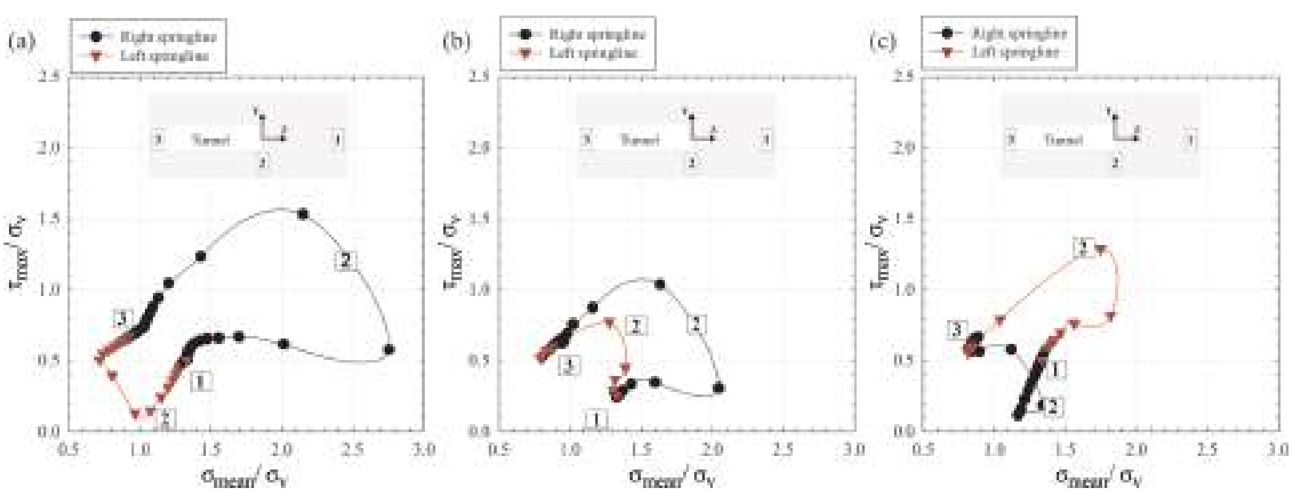

Figure 18 - Normalized stress paths with respect to the vertical stress for unsupported tunnel. (a) Case 1: σ_H perpendicular to the strike; (b) Case 2, no far-field axial shear stress; and (c) Case 3, σ_H parallel to the strike. Position (1) represents a point far ahead of the face of the tunnel; (2), at the face (*i.e.* Z = 0); and (3), far-behind the face.

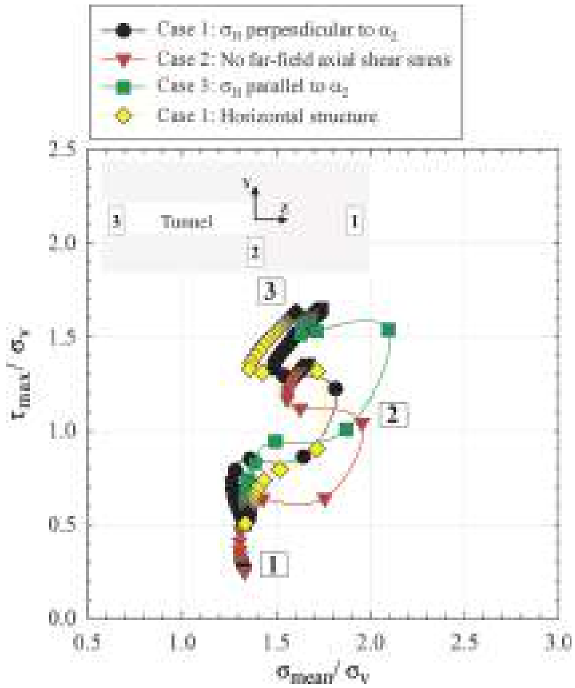

Figure 19 - Stress paths at the crown. Position (1) represents a point far ahead of the face of the tunnel; (2), at the face (*i.e.* Z = 0); and (3), far-behind the face.

the face of the tunnel, but has limited influence on the stresses around the tunnel far-behind the face.

The asymmetric deformations found near the face may affect the liner, if the tunnel is supported. This is investigated by running three new cases, all analogous to the previous cases discussed, but with a liner placed close to the face (Fig. 2). The results are presented in Figs. 20 and 21. Figure 20 shows the normalized radial stresses with the normalized distance from the tunnel face. As a consequence of the asymmetric deformations near the face, the radial stresses at the tunnel perimeter are asymmetric near and far-behind the face. The largest stress asymmetries occur for Case 1, when σ_H is perpendicular to the strike, and the smallest for Case 2, no far-field axial shear stress. The radial stresses are larger at the right springline when σ_H is perpendicular to the strike and when there is no far-field axial shear stress, but are larger at the left when σ_H is parallel to the strike. This is consistent with the direction of the tunnel cross section translation observed. The radial stresses at the crown are similar for the three cases and are larger than the stresses at the springline, given that the horizontal stress is larger than the vertical (*i.e.* stress concentrations are larger at the crown). Figure 21 shows the internal forces of the liner normalized with respect to the vertical stress and the tunnel radius. The internal forces are always asymmetric. The thrust is larger at the crown and at the invert and is smaller at the springline, while the bending moments are larger at the springline. The internal forces are larger for Case 1, when σ_H is perpendicular to the strike and are smaller for Case 3, when σ_H is parallel to the strike. This is expected because the radial deformations are larger for Case 1 and smaller for Case 3, as shown in Figs. 15, 16 and 17. It is interesting to note that the internal forces for the cases with far-field axial shear stress (Cases 1 and 3) are more asymmetric than the case with no far-field axial shear stress (Case 2).

5. Conclusions

The effects of the tunnel misalignment with the geostatic principal stress directions in anisotropic rock masses are investigated in this paper. Far-field axial shear stresses are present when the tunnel is not aligned with the geostatic principal stress directions. Anti-symmetric axial displacements and axial shear stresses are induced around the tunnel due to the tunnel misalignment with the geostatic principal stress directions and with the principal material directions. Near the face, axial displacements are constrained by the face of the tunnel; as a consequence, asymmetric radial deformations occur near the face. 3D FEM

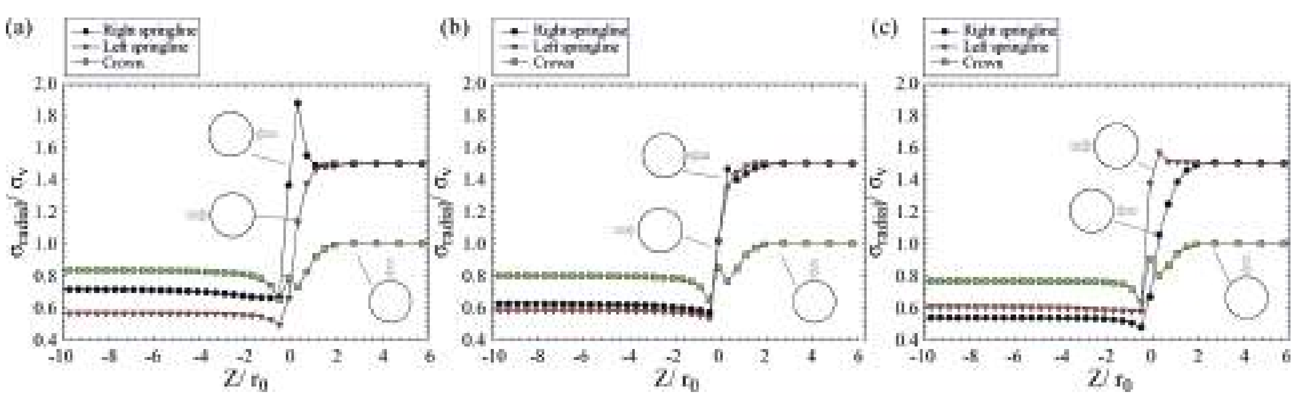

Figure 20 - Normalized radial stresses with respect to the vertical stress *vs.* the normalized distance from the face with respect to the tunnel radius, for supported tunnel. (a) Case 1, σ_H perpendicular to the strike; (b) Case 2, no far-field axial shear stress; and (c) Case 3, σ_H parallel to the strike. Z is the distance from the face of the tunnel (Fig. 2); r_0, the tunnel radius, is 5 m. The circles represent the tunnel cross section and the arrows indicate the direction and location of the radial stresses plotted.

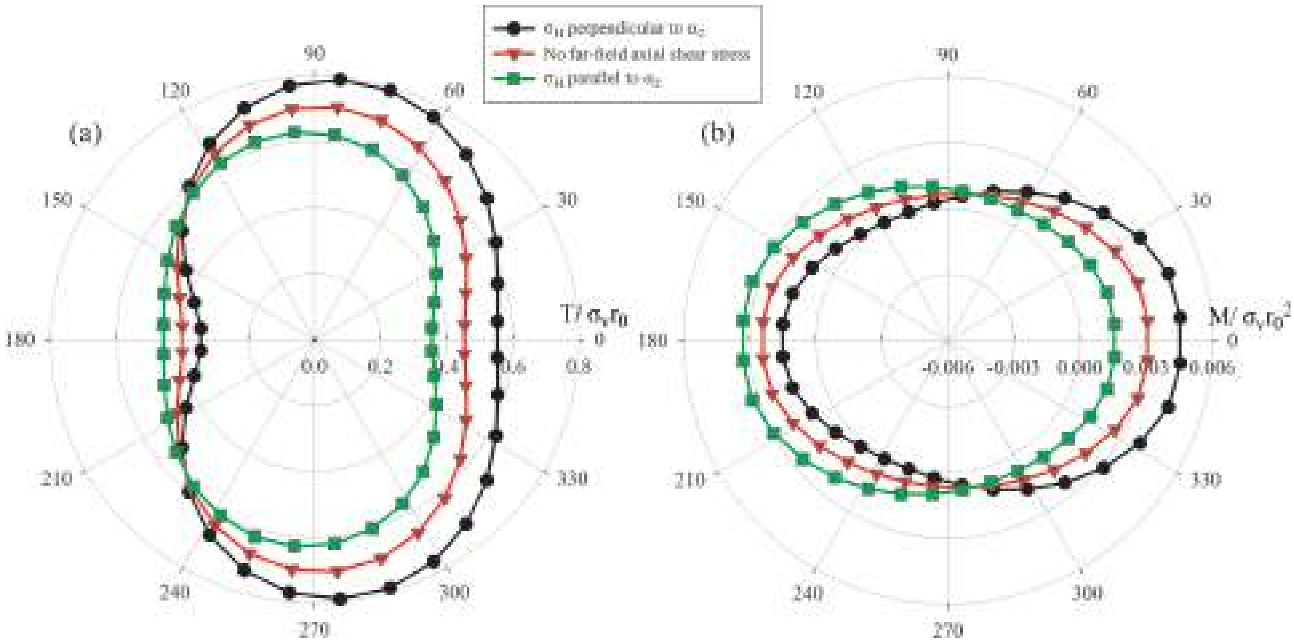

Figure 21 - Normalized internal forces with the vertical stress and tunnel radius. (a) Thrust; (b) Bending moment.

simulations of a tunnel at 45° with the horizontal principal stresses have been performed, with an anisotropic geostatic stress field. Two scenarios have been investigated: a horizontal tunnel in rock mass with horizontal structure, and in a rock mass with a vertical structure. In both scenarios, the rock response is approximated through a transversely anisotropic elastic model. Both unsupported and supported tunnels are considered.

For the scenario with the horizontally-structured rock mass, the tunnel is always aligned with the rock mass structure. Asymmetric radial deformations near the face of the tunnel occur when a far-field axial shear stress is present. Far-behind the face, for the unsupported tunnel, the radial displacements are symmetric, which indicates that the far-field axial shear stress does not affect the radial displacements far-behind the face. The reason is that, when the tunnel is aligned with one of the principal material directions, in-plane and out-of-plane deformations are decoupled. For supported tunnels, the asymmetric deformations near the face affect the liner response. Far behind the face, asymmetric radial displacements and stresses are present, so the internal forces in the liner are asymmetric.

For the scenario where the rock mass structure is vertical and the tunnel axis makes an angle of 45° with the strike or the rock structure, axial displacements and axial shear stresses are induced around the tunnel. Three scenarios are being investigated: major horizontal stress parallel to the strike direction, major horizontal stress perpendicular to the tunnel direction and no far-field axial shear stress. Far-behind the face, the induced axial displacements are always anti-symmetric with respect to the vertical axis. The largest axial displacements occur when σ_H is perpendicular to the strike and the smallest when σ_H is parallel to the strike. This is because, when σ_H is perpendicular to the strike, the axial distortion of the tunnel cross section produced by the far-field axial shear stress and by the rock mass structure complement each other. The opposite happens when σ_H is parallel to the strike. Near the face, asymmetric deformations are induced. The asymmetric radial deformations near the face are larger when σ_H is perpendicular to the strike and smaller when σ_H is parallel. The same is true far-behind the face of the tunnel. In other words, the far-field axial shear stress affects the radial displacements far-behind the face when the tunnel is misaligned with the principal directions of material anisotropy. For supported tunnels, the radial stresses at the tunnel perimeter are asymmetric near the face and far-behind the face. Thus, the internal forces in the tunnel liner are asymmetric. The largest internal forces occur when σ_H is perpendicular to the strike and the smallest when σ_H is parallel to the strike.

The ground deformations far-behind the tunnel face are heavily affected by the orientation of the rock mass structure with the tunnel. For the horizontally structured rock mass, the deformed tunnel cross section far-behind the face has a slightly ellipsoidal shape (*i.e.* the radial displacements at the springline are similar to those at the crown and invert). In contrast, for vertically-structured rock mass, the deformed tunnel cross section has a pronounced ellipsoidal shape, where the radial displacements at the springline are substantially larger than at the crown and invert. For this specific case, the far-field horizontal stress is larger than the vertical. Thus, for horizontally-structured rock mass, the largest stresses are aligned with the stiffest material direction (*i.e.* parallel to the rock structure) and the smallest stresses are aligned with the softest material direction (*i.e.* perpendicular to the strike). The opposite occurs for vertically-structured rock mass. The rock stresses near the tunnel perimeter for horizontally- and vertically-structured rock mass are similar far-behind the face, which seems to suggest that rock anisotropy has a modest influence on the stresses far behind the face of the tunnel.

The results presented in this paper provide insight into the complex behavior of tunnels in anisotropic rock masses, and highlight the importance of considering the tunnel misalignment with the geostatic principal stress directions and with the rock mass structural planes. Also, the results show the importance of the orientation of the geostatic principal stress directions with respect to the principal directions of material anisotropy.

Acknowledgments

The research is being partially supported by the research funding agency of the Brazilian government CNPq ("Conselho Nacional de Desenvolvimento Científico e Tecnológico"). The authors acknowledge the support from CNPq and from Midas company, which kindly provided the license of Midas GTX NX software, used in the present work.

References

Armand, G.; Noiret, A.; Zghondi, J. & Seyedi, D.M. (2013). Short- and long-term behaviors of drifts in the Callovo-Oxfordian claystone at the Meuse/Haute-Marne Underground Research Laboratory. Journal of Rock Mechanics and Geotechnical Engineering, 5(3):221-230.

Brady, B.H.G. & Brown, E.T. (2006). Rock Mechanics for Underground Mining. 3rd ed. Springer, New York, 628 p.

Brown, E.T. & Hoek, E. (1978). Trends in relationships between measured in-situ stresses and depth. Int. J. Rock Mech. Min. Sci., 15(4):211-215.

Button, E.; Leitner, R.; Poetsch, M. & Schubert, W. (2006). Spatial relationships between discontinuity orientation and system behavior in underground excavations. Proc. ARMA 41st U.S. Symposium on Rock Mechanics. ARMA/USRMS 06-957.

Evans, K.F.; Engelder, T. & Plumb R.A. (1989). Appalachian Stress study .1. a detailed description of in-situ stress variations in devonian shales of the appalachian plateau. J. Geophys. Res. Earth Planets, 94:7129-7154.

Fortsakis, P.; Nikas, K.; Marinos, K.V. & Marinos, P. (2012). Anisotropic behaviour of stratified rock masses in tunnelling. Eng. Geol., 141-142:74-83.

Goodman, R.E. (1989). Introduction to Rock Mechanics. 2nd ed. Willey, New York, 576 p.

Goricki, A.; Button, A.E.; Schubert, W.; Pötsch, M. & Leitner, R. (2005). The influence of discontinuity orientation on the behaviour of tunnels. Felsbau., 23(5):12-18.

Gysel, M. (1975). In-Situ stress measurements of the primary stress state in the Sonnenberg tunnel in Lucerne, Switzerland. Tectonophysics, 29:301-314.

Haimson, B.C.; Lee, M.Y. & Song, I. (2003). Shallow hydraulic fracturing measurements in Korea support tectonic and seismic indicators of regional stress. Int. J. Rock Mech. Min. Sci., 40(7-8):1243-1256.

Hoek, E. (2007). Practical Rock Engineering, 2007 ed. Available for download at: https://www.rocscience.com/learning/hoeks-corner/course-notes-books (last visit on March, 23rd, 2020).

Klopcic, J. & Logar, J. (2014). Effect of relative orientation of anisotropy planes to tunnel axis on the magnitude of tunnelling displacements. International Journal of Rock Mechanics and Mining Sciences, 71:235-248.

Lenz, G.; Kluckner, A.; Holzer, R.; Stadlmann, T.; Schachinger, T. & Gobiet, G. (2017). Prediction of fault zones based on geological and geotechnical observations during tunnel construction. Geomechanics and Tunneling, 10(4):366-379.

Martin, C.D. (1997). Seventeenth Canadian Geotechnical Colloquium: The effect of cohesion loss and stress path on brittle rock strength. Canadian Geotechnical Journal, 34(5):698-725.

McGarr, A. & Gay, N.C. (1978). State of Stress in the Earth's Crust. Ann. Rev. Earth Planet., Sci. 6:405-436.

Park, E.S.; Choi, B.H.; Bae, S.H. & Jeon, S. (2014). Horizontal stresses at shallow depths in Seoul (Korea) gneissic region. Proc. EUROCK 2014, Rock Eng. Rock Mech. Struct. Rock Masses, ISRM European Regional Symposium, pp. 399-404.

Perras, M.A.; Wannenmacher, H. & Diederichs, M.S. (2015). Underground excavation behaviour of the Queenston formation: tunnel back analysis for application to shaft damage dimension prediction. Rock Mech. Rock Eng., 48(4):1647-1671.

Schubert, W. & Budil, A. (1995). The importance of longitudinal deformation in tunnel excavation. Proc. 8th ISRM Congress on Rock Mechanics, pp. 1411-1414.

Schubert, P.; Klopcic, J.; Stimulak, A.; Ajdic, I. & Logar, J. (2005). Analysis of characteristic deformation patterns at the Trojane tunnel in Slovenia. Felsbau, 23(5):25-30.

Schubert, W. & Moritz, B. (2011). State of the art in evaluation and interpretation of displacement monitoring data in tunnels. Geomechanics and Tunneling, 4(5):371-380.

Souce, K.; Vavro, M.; Stas, L.; Vavro, L.; Waclawik, P.; Konicek, P.; Ptácek, J. & Vondrovic, L. (2017) Geotechnical characterization of Bukov underground research facility. Procedia Engineering, 191:711-718.

Tonon, F. & Amadei, B. (2002). Effect of elastic anisotropy on tunnel wall displacements behind a tunnel face. Rock Mech. Rock Eng., 35(3):141-160.

Tonon, F. & Amadei, B. (2003). Stresses in anisotropic rock masses: An engineering perspective building on geological knowledge. Int. J. Rock Mech. Min. Sci., 40(7-8):1099-1120.

Vitali, O.P.M.; Celestino, T.B. & Bobet, A. (2017). 3D finite element modelling optimization for deep tunnels with material nonlinearity. Undergr. Sp., 3(2):125-139.

Vitali, O.P.M.; Celestino, T.B. & Bobet, A. (2018). Analytical solution for tunnels not aligned with geostatic principal stress directions. Tunn. Undergr. Sp. Technol., 82:394-405.

Vitali, O.P.M.; Celestino, T.B. & Bobet, A. (2019a). Shallow tunnel not aligned with the geostatic principal stress directions. Proc. Geo-Congress2019, GSP, 313:214-222.

Vitali, O.P.M.; Celestino, T.B. & Bobet, A. (2019b). Shallow tunnels misaligned with geostatic principal stress directions: analytical solution and 3D face effects. Tunn. Undergr. Sp. Technol., 89:268-283.

Vitali, O.P.M.; Celestino, T.B. & Bobet, A. (2019c). Progressive failure due to tunnel misalignment with geostatic principal stresses. Proc. ISRM 14th International Congress on Rock Mechanics, pp. 2292-2299.

Vitali, O.P.M.; Celestino, T.B. & Bobet, A. (2020). Analytical solution for a deep circular tunnel in anisotropic ground and anisotropic geostatic stresses. Manuscript under review for publication in a peer-reviewed journal.

Wileveau, Y.; Cornet, F.H.; Desroches, J. & Blumling, P. (2007). Complete in situ stress determination in an argillite sedimentary formation. Phys. Chem. Earth, 32(8-14):866-878.

Worotnicki, G. (2013). CSIRO Triaxial Stress Measurement Cell. In: Rock testing and site characterization: principles, practice and projects: 329-394.

Zhao, X.G.; Wang, J.; Cai, M.; Ma, L.K.; Zong, Z.H.; Wang, X.Y.; Su, R.; Chen, W.M.; Zhao, H.G.; Chen, Q.C.; An, Q.M.; Qin, X.H.; Ou, M.Y. & Zhao, J.S. (2013). In-situ stress measurements and regional stress field assessment of the Beishan area, China. Eng. Geol., 163:26-40.

Zhao, X.G.; Wang, J.; Qin, X.H.; Cai, M.; Su, R.; He, J.G.; Zong, Z.H.; Ma, L.K.; Ji, R.L.; Zhang, M.; Zhang, S.; Yun, L.; Chen, Q.C.; Niu, L.L. & An, Q.M. (2015). In-situ stress measurements and regional stress field assessment in the Xinjiang candidate area for China's HLW disposal. Eng. Geol., 197:42-56.

Technical Notes

A Model of Energy Dissipation for the Mode of Rupture of Shallow Foundations in Sandy Soils

L.F. dos Santos, A. Saraiva, A.C. de Freitas

Abstract. The plastic deformation of sandy soils is poorly understood from a microscopic point of view. The criteria to predict the mode of rupture of shallow foundations are mostly based on phenomenological arguments and may fail to explain the results obtained experimentally in model foundations. This work validates a model to determine the mode of rupture of sandy soils underlying shallow foundations based on the assumption that the complex rupture behavior of sand may be described approximately as a trade-off between the energy dissipation in a sand slip and the subsequent reduction of elastic potential energy in the surrounding sand mass. This theoretical framework describes more accurately experimental results found in the literature than the approach based on the rigidity index of the soil. In order to extrapolate results from small-size model experiments to large-size foundations, direct dimensional arguments may be used, since the proposed account of the failure mechanism is based on the laws of mechanics, not on phenomenological equations.
Keywords: bearing capacity, sandy soils, shallow foundations, stress relief.

1. Introduction

Sand under the gravitational field presents a unique set of mechanical properties. While soft sand resembles a fluid, it becomes rigid under pressure at higher depths. As a result, shallow foundations under extreme stress induce different rupture modes, depending on the details of the foundation design and the characteristics of the sandy soil. Even at typical stresses, well below the maximum load for the foundation, this complex range of behavior impacts the prediction of the foundation settlement, affecting the overall soil compressibility.

Soil incompressibility is a common assumption in analytical calculations of the bearing capacity of shallow foundations (Terzaghi, 1943). This approximation is known to lead to significant errors that could compromise the safety of the structure, overestimating the maximum allowable load (Vesic, 1975). In the absence of a full scale field test, it is challenging to determine the validity of this approximation *a priori*. Early attempts to address this problem were based on the analysis of a compressibility factor that amends the equation for the shear failure load (Vesic, 1975). To determine when this factor is applicable, the rigidity index of the soil is determined and compared to a critical rigidity index that separates general failure from non-general (either punching or local) failures.

This method leads to significant disparity between theory and experimental results. The criterion for the critical rigidity index is based solely on the mathematical form of the compressibility factor – a correction being added whenever this factor is less than one (*i.e.*, when this correction is responsible for reducing the maximum allowable load). Comparison between this criterion and experimental data from extensive tests performed by Vesic (1963) reveals that often a local or punching failure (which indicate a soil that is necessarily compressible) is observed with sands of rigidities predicted to lead to general failure. This is worrisome, since this error leads to discarding the correction factor and overestimating the bearing capacity of a foundation.

A physical criterion is derived here for determining the type of rupture a sand will suffer under a foundation load above the bearing capacity. This criterion is based on an analogy with the formation and propagation of cracks in solids, which dissipate the elastic potential energy of the surrounding mass under stress. This argument is adapted to the case of shallow foundations on sandy soils by estimating the energy cost of dislocating a mass of sandy soil against shearing stress. This sets a maximum total length L_{total} for the crack that is compared to the hypothetical length of the failure surface in the case of general, local or punching shearing failures. The results of this model are validated against experimental results of Vesic (1963), showing greater accuracy than the criterion based on the rigidity index proposed by the same author.

2. Bearing Capacity

Vesic (1975) observed the existence of 3 modes of failure: general shear failure, local shear failure and punch-

Luiza Fernandes dos Santos, M.Sc. Researcher, Programa de Projeto de Estruturas, Escola Politécnica, Universidade Federal do Rio de Janeiro, Av. Athos da Silveira Ramos 149, Ilha do Fundão, Centro de Tecnologia, Bloco A, 2° andar, Cidade Universitária, Rio de Janeiro, Brazil. e-mail: luizadosfs@gmail.com.
André Saraiva, D.Sc., Associate Professor, Departamento de Física, Instituto de Física, Universidade Federal do Rio de Janeiro, Av. Athos da Silveira Ramos 149, Ilha do Fundão, Centro de Tecnologia, Bloco A, 2° andar, Cidade Universitária, Rio de Janeiro, Brazil. e-mail: also@if.ufrj.br.
Alessandra Conde de Freitas, D.Sc., Associate Professor, Escola Politécnica, Universidade Federal do Rio de Janeiro, Av. Athos da Silveira Ramos 149, Ilha do Fundão, Centro de Tecnologia, Bloco A, 2° andar, Cidade Universitária, Rio de Janeiro, Brazil. e-mail: alessandracfreitas@poli.ufrj.br.
Submitted on April 17, 2018; Final Acceptance on October 1, 2019; Discussion open until August 31, 2020.
DOI: 10.28927/SR.431141

ing shear failure. He concluded that the bearing capacity is related to the rupture mode, the foundation geometry, relative density, scale and loading conditions. The calculation of the soil rupture load for shallow foundations based on soils represents a challenging problem of elastic-plastic equilibrium. A common approach is to disregard the soil compressibility, considering the failure mechanism to be approximately described as a rigid-plastic transition at a rupture stress σ_{rup}.

Investigating a shallow footing resting on a sandy (cohesionless) soil, in the absence of a water level and with homogeneous mechanical properties – namely, the friction angl ϕ and the unit weight γ – Buisman (1940) and Terzaghi (1943) propose an expression for the ultimate vertical stress that may be aplied at the center of the foundation. This expression takes a particularly simple form in the case of a long rectangular footing ($L >> B$ in Fig. 1), given by:

$$\sigma_{rup} = \frac{1}{2}\gamma \cdot B \cdot N_\gamma \tag{1}$$

where N_γ is a dimensionless bearing capacity factor, which was investigated by several authors (see Michalowski (1997) and references therein). One of the canonical expressions for N_γ is given by Vesic (1975) as

$$N_\gamma = 2\left\{e^{\pi \tan\phi}\left[\tan\left(\frac{\pi}{4}+\frac{\phi}{2}\right)\right]^2 + 1\right\}\tan\phi \tag{2}$$

This analysis may also be performed with corrections for foundations with overburden, but this is beyond the scope of the present work and will not be discussed here.

2.1. Effect of foundation shape

For foundation shapes other than $L >> B$ (long rectangular), the mathematical difficulties in obtaining solutions for the ultimate pressure (σ_{rup}) are considerable, since no longer the plane strain condition may be assumed. The expression proposed by Buismann (1940) and Terzaghi (1943) (Eq. 1) is not valid for foundations with $L < 5B$, including circular and square foundations.

Due to the difficulties described, the approach to the problem is semi-empirical. Several experiments were performed by Vesic with different shapes of foundations and, from these results, a shape correction factor ζ_γ was introduced in Eq. 1. This way, the phenomenologically amended equation is written as

$$\sigma_{rup} = \frac{1}{2}\gamma \cdot B \cdot N_\gamma \cdot \zeta_\gamma \tag{3}$$

where the shape factor ζ_γ is calculated according to Table 1.

2.2. Influence of soil compressiblity and scale effect

It has been previously emphasized that the whole procedure of ultimate pressure (σ_{rup}) analysis is based on the incompressible soil hypothesis and, strictly speaking, this should be applied only to cases where general shear failure is expected. There is a lack of rational methods for the analysis of rupture surfaces in the other two forms (local and punching), characteristic of compressible soil.

The criterion to discern the mode of failure will be proposed below and will be compared to the criterion proposed by Vesic (1975).

3. A Model of Energy Dissipation for the Rupture of Shallow Foundation on Sandy Soils

The present work proposes comparison between the ultimate pressure (σ_{rup}) and the stress necessary to obtain a maximum length L_{total} (σ_L). To define σ_L, a model of the tension necessary to generate a crack of length L_{total} in solids will be devised. This stress is expressed as (see Appendix 1):

$$\sigma_L = 2\sqrt{\frac{E \cdot \eta}{\pi \cdot L_{total}}} \tag{4}$$

Equation 4 may be interpreted as the stress relieved in a material of elastic modulus E when a shear failure of length L_{total} is created. The energy cost η per unit area for forming this failure has an obvious interpretation for solids (related to the density of chemical bonds broken by the crack), but must be reinterpreted for sandy soil. Energy is dissipated at the shear failure surface by means of internal friction.

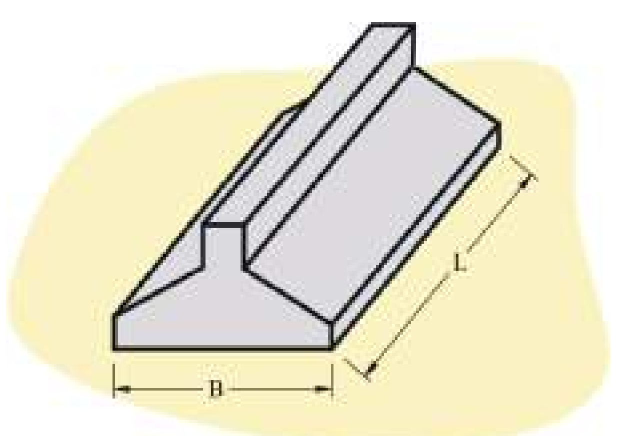

Figure 1 - Load capacity problem in shallow foundations.

Table 1 - Shape correction factor (ζ_γ).

Shape of Base	ζ_g
Strip	1.00
Rectangle	1-0.4(B/L)
Circle and Square	0.60

A detailed demonstration of the mechanics of an element of soil near the failure surface is given in the Appendix 1.

In the case of general failure, the surface density of energy is thus written as the sum of three parts:

$$\eta = \eta_{ZRI} + \eta_{el} + \eta_{ZRIII} \quad (5)$$

where each term refers to a contribution related to the the three zones depicted in Fig. 2.

These terms are given by (see Appendix 2)

$$\eta_{ZRI} = \gamma \cdot B^2 \frac{\tan\phi}{8} \tan\left(\frac{\pi}{4} + \frac{\phi}{2}\right) \quad (6)$$

$$\eta_{el} = \frac{B^2 \gamma}{8(-1+\sin\phi)}[1 - 2\sin\phi + \sin 3\phi + e^{\pi\tan\phi}(-1 - 2\sin\phi + \sin 3\phi)] \quad (7)$$

$$\eta_{ZRIII} = \gamma B^2 \frac{\tan\phi}{8\left(\cos\frac{\phi}{2} - \sin\frac{\phi}{2}\right)} \times \tan\left(\frac{\pi}{4} - \frac{\phi}{2}\right)\cos^2\phi \, e^{\pi\tan\phi} \quad (8)$$

The final expression for η then reads

$$\eta = \frac{B^2 \gamma}{8(-1+\sin\phi)}[+1 - 3\sin\phi + \sin 3\phi + e^{\pi\tan\phi}(-1 - 3\sin\phi + \sin 3\phi)] \quad (9)$$

The maximum length (L_{total}) may be defined as

$$L_{total} = L_{ZRI} + L_{el} + L_{ZRIII} \quad (10)$$

$$L_{total} = B\left[\frac{\sin\phi + e^{\frac{\pi\tan\phi}{2}} + e^{\frac{\pi\tan\phi}{2}}\sin\phi - 1}{\sqrt{2}\sin\phi\left(\cos\frac{\phi}{2} - \sin\frac{\phi}{2}\right)}\right] \quad (11)$$

where,

$$L_{ZRI} = \frac{B}{\sqrt{2}\left(\cos\frac{\phi}{2} - \sin\frac{\phi}{2}\right)} \quad (12)$$

$$L_{el} = \frac{B e^{\tan\phi\left(\frac{3\pi}{4} - \frac{\phi}{2}\right)}\sec\phi}{-\tan\phi\sqrt{2}\left(\cos\frac{\phi}{2} - \sin\frac{\phi}{2}\right)} \times \left(e^{-\tan\phi\left(\frac{3\pi}{4} - \frac{\phi}{2}\right)} - e^{\tan\phi\left(\frac{\pi}{4} - \frac{\phi}{2}\right)}\right) \quad (13)$$

$$L_{ZRIII} = \frac{B e^{\tan\phi\left(\frac{\pi}{2}\right)}\sec\phi}{\sqrt{2}\left(\cos\frac{\phi}{2} - \sin\frac{\phi}{2}\right)} \quad (14)$$

At the ultimate pressure, the failure reaches a maximum length L_{total} in the general mode. If this ultimate pressure is greater than the value required to generate a maximum failure length L_{total} of the sliding sand strip, the failure is general.

If the failure mode is not general, this analysis may be extended to differentiate local and punching shear failures. Current models only differentiate between general rupture and non-general rupture (Vesic, 1975).

The idea is to repeat the two arguments, adapting Eqs. 3 and 4. Equation 3 still holds, but Eq. 4 will have a change in two quantities: the surface energy density, and the maximum length, which are now calculated within zone

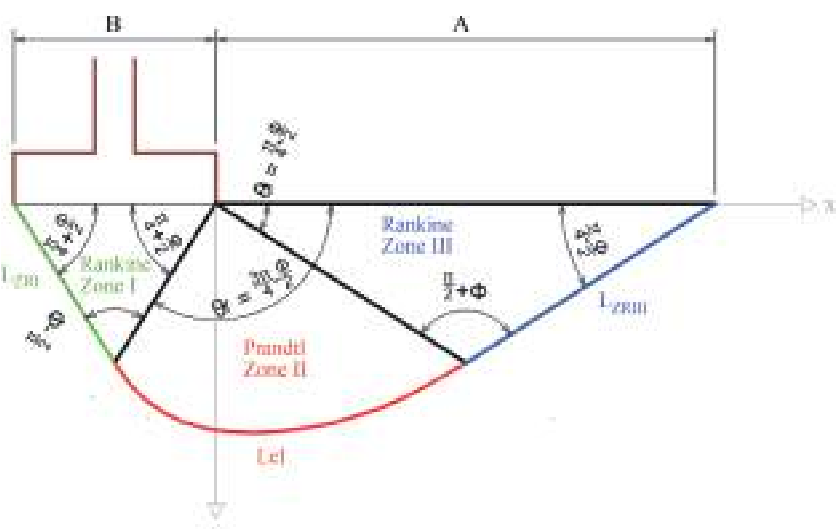

Figure 2 - Zones of failure in generalized rupture.

I. Therefore σ_L may be separately calculated for shearing failures within zone I (punching) and be referred to as σ_{punc}, or for the full extent of a general failure, referred to as σ_{gen}. In summary,

$$\sigma_{gen} = \sigma_L \left(L_{tot} = L_{ZRI} + L_{el} + L_{ZRIII}, \eta = \eta_{tot}\right) \tag{15}$$

$$\sigma_{punch} = \sigma_L \left(L_{tot} = L_{ZRI}, \eta = \eta_{ZRI}\right) \tag{16}$$

and the criteria for each failure mode reads

$\sigma_{rup} > \sigma_{gen} \rightarrow$ general shear failure

$\sigma_{punc} < \sigma_{up} < \sigma_{gen} \rightarrow$ local shear failure

$\sigma_{rup} > \sigma_{punc} \rightarrow$ punching shear failure

To account for circular, square and rectangular foundations, that is, when L is not much larger than B, one must consider a correction multiplier factor in Eq. 4. This correction factor is demonstrated in Santos (2017), and reads:

$$\sigma_L = 2\sqrt{\frac{E \cdot \eta}{\pi L_{total}}} \sqrt{\frac{1+2\chi}{1+\frac{3}{2}\chi}} \tag{17}$$

where the form of χ depends on whether the rupture is general or not. For general failure (Eq. 18) and non-generalized failure (Eq. 19), these are the respective equations:

$$\chi_{gen} = \frac{L_{total}}{L} \tan\left(\frac{\pi}{4} + \frac{\phi}{2}\right) \tag{18}$$

$$\chi_{punch} = \frac{L_{ZRI}}{L} \tan\left(\frac{\pi}{4} + \frac{\phi}{2}\right) \tag{19}$$

4. Vesic's Theory

Based on observations from experiments, Vesic (1973) points out that the determination of the failure mode quantitatively was not within the scope of his theory. Still, he proposes a tentative criterion to determine whether a compressibility and scale analysis is in order. While Vesic is careful to distinguish between the criterion for compressibility and the actual determination of the failure mode, he explicitly associates relative incompressibility to general shear failure. Therefore, this criterion is the only qualitative prediction of the failure mode available in the context of his work.

Vesic proposes a comparative evaluation between the rigidity index I_r, defined as:

$$I_r = \frac{G}{c + \sigma_{med} \tan\phi} \tag{20}$$

and the critical rigidity index:

$$I_{r\,crit} = \frac{1}{2} e^{\left[\left(3.30 - 0.45\frac{B}{L}\right)\cot\left(\frac{\pi}{4} - \frac{\phi}{2}\right)\right]} \tag{21}$$

where G (kPa) is the shear modulus, ϕ is the friction angle of the soil and σ_{med} (kPa) is a mean stress at a depth $B/2$ below the base of the footing. The shear modulus and mean stress could be defined respectively as

$$G = \frac{E}{2(1+\nu)} \tag{22}$$

$$\sigma_{med} = \frac{\sigma_v + 2\sigma'_h}{3} \tag{23}$$

where E (kPa) is the modulus of deformation, ν is the Poisson coefficient and σ_v (kPa) and σ_h (kPa) are the effective vertical stress and horizontal stress. These stresses are estimated at a depth $B/2$ below the base of the footing as $\sigma'_v = B\gamma / 2$ and $\sigma'_h = \sigma'_v k_0$, where k_0 is the coefficient of earth pressure at rest and it is defined as $k_0 = 1 - \sin\phi$.

The comparison proposed by Vesic is as follows:

$I_r > I_{r\ critical} \rightarrow$ general shear failure

$I_r < I_{r\ critical} \rightarrow$ non general (local or punching) shear failure

5. Comparison between models and experimental results

The model presented here will now be validated against experimental tests from Vesic (1963), showing fair agreement with the observation and outperforming the criterion of soil incompressibility.

In this series of experiments, Vesic provides all the data required for applying both criteria, either directly (as, for instance, the unit weight of the dry soil γ_d) or indirectly in terms of fitting equations (as in the example of the relation between the friction angle ϕ and the void ratio e). The elastic modulus E was not provided in Vesic (1963), but an expression is reported in Vesic (1973) associating this modulus to the mean normal stress $E = E_1\sqrt{\sigma_m / \sigma_1}$, with E_1 = 39,180.65 kN/m^2 (364 ton/ft^2) being the modulus at mean normal stress of σ_1 = 104.64 kN/m^2 (1 ton/ft^2).

All results are summarized in Table 1. The main quantities related to both criteria are shown, as well as the predictions.

The results shown in green match those obtained experimentally, but the ones in red do not (the ninth and the last columns from Table 2). The model presented here gives correct results in all instances, except for tests 34, 64 and 1 (last column from Table 2).

Vesic (1975) considers that the plane strain condition may be assumed whenever $L/B > 5$, but in Table 1 there are instances of L/B over this limit that can only be accounted for by using Eq. 17.

From the application of the mode of failure of sandy soils it was possible to generate the diagram shown in Fig. 3 for foundations based on the surface of the ground, that is,

Table 2 - Experimental results from Vesic (1963) and the predictions adopting the criterion in Vesic (1975) and the present work.

Experimental results from Vesic (1963)					Vesic (1973)	The predictions adopting the criterion in Vesic (1975)				The present work results		
Tests	B (m)	γ_d (kN/m^3)	ϕ (°)	Failure	E (kN/m^2)	$(I_r)_{crit}$	I_r	Failure	σ_{punc} (kPa)	σ_{rup} (kPa)	σ_{gen} (kPa)	Failure
34	0.05	15.37	43.15	General	1,821.75	359.58	3,463.46	General	22.93	47.74	58.35	Local
21		14.90	41.09	Local	1,820.36	263.39	3,681.14	General	21.65	31.93	51.34	Local
22		14.38	38.85	Local	1,820.43	192.85	3,934.37	General	20.31	20.95	44.72	Local
23		13.23	34.10	Punching	1,811.57	107.58	4,581.91	General	17.55	8.94	33.40	Punching
44	0.10	15.50	43.72	General	2,476.09	393.74	2,506.39	General	36.96	98.93	95.95	General
41		15.02	41.61	Local	2,476.26	284.25	2,665.09	General	34.88	65.36	84.16	Local
42		14.58	39.70	Local	2,479.70	216.41	2,815.84	General	33.04	45.45	74.81	Local
43		13.34	34.54	Punching	2,464.05	113.11	3,317.25	General	28.26	17.88	54.48	Punching
61	0.15	15.41	43.33	General	3,057.14	369.95	2,053.11	General	50.17	139.67	128.48	General
62		14.89	41.04	Local	3,059.30	261.49	2,193.6	General	47.09	89.27	111.44	Local
63		14.69	40.18	Local	3,059.14	231.33	2,250.15	General	45.95	75.80	105.68	Local
64		15.22	42.49	Punching	3,058.21	324.55	2,103.16	General	49.03	118.25	121.92	Local
84	0.20	15.41	43.33	General	3,530.08	369.95	1,778.05	General	62.25	186.22	159.42	General
81		15.25	42.62	General	3,531.21	331.10	1,814.55	General	61.05	161.76	152.51	General
82		15.25	42.62	General	3,531.21	331.10	1,814.55	General	61.05	161.76	152.51	General
83		14.09	37.63	Local	3,528.89	164.46	2,105.97	General	52.92	63.04	112.11	Local
16	0.051 × 0.30	15.44	43.46	General	1,764.97	903.27	3,542.85	General	20.92	74.33	56.15	General
1		14.99	41.48	Local	1,766.13	640.82	3,750.94	General	19.78	50.37	49.54	General
2		14.72	40.31	Local	1,766.21	529.55	3,882.37	General	19.13	40.28	46.03	Local
3		13.45	34.98	Punching	1,759.65	244.54	4,586.13	General	16.27	15.27	32.98	Punching

without overburden. This is the main result of this work. The vertical axis represents the relation $\gamma B/\psi_0$, where $\psi_0 = E_1^2/\sigma_1$, *i.e.*, a constant. In the horizontal axis the soil friction angle (ϕ) is presented. When γB and ϕ have high values, according to the mode of failure of sandy soils, there will be general shear failure. However, as γB and ϕ decrease, the rupture is no longer general and becomes local or punching shear failure even if these parameters are even smaller.

By replacing values in the parameters that make up the ordinate axis, it is possible to see how the rupture mode varies with the dimension *B* of the foundation base.

The graph (Fig. 4) shows typical values of the dimensionless $\gamma B/\psi_0$. For example, if γ remains constant and equal to 18 kN/m^3, and B is taken as 0.60 m, 2 m and 10 m, the axis of the ordinate will have values, respectively, equal to 7.39×10^{-7}; 2.46×10^{-6} and 1.23×10^{-5}. In Fig. 4 it can be seen that, when maintaining a friction angle equal to 30°, the respective modes of rupture vary from localized to generalized rupture for the established values of *B* and γ.

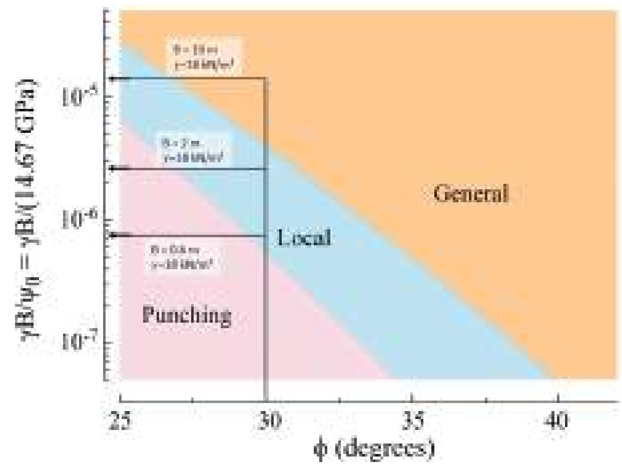

Figure 4 - Typical values of dimensionless $\gamma B/\Psi_0$.

6. Conclusion

The experimental results confirm the validity of the present model in most instances, suggesting its validity at least for the scale of footing adopted. It is important to check this validity for larger footings as well, but no comprehensive analysis of this sort was found in the literature.

When the criterion of Vesic (1975) for the mode of failure of sandy soils was compared with the experimental results provided in the 1963 article by the same author, it was verified that it is not accurate (from 20 experiments, 13 predict different results found experimentally - the ninth column from Table 2). This inaccuracy is a possible issue for the safety of foundations, since soils that fail in a non-generalized way, *i.e.*, localized or punching, would require the application of a reduction factor in the expression proposed by Buismann (1940) and Terzaghi (1943) (Eq. 1). Thus, using Eq. 1 without any reduction, the geotechnical engineer would work with an overestimated rupture stress, that is, against security.

The injudicious use of this criterion (using Eq. 1 without any reduction) jeopardizes foundation safety, since a prediction of general failure when the soil-foundation system is actually well-compressible leads to an overestimated ultimate bearing capacity.

Finally, it should be stressed that this agreement is obtained with a theory that is derived from a physical principle of energy balance, and this reasoning may be extended to study other aspects of soil mechanics and geotechnical engineering.

7. Appendix 1: Stress Relief (σ_L)

The rationale for calculating the stress (σ_L) necessary to obtain a maximum length L_{total} is that there is a dispute between the energy cost necessary for breaking the chemical bonds in a solid and in the reduction of elastic potential energy by relieving the stress.

Imagine a solid (assuming a thin plate) in which there is a stress, for example tensile, which is applied too far apart, so that it is homogeneously applied, according to Fig. 5. It is intended here to understand the energy advantage in forming a crack of length *L* in the solid in question (total energy of the tensioned solid system plus crack, E_t).

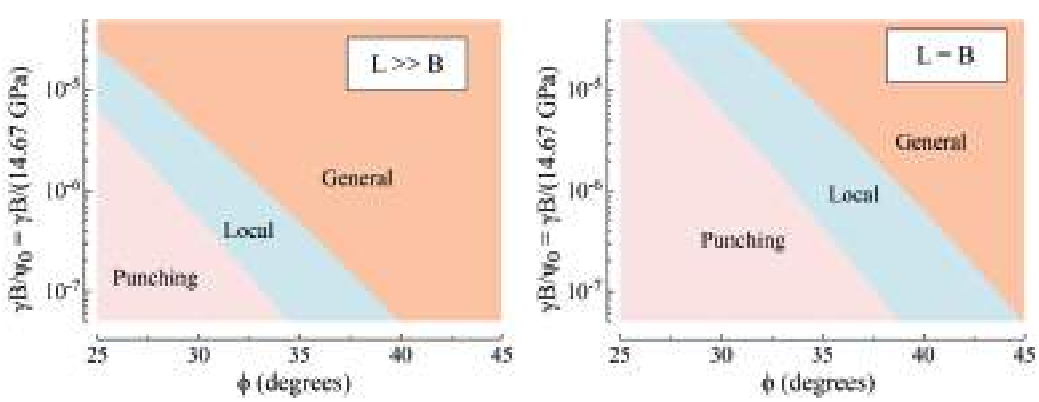

Figure 3 - Diagram showing the rupture mode as a function of the dimensionless ϕ and $\gamma B/\Psi_0$ for surface foundation based on sandy soil.

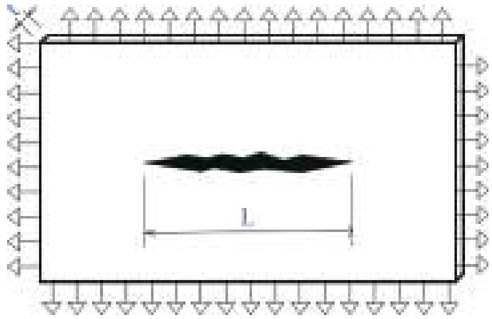

Figure 5 - Thin plate homogeneously tensioned and its crack.

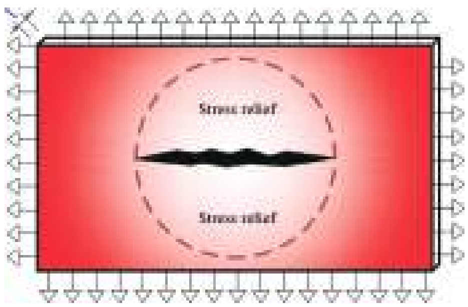

Figure 6 - Thin plate rupture and stress relief.

Therefore, it is necessary to estimate both the energy cost W of generating the crack and the gain U from relieving the tension in the region indicated by the circle in Fig. 6.

If the chemical bonds have a surface energy density η, which is the critical rate of energy release per unit area, then W is defined by equation:

$$W = \eta \cdot L \cdot t \tag{24}$$

where $L.t$ is the area of the crack, since L is the length of the rupture surface and t is the thickness of the thin plate, hence the thickness of the crack, as shown in Fig. 7.

The surface density of energy η can be estimated microscopically for solids as the dissociation energy multiplied by the surface density of chemical bonds. The energy U (energy gain to relieve the stress) can be obtained from an estimate of the elastic energy density (u), as shown below.

It is known that in the case of springs, the Hooke's Law ($F = k.x$) is valid. The elastic energy is given by: $U_{el} = \frac{k \cdot x^2}{2}$ or alternatively $U_{el} = \frac{F2}{2k} = \frac{(k \cdot x)^2}{2k} = \frac{k \cdot x^2}{2}$.

By direct analogy, in tensile solids the elastic energy density (u) can be estimated as $u = \frac{E \cdot \varepsilon^2}{2}$ (possessing information about the strain (ε), or $u = \frac{\sigma^2}{2E}$, with stress, since

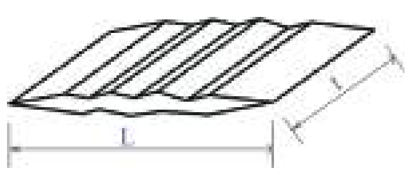

Figure 7 - Crack perspective.

$\sigma = E.\varepsilon$). Here, the elastic modulus E is analogous to the force constant k of the spring.

Thus, the total energy released in the circle of model is given by multiplying the elastic energy density (u) by the volume of the released energy zone, which is in the form of a cylinder, as shown in Fig. 8:

$$U = u \cdot Volume \tag{25}$$

$$U = \frac{\sigma^2}{2E} \pi \left(\frac{L}{2} \right)^2 t \tag{26}$$

Thus, the total energy of the tensioned solid system plus fissure becomes:

$$E_T = W - U \tag{27}$$

Substituting Eqs. 24 and 26 into Eq. 27, there is:

$$E_T = \eta \cdot L \cdot t - \frac{\sigma^2}{8E} \pi \cdot L^2 \cdot t \tag{28}$$

To determine the total length L that optimizes the energy, it is enough to derive Eq. 28 with respect to L and equate it to zero.

$$\frac{dE_T}{dL} = 0 = \eta \cdot t - \frac{\sigma^2}{4E} \pi \cdot L \cdot t \tag{29}$$

Then, by extracting from Eq. 29 the value of the stress σ, it is possible to obtain the stress necessary to generate a crack of length L (Eq. 4).

8. Appendix 2: Surface Energy Density

The energy of formation for the failure surface will be estimated based on the mechanics of an infinitesimal mass volume (Fig. 9), neglecting the weight of the element and considering only the transmission of the weight of the

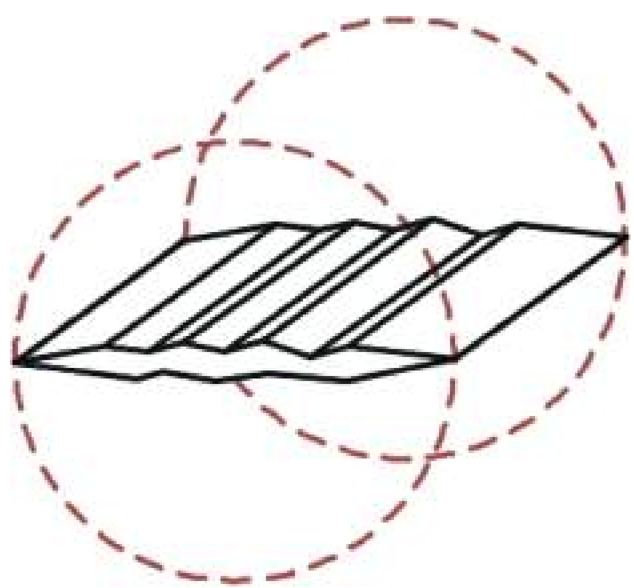

Figure 8 - Crack perspective in the circular region.

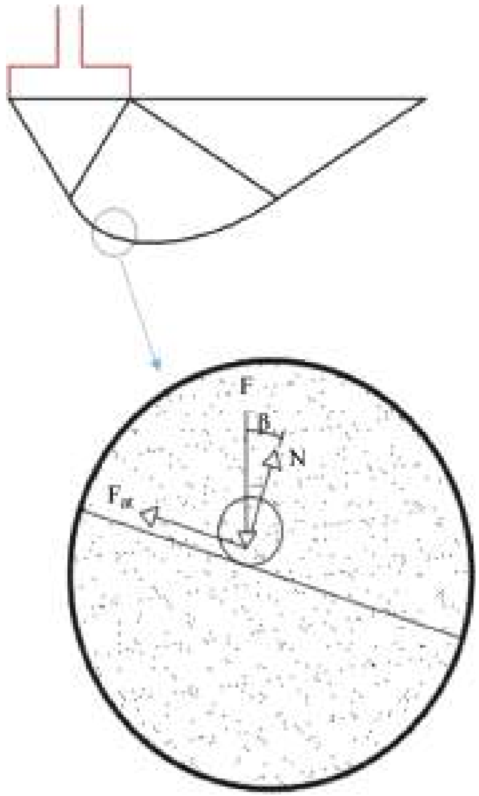

Figure 9 - Force diagram for the surface energy density.

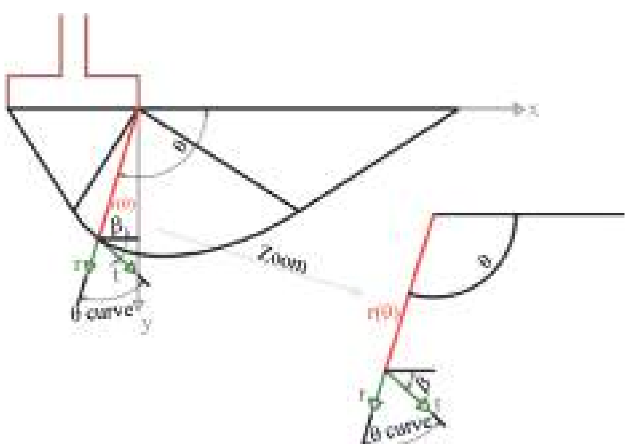

Figure 10 - Parameters for Zone II.

grains above (force F), which exert a pressure σ_y on the element of mass with a cross section (A).

$$dE = \tan\phi(\gamma \cdot y) A \cos\beta \cdot dl \tag{30}$$

Thus, the surface energy density is estimated as

$$d\eta = \tan\phi(\gamma \cdot y) \cdot \cos\beta \cdot dl \tag{31}$$

The value of the angle β depends on the zone being analyzed, as shown in Figures: Figs. 10 and 11 (a) and (b). In Zone I, the angle β is equal to $\frac{\pi}{4}+\frac{\phi}{2}$; in Zone II, $\beta = \theta + \phi - \frac{\pi}{2}$; and in Zone III, $\frac{\phi}{2}$.

The depth of the infinitesimal portion of soil varies according to

$$y = \tan\left(\frac{\pi}{4}+\frac{\phi}{2}\right)x \quad (\text{Zone I}) \tag{32}$$

$$y = r(\theta)\sin\theta \quad (\text{Zone II}) \tag{33}$$

$$y = \tan\left(\frac{\pi}{4}-\frac{\phi}{2}\right)x \quad (\text{Zone III}) \tag{34}$$

The polar function $r(\theta)$ in Eq. 33 comes from logarithmic spiral equation of Zone II [Fig. 10]. It can be defined as

$$r(\theta) = ae^{b\theta} \tag{35}$$

$$r(\theta) = \frac{Be^{\tan(\phi)\left(\frac{3\pi}{4}-\frac{\phi}{2}\right)}}{\sqrt{2}\left[\cos\frac{\phi}{2}-\sin\frac{\phi}{2}\right]} e^{-\tan(\phi)\theta} \tag{36}$$

In Zones I and III, cosβ.dl is equal to dx. Because of that, Eq. 31 becomes, for Zone I and III:

$$d\eta = \tan\phi(\gamma \cdot y + q)dx \tag{37}$$

In Zone II, dl is readily obtained through the equation of the length of a curve in polar coordinates

$$dl = \frac{Be^{\tan(\phi)\left(\frac{3\pi}{4}-\frac{\phi}{2}\right)}}{\sqrt{2}\left[\cos\frac{\phi}{2}-\sin\frac{\phi}{2}\right]} e^{-\tan(\phi)\theta} \sec\theta d\theta \tag{38}$$

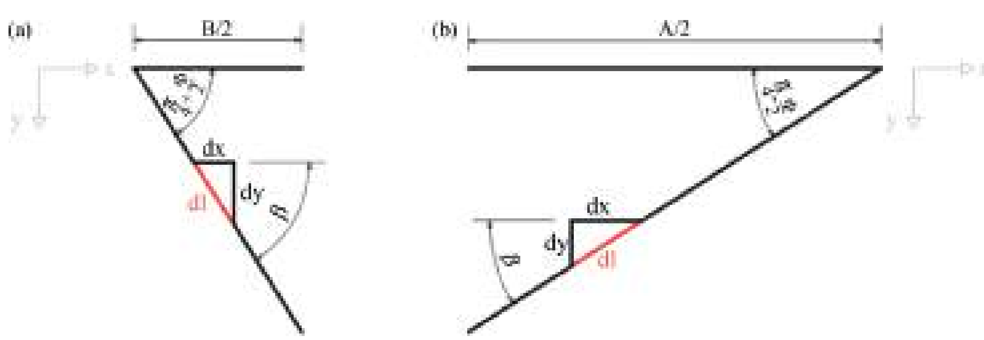

Figure 11 - Parameters for Zone I (a) and Zone III (b).

With this, integrating Eq. 38 from both sides leads to the final equation cited in Eq. 9. The integration intervals are: $x \in (0, \frac{B}{2})$ for Zone I, $\theta \in \left(\frac{\pi}{4} - \frac{\phi}{2}, \frac{3\pi}{4} - \frac{\phi}{2}\right)$ for Zone II and $x \in (\frac{A}{2}, A)$. For Zone III, this is equivalent to $x \in (0, \frac{A}{2})$.

The reach of the failure surface, *i.e.*, the distance from the outermost edge of the foundation and the point where the failure surface reaches ground level (see Fig. 2) is given by $A = B\frac{\cos\phi e^{\tan(\phi)\frac{\pi}{2}}}{\left[\cos\frac{\phi}{2} - \sin\frac{\phi}{2}\right]^2}$.

All calculations in this article are detailed in Santos (2017).

References

Buisman, A.S.K. (1940). Grondmechanica. 1st ed., Waltman, Delft.

Michalowski, R.L. (1997). An estimate of the influence of soil weight on bearing capacity using limit analysis. Soil and Foundation, 37(4):57-64.

Santos, L.F. dos (2017). Um Modelo de Dissipação de Energia Para o Modo de Ruptura de Fundações Rasas em Solos Arenosos. Dissertação de Mestrado, Programa de Projeto de Estruturas, Escola Politécnica, UFRJ.

Terzaghi, K. (1943). Theoretical Soil Mechanics, John Wiley & Sons, New York.

Vesic, A.B. (1963). Bearing Capacity of Deep Foundations in Sand. Highway Research Record, 39:112-153.

Vesic, A.B. (1973). Analysis of ultimate loads of shallow foundations. J. Soil Mech. Found. Div., 99(1):53.

Vesic, A.B. (1975). Bearing capacity of shallow foundations. In: Foundation Engineering Handbook, McGraw-Hill, New York, pp. 121-147.

List of Symbols

B - smaller length of shallow foundations
E - elastic modulus
e - void ratio
E_1 - modulus to the mean normal stress - provided by Vesic (1973)
E_t - total energy of the tensioned solid system plus crack
G - shear modulus
I_r - rigidity index
$I_{r\ critial}$ - critical rigidity index
k_0 - coefficient of earth pressure at rest
L - longer length of shallow foundations (in appendix 1, L is the length of rupture surface)
L_{el} - length of shear failure for zone II
L_{total} - total length of shear failure
L_{ZRI} - length of shear failure for zone I
L_{ZRIII} - length of shear failure for zone III
N_γ - bearing capacity factor
t - thickness of the thin plate
u - elastic energy density
U - the energy gain to relieve the tension
W - energy cost of generating the crack
ζ_γ - shape correction factor from σ_{rup}
σ_{rup} - rupture stress/ultimate pressure
χ - shape correction factor from σ_L
χ_{gen} - shape correction factor from general failure
χ_{punch} - shape correction factor from non-generalized failure
ϕ - friction angle
γ - specific unit weight
γ_d - specific unit weight of the dry soil
η - surface density of energy
η_{el} - surface density of energy for zone II
η_{ZRI} - surface density of energy for zone I
η_{ZRIII} - surface density of energy for zone III
ν - Poisson coefficient
σ_1 - resistance at mean normal stress - provided by Vesic (1973)
σ_{gen} - stress necessary to obtain a maximum length (L_{total})
σ_h - horizontal stress
σ_L - stress necessary to obtain a maximum length L_{total} (stress relieved)
σ_{med} - mean stress at a depth $B/2$ below the base of the footing
σ_{punc} - stress necessary to obtain a maximum length of zone I (L_{ZRI})
σ_v - vertical stress

Circular Footing on Geocell-Reinforced Granular Residue from Precious Gem Processing over a Sand Bed

J. Favretto, G.D. Miguel, M. Donato, M.F. Floss

Abstract. Geocell is a tridimensional confinement structure used for soil reinforcement, which significantly improves the performance of foundation systems. Aiming at a more sustainable engineering project and promoting a correct destination of a residual material, an alternative to fill the geocell is through the use of precious gem processing waste. The performance of geocell reinforcement filled with this granular residue overlying a sand subgrade, as well as the influence of geocell mattress height, have been studied by model tests in the laboratory. The layers were prepared in a test tank and subjected to static loading by a rigid circular footing. Footing load, footing settlement and displacements on the fill surface were measured during the tests. Comparing the tests on unreinforced and reinforced residue layer, the results indicate that the provision of geocell leads to a significant increase in the bearing capacity, presenting improvement factors of bearing capacity of up to 1.7. In addition, the reinforcement provides more uniform settlements and less expressive soil heaves around the footing.

Keywords: bearing capacity, gemstone residue, geosynthetic reinforcement, plate load test.

1. Introduction

The expansion of urban and industrial centers in developing cities, as well as the growth of infrastructure works, has led an increasing demand for materials to produce aggregates, cements, concrete, asphalt, etc. The production of aggregates comes, for the most part, from the extraction of primary sources. Engineering projects must be designed to minimize resource depletion, energy consumption, degradation and environmental impact. Therefore, the use of residues to replace natural materials is an alternative way of achieving those objectives. Many of the waste generated in the processing of industrial inputs or by-products is potentially capable of performing similar functions to those of natural aggregates (Sarsby, 2013). The decision to use such materials is based on technical needs, economic factors and environmental benefits.

Several gems and jewelry companies are located in the South of Brazil, whose activities consist in the extraction and processing of gemstones. These processes are responsible for generating a large amount of granular residue, in the form of refuse, semi-finished or little-benefited pieces, that ends up being stored improperly in the corporate yards, which could cause environmental damage (Thomé *et al.*, 2010). Aiming at the reuse of a waste material, some researches were developed using residues of scrolling of precious gems as geocell filling material in soil reinforcement systems (Miguel *et al.*, 2016; Baruffi *et al.*, 2016). With similar purpose of using residues, Kolathayar & Kumar (2019) performed model tests on geocell retaining walls filled with tire crumb mixed with sand and observed that the mixture performed well as infill material.

Geocells are one of the main developments from the geosynthetics industry used to enhance the performance of soils and are used specifically for stabilization and protection applications in geotechnical engineering, such as beneath road pavements and railways, at the base of earth embankments and foundations (Bathurst & Jarrett, 1988; Bush *et al.*, 1990; Dash *et al.*, 2008; Sireesh *et al.*, 2009; Zhang *et al.*, 2010). It consists of a three-dimensional honeycombing structure of interconnected cells, devised by Webster & Watkins (1977) and Webster & Alford (1978), which contains and confines the soil within its pockets. The reinforcing mechanism in the geocells is by confinement of soil within its pockets that completely arrests the lateral spreading of soil (Dash *et al.*, 2003). Studies carried out on soils reinforced with geocells, taking as an example those conducted by Mandal & Gupta (1994), Dash *et al.* (2001) and Dash (2010), suggest that the effect of soil confinement results in a stiffer reinforcement system, capable of improving performance and increase resistance of the foundation. The height of the geocell is an important parameter in the behavior of geocell reinforced structures. It is found that with increase in geocell height, the rigidity of geocell mattress enhances (Sireesh *et al.*, 2009; Rai, 2010). The en-

Julia Favretto, Ph.D. Student, Programa de Pós-Graduação em Engenharia Civil e Ambiental, Universidade de Passo Fundo, Passo Fundo, RS, Brazil. e-mail: juliafavretto@hotmail.com.
Gustavo Dias Miguel, Ph.D. Student, Programa de Pós-Graduação em Engenharia Civil, Universidade Federal do Rio Grande do Sul, Porto Alegre, RS, Brazil. e-mail: gustavo.miguel@ufrgs.br.
Maciel Donato, Ph.D., Associate Professor, Faculdade de Engenharia e Arquitetura, Universidade de Passo Fundo, Passo Fundo, RS, Brazil. e-mail: mdonato@upf.br.
Márcio Felipe Floss, Ph.D., Associate Professor, Programa de Pós-Graduação em Engenharia Civil e Ambiental, Universidade de Passo Fundo, Passo Fundo, RS, Brazil. e-mail: marciofloss@upf.br.
Submitted on February 5, 2019; Final Acceptance on November 6, 2019; Discussion open until August 31, 2020.
DOI: 10.28927/SR.431151

hancement is because with increase in height, the soil remains confined within the cell and the entire mattress deflects as a composite mass (Dash *et al.*, 2001).

Different infill materials have been tested through laboratory model tests (Han *et al.*, 2010; Hegde & Sitharam, 2015; Tavakoli Mehrjardi *et al.*, 2019). In general, the filling of the geocell is provided by granular materials, such as sand or gravel, because they have better interface properties and high control in the cell filling process (Rajagopal *et al.*, 1999; Biswas & Krishna, 2017).

This paper presents an experimental study conducted to investigate the benefits of the use of geocell reinforcement and the influence of two different heights of the geocell mattress on the behavior of the foundation. Attempting to reduce the consumption of primary aggregates and to reuse a residual material, promoting its correct destination, precious gem processing waste was used as filling material in the investigation. Plate load tests under static loading were carried out on geocell-reinforced residue over a sand bed.

2. Experimental Setup

Plate load tests have been conducted in a medium scale loading apparatus at the University of Passo Fundo, Brazil. The foundation bed was prepared in a wood test tank having 900 mm length, 900 mm width and 700 mm height. The footing used was made of a rigid steel plate with 150 mm diameter (D) and 12 mm thickness. The footing was centered in the tank and was loaded with a hydraulic jack supported against the reaction frame. To avoid interference of the tank walls with the stress zone propagated from the loading surface, the minimum dimension requirement should be about 5 and 2.5 times the plate size in plane and depth, respectively (Tavakoli Mehrjardi *et al.*, 2019).

2.1. Materials

The soil underneath the geocell mattress used was characterized by Donato (2007), indicating a poorly graded sand according to the Unified Soil Classification System, with unit weight of solids $\gamma_s = 26.30$ kN/m^3, mean grain size $D_{50} = 0.16$ mm, coefficient of uniformity $C_u = 2.10$ and of curvature $C_c = 1.00$. The minimum and maximum void ratios presented by Miguel & Floss (2017) are $e_{min} = 0.702$ and $e_{max} = 0.913$, respectively.

A diamond pattern polypropylene geocell was used in this study. Each cell is 270 mm long and 270 mm wide. It was tested two heights (h) of geocell mattress, 50 mm and 200 mm. The wall surfaces of the geocells are smooth, without texture or openings. The producers catalog suggests a transverse joint resistance of 900 N and 3,700 N for each height, respectively, tested according to NBR ISO 10321 (ABNT, 2013b). In addition, it indicates a wide-width tensile strength of geotextile equal to 26 kN/m and strain greater than or equal to 50 % for both geocells according to NBR ISO 10319 (ABNT, 2013a).

The pocket size is the equivalent diameter of the cell opening, in this case equal to 270 mm. It is found that this parameter must be smaller than the footing area, in such a way that the footing can cover at least one full pocket opening (Rai, 2010). However, a 150-mm-diameter plate was used to conduct the tests because the proposal was to evaluate if there would be benefits in the use of the reinforcement even for smaller contact surfaces.

Granular residue, resulting from the processing of precious gems in gem and jewelry companies located in southern Brazil, was used to fill the geocells. The original material was sieved, obtaining the particles passing through and retained in the sieves #3/8 (9.50 mm) and #40 (0.42 mm), respectively. The residue can be classified as well-graded sand according to the Unified Soil Classification System, with unit weight of solids $\gamma_s = 25.94$ kN/m^3, mean grain size $D_{50} = 3.20$ mm, coefficient of uniformity and curvature $C_u = 6.15$ and $C_c = 1.25$. The minimum and maximum void ratios are $e_{min} = 0.40$ and $e_{max} = 0.68$, respectively. The grain size distribution of sand and residue is shown in Fig. 1.

2.2. Foundation bed preparation

For the preparation of the subgrade, the sand was mixed with a moisture content $w_s = 10$ % and compacted to target relative density $D_r = 50$ %. The selection criterion for the relative density value was the fact that this work is part of geosynthetic research group of University of Passo Fundo. The molding of the test layers started by spreading the homogenized sand to a total thickness of 400 mm, molded and compacted manually in 100-mm-thick layers. The uniform density of soil in the foundation bed was checked by placing small aluminum cylinders with known volumes at different locations in the test tank.

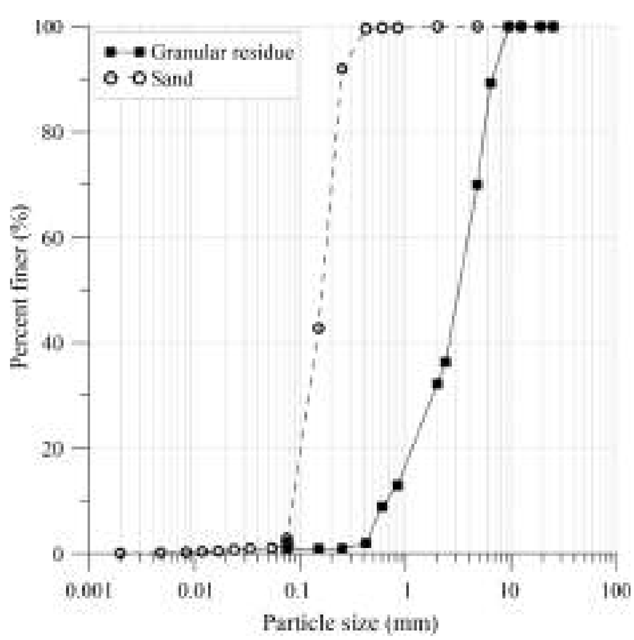

Figure 1 - Grain size distribution of materials.

In total, four tests were conducted, two unreinforced (Test Series A) and two reinforced (Test Series B). The reinforcement element overlying a 400-mm-thick sand bed was composed by a 50 or 200-mm-high geocell, filled with granular residue. The residue samples were molded dry (w_r = 0 %) and manually compacted in a single layer at relative density D_r = 50 %. In order to quantify the enhancement in bearing capacity due to the insertion of the geocell, unreinforced residue configurations were also tested, in the same heights. To avoid direct contact between the plate and the geocell, the reinforcement was placed to the full width of the tank at the depth of 0.13 *D* below the bottom of the footing. Dash *et al.* (2001) reported good results of depth of placement of the geocell between 0 and 0.25 *D* below the footing. The geometry of the test settings used in this investigation is shown in Fig. 2 and the test model details are provided in Table 1.

2.3. Testing procedure

The footing was placed at the top of the bed, centralized. In addition, the plate was positioned so that the loading occurred at the center of a cell, which is the worst loading situation. The loads were applied in small increments, according to NBR 6489 (ABNT, 1984), in equal steps, and measured through a pre-calibrated load cell placed between the hydraulic jack and the reaction frame (Donato, 2007). Each incremental increase was maintained constant until the footing settlement had stabilized.

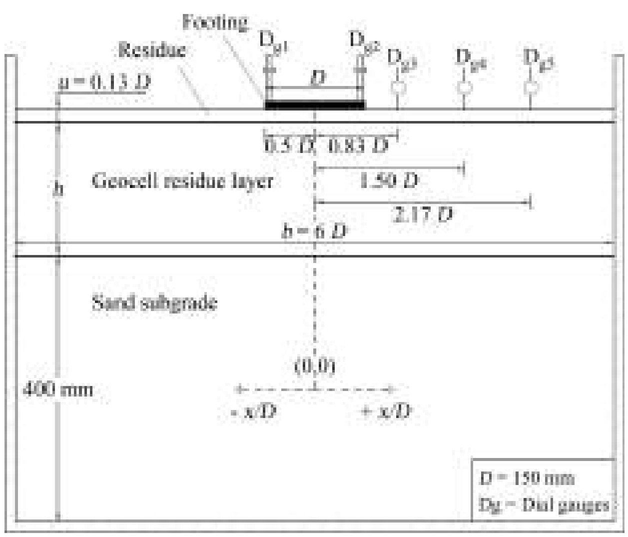

Figure 2 - Geometry of the reinforced foundation bed.

Settlements of the footing were measured by two dial gauges (Dg_1, Dg_2) placed in diagonal directions. The displacements on the fill surface, settlement and heave, were measured by dial gauges (Dg_3, Dg_4, Dg_5) placed at a distance (*x*) of 0.83 *D*, 1.50 *D* and 2.17 *D* to the right of the footing center line, respectively. The geometry of the setup is shown in Fig. 2. In the absence of a clear failure, loading was applied until a footing settlement of 25 mm was reached.

In all the tests, the pocket size of the geocell or the equivalent diameter (*d*), width of the geocell layer (*b*), and the depth of the placement of the geocell layer (*u*) were kept constant, that is, d/D = 1.80, b/D = 6.00, and u/D = 0.13. The variable parameters were the residue configuration, unreinforced and reinforced, and the residue layer height, which were tested with relation h/D = 0.33 and h/D = 1.33. The footing settlement (*s*) and the surface settlement and heave (δ) were normalized by footing diameter to express them in non-dimensional form as s/D (%) and δ/D (%). In all the plots, settlements are reported with the positive sign and heave with the negative sign.

3. Results and Discussion

3.1. Bearing pressure settlement curve

Figure 3 represents the bearing-settlement response of the different test settings. The reference test on the sand subgrade was carried out by Miguel & Floss (2017).

It is observed that the presence of residue layer over the base soil reduces the bearing capacity of the sand, even when the reinforcement is used. This result indicates that the sand subgrade has greater stiffness than the material proposed to fill the geocells. The explanation could be the difference in the friction angle of the materials that, even though not measured, has influence on rigidity of soil. As the material is obtained from the processing of the stones, its particles have a more rounded shape which, according to Pokharel *et al.* (2010), results in a relatively weak material. Although the use of the precious gem waste as geocell filling material did not show improvement in the foundation

Table 1 - Details of laboratory model tests.

Test series	Type of test	Details of test parameters
A	Unreinforced	Variable parameter: h/D = 0.33, 1.33
		Constant parameter: D_r = 50 %, w_s = 10 %, w_r = 0 %
B	Reinforced (geocell)	Variable parameter: h/D = 0.33, 1.33
		Constant parameter: d/D = 1.80, b/D = 6.00, u/D = 0.13, D_r = 50 %, w_s = 10 %, w_r = 0 %

Notes: b = 900 mm (geocell width); d = 270 mm (pocket size of the geocell); D = 150 mm (diameter of the footing); D_r= relative density; h = 50 or 200 mm (geocell height); u = 20 mm (placement depth of the geocell); w_r = moisture content of the residue; w_s = moisture content of the sand.

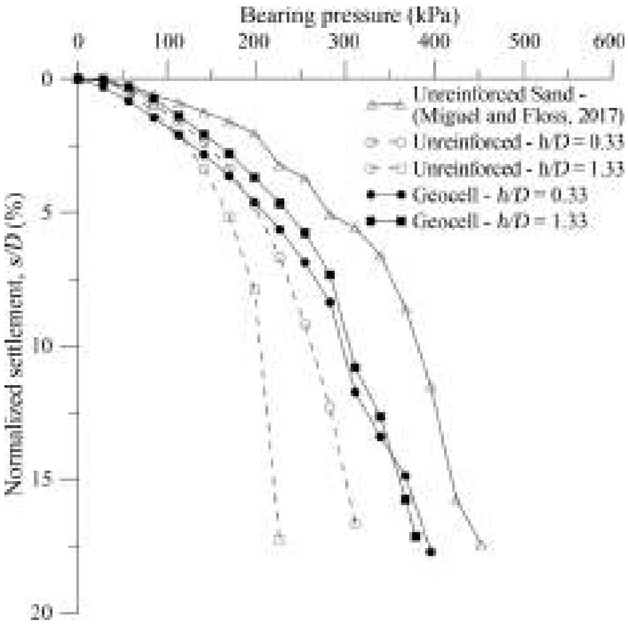

Figure 3 - Variation of bearing pressure with footing settlement.

performance, the environmental benefits could justify its use. Proposing the insertion of this residue in soil reinforcement, new tests can be carried out with a better graded particle size distribution and higher densities.

In addition, another parameter has influenced the results. It is found that the decrease in pocket size increases the bearing capacity due to the overall increase of mattress rigidity. Also, the confinement promoted by cells is larger as the pocket size decreases (Dash *et al.*, 2001). Dash *et al.* (2003) suggest a relation $d/D = 0.8$. In this study, this is not verified, since the cell has a mean opening of 270 mm and the footing has a diameter of 150 mm, resulting in $d/D = 1.8$. Thus, the insufficient performance of the studied foundation is also related to the influence of this ratio, because the cell involves the whole dimension of the footing.

However, comparing only the results of Test Series A and B (unreinforced and reinforced residue), it is noted a clear increase in the resistance using geocell reinforcement, for both heights tested. For the unreinforced and reinforced tests on 50-mm-high geocell ($h/D = 0.33$), the bearing capacity verified at the end of the tests was 311 kPa and 396 kPa, respectively. For unreinforced and reinforced tests on 200-mm-high geocell ($h/D = 1.33$), the bearing capacity verified at the end of the tests was 226 kPa and 379 kPa, respectively. The ultimate bearing capacity increased around 27 % and 68 % for $h/D = 0.33$ and $h/D = 1.33$, respectively.

It was shown that the unreinforced section with a smaller thickness had higher ultimate bearing capacity than that with a larger thickness. As the residue is a weaker material in comparison to the sand, the increase of the residue layer decreases the resistance of foundation due to greater displacements of the material. Also, the firm bottom in the thinner section contributed to the enhance the bearing capacity (Pokharel *et al.*, 2010).

Dash *et al.* (2001) states that the increase of geocell height improves the overall performance of the geocell mattress. However, Fig. 3 shows a similar behavior of reinforced sections for both heights, reaching very close bearing pressure throughout the test, including the ultimate pressure, in the rupture moment. Considering the geocell models tested, this means that the increase in geocell height does not enhance the bearing capacity of the foundation studied. As previously mentioned, this can be explained by the low resistance of the filling material tested.

3.2. Improvement factor I_f

The increase in the bearing capacity due to the provision of the reinforcement can be quantified through a non-dimensional parameter called improvement factor (I_f), which is defined as the applied pressure at a given settlement for the tests with reinforcement divided by the pressure at the same settlement without geocell. The factor has as reference limit a value equal to one, so the results of factors above the unit mean that the use of geocell contributes to an increased resistance. Figure 4 represents the variation of the improvement factors with the footing settlement, by comparing the results of Test Series A and B. The unit value is indicated in the graph. The reference test performed on sand bed was not used in this analysis because, as seen in Fig. 3, the soil resistance reduces with the overlying fill material. Therefore, the focus is to evaluate the performance improvement due to the use of the geocell.

The I_f value increases with the evolution of the settlement. For the 200-mm-high geocell, this increasing behav-

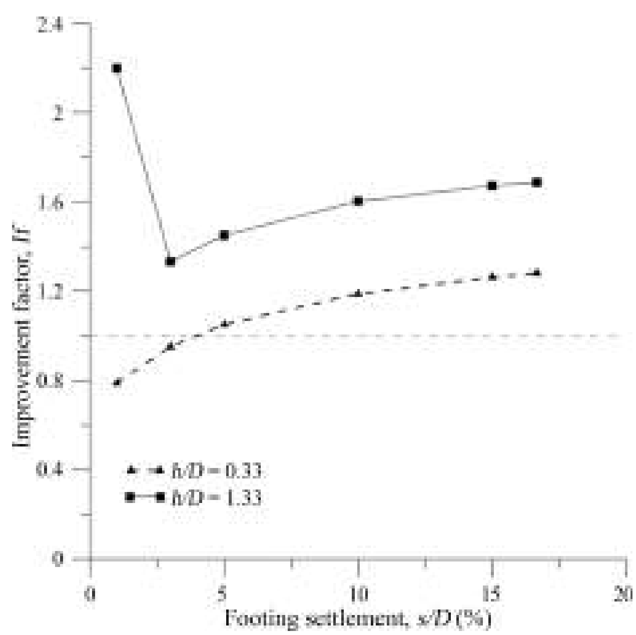

Figure 4 - Variation of improvement factors of bearing capacity with footing settlement.

ior was observed from s/D = 3 %. The results obtained for the improvement factor indicate that the influence of the geocell is more significant for higher levels of settlement and that higher values of I_f are observed for the greater height of geocell, reaching values of up to 1.27 and 1.68 for the 50-mm-high and 200-mm-high geocell, respectively. The variation of the values of I_f for the different geocell heights is due to the variation of the bearing pressure of unreinforced tests, since both curves (for h/D = 0.33 and h/D = 1.33) of reinforced tests present similar behavior, as seen in Fig. 3.

3.3. Surface displacement

Surface displacement characteristics of the geocell reinforced residue over a sand bed are discussed in this section. Figure 5 represents the variation of the surface settlement and heave with the footing settlement for the unreinforced (Figs. 5*A* and 5*B*) and reinforced section (Figs. 5*C* and 5*D*).

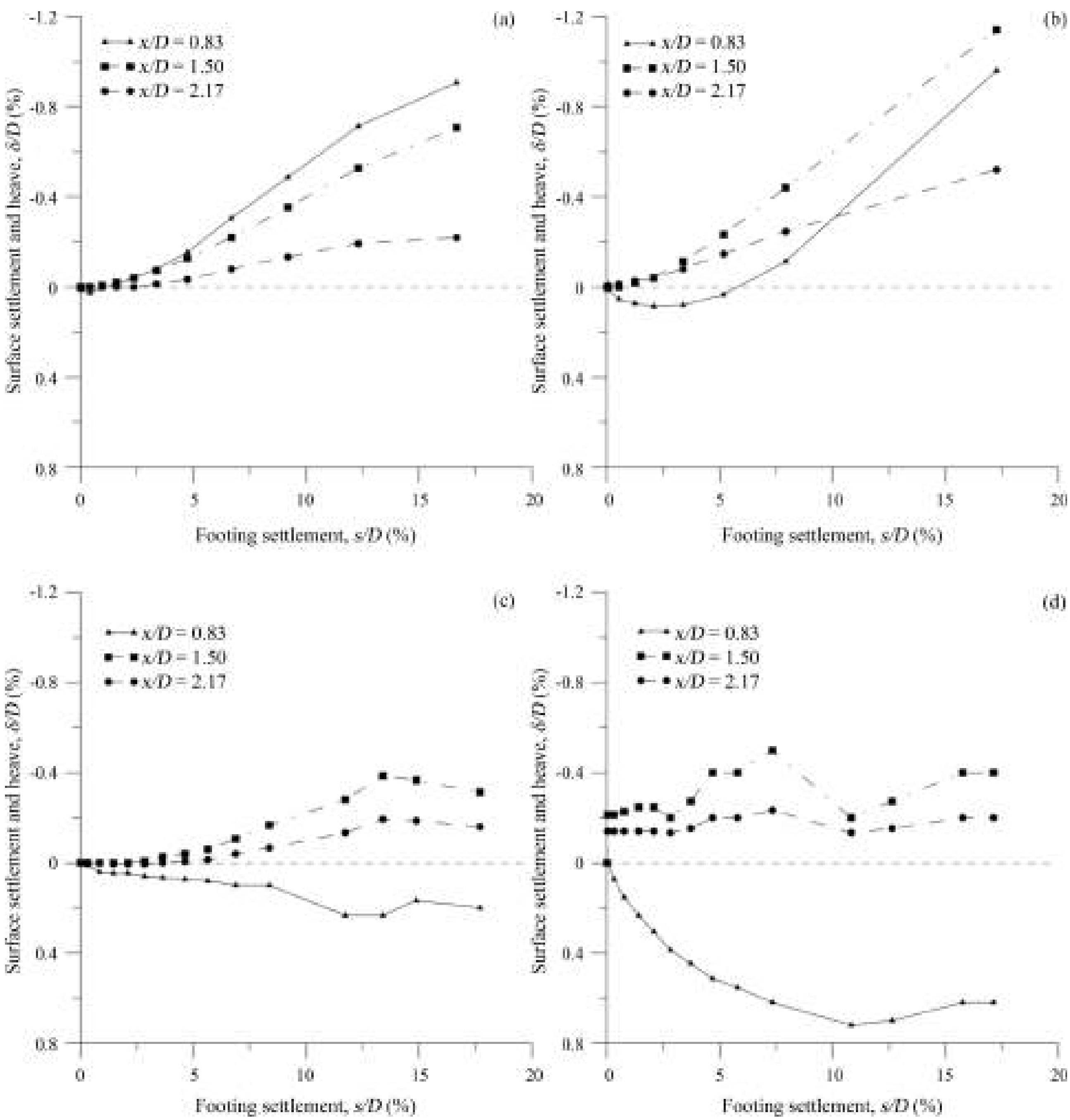

Figure 5 - Variation of surface settlement and heave with footing settlement (*A*) unreinforced h/D = 0.33, (*B*) unreinforced h/D = 1.33, (*C*) geocell h/D = 0.33, (*D*) geocell h/D = 1.33.

In the unreinforced tests, surface heaving has been observed. In general, the displacements show the increase of the surface heaving with the increase of the plate settlement. Also, it is observed that the surface displacements are higher closer to the footing.

Contrary to what occurs in unreinforced soils, where higher heave is observed on the surface, in reinforced soils this heave is less expressive. According to Dash *et al.* (2001), this behavior is due to the use of geocell, which leads to a more uniform surface settlement. Because of the effect of the stress distribution, or slab effect, the applied loading is distributed over a wider area, resulting in lower stress transmitted to the base soil. Hegde & Sitharam (2015) noted, for different filling materials, that since the foundation did not undergo any failure, surface heaving was not observed in the presence of geocells. They mention that the possible reason for this could be that the failure surfaces might have been arrested within the geocell pockets.

To complement the results of surface displacements, Figure 6 presents the progression of the settlement and heave profiles for each increment of load, expressed by normalized settlement. This type of graph is important because besides observing the direction of the displacements, it is possible to verify the differential settlement and the rotation of the footing. At higher loads a small change in the density of the bed is enough to cause differential settlement. The tilting of the footing is a common phenomenon in small scale laboratory tests (Hegde & Sitharam, 2015).

Both in Test Series A and B, unreinforced and reinforced sections, greater displacements were observed in test with larger thickness of residue. This may be related to compaction problems in certain areas of the test tank, since

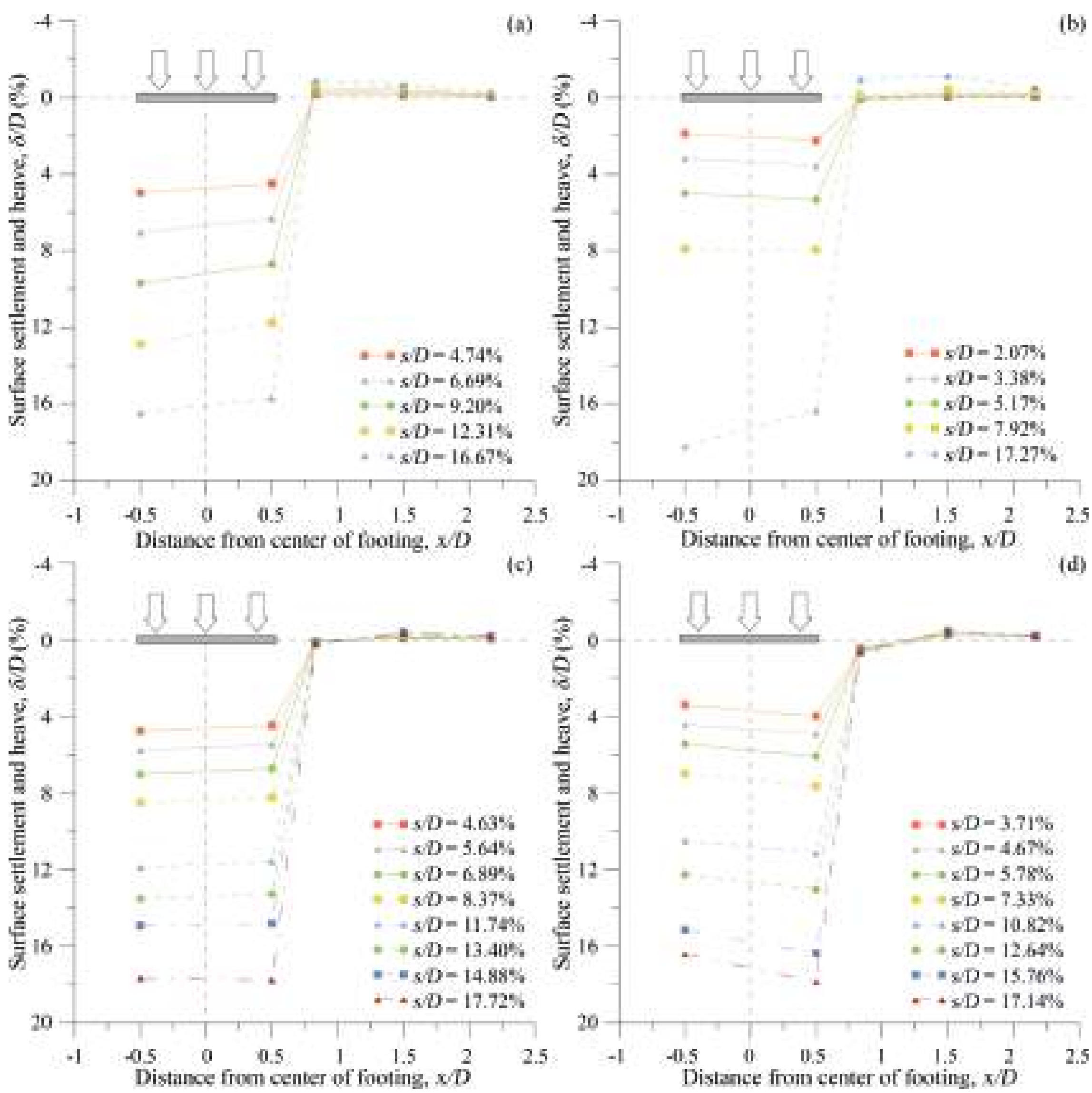

Figure 6 - Surface settlement and heave profiles (*A*) unreinforced $h/D = 0.33$, (*B*) unreinforced $h/D = 1.33$, (*C*) geocell $h/D = 0.33$, (*D*) geocell $h/D = 1.33$.

it is difficult to maintain the homogeneity of the material in relation to grain sizes. Besides, as previously mentioned, another reason may be the low resistance of the granular residue layer, that allows the material to move easily under load application.

4. Conclusions

This paper presents the laboratory model results of load tests on circular footing supported on geocell-reinforced residue underlying sand subgrade. The plate diameter was a significant limitation of the tests, considering that the pocket size of the cell involved the whole dimension of the footing. This influences the resistance mechanisms of the reinforcement because the higher strength of the geocell is not mobilized. Based on the findings from the present investigation, the following conclusions can be made on the foundation performance.

(i) Provision of geocell in the overlying granular residue improves the bearing capacity and reduces the surface heaving of the foundation, considering tests using the residue with and without geocell.

(ii) The use of the geocell results in more uniform settlements and less expressive heaves of the soil around the footing. Higher surface heaving was observed in soil without reinforcement. This behavior was verified for both geocell heights tested.

(iii) The largest displacements, as well as the lower resistance of the foundation, were observed in the unreinforced tests with a greater thickness of residue. Because of the low stiffness of the residue layer, displacements occur under vertical stress. In the thinner residue layer, the firm base soil contributed to the increase of the bearing capacity.

(iv) Similar bearing pressure settlement behavior was observed for both geocell heights tested, indicating that this parameter does not influence the resistance of the foundation studied.

Acknowledgments

This study was financed in part by the Coordenação de Aperfeiçoamento de Pessoal de Nível Superior - Brasil (CAPES) - Finance Code 001.

References

ABNT (1984). Prova de Carga Direta Sobre Terreno de Fundação - NBR 6489. Associação Brasileira de Normas Técnicas, Rio de Janeiro, Brasil, 2 p.

ABNT (2013a). Geossintéticos: Ensaio de Tração Faixa Larga - NBR ISO 10319. Associação Brasileira de Normas Técnicas, Rio de Janeiro, Brasil, 11 p.

ABNT (2013b). Geossintéticos: Ensaio de Tração de Emendas pelo Método da Faixa Larga - NBR ISO 10321. Associação Brasileira de Normas Técnicas, Rio de Janeiro, Brasil, 11 p.

Baruffi, A.; Miguel, G.D. & Floss, M.F. (2016). Geocells filled with semiprecious gem waste. Proc. XVIII Congresso Brasileiro de Mecânica dos Solos e Engenharia Geotécnica, COBRAMSEG, Belo Horizonte.

Bathurst, R.J. & Jarrett, P.M. (1988). Large-scale model tests of geocomposite mattresses over peat subgrades. Journal of the Transportation Research Board, n. 1188, p. 28-36.

Biswas, A. & Krishna, A.M. (2017). Geocell-reinforced foundation systems: A critical review. International Journal of Geosynthetics and Ground Engineering, v. 3, n. 2, p. 1-18.

Bush, D.I.; Jenner, C.G. & Bassett, R.H. (1990). The design and construction of geocell foundation mattresses supporting embankments over soft ground. Geotextiles and Geomembranes, v. 9, n. 1, p. 83-98.

Dash, S.K.; Krishnaswamy, N.R. & Rajagopal, K. (2001). Bearing capacity of strip footings supported on geocell-reinforced sand. Geotextiles and Geomembranes, v. 19, n. 4, p. 235-256.

Dash, S.K.; Sireesh, S. & Sitharam, T.G. (2003). Model studies on circular footing supported on geocell reinforced sand underlain by soft clay. Geotextiles and Geomembranes, v. 21, n. 4, p. 197-219.

Dash, S.K.; Reddy, P.D. & Raghukanth, T.G. (2008). Subgrade modulus of geocell-reinforced sand foundation. Proc. Institution of Civil Engineers - Ground Improvement, v. 161, n. 2, p. 79-87.

Dash, S.K. (2010). Influence of relative density of soil on performance of geocell-reinforced sand foundations. Journal of Materials in Civil Engineering, v. 22, n. 5, p. 533-538.

Donato, M. (2007). Direct Tension Measurements on Reinforced Soil with Polypropylene Fibers. Ph.D. Dissertation, Federal University of Rio Grande do Sul, Porto Alegre, 146 p. (in Portuguese).

Han, J.; Pokharel, S.K.; Parsons, R.L.; Leshchinsky, D. & Halahmi, I. (2010). Effect of infill material on the performance of geocell-reinforced bases. Proc. 9th International Conference on Geosynthetics, ICG, Guarujá, p. 1503-1506.

Hegde, A.M. & Sitharam, T.G. (2015). Effect of infill materials on the performance of geocell reinforced soft clay beds. Geomechanics and Geoengineering - An International Journal, v. 10, n. 3, p. 163-173.

Kolathayar, S. & Kumar, C.R. (2019). Potential of tire waste as infill material in geocells for soil retention systems. Proc. 8th International Conference on Case Histories in Geotechnical Engineering: Geoenvironmental Engineering and Sustainability, Geo-Congress 2019, Geotechnical Special Publication, GSP 312, Philadelphia, Pennsylvania, p. 193-201.

Mandal, J.N. & Gupta, P. (1994). Stability of geocell-reinforced soil. Construction and Building Materials, v. 8, n. 1, p. 55-62.

Miguel, G.D.; Silva Abido, L.C.; Baruffi, A. & Floss, M. F. (2016). Utilization of semiprecious gem processing waste in geocells. Proc. VIII Congresso Luso-Brasileiro de Geotecnia, CLBG, Porto, Portugal (in Portuguese).

Miguel, G.D. & Floss, M.F. (2017). A study of geocell performance when used in granular soils. Proc. IX Seminário de Engenharia Geotécnica do Rio Grande do Sul, GEORS, Caxias do Sul, Brasil. (in Portuguese).

Pokharel, S.K.; Han, J.; Leshchinsky, D.; Parsons, R.L. & Halahmi, I. (2010). Investigation of factors influencing behavior of single geocell-reinforced bases under static loading. Geotextiles and Geomembranes, v. 28, n. 6, p. 570-578.

Rai, M. (2010). Geocell-Sand Mattress Overlying Soft Clay Subgrade: Behavior Under Circular Loading. Ph.D. Dissertation, Indian Institute of Technology Guwahati, Guwahati, 261 p.

Rajagopal, K.; Krishnaswamy, N.R. & Latha, G.M. (1999). Behavior of sand confined with single and multiple geocells. Geotextiles and Geomembranes, v, 17, n. 3, p. 171-184.

Sarsby, R.W. (2013). Environmental Geotechnics. 2nd ed. ICE Publishing, London, 519 p.

Sireesh, S.; Sitharam, T.G. & Dash, S.K. (2009). Bearing capacity of circular footing on geocell-sand mattress overlying clay bed with void. Geotextiles and Geomembranes, v. 27, n. 2, p. 89-98.

Tavakoli Mehrjardi, G.; Behrad, R. & Moghaddas Tafreshi, S.N. (2019).Scale effect on the behavior of geocell-reinforced soil. Geotextiles and Geomembranes, v. 47, n. 2, p. 154-163.

Thomé, A.; Abreu, A.G.; Brandli, L.L.; Fernandes, V.M.C. & Prietto, P.D.M. (2010). Diagnosis of waste generated by the gemstone sector of the municipality of Soledade/RS. Hartmann, L.A. & Da Silva, J.T. (eds.), Tecnologias para o Setor de Gemas, Joias e Mineração, IGEO/UFRGS, Porto Alegre, p. 90-105.

Webster, S.L. & Watkins, J.E. (1977). Investigation of construction techniques for tactical bridge approach roads across soft ground. Technical Report S-77-1, Soils and Pavements Laboratory, U.S. Army Corps of Engineers Waterways Experiment Station, Vicksburg, p. 23.

Webster, S.L. & Alford, S.J. (1978). Investigation of construction concepts for pavements across soft ground. Technical Report S-78-6, Geotechnical Laboratory, U.S. Army Corps of Engineers Waterways Experiment Station, Vicksburg, p. 23.

Zhang, L.; Zhao, M.; Shi, C. & Zhao, H. (2010). Bearing capacity of geocell reinforcement in embankment engineering. Geotextiles and Geomembranes, v. 28, n. 5, p. 475-482.

List of Symbols

b: Width of the geocell layer
C_c: Coefficient of curvature
C_u: Coefficient of uniformity
d: Pocket size of the geocells
D: Diameter of the footing
D_{50}: Mean grain size
D_r: Relative density
e_{max}: Maximum void ratio
e_{min}: Minimum void ratio
h: Geocell mattress height / residue layer height
I_f: Improvement factor of bearing capacity
s: Footing settlement
u: Depth of the placement of the geocell layer
w_r: Moisture content of the residue
w_s: Moisture content of the sand
x: Distance from the footing center line
δ: Surface settlement and heave
γ_s: Unit weight of solids

Modifications in the Chemical and Mineralogical Composition of Compacted Mature Residual Soil Submitted to the Percolation of Acidic Leachates

E.P. Korf, P.D.M. Prietto, A.A. Silveira, C. Ulsen, N.C. Consoli, L. Bragagnolo

Abstract. The main goal of this paper is to evaluate the chemical and mineralogical composition of a compacted residual clay soil with the addition of Portland cement and under different compaction conditions to observe and to understand the chemical and mineralogical changes that these structures undergo. Results of chemical and mineralogical composition of compacted specimens in different unit weights (14.5, 15.0 and 15.5 kN/m^3) and percolated by different concentrations of aqueous solution of sulfuric acid (0, 1 and 2 %), under the application of a vertical load of 280 kPa. The modifications in the chemical and mineralogical composition of the specimens were evaluated by the combination of X-ray fluorescence (XRF), X-ray diffraction (XRD), scanning electron microscopy (SEM) and thermogravimetry with differential thermal analysis and exploratory differential calorimetry (TG/DTG/DSC). The results have shown that the percolation of H_2SO_4 resulted in changes in the Fe_2O_3, CaO and SO_3 contents for different cement contents and for specific weights; it was also evidenced dissolution of Fe_2O_3 in the upper layers and the formation of Ca and S compounds in the lower layers. No changes in mineralogy and soil morphology were found out.

Keywords: compact residual soil, acid attack, cement content, specific weight, containment barriers, chemical and mineralogical composition

1. Introduction

Industrial and mining processes are responsible for environmental impacts resulting from the production of contaminated waste, mainly by acidic compounds. These compounds can affect geotechnical structures, such as barriers of compacted soil and can promote changes in micro and macrostructural scales, such as the increase of hydraulic conductivity, reduction of reactive power and resistance of these structures (Broderick & Daniel, 1990; Favaretti *et al.*, 1994; Hueckel *et al.*, 1997; Knop *et al.*, 2008; Rubinos *et al.*, 2016). When in contact with soil particles, acidic compounds can promote complex reactions that result in changes in the mineral and physicochemical composition of the soil and, consequently, changes in its properties (Šucha *et al.*, 2002).

One of the alternatives that has been evaluated in the literature refers to the usage of soil-cement mixtures as a material component of containment barriers (Fall *et al.*, 2009; Forcelini *et al.*, 2016; Helson *et al.*, 2018; Iravanian & Bilsel, 2016; Joshi *et al.*, 2010). However, few of these studies present a chemical, mineralogical and microstructural evaluation of this type of structure under the action of aggressive chemical compounds, as well as their effects on the macrostructural response, aiming to improve the knowledge about the behavior of containment structures and to understand the interaction between contaminants, soil particles and cement (Lloret *et al.*, 2003; Romero, 2013; Romero & Simms, 2009).

Therefore, the paper's novelty stems from the understanding of physicochemical alterations, which is essential to the search for an ideal condition for the design of compacted soil-cement barriers, in order to ensure structural durability and chemical/physical containment.

In this context, this work aims to evaluate the chemical and mineralogical composition of a compacted residual clay soil with the addition of Portland cement and under different compaction conditions to observe and to understand the chemical and mineralogical changes that these structures undergo. A better understanding of these phe-

Eduardo Pavan Korf, D.Sc., Associate Professor, Universidade Federal da Fronteira Sul, Programa de Pós-Graduação em Ciência e Tecnologia Ambiental, ERS 135, km 72, n. 200, 99700-970, Erechim, RS, Brazil. e-mail: eduardo.korf@uffs.edu.br.
Pedro Domingos Marques Prietto, D.Sc., Associate Professor, Universidade de Passo Fundo, Programa de Pós-Graduação em Engenharia Civil e Ambiental, BR 285, km 292, 99052-900, Passo Fundo, RS, Brazil. e-mail: pdmp@upf.br.
Adriana Augustin Silveira, D.Sc., Professor, Universidade de Passo Fundo, Faculdade de Engenharia, BR 285, km 292, 99052-900, Passo Fundo, RS, Brazil. e-mail: aas@upf.br.
Carina Ulsen, D.Sc., Professor, Universidade de São Paulo, Laboratório de Caracterização Tecnológica, Departmento de Engenharia de Minas e Petróleo, Prof. Mello Moraes Avenue, 05508-030, Butantã, São Paulo, SP, Brazil. e-mail: carina@lct.poli.usp.br.
Nilo Cesar Consoli, D.Sc., Full Professor, Universidade Federal do Rio Grande do Sul, Departamento de Engenharia Civil, Osvaldo Aranha Avenue, 99, 3º andar, 90035-190, Porto Alegre, RS, Brazil. e-mail: consoli@ufrgs.br.
Lucimara Bragagnolo, M.Sc. Student, Universidade Federal da Fronteira Sul, Programa de Pós Graduação em Ciência e Tecnologia Ambiental, ERS 135, km 72, n. 200, 99700-970, Erechim, RS, Brazil. e-mail: lucimarabragagnolo@estudante.uffs.edu.com.
Submitted on April 17, 2019; Final Acceptance on January 29, 2020; Discussion open until August 31, 2020.
DOI: 10.28927/SR.431159

nomena will allow the improvement of techniques for the use of soil-cement mixtures in impermeable barriers subjected to vertical static loading and to the percolation of acidic leachates.

2. Materials and Methods

The experimental procedure has involved the following steps:

(a) Sampling of residual clay soil from the experimental field of Geotechnics of the University of Passo Fundo (UPF), located in Passo Fundo city - RS, Southern Brazil;

(b) The soil samples collected were characterized by X-ray fluorescence analysis (XRF), Loss on ignition (LOI) and mineralogical composition by X-ray diffractometry (XRD) using the powder method. It was also determined the organic matter content and pH by the method described by Tedesco *et al.* (1995), and the clay content (ABNT, 2016);

(c) Physical-mechanical characterization and analysis of the chemical composition of Portland cement CPV-ARI:

I. The physical-mechanical characterization was performed through unconfined axial tests at 3, 7, 14 and 28 days of curing, particle density and initial and final time of handle according to the norms (ABNT, 1997, 2001, 2003).

II. The chemical characterization was performed by XRF, followed by loss on ignition. The mineralogical analysis was conducted by XRD, using the powder method.

(d) Molding of cylindrical specimens with addition of different cement contents and under different dry specific compacting weights, followed by percolation with acidic aqueous solution;

(e) Section and preparation of remolded and not remolded samples of percolated specimens;

(f) Characterization of percolated specimens in chemical, mineralogical and morphological composition by scanning electron microscopy (SEM), XRD, XRF and thermogravimetry with differential thermal analysis and differential scanning calorimetry (TG / DTG / DSC).

To define the variables to be considered in the percolation tests, a 2k factorial experimental design (k = 2) was performed, with the addition of central points, with the variables cement content added to the soil (0 and 2 %) and dry unit weight. The values of dry unit weight and molding moisture content corresponding to the energy of the Normal Proctor type were used as reference. Thus, dry unit weight of 14.5 and 15.5 kN/m^3 with 26 % molding moisture content were used.

The experimental planning resulted in 4 factorial points with addition of 4 more central points (1 % cement addition and dry unit weight of 15.0 kN/m^3). The 8 combinations resulting from this planning were divided into 2 blocks, each one with percolation of aqueous solution with volumetric concentration of 0 % and 2 % of sulfuric acid. This planning allows the evaluation of the behavior and mathematical modelling of a response surface and the identification of the existence of non-linearity (Montgomery, 2001).

Thus, for each combination of cement content and dry compaction specific gravity, specimens of 7 cm in diameter by 6 cm in height were subjected to long-term percolation tests (from 30 to 70 days), with and without percolation of sulfuric acid solution. A hydraulic gradient of 8.33 and a vertical pressure of 280 kPa were applied to represent the disposal of 15 m rejects on the barrier with unit weight of 18.6 kN/m^3, according to literature data (Bedin, 2010).

The test specimens were then sectioned in three layers (referred to as top, middle and bottom, considering downflow) from which an undisturbed and a remolded sample were extracted per layer to be subjected to chemical and mineralogical analysis. The undisturbed sample was segmented in a prismatic format with dimensions of approximately 2.0 0.7 0.7 cm and identified by layer (S = upper, M = medium, I = lower). The layers were identified from measurements, dividing the specimen into 3 equally spaced pieces with the aid of a pachymeter. This set of samples was dried in an oven up to 45 °C and duly preserved from humidity. For scanning electron microscope (SEM) analysis, the samples were prepared in polished sections by the impregnation with epoxy-liquid resin, followed by sanding, polishing and gold plating. It was also prepared 50 g of remolded sample from each specimen for performing XRD, XRF and TG / DTG / DSC analyses. To do so, these samples were dried at 105 °C and deagglomerated to obtain a product with less than 0.044 mm granulation.

The SEM analysis was performed on the undisturbed samples sectioned from each test specimen in a high-resolution scanning electron microscope (W or Lab6), manufactured by Shimadzu, model Vega 3. The analyses were performed in the Scientific and Technological Park of the University of Passo Fundo. The following analytical conditions were used in the analyses: secondary electrons mode with magnification of above 1000 times, electron beam of nominal resolution of 3.0 nm, voltage of 20 kV and vacuum of 10^{-4} Pa, which allowed the morphological evaluation of the samples and microstructure of the particles. The XRD analyses were performed in an X-ray diffractometer, manufactured by PANalytical, model EMPYREAN, with detector X'Celerator, copper tube and by the powder method. The analytical conditions were: angle intervals 2θ from 3 to 70°, time lapses of 10 s and Cu Kα radiation. The identification of the crystalline phases was obtained by comparing the diffractogram of the sample with the PDF-2 databases of the ICDD International Centre for Diffraction Data (2003) and PAN-ICSD PANalytical Inorganic Crystal Structure Database (2007).

The XRF analyses were performed on an X-ray fluorescence spectrometer, manufactured by PANalytical, Axios Max model with X-ray tube (Rhodium 4 kV) at the Mineral and Rock Analysis Laboratory of the Federal University of Paraná (UFPR), using semiquantitative method with detection above 0.1 % and scanning time of approximately 6 min in pulverized and pressed samples. The loss on ignition was determined at 1000 °C for 2 h. Finally, the TG/DTG/DSC analyses were performed at the laboratory of minerals and rocks analysis at the Federal University of Paraná (UFPR), in a thermogravimetry equipment manufactured by Netzsch, model STA 409 PC/PG with heating from 25 °C to 1000 °C and heating rate of 10 °C / min and atmosphere of N_2 - 60 mL/min.

3. Results and Discussion

3.1. Soil and cement

The studied soil is a mature residual soil from basalt and its pedological classification according to Streck *et al.* (2008) is as an oxisol.

According to the carried out characterization, this soil has low organic matter content (< 0.8 %), high clay content (68 %) and acid pH (pH 5.5). X-ray diffraction analysis (Fig. 4) and its chemical composition (Table 1) shows the presence of kaolinite as a source of clay (also confirmed by the aluminum content), as well as the presence of hematite (Fe_2O_3 content of 11.7 %) and quartz. These characteristics are conditioned with good capacity for use of this soil as a base material for compacted barriers.

As for cement, significant amounts of SiO_2 (18 %) and CaO (66.2 %) identified by XRF were observed (Table 2). Through the cement physical-mechanical characterization, it was observed that the resistance and the initial and final handle times, 40 MPa, 160 and 265 min, respectively, agreed with the values proposed by the related standards (ABNT, 1991), setting initial time greater or equal to 60 min and the final one less than or equal to 600 min.

3.2 Chemical and mineralogical composition

The chemical composition of the tested samples indicates variations in the iron oxide (Fe_2O_3), calcium oxide (CaO) and sulfuric oxide (SO_3), in the test specimens submitted to acid percolation and under different values of cement content and specific weight.

The main effects of the cement content on the CaO and SO_3 contents were classified as significant by the variance analysis ($p < 0.05$) through ANOVA (analysis of variance). However, the specific weight variable and the interaction between both variables did not reveal a significant influence on the compound contents in the samples, as presented in Table 3. It was also verified that the cement content significantly interfered in the contents of CaO in all the layers of the samples, for both percolated by acid and not percolated ones ($p < 0.05$ for all this samples). In relation to SO_3, the influence of the cement content was only observed for the samples after the percolation test ($p < 0.05$). Such behavior indicates a possible interaction between CaO and SO_3 compounds, since the P values for CaO after percolation of sulfuric acid are higher than before. In addition, it indicates reactions with the percolated agent itself, with possible formation of Ca and S compounds.

In relation to Fe_2O_3, although the values did not reach the significance level of 5 %, there was a significant decrease of the P values between the percolated and non-percolated samples by sulfuric acid, which shows that there was an acid attack to this phase of iron oxides and solubilisation. Such behavior is more pronounced in relation to the unit weight variable, which is related to the variation of the number of voids and, consequently, it makes the passage of the percolating agent difficult. The same occurs in SiO_2 contents, although the P values are not so significant ($p > 0.05$). For Al_2O_3, the percolation of sulfuric acid re-

Table 1 - Soil chemical characterization (XRF) and LOI.

Oxide	Content(%)	Element	Content(%)
SiO_2	47.9	Si	22.4
Fe_2O_3	11.7	Fe	8.2
Al_2O_3	26.6	Al	14.1
CaO	< 0.1	Ca	< 0.1
TiO_2	1.7	Ti	1.0
K_2O	0.4	K	0.3
ZrO_2	0.1	Zr	< 0.1
SO_3	< 0.1	S	< 0.1
MgO	0.4	Mg	0.2
P_2O_5	0.1	P	< 0.1
MnO	< 0.1	Mn	< 0.1
Na_2O	< 0.1	Na	< 0.1
V_2O_5	< 0.1	V	< 0.1
LOI (1.000 °C)	10.9	O	50.6
		C	3.0

Table 2 - Chemical composition of Portland cement CPV-ARI.

Content (%)								LOI (1.000 °C) (%)	Insoluble residue (%)
SiO_2	Fe_2O_3	Al_2O_3	CaO	TiO_2	K_2O	SO_3	MgO		
18.0	2.68	4.19	66.2	0.28	0.8	1.79	2.43	3.58	0.7

Table 3 - Result of analysis of the variables' variance under study.

	0 % of H_2SO_4 (P values)					2 % of H_2SO_4 (P values)				
Superior	SiO_2	Fe_2O_3	Al_2O_3	CaO	SO_3	SiO_2	Fe_2O_3	Al_2O_3	CaO	SO_3
% Cement	0.406	0.627	0.388	< 0.001	1	0.132	0.284	0.729	0.062	0.029
Unit weight	1	1	1	1	1	0.21	0.09	0.327	0.116	0.116
Interaction	1	1	1	1	1	0.526	1	0.627	0.143	0.333
Middle	SiO_2	Fe_2O_3	Al_2O_3	CaO	SO_3	SiO_2	Fe_2O_3	Al_2O_3	CaO	SO_3
% Cement	0.212	0.637	0.97	< 0.001	1	0.411	0.208	0.091	0.024	0.009
Unit weight	1	0.637	0.97	0.727	1	0.373	0.123	0.928	1	0.758
Interaction	0.631	0.325	0.537	0.727	1	0.678	0.876	0.928	1	0.918
Inferior	SiO_2	Fe_2O_3	Al_2O_3	CaO	SO_3	SiO_2	Fe_2O_3	Al_2O_3	CaO	SO_3
% Cement	0.184	0.147	0.557	0.021	1	0.114	0.409	0.023	0.013	0.006
Unit weight	1	1	1	1	1	0.527	0.093	0.786	0.702	0.756
Interaction	1	1	1	1	1	0.787	0.479	0.536	0.702	0.608

sulted in the decrease of P values only for the middle and lower layers. The interaction between the two variables was not significant for any of the compounds.

The difference in the Fe_2O_3 content between the upper, middle and lower layers (Fig. 1) indicates that the acid attack promotes the dissolution of Fe_2O_3 present in the soil, which can cause up to half of the original contents in the upper layers to be reduced (Average from 12 to 7 %, Fig. 1a). Wang (2002) proposes that the acid attack in soil-cement mixtures is mainly due to the reaction involving the minerals, since the reaction of the sulphates with the cement is considered of second importance. This justifies the small variations between the Fe_2O_3 contents for each layer in relation to the increase of the cement content, as presented in Table 3, in which the variable cement content did not present significance in all the layers ($p > 0.05$).

Regarding the unit weight, there was a smaller reduction in the Fe_2O_3 content with the increase of the value of this variable, as presented in Fig. 1b. This fact is related to the decrease of the voids due to the increase of the compaction energy, as observed by (Korf *et al.*, 2018), which verified the decrease of the porosity of the specimens after being submitted to the vertical load. This eventually hampered the passage of the sticky agent and prevented the acid attack as well as the degradation of the compound. This relationship can be corroborated by the analysis of variance (Table 3) referring to the unit weight for this compound. The P values for all the layers are of the order of 10 %, indicating a relative part of statistical significance, as well as a significant difference when compared with the samples without percolation of sulfuric acid. For the samples without acid percolation, the studied variables had no influence on the Fe_2O_3 content.

Figure 2 shows the CaO content in relation to the variable cement content for samples with percolation of 0 and 2 % acid solution. No differences were observed between the studied layers for samples without acid percolation. With the analysis of Fig. 2a, the increase of cement content in the soil caused an increase in the CaO content. This is a result of the hydration reactions and cement hardening with the soil, providing the formation of this compound. This observation justifies the P values observed for the relation between CaO and cement contents (< 0.05). The samples percolated by sulfuric acid presented variation in the CaO content between the upper, middle and lower layers. In the upper portion a reduction in the CaO content was observed in relation to the results of the samples without percolation of sulfuric acid.

While analyzing the Fig. 2b, higher concentrations of this compound were observed in the lower layer compared to the upper layers and the non-percolated samples, which is possibly the result of a leaching process in which the CaO present in the upper layer was transported to the lower regions of the samples due to the acid attack or also because of chemical reactions resulting from chemical attack, thus

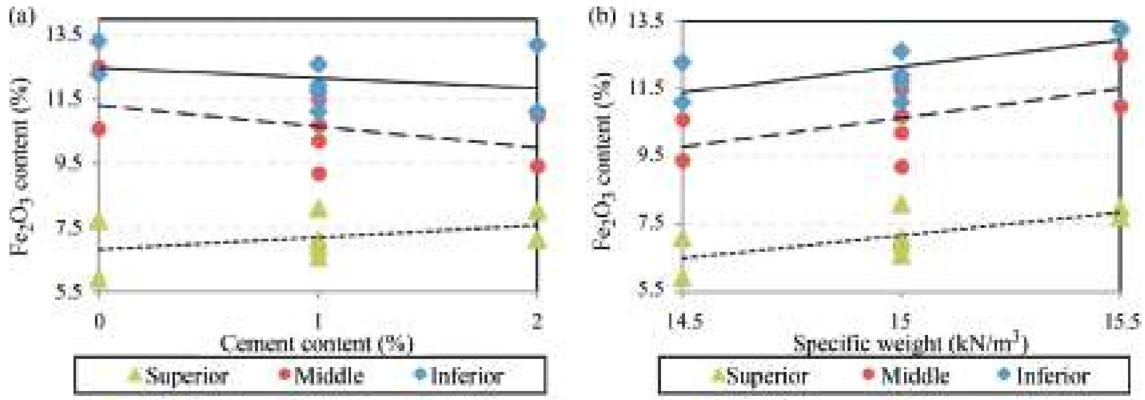

Figure 1 - Fe_2O_3 content for percolated samples per acid solution in relation to (a) cement content and (b) specific gravity.

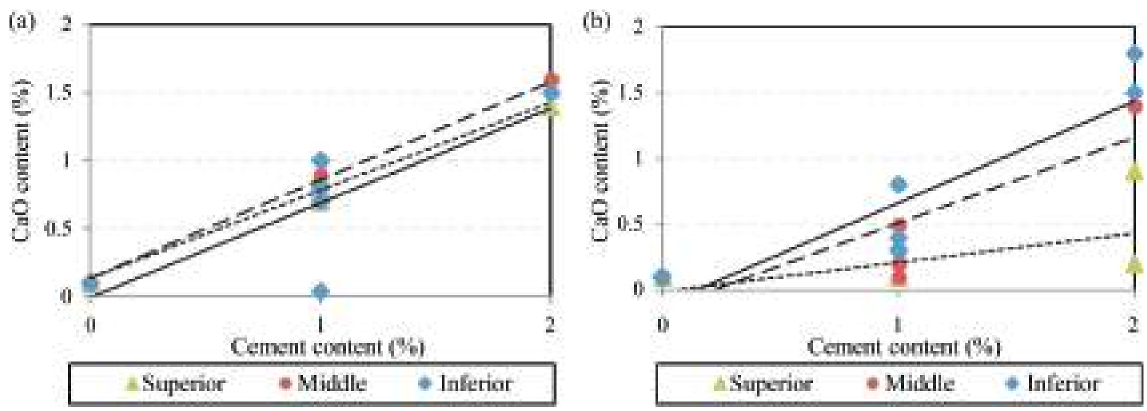

Figure 2 - CaO content in relation to the variable cement content for (a) samples without percolation - 0 % H_2SO_4 and (b) percolated samples - 2 % H_2SO_4.

forming new compounds. This behavior was also evidenced by observing the data of the statistical analysis presented in Table 3. The variable cement content for CaO showed higher significance (lower P values) in the lower layer of percolated samples by sulfuric acid. Since the increase of cement has a direct relation with the increase of CaO contents, the greater part of the compound has been deposited in the lower layer, resulting in the highest statistical significance observed. The unit weight variable did not influence on the contents of this compound, as corroborated by the statistical analysis (Table 3).

Figure 3 shows the behavior of the SO_3 content between the analyzed layers of samples percolated by sulfuric acid in relation to the variable cement content. The results show that the middle and lower layers had higher SO_3 levels (varying from average values of about 2 % to 4 %), as well as higher values were observed with increasing cement content. This fact may be related to chemical reactions involving CaO and the aggressive agent. Likewise, the statistical analysis presented in Table 3 indicated that the highest significance of the variable cement content was in the middle and lower layers (0.009 and 0.006, respectively), which reinforces the evidence presented.

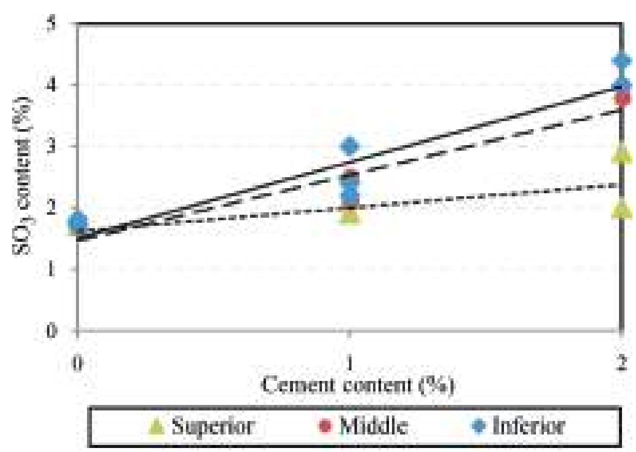

Figure 3 - SO_3 content in relation to the variable cement content in samples percolated with 2 % H_2SO_4.

The variables studied did not exert influence on the SO_3 content in the non-percolated samples (Table 3). Also, the unit weight variable had no influence on the samples submitted to acid leaching.

Figure 4 shows the XRD test data with the mineralogical identification for samples in the crystalline mineralogical phase with and without percolation of sulfuric acid. The test specimen selected for XRD analysis, with 0 % cement, was the one that underwent the most significant chemical modifications in the oxide content, evidenced in the XRF analyses. In this case, the mineralogical composition of the material with and without the percolation of H_2SO_4, no changes were detected in the crystalline mineralogical composition of the sample and that, according to the analysis, the samples remain with the clay minerals present (kaolinite essentially). This can be related to the low sensitivity of the XRD method for small variations of contents, since the changes in the chemical composition were proved by the chemical analyses.

The results obtained in this work resemble those obtained by MacCarthy *et al.* (2014) that analyzed the dissolution of hematite and quartz from a lateritic soil, with similar constitution of the samples from this study. MacCarthy *et al.* (2014) performed batch dissolution tests in a solution of 98 % H_2SO_4 and KNO_3 at pH 1 and at 25 °C and verified in their studies that the dissolution occurs more strongly in the oxides phase as iron oxide - hematite than in the quartz. The authors' argument also allows us to infer that the sulfuric acid concentration used in this work was only able to cause chemical changes in the oxide phase present on the surface of the particles, not leading to significant mineralogical changes on the crystalline phase (MacCarthy *et al.*, 2014).

Figure 5 shows the results of the TG / DTG / DSC technique for the test specimens with and without the presence of sulfuric acid, which most evidenced acid attack, respectively. For the acid-percolated sample, the loss of mass was more pronounced in Event 1, featured by pore water dehydration, which is related to the increase in porosity due to acid etching and particulate leaching, allowing greater accumulation of water in the voids and consequent loss of mass due to water dehydration. In the samples percolated by sulfuric acid, it was observed a reduction in the values of the thermal events observed for DSC, possibly due to the acid attack that promoted the reaction of certain compounds, like Ca, or even the dissolution of these ones. This behavior is corroborated by the XRF study in which it is possible to visualize the fall in CaO contents and a consequent formation of SO_3 for samples percolated by sulfuric acid. The major thermal events are shown in Figs. 5a and 5b.

Figure 6 shows the scanning electron microscopy image for the sample with 0 % of cement, but with non-percolation (0 %) and percolation (2 %) of sulfuric acid. The images, when compared to each other, do not allow the identification of significant modifications in the soil particles morphology. This fact corroborates the mineralogical and chemical analysis results, in which no significant changes were observed in the crystalline clay minerals structure, just only in the oxides fraction. This behavior is also related to the results presented in the XRD analysis, in which no differences were observed between the acid-percolated and acid-non-percolated samples.

Studies in the literature, such as Yang *et al.* (2013), show that, under extreme conditions of acid pH, soil-cement structures can present a high degree of degradation and even cracks. In this work, only changes in chemical composition were verified, no changes were observed in the crystalline clay minerals structure. No degradation of the microstructure and / or cracking was observed, possibly due to the stiffness of the structure due to the presence of cement, soil type and compaction, as well as a degree of acidity not so high (2 % sulfuric acid), which possibly had to be neutralized due to the presence of cement.

In the same way, Knop *et al.* (2008), when studying the soil-cement interactions in the presence of sulfuric acid, verified that the addition of cement to the soil is responsible

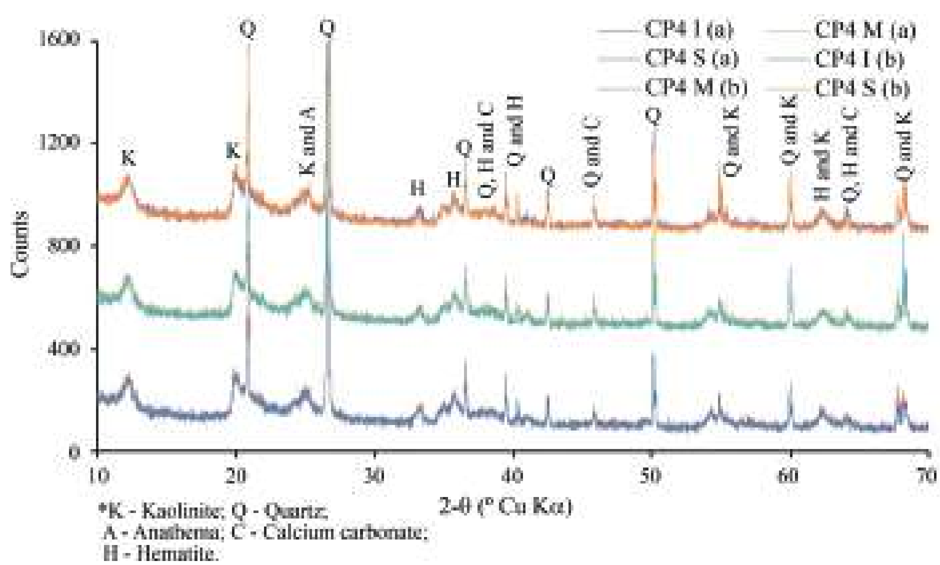

Figure 4 - XRD analysis and mineralogical identification of test specimen (a) 0 % H_2SO_4 and (b) 2 % H_2SO_4.

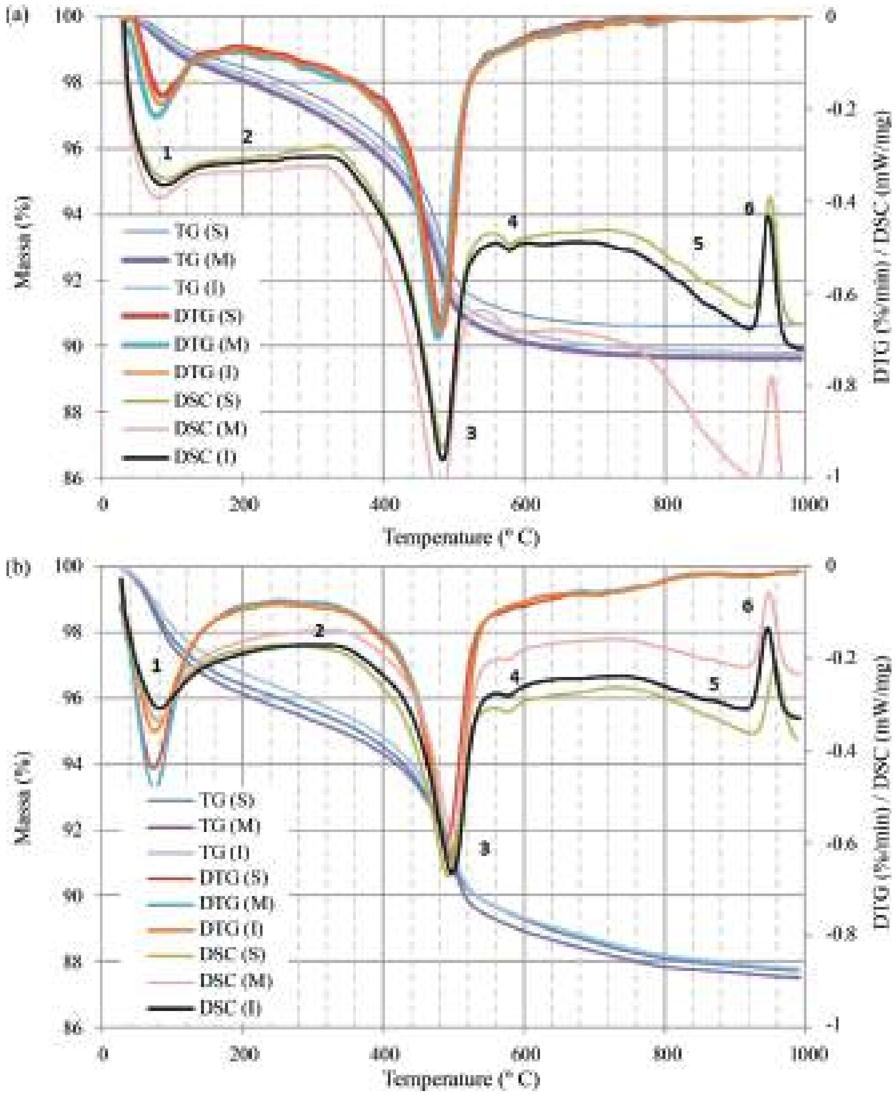

Figure 5 - TG / DTG / DSC Sample analysis (a) 0 % H_2SO_4 and (b) 2 % H_2SO_4. Thermal events: 1 - Dehydration of pore water; 2 - $CaSO_4$ (Karathanasis & Hajek, 1982); 3 - Kaolinite (Critter & Airoldi, 2006); 4 - Quartz (Bartenfelder & Karathanasis, 1989); 5 - $CaCO_3$ (Rowland, 1954; Todor, 1976); 6 - Amorphous aluminum phase crystallization (Kauffman & Dilling, 1950).

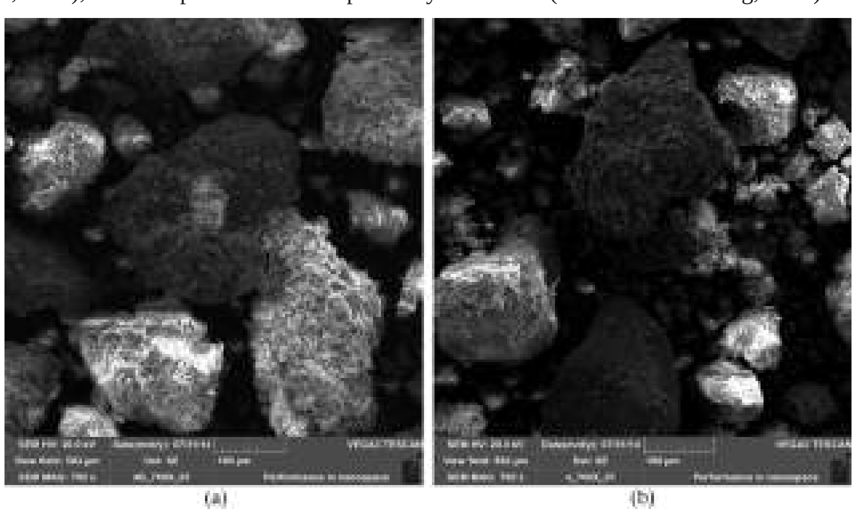

Figure 6 - Scanning electron microscopy (SEM) microstructure visualization of (a) sample containing 0 % sulfuric acid and (b) sample containing 2 % sulfuric acid.

for increasing the delay factor and the sulfuric acid distribution coefficient. This means that such mixtures have a greater ability to mitigate the spread of contaminants.

Also, the results presented here are similar to those found by Shaw & Jim Hendry (2009) in regard to the attack on the clay minerals structures. Shaw & Jim Hendry (2009) found that the greatest impact occurred on silicon compounds rather than on aluminum ones. Furthermore, these modifications may have occurred in a less expressive way, which makes it difficult to evaluate by certain techniques that do not have high sensitivity, such as X-ray diffraction.

4. Conclusion

This work presented the effect of the percolation of acid solutions in mature residual soils with different unit weights and cement contents. Significant changes were observed in the Fe_2O_3 present in the soil on the upper layers of samples which indicates that the acid attack promotes the dissolution of this iron oxide, this being mainly this being enhanced by the increasing unit weight, reduction in voids ratio and, consequently, contamination percolation delay. Besides, significant changes were observed in the CaO and SO_3 contents, indicating formation of Ca and S compounds in the lower layers of samples, being it also enhanced by higher unit weight and cement content addition. These results were also corroborated by the differential thermal and differential scanning calorimetry analyses (DTG / DSC). No changes were detected in the crystalline mineralogical phase and morphology of the studied soil, observing results with XRD and SEM analyses. Therefore, acidic attack caused changes to minerals as oxides and not in the crystalline structures of mineral clay and quartz.

References

ABNT (1991). Cimento Portland de alta resistência inicial - NBR 5733. Associação Brasileira de Normas Técnicas - ABNT, Rio de Janeiro, RJ, Brazil, 5 p.

ABNT (1997). Cimento Portland - Determinação da resistência à compressão - NBR 7215. Associação Brasileira de Normas Técnicas - ABNT, Rio de Janeiro, RJ, Brazil, 8 p.

ABNT (2001). Cimento Portland e outros materiais em pó - Determinação da massa específica - NBR NM 23. Associação Brasileira de Normas Técnicas - ABNT, Rio de Janeiro, RJ, Brazil, 15 p.

ABNT (2003). Cimento Portland - Determinação do tempo de pega - NBR NM 65. Associação Brasileira de Normas Técnicas - ABNT, Rio de Janeiro, RJ, Brazil, 4 p.

ABNT (2016). Solo - Análise Granulométrica - NBR 7181. Associação Brasileira de Normas Ténicas - ABNT, Rio de Janeiro, RJ, Brazil, 12 p.

Bartenfelder, D.C.; Karathanasis, A.D. (1989). A differential scanning calorimetry evaluation of quartz status in geogenic and pedogenic environments. Soil Science Society of America Journal, 53(3):961-967.

Bedin, J. (2010). Estudo do Comportamento Geomecânico de Resíduos de Mineração. Universidade Federal do Rio Grande do Sul. Ph.D. Thesis, Departamento de Engenharia Civil, Universidade Federal da Fronteira Sul, Porto Alegre, 205 p.

Broderick, G.P. & Daniel, D.E. (1990). Stabilizing compacted clay against chemical attack. Journal of Geotechnical and Geoenvironmental Engineering, 116(10):1549-1567.

Critter, S.A.M. & Airoldi, C. (2006). Thermal analysis of Brazilian tropical soils originating from different sources. Journal of the Brazilian Chemical Society, 17(7):1250-1258.

Fall, M.; Célestin, J.C. & Han, F.S. (2009). Suitability of bentonite-paste tailings mixtures as engineering barrier material for mine waste containment facilities. Minerals Engineering, 22(9-10):840-848.

Favaretti, M.; Moraci, N. & Previatello, P. (1994). Effects of leachate on the hydraulic and mechanical behavior of clay liners. Proc. 1st Congress on Environmental Geotechnics, Alberta, Canada, pp. 221-226.

Forcelini, M.; Garbin, G.R.; Faro, V.P. & Consoli, N.C. (2016). Mechanical behavior of soil cement blends with Osorio sand. Procedia Engineering, 143(1):75-81.

Helson, O.; Eslami, J.; Beaucour, A.L.; Noumowe, A. & Gotteland, P. (2018). Hydro-mechanical behaviour of soilcretes through a parametric laboratory study. Construction and Building Materials, 166(1):657-667.

Hueckel, T.; Kaczmarek, M. & Caramuscio, P. (1997). Theoretical assessment of fabric and permeability changes in clays affected by organic contaminants. Canadian Geotechnical Journal, 34(4):588-603.

ICDD. International Centre for Diffraction Data (2003). PDF-2 database.

Iravanian, A. & Bilsel, H. (2016). Tensile Strength properties of sand-bentonite mixtures enhanced with cement. Procedia Engineering, 143(1):111-118.

Joshi, K.; Kechavarzi, C.; Sutherland, K.; Ng, M.Y.A.; Soga, K. & Tedd, P. (2010). Laboratory and in situ tests for long-term hydraulic conductivity of a cement-bentonite cutoff wall. Journal of Geotechnical and Geoenvironmental Engineering, 136(4):562-572.

Karathanasis, A.D. & Hajek, B.F. (1982). Revised methods for rapid quantitative determination of minerals in soil clays. Soil Science Society of America Journal, 46(1):419-425.

Kauffman, A.J. & Dilling, D. (1950). Differential thermal curves of certain hydrous and anhydrous minerals, with a description of the apparatus used. Economic Geology, 45(3):222-244.

Knop, A.; VanGulck, J.; Heineck, K.S. & Consoli, N.C. (2008). Compacted artificially cemented soil-acid leachate contaminant interactions: Breakthrough curves and transport parameters. Journal of Hazardous Materials, 155(1-2):269-276.

Korf, E.P.; Prietto, P.D.M.; Silveira, A.A.; Ulsen, C. & Bragagnolo, L. (2018). Porosity changes of compacted soil percolated with acidic leachate. Soils and Rocks, 41(3):369-377.

Lloret, A.; Villar, M.V.; Sanchez, M.; Gens, A.; Pintado, X. & Alonso, E. (2003). Mechanical behaviour of heavily compacted bentonite under high suction changes. Geotechnique, 53(1):27-40.

MacCarthy, J.; Nosrati, A.; Skinner, W. & Addai-Mensah, J. (2014). Dissolution and rheological behaviour of hematite and quartz particles in aqueous media at pH 1. Chemical Engineering Research and Design, Institution of Chemical Engineers, 92(11):2509-2522.

Montgomery, D.C. (2001). Design and Analysis of Experiments. John Wiley & Sons, New York, 790 p.

PANalytical (2007). PAN-ICSD PANalytical Inorganic Crystal Structure Database. Almelo, The Netherlands.

Romero, E. (2013). A microstructural insight into compacted clayey soils and their hydraulic properties. Engineering Geology, 165:3-19.

Romero, E. & Simms, P.H. (2009). Microstructure investigation in unsaturated soils: A review with special attention to contribution of mercury intrusion porosimetry and environmental scanning electron microscopy. Geotechnical and Geological Engineering, 26(6):705-727.

Rowland, R.A. (1954). Differential thermal analysis of clays and carbonates. Clays and Clay Technology, 169:151-164.

Rubinos, D.A.; Spagnoli, G. & Barral, M.T. (2016). Chemical and environmental compatibility of red mud liners for hazardous waste containment. International Journal of Environmental Science and Technology, 13(3):773-792.

Shaw, S.A. & Jim Hendry, M. (2009). The impact of sulfuric acid on element migration and mineralogy of compacted clays: pH 1.0 to -3.0. Applied Geochemistry, 24(10):1978-1989.

Streck, E.V.; Kämpf, N.; Klamt, E.; Nascimento, P.C.; Schneider, P.; Giasson, E. & Pinto, L.F.S. (2008). Solos do Rio Grande do Sul. Emater, Porto Alegre, 222 p.

Šucha, V.; Dubiková, M.; Cambier, P.; Elsass, F. & Pernes, M. (2002). Effect of acid mine drainage on the mineralogy of a dystric cambisol. Geoderma, 110(3-4):151-167.

Tedesco, M.J.; Gianello, C.; Bissani, C. A.; Bohnen, H. & Volkweiss, S. J. (1995). Análises de solo, plantas e outros materiais: Boletim técnico nº 5. Departamento de Solos, Faculdade de Agronomia, UFRGS, Porto Alegre, 174 p.

Todor, D.N. (1976). Thermal analysis of minerals. Abacus Press, Kent, 256 p.

Wang, L. (2002). Cementituous Stabilization of Soils in the Presence of Sulfate. M.Sc. Dissertation, Department of Civil and Environmental Engineering, Louisiana State University and Agricultural and Mechanical College, Louisiana, 118 p.

Yang, Y.; Wang, G.; Xie, S.; Tu, X. & Huang, X. (2013). Effect of mechanical property of cemented soil under the different pH value. Applied Clay Science, 79(1):19-24.

SOILS and ROCKS
An International Journal of Geotechnical and Geoenvironmental Engineering

Publication of
ABMS - Brazilian Association for Soil Mechanics and Geotechnical Engineering
SPG - Portuguese Geotechnical Society
Volume 43, N. 1, January-March 2020

Author index

Conheça mais:
www.geobrugg.com/pt/taludes

GEOBRUGG®
BRUGG
Safety is our nature

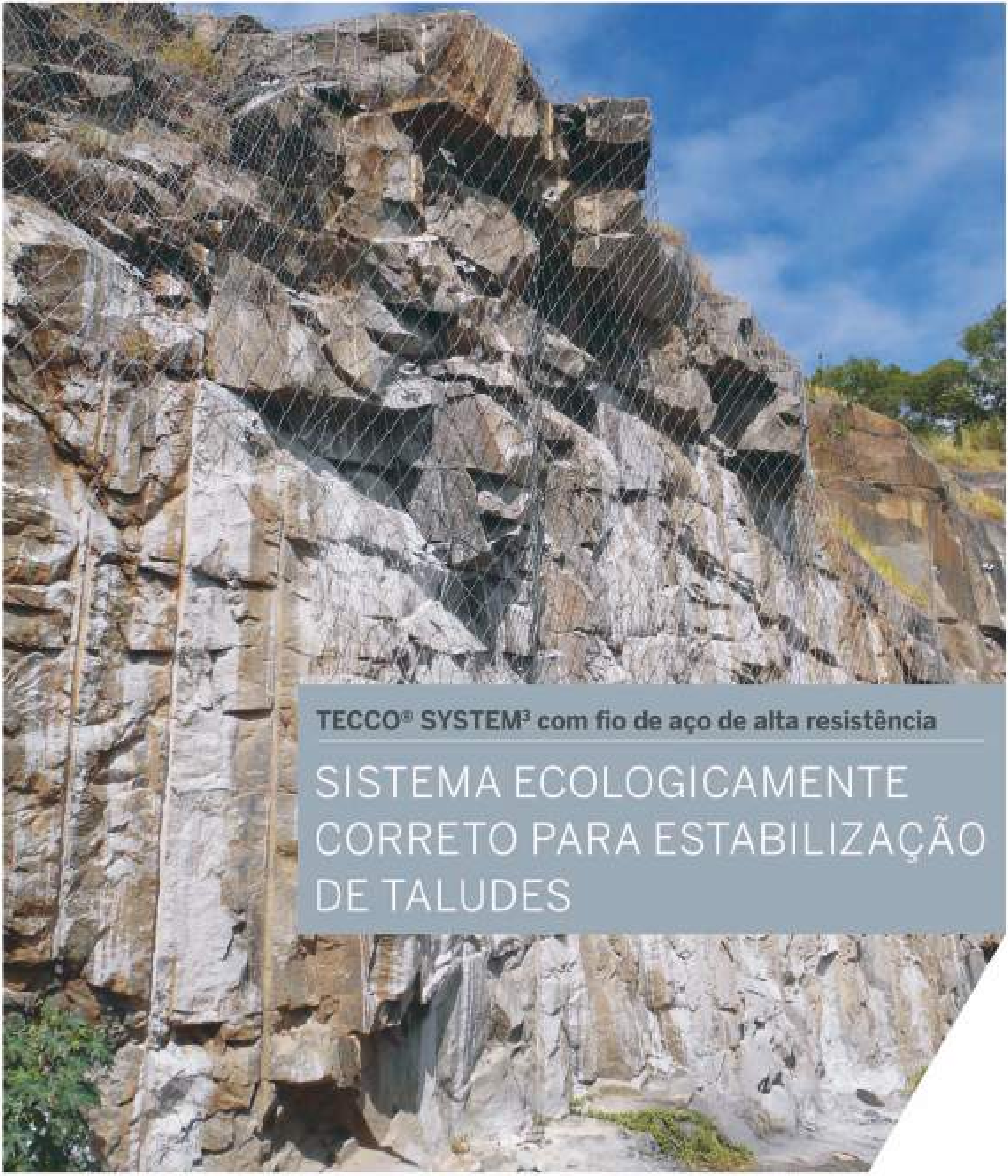

TECCO® SYSTEM³ com fio de aço de alta resistência

SISTEMA ECOLOGICAMENTE CORRETO PARA ESTABILIZAÇÃO DE TALUDES

Geobrugg AG | Rua Visconde de Pirajá, 82 sl 606 | 22410-003 - Rio de Janeiro, Brasil | Phone + 55 21 3624 1449 | www.geobrugg.com | info@geobrugg.com

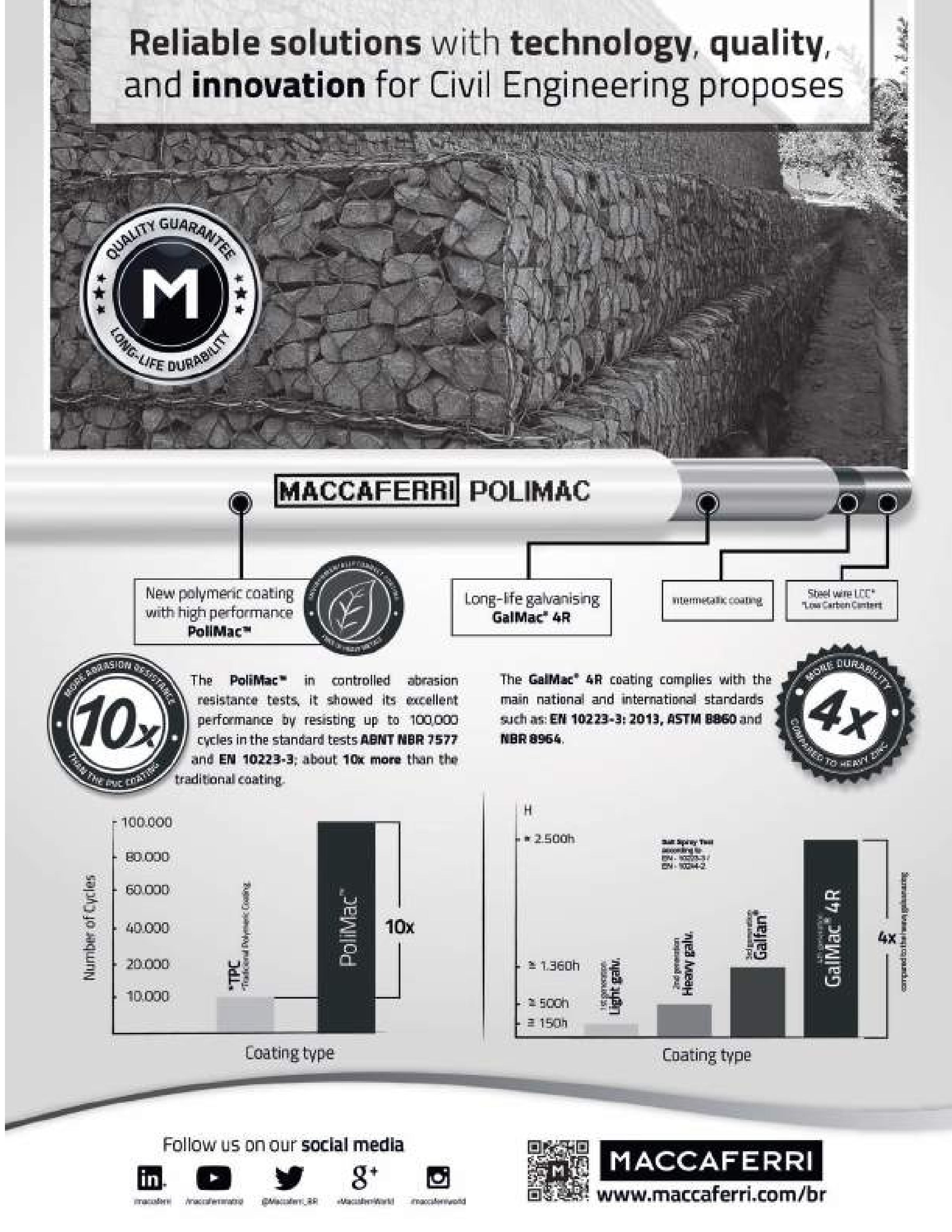

Reliable solutions with technology, quality, and innovation for Civil Engineering proposes
QUALITY GUARANTEE
M
LONG-LIFE DURABILITY
MACCAFERRI POLIMAC
New polymeric coating with high performance PoliMac™
Long-life galvanising GalMac® 4R
Intermetallic coating
Steel wire LCC* *Low Carbon Content
MORE ABRASION RESISTANCE 10x THAN THE PVC COATING
The PoliMac™ in controlled abrasion resistance tests, it showed its excellent performance by resisting up to 100,000 cycles in the standard tests ABNT NBR 7577 and EN 10223-3; about 10x more than the traditional coating.
The GalMac® 4R coating complies with the main national and international standards such as: EN 10223-3: 2013, ASTM B860 and NBR 8964.
MORE DURABILITY 4x COMPARED TO HEAVY ZINC
100.000
80.000
60.000
40.000
20.000
10.000
Number of Cycles
*TPC *Traditional Polymeric Coating
PoliMac™
10x
Coating type
H
≈ 2.500h
≅ 1.360h
≅ 500h
≅ 150h
Light galv.
Heavy galv.
Galfan®
GalMac® 4R
4x
Coating type
Follow us on our social media
www.maccaferri.com/br
MACCAFERRI

Volume 43, N. 1, January-March 2020

Table of Contents